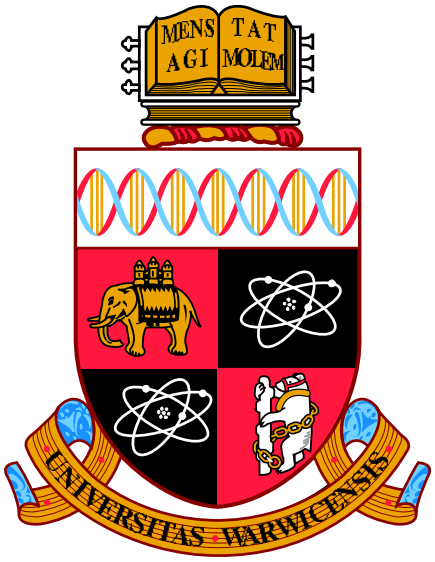


# Characterisation of Half-Metallic Thin Films using Polarised Neutron Reflectometry

by

**Stephanie E. Glover**

**Thesis**

Submitted to the University of Warwick

for the degree of

**Doctor of Philosophy**

**Department of Physics**

June 2018

THE UNIVERSITY OF WARWICK

# Contents

**List of Figures** iv

**List of Tables** viii

**Acknowledgments** ix

**Declarations** xiv

**Abstract** xvii

**Abbreviations** xviii

**Chapter 1 Introduction** 1

1.1 Overview of Thesis . . . . . 5

**Chapter 2 Complementary Techniques** 6

2.1 Magnetometry . . . . . 6

2.2 Microscopy . . . . . 7

2.2.1 Transmission Electron Microscopy . . . . . 8

2.2.2 High Annular Angular Dark Field Imaging . . . . . 8

2.2.3 Electron Energy Loss Spectroscopy . . . . . 8

2.3 X-ray Diffraction . . . . . 9

2.3.1 X-ray Reflectivity . . . . . 11

2.4 Polarised Neutron Reflectivity . . . . . 12

2.4.1 Complementary Techniques Summary . . . . . 14

**Chapter 3 Reflectivity Theory** 15

3.1 Optical Reflectivity . . . . . 16

3.2 X-ray Reflectivity . . . . . 19

3.2.1 X-ray Fresnel and Parratt Equations . . . . . 21

3.3 Neutron Reflectivity . . . 23
3.3.1 Unpolarised Neutrons . . . 24
3.3.2 Polarised Neutrons . . . 25
3.3.3 Roughness . . . 27
3.3.4 GenX Reflectivity Package . . . 30

**Chapter 4 Fitting of Reflectivity Data** **37**
4.1 GenX Setup . . . 38
4.1.1 GenX Start-up Options . . . 38
4.1.2 Inserting Data Sets . . . 40
4.1.3 Defining Instrument Settings . . . 41
4.1.4 Setting the Sample . . . 43
4.1.5 Setting the FOM and Computational Power . . . 45
4.1.6 Sample Parameter Grid Import. . . . 46
4.2 Fitting the Data . . . 47
4.2.1 Setting Custom Parameters . . . 48
4.2.2 Data Fit Continuation . . . 48

**Chapter 5 $Co_2FeAl_{0.5}Si_{0.5}$ grown on Si(111)** **56**
5.1 Introduction . . . 56
5.2 Complementary Techniques . . . 60
5.2.1 Growth . . . 60
5.2.2 Microscopy . . . 60
5.2.3 X-ray Diffraction . . . 64
5.2.4 X-ray Reflectivity . . . 66
5.2.5 Magnetometry . . . 67
5.2.6 Polarised Neutron Reflectivity . . . 68
5.3 Reflectivity Data Fitting . . . 69
5.3.1 Model 1 with Nominal Composition . . . 73
5.3.2 Model 2 with EELS compositional interface profile . . . 73
5.3.3 Model 3 with EELS film composition . . . 76
5.3.4 $Co_2FeAl_{0.5}Si_{0.5}$ Model comparison . . . 76
5.4 Conclusions . . . 87

**Chapter 6 $Co_2FeAl_{0.5}Si_{0.5}$ grown on Ge(111)** **89**
6.1 Introduction . . . 89
6.2 $Co_2FeAl_{0.5}Si_{0.5}$ grown on Ge(111) . . . 90
6.2.1 Transmission Electron Microscopy . . . 90

6.2.2 High Angular Annular Dark Field and Electron Energy Loss Spectroscopy . . . 90
6.2.3 Partial Density of States . . . 93
6.2.4 X-ray Diffraction . . . 94
6.2.5 X-ray Reflectivity . . . 96
6.2.6 Fitting . . . 96
6.2.7 Conclusion . . . 112
6.3 $Co_2FeAl_{0.5}Si_{0.5}$ grown Ge(111) - "Ge2" . . . 113
6.3.1 X-ray Diffraction and X-ray Reflectivity . . . 113
6.3.2 Reflectivity fitting . . . 115
6.3.3 Conclusion . . . 124

**Chapter 7 $Fe_3O_4$ grown on MgO(111) 125**
7.1 Introduction . . . 125
7.2 MgO Structural Study . . . 128
7.2.1 MgO 950 . . . 132
7.2.2 MgO 400 . . . 140
7.2.3 MgO 300 . . . 144
7.2.4 MgO Sample Comparison . . . 152
7.3 Verwey Transition . . . 157
7.3.1 Low Temperature Polarised Neutron Reflectivity . . . 158
7.3.2 Low Temperature Comparison . . . 167
7.4 Conclusion . . . 168

**Chapter 8 Conclusion 169**

# List of Figures


1.1 Magnetic tunnel junction . . . 2
1.2 Density of States . . . 4

2.1 Schematic of the available rotations in a diffraction experiment. . . . 10
2.2 Polarising and spin-flip options for PNR experimental setup. . . . 13
2.3 Polarised neutron reflectivity geometry at sample. . . . 14

3.1 Snell's law . . . 17
3.2 Fresnel coefficients for multiple layers. . . . 19
3.3 Interference fringes. . . . 23
3.4 Interference fringes for XRR and PNR. . . . 27
3.5 Roughness comparions Sub1:Sur1 vs Sub4:Sur4. . . . 28
3.6 Roughness comparions Sub1:Sur1 vs Sub4:Sur1. . . . 29
3.7 Roughness comparions Sub1:Sur1 vs Sub1:Sur4. . . . 29
3.8 Roughness comparions Sub1:Sur1 vs Sub1:Sur8. . . . 30
3.9 SLD corresponding to interference fringes. . . . 31
3.10 SLD vs sample structure. . . . 33
3.11 Footprint correction. . . . 34
3.12 FOM scan. . . . 36

4.1 GenX Model Loader . . . 38
4.2 GenX Window Labels 1-19. . . . 39
4.3 GenX sample tab, buttons 20-27. . . . 41
4.4 Instrument editor window . . . 42
4.5 GenX Simulations Tab. . . . 43
4.6 GenX sample tab. . . . 44
4.7 GenX optimizer window. . . . 45
4.8 GenX parameter grid. . . . 47
4.9 GenX model parameter first guess. . . . 49

4.10 GenX first minimised fit. . . . . 50
4.11 GenX model showing manual modification after first fitting procedure. 51
4.12 GenX model after first manual refit. . . . . 52
4.13 GenX model with substrate, film and surface fitted using logR1. . . 53
4.14 Manually fitted GenX model with substrate, interface, film and surface. 53
4.15 Final GenX model. . . . . 54
4.16 SLD coresponding to GenX final model. . . . . 55

5.1 CFAS crystal structure. . . . . 57
5.2 CFAS spin polarised DOS. . . . . 58
5.3 Visual representation of X-ray and neutron SL for Co, Fe, Al, Si. . . 59
5.4 CFAS / Si(111) 50 nm STEM . . . . . 61
5.5 STEM from a section of CFAS/Si interface 2 nm. . . . . 61
5.6 CFAS / Si HAADF STEM . . . . . 62
5.7 CFAS / SI SAD. . . . . 63
5.8 CFAS / Si EELS. . . . . 63
5.9 CFAS/Si(111) $\theta - 2\theta$ scan aligned to the Si(111) substrate peak. . . 66
5.10 CFAS/Si $\theta - 2\theta$ aligned to CFAS(200). . . . . 66
5.11 CFAS / Si XRR data. . . . . 67
5.12 CFAS / Si magnetometry data. . . . . 68
5.13 CFAS / Si reflectivity data. . . . . 69
5.14 CFAS / Si fitted reflectivity data. . . . . 71
5.15 CFAS / Si SLDs. . . . . 72
5.16 CFAS / Si EELS data conversion to neutron and X-ray SL. . . . . 75
5.17 CFAS / Si Model 2 and 3 reflectivity fit comparison. . . . . 78
5.18 CFAS / Si Model 2 and 3 SLD comparison. . . . . 79
5.19 CFAS / Si Model 2 and 3 reflectivity fit comparison. . . . . 81
5.20 CFAS / Si Model 2 and 3 SLD comparison. . . . . 82
5.21 CFAS / Si EELS surface map. . . . . 83
5.22 CFAS / Si manually edited Model 1 reflectivity fit and SLD. . . . . 86

6.1 CFAS / Ge low magnification HAADF STEM and SAD. . . . . 91
6.2 CFAS / Ge HAADF STEM . . . . . 92
6.3 CFAS / Ge EELS . . . . . 92
6.4 CFAS / Ge PDOS . . . . . 94
6.5 CFAS / Ge $\theta - 2\theta$ scan. . . . . 95
6.6 CFAS / Ge $\theta - 2\theta$ aligned to CFAS(200) . . . . . 96
6.7 CFAS / Ge XRR. . . . . 97

6.8 CFAS / Si and Ge reflectivity data. . . . . 99
6.9 CFAS / Ge Model 1 reflectivity fit and SLD. . . . . 101
6.10 CFAS / Ge Model 2 reflectivity fit and SLD. . . . . 102
6.11 CFAS / Ge Model 3 reflectivity fit and SLD. . . . . 103
6.12 CFAS / Ge Model 4 reflectivity fit and SLD. . . . . 104
6.13 CFAS / Ge Model 5 reflectivity fit and SLD. . . . . 105
6.14 CFAS / Ge Model 6 reflectivity fit and SLD. . . . . 107
6.15 CFAS / Si and Ge SLD comparison. . . . . 109
6.16 CFAS / Ge Model 4 and 6 SLD comparison. . . . . 111
6.17 CFAS / Ge2 $\theta - 2\theta$ scan. . . . . 114
6.18 CFAS / Ge2 XRR data. . . . . 114
6.19 CFAS / Ge and Ge2 reflectivity data comparison. . . . . 115
6.20 CFAS / Ge2 Model 1 reflectivity fit and SLD. . . . . 117
6.21 CFAS / Ge2 Model 2 reflectivity fit and SLD. . . . . 118
6.22 CFAS / Ge2 Model 3 reflectivity fit and SLD. . . . . 119
6.23 CFAS / Ge and Ge2 SLD comparison. . . . . 121
6.24 CFAS / Ge2 example of invalid model. . . . . 123

7.1 $Fe_3O_4$ RT crystal structure . . . . . 126
7.2 Visual representation of X-ray and neutron SL for Fe, O and Mg. . . 127
7.3 MgO magnetometry measurements. . . . . 128
7.4 All MgO samples: XRR data comparison . . . . . 130
7.5 All MgO samples: PNR data comparison . . . . . 131
7.6 MgO 950 XRR . . . . . 133
7.7 MgO 950 $\theta - 2\theta$. . . . . 134
7.8 MgO 950: MgO(111) $\omega$ rock. . . . . 135
7.9 MgO 950: MgO(111) texture map. . . . . 136
7.10 MgO 950: $Fe_3O_4$(400) texture map. . . . . 136
7.11 MgO 950 TEM . . . . . 138
7.12 MgO 950 fitted reflectivity with corresponding SLDs. . . . . 139
7.13 MgO 400 XRR. . . . . 140
7.14 MgO 400 $\theta - 2\theta$. . . . . 141
7.15 MgO 400: MgO(111) texture map. . . . . 142
7.16 MgO 400: $Fe_3O_4$(400) texture map. . . . . 143
7.17 MgO 400 TEM. . . . . 144
7.18 MgO 400 fitted reflectivity and SLDs. . . . . 145
7.19 MgO 300 XRR. . . . . 146

7.20 MgO 300 $\theta - 2\theta$ scan. . . . . 147
7.21 MgO 300 $\theta - 2\theta$aligned to $Fe_3O_4$(111). . . . . 148
7.22 MgO 300: MgO(111) texture map. . . . . 148
7.23 MgO 300: $Fe_3O_4$(400) texture map. . . . . 149
7.24 MgO 300: $Fe_3O_4$(333) texture map. . . . . 150
7.25 MgO 300 fitted reflectivity . . . . . 152
7.26 All MgO $\theta - 2\theta$ aligned to $Fe_3O_4$(400) peak comparison. . . . . 154
7.27 All MgO samples SLD . . . . . 155
7.28 Magnetometry measurements divided by MSLD integral. . . . . 156
7.29 MgO 950 low T PNR. . . . . 158
7.30 MgO low T PNR asymmetry. . . . . 159
7.31 MgO 400 low T PNR data. . . . . 160
7.32 MgO 400 low T asymmetry. . . . . 160
7.33 MgO 400 low T PNR fits. . . . . 161
7.34 MgO 400 low T SLDs. . . . . 162
7.35 MgO 300 low T PNR data. . . . . 164
7.36 MgO 300 low T asymmetry. . . . . 164
7.37 MgO 300 low T PNR fits. . . . . 165
7.38 MgO 300 low T SLDs. . . . . 166

# List of Tables


2.1 Different PNR experimental configurations. . . . . 13
2.2 Complementary techniques contribution. . . . . 14

4.1 GenX buttons 1-27. . . . . 40

5.1 $Co_2FeAl_{0.5}Si_{0.5}$ and Si nominal parameters. . . . . 59
5.2 $Co_2FeAl_{0.5}Si_{0.5}$ / Si(111) DFT. . . . . 64
5.3 $Co_2FeAl_{0.5}Si_{0.5}$ / Si PNR model parameter comparison. . . . . 77

6.1 CFAS / Ge nominal parameters . . . . . 90
6.2 CFAS / Ge SDOS . . . . . 93
6.3 CFAS / Ge complementary techniques parameter summary. . . . . 98
6.4 CFAS / Ge Model FOM comparison. . . . . 100
6.5 CFAS / Ge2 Model FOM comparison. . . . . 116

7.1 $Fe_3O_4$ MgO nominal parameters. . . . . 127
7.2 $Fe_3O_4$ thickness comparison from different experimental techniques. 132
7.3 $Fe_3O_4$ lattice constants above and below $T_V$. . . . . 157
7.4 MgO sample $\mu_B$/f.u. comparison. . . . . 167

# Acknowledgments

I don't think anyone quite realises how much support I needed from my family and friends during my PhD, particularly how much I needed everyone the final few months. I take this opportunity to give short thanks (there is an extended version).

To my supervisor Gavin Bell, thank you for all the support you gave me, including the seemingly unlimited "piggy bank" that allowed my trip to Grenoble amongst all other conferences I went to. I appreciated the random "pub o'clocks" and turning up with the yard glass at my viva celebrations in full PPE!

Tom Hase, you were always there to help me out during my last minute panics before deadlines. It's as if you turned up at the perfect moment, a little like a fairy godmother (but not quite). We had some great trips to beamtimes and conferences (esp New Orleans), and I won't forget our food and alcohol tasting sessions.

Thomas Saerbeck, this thesis wouldn't exist without you. You seem to be the only person in the world who understands my research, and was able to decode "Steph" in record time, and worse, "Steph attempting science sans sleep". Danke!

To my parents Ange and Jim, your love and support have enabled me to get through the entirety of my academic career and especially in this last year when I really depended on you. Thank you. Sorry I didn't give it up for a life of cleaning your dishes, Mum. To my brother David, thanks for your encouragement to face all of the challenges that lie ahead of me; and throw me a mars bar when I'm done. I would also like to thank my Nanar and Grandad for the support and "Nanar pie" I often get when I visit. To my Nan, I'd like to thank her for the many holidays and maths exercises we used to do when I was younger. I truly believe this is why I have always enjoyed maths and problem solving.

To Natalie, thanks for being there for me since we were 11, I love you lots. Heather, you're always there for emotional support even if we think each other are mad, thank you. To Lexie, you and your Sheffield clan have made this last year and a half so adventurous, and I have really appreciated the distractions. Thank you for your support and checking in on me. Thank you to my Moorlands 6th form friends. You took me under your wing when I needed you and we have had many happy memories since; parties, hen do's, weddings, and there will be babies in the near future. Andrew, thank you for the travel bug and continued support.

For your ability to always get me to smile, and your magic powers that make all my worries disappear when I'm around you, thank you Thomas Hine.

PS001: the theory boys, thank you for adopting me and not forgetting about me when organising events (most of the time anyway...). To the Physics Pub Wednesday Karaoke gang, thank you for endless drunken laughter that kept me going, even when I couldn't make it out to the Duck.

Thanks to Matthew Rawlings for being there every single day ($\pm$ 1) for the past two years. You know exactly how important you've been to me. *star-owl*

My Physics possé, you have been my best friends throughout my Ph.D. We've had the most random conversations at lunch, holidayed, had stag dos, been groomsmen and I hope we stay friends for eternity. I don't like to single out any of the bros out, but an extra special thanks has to goes to my postdoc and best friend Chris Burrows. You have been there for me for everything I might ever need you for. You taught me how to use the experimental equipment, proof read almost everything I've ever written, helped me on my beamtimes, let me chill at yours at the weekend, and let me meow at you endlessly including all the "thingies" and "wotsits". I wouldn't have finished this thesis without your support, and you never disappeared even after you'd left Warwick (possibly because I'm a stalker-bro). You probably know me better than anybody, and for that I apologise. :P <3

To my other close friends, my thanks to you are also important, but it would take another thesis to explain, so I have included a collection of photos so you don't feel unloved. I needed every single one of you.

# Declarations

I declare that this thesis reports my work between October 2013 and January 2018 under the supervision of Dr Gavin Bell. The studies in this thesis have not been submitted either wholly or in part, in this or any other academic institution for the admission of a higher degree. Where reported work is from another source, it is referenced or declared below.

Chapter 5, this work has been previously published and builds on thesis work from:

- S. E. Glover, T. Saerbeck, B. Kuerbanjiang, A. Ghasemi, D. Kepaptsoglou, Q. M. Ramasse, S. Yamada, K. Hamaya, T. P. A. Hase, V. K. Lazarov, and G. R. Bell. *Magnetic and structural depth profiles of Heusler alloy $Co_2FeAl_{0.5}Si_{0.5}$ epitaxial films on Si(111).* Journal of Physics: Condensed Matter, 30(6):065801, 2018.

- B. Kuerbanjiang, Z. Nedelkoski, D. Kepaptsoglou, A. Ghasemi, S. E. Glover, S. Yamada, T. Saerbeck, Q. M. Ramasse, J. Hasnip, T. P. A. Hase, G. R. Bell, K. Hamaya, and A. Hirohata. *The role of chemical structure on the magnetic and electronic properties of $Co_2FeAl_{0.5}Si_{0.5}$.* Applied Physics Letters, 108(172412), 2016.

- Z. Nedelkoski. *The atomic and spin-electronic structure of interfaces and extended structural defects in the Co-based full Heusler alloys.* Ph.D. thesis, University of York, Jan 2017.

where specific acknowledgements of work go to

- Sample growth - Shinya Yamada, (Osaka University, Japan).
- DOS calculations - Zlatko Nedelkoski (University of York U.K.).
- DFT calculations - Zlatko Nedelkoski and Phil Hasnip (University of York U.K.).
- Microscopy samples prepared by Arsham Ghasemi (University of York U.K.).
- TEM, SAD, XRD (Figure 5.10) images - Balati Kuerbanjiang (University of York U.K.).
- AB STEM and EELS - Demie Kepaptsoglou (SuperSTEM EPSRC national facility, Daresbury U.K.).

Chapter 6, part of this work has previously been published and builds on thesis work from:

- Z. Nedelkoski, B. Kuerbanjiang, S. E. Glover, A. M. Sanchez, D. Kepaptsoglou, A. Ghasemi, C. W. Burrows, S. Yamada, K. Hamaya, Q. M. Ramasse, P. J. Hasnip, T. P. A. Hase, A. Bell, G. R. Hirohata, and V. K. Lazarov. *Realisation of magnetically and atomically abrupt half-metal/semiconductor interface: $Co_2FeAl_{0.5}Si_{0.5}$ / Ge(111).* Scientific Reports, 6:37282, 2016.
- Z. Nedelkoski. *The atomic and spin-electronic structure of interfaces and extended structural defects in the Co-based full Heusler alloys.* Ph.D. thesis, University of York, Jan 2017.

where specific acknowledgements go to

- Sample growth - Shinya Yamada, (Osaka University, Japan).
- DOS and DFT calculations - Zlatko Nedelkoski (University of York U.K.).
- Microscopy samples prepared by Arsham Ghasemi (University of York U.K.).
- TEM, SAD, XRD (Figure 5.10) images - Balati Kuerbanjiang (University of York U.K.).

- STEM and EELS - Demie Kepaptsoglou (SuperSTEM EPSRC national facility, Daresbury U.K.).

Chapter 7 builds on work from thesis:

- D. Gilks. *Atomistic study of magnetite thin film interfaces and defects for Spintronic applications.* Ph.D. thesis, University of York, June 2015.

where specific acknowledgements go to

- Sample growth - Dan Gilks (University of York).
- Microscopy samples prepared by Dan Pingstone and Balati Kuerbanjiang (University of York).
- TEM images - Leonardo Lari (University of York).

# Abstract

Half-metallic (HM) materials are promising candidates for spintronic devices due to their 100 % spin polarisation at the Fermi level and their high $T_C$, making them robust to thermal fluctuations. For HM to be used in devices, they need to be in thin film form and retain both SP and magnetisation through the film and at the substrate/interface. High quality thin films of both $Co_2FeAl_{0.5}Si_{0.5}$ and $Fe_3O_4$ described in this thesis have been grown by collaborators, and are theoretically predicted to be HM. HM in a film can be indicated by measurements of the magnetic moment. This thesis shows that polarised neutron reflectivity (PNR) data from these HMs can be fitted to obtain the magnetisation profiles perpendicular to the surface.

PNR measurements are fitted simultaneously with X-ray reflectivity. Complementary techniques such as microscopy, magnetometry and X-ray diffraction are used in order to limit the fit, give confidence in the extracted structural and magnetic profiles and to help explain the underlying reasons for the magnetic properties. One chapter is dedicated to describing the set up and methodology of reflectivity fitting.

$Co_2FeAl_{0.5}Si_{0.5}$ grown on Si(111) has both extended surface and interface regions, the latter due to Si diffusion as shown by microscopy. The structural and magnetic parameters in this region are not well defined and become strongly coupled creating non-unique solutions to the fit of the reflectivity data. One model uses electron energy loss spectroscopy data to constrain the composition across the interface, which limits the fit. This sample is found to have a magnetic dead layer at the interface. $Co_2FeAl_{0.5}Si_{0.5}$ grown on Ge(111) on the other hand, has a small interface region due to lack of Ge diffusion from the substrate. As the fit parameters are better defined, a unique solution to the reflectivity data is obtained. A magnetic moment corresponding to HM is obtained for both Ge grown films with the decrease in magnetisation towards the substrate. Three samples of $Fe_3O_4$ grown on MgO(111) with different post-annealing temperatures were also studied. Structural and magnetic experimental techniques are combined to understand the affect post-annealing temperature has on the film properties. An unusual substrate/film epitaxial relationship is found out of plane: $MgO(111)\|Fe_3O_4(100)$. Further temperature dependent studies investigate the change in magnetism below the Verwey transition $T_V \sim 120\,\mathrm{K}$.

# Abbreviations

**CFAS** $Co_2FeAl_{0.5}Si_{0.5}$ ..... 56

**DFT** density functional theory ..... 64

**DOS** density of states ..... 3

**EELS** electron energy loss spectroscopy ..... 8

**FOM** figure of merit ..... 34

**f.u.** formula unit ..... 4

**FWHM** full width half maximum ..... 32

**HAADF** high angle annular dark field ..... 60

**HM** half-metallic ..... 7

**MR** magneto-resistance ..... 126

**MBE** molecular beam epitaxy ..... 128

**MSLD** magnetic scattering length density ..... 25

**MTJ** magnetic tunnelling junction ..... 1

**NR** neutron reflectivity ..... 11

**PDOS** partial density of states ..... 93

**PNR** polarised neutron reflectivity ..... 4

**SAD** selected area diffraction ..... 8

**SL** scattering length ..... 11

**SLD** scattering length density ..... 16

**SP** spin-polarised . . . 2

**SQUID** superconducting quantum interference device . . . 7

**STEM** scanning transmission electron microscopy . . . 60

**TEM** transmission electron microscopy . . . 63

**TOF** time of flight . . . 130

**UHV** ultra high vacuum . . . 128

**VSM** vibrating sample magnetometry . . . 7

**XRD** X-ray diffraction . . . 10

**XRR** X-ray reflectivity . . . 11

# Chapter 1

# Introduction

The size of semiconductor based devices has been decreasing in order to increase memory capacity, speed, and power efficiency of electronics within the same overall footprint. Size can be reduced both in width, demonstrating research into device patterning using nanostructures such as stripes, rings and triangles, and in thickness leading to thin film materials [1]. Reducing the size in either direction deviates the material's behaviour from bulk-like properties. This deviation can be desirable as thin layers can allow electron tunnelling, but often effects such as changes in resistance and drops in Curie temperature are caused by growth defects which are generally unwanted for devices.

Giant magnetoresistance (GMR) is an innovative technology that makes use of the reduction in material sizes in order to utilize the electron spin degree of freedom in materials for information manipulation, memory storage and transmission by resistance measurements [2]. Magnetic materials such as Fe, Co and Ni in thin film form have been used in heterostructures (vertically stacked magnetic layers). Here a non-magnetic layer is sandwiched between two magnetic materials that are polarised in plane, these devices are called spin-valves (Figure 1.1 [3, 4]), however if the non-magnetic layer is replaced by an oxide insulator, it is referred to as a magnetic tunnelling junction (MTJ) as electrons need to tunnel through the spacer material. The top layer is able to flip magnetisation where as the bottom electrode is pinned. Current flows through the device perpendicular to the magnetised directions, and electrons are scattered from layers of anti-parallel polarisation, where as electrons with parallel polarisation are unaffected. The path with the most scattering has the highest resistance [3, 5], with differences in low/high resistance states of up to $\sim$600 % at room temperature [6]. The resistivity $\rho$ for electrons of spin $\uparrow$ and

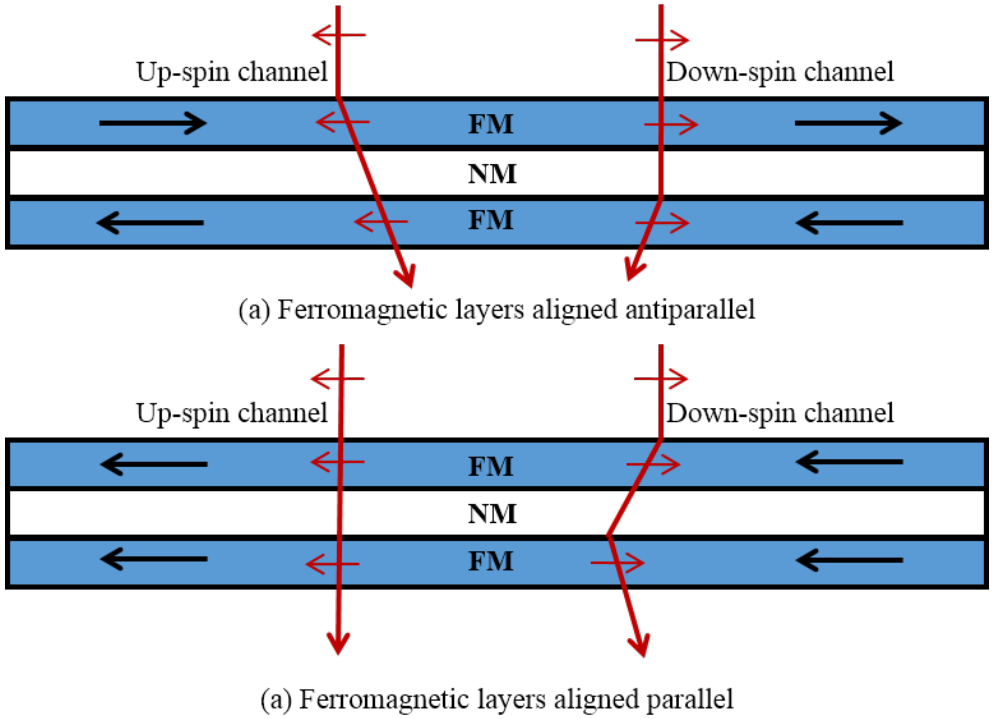


Figure 1.1: Magnetic tunnel junction showing ferromagnetic electrodes magnetically aligned antiparallel (a) and parallel (b) either side of a non-magnetic spacer layer. The scattering probability is the same for both spin states in (a) where resistance is equal, and different in (b) where each spin state has a different resistance.

$\downarrow$ is given as

$$\rho_{ap} = \frac{\rho^{\uparrow} + \rho^{\downarrow}}{2} \quad \text{and} \quad \rho_p = \frac{2\rho^{\uparrow}\rho^{\downarrow}}{\rho^{\uparrow} + \rho^{\downarrow}} \tag{1.1}$$

where $\rho_{ap}$ is the resistivity with electrodes magnetised anti-parallel and $\rho_p$ refers to parallel electrodes. The spin-polarised (SP) of the ferromagnetic electrodes is given as

$$SP(E) = \frac{N(E)^{\uparrow} - N(E)^{\downarrow}}{N(E)^{\uparrow} + N(E)^{\downarrow}} \tag{1.2}$$

where $N(E)^{\uparrow}$ and $N(E)^{\downarrow}$ are the spin dependent density of states for majority and minority states respectively. More generally the SP at the Fermi level is

$$SP(\varepsilon_F) = \frac{\nu_{\uparrow}^x N(\varepsilon_F)^{\uparrow} - \nu_{\downarrow}^x N(\varepsilon_F)^{\downarrow}}{\nu_{\uparrow}^x N(\varepsilon_F)^{\uparrow} + \nu_{\downarrow}^x N(\varepsilon_F)^{\downarrow}} \tag{1.3}$$

where $\nu_{\uparrow}$ and $\nu_{\downarrow}$ are the Fermi velocities for majority and minority electrons respectively and $x$ is the power with which the Fermi velocity contributes to the

property being measured in a ballistic regime [5, 7–9]. A discriminatory SP spectroscopic technique is needed in order to experimentally measure SP [10]. Several different techniques are Andreev reflection [11, 12], spin-polarised tunnelling [13], spin-resolved photoemission [14], which are more surface sensitive, and magnetic Compton scattering which probes the bulk [15, 16]. Dowben et al. [9] discuss different experimental methods, and how the different techniques give a range of SP values due to the difficulty in knowing what exactly is being measured. Tanaka et al also discuss the difference between SP values when using spin-polarised tunnelling and Andreev reflection [13].

The GMR of a spin-valve and MTJ can be calculated using

$$\text{GMR} = \frac{\Delta\rho}{\rho} = \frac{\rho_{ap} - \rho_p}{\rho_p} = \frac{(\rho^{\downarrow} - \rho^{\uparrow})^2}{4\rho^{\uparrow}\rho^{\downarrow}} = \frac{2(SP_1)(SP_2)}{1 - (SP_1)(SP_2)} \tag{1.4}$$

where $SP_1$ and $SP_2$ are the spin polarisations of the two electrodes respectively. This is a well known method for estimating the spin polarisation of ferromagnetic electrodes [5, 7, 17].

For successful spintronic devices there are three requirements 1) a highly polarised injection source, 2) long spin transport coherence lengths and 3) efficient detection methodologies [18]. Current semiconductor Si and Ge devices have already been shown to have long coherence lengths, 300 $\mu$m [19] and 10 $\mu$m [20] respectively, where only 100 nm is necessary; therefore fulfilling requirement 2. GMR devices such as the MTJ, already successfully detect the change in spin-polarisation via the large change in resistance, therefore fulfilling requirement 3. Only requirement 1 is left to be realised. A highly polarised spin-injection material must be able to polarise an injected current and be compatible with current semiconductor technology. The compatibility with materials such as Si and Ge requires materials of similar properties and lattice constants to minimise growth defects when grown in thin film forms. Growth defects such as elemental diffusion, the mixing of different crystal phases and dislocations reduce the spin polarisation of the material at interface boundaries. Often these defects are so severe, even a well grown film cannot recover from the poor interfacial epitaxy.

The use of half-metallic materials in GMR and tunnelling magnetoresistance devices (TMR) is desirable due to their theoretically predicted 100% spin polarisation at the Fermi level for minority states, theorised originally by de Groot for NiMnSb [22]. The density of states (DOS) (Figure 1.2), demonstrates the differences between a metal, ferromagnet, half-metal and semiconductor [21]. A clear gap in the minority states can be seen replicating the semiconductor behaviour and the

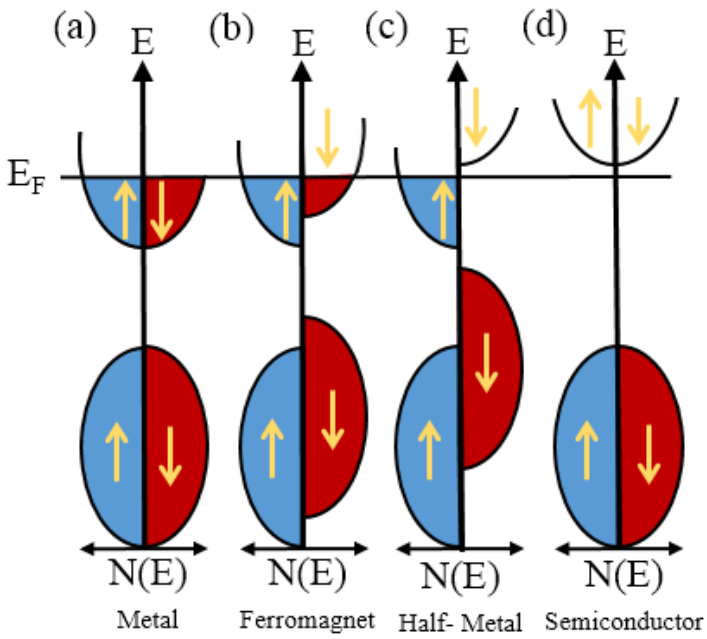


Figure 1.2: Schematic density of states for (a) metal, (b) ferromagnet, (c) half-metal and (d) semiconductor. The downwards arrows represent the minority spin states, and the upwards arrows represent the majority spin states [21].

majority spin states are similar to the metal. The energy gap in the minority band structure ensures no down-spin electrons pass through the material because of the lack of available states. Using a half-metal (HM) will then enable efficient devices to be fabricated due to the annihilation of current leakages, fulfilling criteria 1 and possibly 3 with the right device designs. This comes along with the caveat that the material has to be realised. Currently the progression of experimentally proven HM materials is plagued with problems due to thin film forms having non bulk-like properties due to defects during growth.

Two indications of a half-metallicity are the spin-polarisation and the value of the magnetic moment/formula unit (f.u.). It is possible to use magnetometry measurements in order to measure the magnetic moment of the thin film to indicate half-metallicity, but this averaging technique includes decreases in magnetisation at the interfaces and surfaces and is therefore not accurate. Through polarised neutron reflectivity (PNR) measurements, absolute magnetic moment in a thin film can be determined alongside the sample's magnetic profile. Importantly, this provides information about the behaviours at the interfaces within the sample where defects can introduce undesirable properties.

## 1.1 Overview of Thesis

The aim of the work in this thesis is to identify specific experimentally grown materials as half-metallic, and therefore their suitability as candidates for device applications. PNR is combined with a range of other experimental techniques to build an understanding of the sample structure and composition, and obtain depth-dependent magnetic profiles. Focus is given to PNR where the intricacies of reflectivity modelling is key throughout.

Chapter 2 gives a short overview of the experimental techniques mentioned in this thesis and how they are used in order to retrieve sample parameters useful to aid reflectivity fitting. Microscopy measurements were performed by collaborators as stated in the Declarations. A short description of the reflectivity experiments is also given here for completeness.

Chapter 3 states the theoretical considerations of reflectivity starting with reflectivity of visible light, and moving on to use the same equations adapted for X-rays and neutrons. The specific features needed to understand and fit reflectivity data, such as scattering length density profiles, are then explained.

Chapter 4 is a step by step example of how to set up and fit reflectivity data using the GenX fitting software [23]. It includes insight into the process and common issues that might occur. Real XRR and PNR data is used from a sample not used in a later experimental chapter: $Fe_3O_4$ grown on YSZ(111) (yttria-stabilised zirconia).

The first experimental chapter (Chapter 5) models the reflectivity data of the quaternary Heusler alloy $Co_2FeAl_{0.5}Si_{0.5}$ grown on Si (111), where a unique solution is not found owing to the complexity of the material, coupling of parameters and the large interfacial region. Three models are found and the validity of each model is discussed before a final model is decided upon.

Chapter 6 demonstrates the robust fitting methodology of $Co_2FeAl_{0.5}Si_{0.5}$ grown on Ge(111). Reflectivity data from a second Ge sample ("Ge2") demonstrates the ability to model data without complementary techniques and it is found that this material is reproducible, a necessary feature for mass production of devices.

The final experimental Chapter 7 focuses on $Fe_3O_4$ grown on MgO(111) substrate. A structural and magnetic comparison is performed on three samples with different post-annealing temperatures. The second part to this chapter models the magnetic behaviour below the Verwey temperature $T_V \sim 120\,\mathrm{K}$ and makes a comparison based on structural information obtained previously.

Finally, Chapter 8 contains concluding remarks and discusses the possibility of extending these studies in regards to experimental work or modelling concepts.

# Chapter 2

# Complementary Techniques

In order to fabricate the next generation devices for technology and electronics, it is important to fully understand the materials used to create them. Most of these materials are needed in thin film from which often have dissimilar properties to their bulk counterparts. Precise growth studies of materials are needed in order to be able to robustly replicate important characteristics of the material. In this thesis, focus is on PNR and the magnetic depth profile through thin films, but the analysis of reflectivity data is difficult due to the coupling of many parameters (e.g. film composition and electron density). In order to find unique solutions to PNR data, parameters must be limited by the use of different techniques which specialise in the corresponding information needed. Below is a short summary of techniques used to complement the PNR data, and what information can be extracted from them.

A good reference is the book by Fong [24], which explains the properties of half-metals, techniques available to characterise them, along with examples of the main types of half-metallic materials. The discussion here adds to the detail in the book with reference to the studies detailed in this thesis.

## 2.1 Magnetometry

Among the properties key to the characterisation of the magnetic properties of half-metallic materials, the saturation magnetisation of the sample is the most important [24], as it can be directly compared to the magnetic moment per formula unit which can indicate half-metallicity. Secondly, the shape of the hysteresis loop can provide insight into the easy-axis of the material, along with possible pinning of spins due to defects within the crystal. It can also describe how "soft" the material is and how easily it can be magnetised. It is important to remember that this technique

is the averaged magnetisation from the entire sample, including the substrate. It is sometimes non-trivial to remove substrate background magnetisation from the data and it is always best to measure the substrate individually from the substrate and film.

There are two magnetometry techniques used in this thesis: vibrating sample magnetometry (VSM) and superconducting quantum interference device (SQUID). Both techniques use the same general principles, although there are slight variations to how the sample magnetisation is measured.

For SQUID a magnetic sample is placed in an external magnetic field of specific value and displaced with respects to the superconducting coil which changes the corresponding current. The coil leads to the SQUID, which has been set up to output voltages for specific changes in current. There is then a correlation between sample position and voltage output. The corresponding sinusoidal curve is fitted to give a value of the magnetisation. The voltage is converted to emu (magnetisation) by comparing data to a calibration sample and magnetisation is plotted against magnetic field (**M**-**H**) [25]. Similarly for VSM, a magnetic sample is placed in a magnetic field but oscillated at a certain frequency. It induces current in pick-up coils which are turned into voltage and then emu by use of a calibration sample.

For half-metallic (HM) materials, they are known to have an integer number of $\mu_B$/f.u. (with some variation for the materials used in this thesis, described in later chapters). The magnetisation found by magnetometry can then be converted from emu into $\mu_B$/f.u. for direct comparison. There is often a large error ($\pm 8\%$) on these values due to the inaccurate measurement of magnetic material volume; both sample size and thickness, and material density. Pd samples are used for calibrations of emu in this thesis as it is a well known Pauli paramagnet with reliable magnetic properties.

## 2.2 Microscopy

Microscopy techniques are a powerful tool as they enable atomic resolution studies of samples which can help to build layered reflectivity models. Microscopy is then on an atomic scale where the sample size is effectvely reduced to nm. Structural and compositional variations over cm length scales are common and should be considered when using microscopy data to compare with the large scale averaging in PNR. A variety of machines are used to produce the microscopy images in this thesis, where this information is known it is specified. As the data is taken by distant collaborators, it is not always possible to obtain this data.

### 2.2.1 Transmission Electron Microscopy

Transmission electron microscopy (TEM) is a $Z$ (atomic number) contrast technique where an electron beam passes through a thin ($\sim$ nm) sample. The sample is a cross section of the original sample where electrons are transmitted in plane. Bright field imaging detects the unscattered electrons where higher $Z$ elements are lighter, and dark field imaging views the scattered electrons and higher $Z$ elements are darker. As the electrons pass through many layers of atoms, thickness variations in the sample can change the intensity of the electron pattern causing bright/dark regions that may look like defects. Both visible structures and defects are useful in order to understand the origins of other properties such magnetism conductivity and resistance. Important extracted parameters for PNR fitting are thickness (especially interfacial), substrate roughness (wavy substrate/mosaic) and density measurements as they are useful to build a first trial model or confirm modelled features.

TEM images were taken on FEI Nova 200 NanoLab, selected area diffraction (SAD) were performed using TEM (JEOL 2011) and SAD simulations by CrystalKit software at the University of York.

### 2.2.2 High Annular Angular Dark Field Imaging

$Z$ contrast in HAADF-STEM (high angle annular dark field-scanning transmission electron microscopy) imaging along with simulated data from QSTEM enables the comparison of disorder within a certain sample area but comparing the intensity of line profiles across atomic sites. Intensity is averaged over the atomic columns in through the thickness of the sample. In this thesis this contrast is used to confirm the presence of the $B2$ Heusler phase, where on specific lattice sites elements are of one type only, and on another they are mixed, varying the intensity (Chapter 5).

HAADF-STEM images were taken on a Nion UltraSTEM 100 microscope equipped with a Gatan Enfina spectrometer, at the SuperSTEM EPRSC national facility, Daresbury, using a voltage of 100 kV.

### 2.2.3 Electron Energy Loss Spectroscopy

In conjunction with TEM, electron energy loss spectroscopy (EELS) detects the inelastic scattering and the energy loss of a high energy electron beam from specific elements within a sample. The electron beam energy is often tuned to the elemental 'edge' under investigation in order to increase detection sensitivity to that material. A compositional map can be fabricated over a certain z slice (substrate-surface direction perpendicular to the surface) of sample, this compositional profile can be

used in order to see the diffusion of elements through interfaces and thus used to fit reflectivity data [26].

EELS images were taken on a Nion UltraSTEM 100 microscope equipped with a Gatan Enfina spectrometer, at the SuperSTEM EPRSC national facility, Daresbury, using a voltage of 100 kV.

## 2.3 X-ray Diffraction

X-ray diffraction is a technique used for the study of crystal structures where Bragg reflections give information on many different sample features. As the beam size is much larger than spectroscopy, mm compared to $\mu$m, mm averaged structural data is obtained bridging the gap between microscopy and reflectivity. In this thesis XRD is used to aid reflectivity fitting and to understand how changes in structure effect the magnetism, as mentioned below.

The general experimental setup is shown in Figure 2.1. In a $\theta-2\theta$ experiment the X-ray beam hits the sample at an angle $\alpha_i$ and is detected at an angle $\alpha_f$ where the wavevector $Q = 4\pi \sin(\frac{2\theta}{2})$ is perpendicular to the sample surface. This is generally called a $\theta - 2\theta$ scan as it is the sample that tilts rather than the incident beam, causing the detector to move $2\theta$ in order to maintain specular scattering conditions. In the case of non-specular geometry $\omega - 2\theta$, when looking at in-plane reflections, $\theta$ is referred to as $\omega$ and $\alpha_f \neq \alpha_i$. The sample can be tilted in 3 directions, $\omega$ which is a tilt in the direction of the beam, $\chi$ is a tilt perpendicular to the beam and $\phi$ is a pivotal rotation about the centre of the sample. Combinations of these rotations enable crystal properties to be studied such as: out of plane and in plane crystal orientations, angle tilts of the crystals, off cuts in substrate and lattice constant measurements.

XRD measurements are normally performed at high values of $2\theta$ between 15° and 120° (much greater than in reflectivity) in order to study crystal diffraction which occurs at higher angles due to Bragg reflection. The X-ray source can also be changed from Cu with a wavelength of 1.54 Å, to other elements e.g. Ag with a wavelength of $\sim 0.56$ Å. The advantage of smaller wavelengths would be to probe smaller crystal structures with higher resolution and for some materials, could lower the fluorescence (and therefore reduce the background) of elements sensitive to the Cu energy.

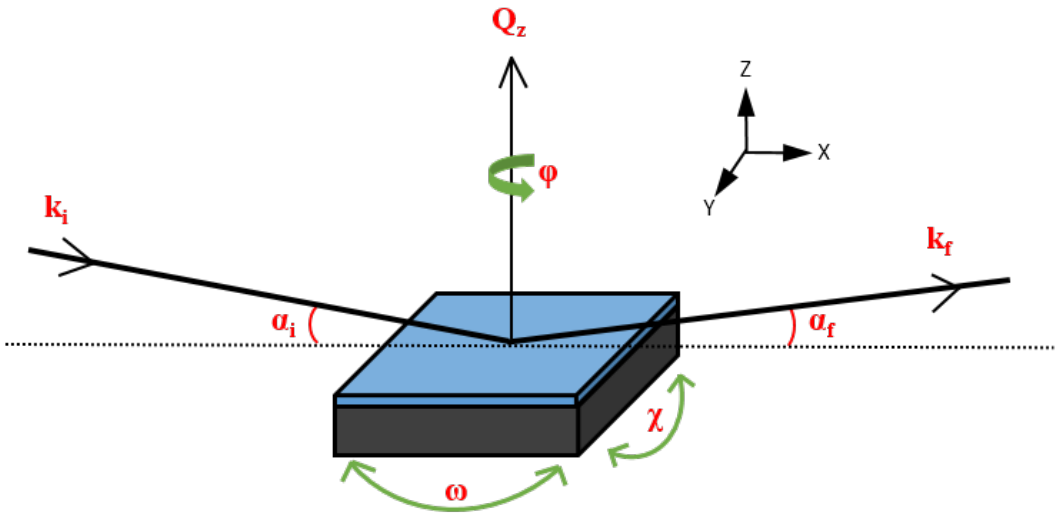


Figure 2.1: Schematic of the available rotations in a diffraction experiment.

The crystal lattice constant can be calculated using

$$a = \sqrt{(h^2 + k^2 + l^2)\left(\frac{\lambda}{\left(2\sin\left(\frac{2\theta}{2}\right)\right)}\right)} \tag{2.1}$$

where $\sin(2\theta/2)$ is in radians, $h$, $k$ and $l$ are the Miller indices and $\lambda$ is the wavelength of the incoming X-ray radiation.

Calculation of structure factor rules indicate which reflections are present in a $\theta-2\theta$ scan, indicated individually in each XRD chapter in this thesis and equations found in References [27, 28].

Unless otherwise stated, all X-ray diffraction (XRD) experimental data is taken using a monochromatic beam $\lambda_{CuK\alpha_1} = 1.54\,\text{Å}$, on a Panalytical X'Pert Pro MRD at the University of Warwick, UK. The set up included incident beam mask at a size comparable to the sample size (10 mm or 4 mm), and a slit width of 1/8 ° which corresponds to a beam height of 0.3 mm. At the detector side, the vertical pixel count is reduced or a parallel plate collimator is used without acceptance slit as only collimated beams will enter the detector.

For further information of X-ray scattering and the experimental set up, the reader is directed towards the book *Thin film analysis by X-ray scattering* by Birkholz [29] and *X-ray and Neutron Reflectivity: Principles and Applications* by Daillant and Gibaud [30].

### 2.3.1 X-ray Reflectivity

X-ray reflectivity is a direct complementary technique to neutron reflectivity (NR) as they both probe the same sample features over the same length scales. The difference mainly comes from the characteristics of the probe. X-rays and neutrons have different sensitivities to elements called the scattering length (SL). The theory of reflectivity is discussed in detail in Chapter 3. The X-ray enters the material above an angle $\theta_c$ (Equation 3.22) and the angle of the beam in the material then depends on its refractive index. This thesis does not consider evanescent waves which occur at angles below $\theta_c$. After interference with one or more layers (potential barriers/boundaries) the X-ray reflects, and due to it being an elastic specular measurement, into the detector. Constructive and destructive interference of X-rays diffracted from layer boundaries cause periodicities called Kiessig fringes. Analysing this data enables the sample average depth (z direction) layer by layer structure to be analysed. The layers exhibit properties such as thickness, SL, density and roughness which change the observed fringes.

SL is not the only difference between probes. X-rays are more surface sensitive and less penetrating but have a much higher flux than neutrons. There is then not enough intensity at higher Q to obtain good data at the interface deeper within the sample. Neutrons penetrate more deeply due to reduced interactions with the nuclei in materials, but have a lower Q range due to intensity drop off and less flux. Lower ranges of Q limit the sensitivity of the interfacial profiles on the reflectivity data. The same experimental conditions apply for X-ray reflectivity (XRR) as XRD for $\theta - 2\theta$ scans (Figure 2.1), but the incident beam is at low angles, 0.2° - 5°.

Off-specular measurements (also known as off-axis) in this thesis are used to observe correlated roughness in the sample. Correlated roughness is a particular pattern which is mimicked through the film to the surface. Off-specular data is also subtracted from the specular scan in order to remove background. To collect this data, $\Delta\omega \sim -0.1$. The offset value to be used must be far enough away that it does not sit on the specular peak. An $\omega$ rock on the first reflectivity fringe will determine this. Off-specular measurements are not needed for NR experiments due to the reduced neutron flux and therefore naturally low background.

Unless otherwise stated, all XRR experimental data is taken using a monochromatic beam $\lambda_{CuK\alpha_1} = 1.54\,\text{Å}$, on a Panalytical X'Pert Pro MRD at the University of Warwick, UK. The set up included incident beam mask at a size comparable to the sample size (10 mm or 4 mm), and slit widths of 1/32 ° or 1/16 ° which correspond to beam heights of 0.075 mm to 0.15 mm respectively. In front of the detector is a parallel plate collimator with a 0.27° acceptance angle slit.

## 2.4 Polarised Neutron Reflectivity

A brief explanation of PNR is given here to give understanding to later sections of this thesis.

Different PNR instruments around the world have different neutron sources, and different modes to which the reflectometer work. Facilities such as ISIS, UK and European Spallation Source (ESS), Sweden use a neutron spallation source which naturally uses time of flight (TOF) mode due to the pulses from the source. Institut Laue-Langevin (ILL), France has a uranium enriched nuclear reactor which uses monochromatic modes but can be upgraded to include TOF [31]. Neutrons are polarised in order to utilise their angular spin degree of freedom which interacts with magnetic moments within magnetic samples. There are several ways of polarising the neutrons including filters, supermirrors and crystals. After a neutron has been polarised it is important to be able to flip the spins to observe the change in interaction. Non-spin flip (NSF) indicates an experimental set up where the neutron polarisation remains the same both before and after sample interaction, denoted only by initial state 'u' or 'd'. 'u' is parallel to externally applied field $\mathbf{H}_{ext}$ and 'd' is antiparallel. Spin flipping of the neutron i.e. 'ud' and 'du' represents neutrons that have interacted with a magnetisation vector at an angle away from $\mathbf{H}_{ext}$ which cause precession and flipping of the neutron caused by non fully saturated samples. All samples in this thesis are fully saturated and use non spin-flip scattering (NSF) therefore are labelled 'u' and 'd' only. Positive scattering materials in addition to materials saturated parallel to the up-spin neutron, cause a higher overall scattering length when compared to the down-spin neutron. This causes the up-spin to have higher scattering probabilities and therefore more intensity, as shown in all figures in this thesis. Negatively scattering materials also exist such as Ti and Mn.

Figure 2.2 shows a amalgamation of the different equipment needed to polarise and flip neutrons for both monochromatic and TOF modes as defined individually in Table 2.1. A white neutron beam of multiwavelength is initially polarised into a specific state with respects to the magnetic field. Before sample interaction there is a choice to flip the neutron beam. If NSF mode is being used, neutrons are assumed to be in the same spin state and enter the unambiguous detector. If SF mode is engaged, the analyser only reflects 'u' neutrons into the detector, and therefore the diffracted spin-flipper must be engaged in order to define the final polarisation state and detect 'ud'.

Figure 2.3 shows the vertically orientated sample geometry where polarised neutrons interact with a sample at a low reflectance angle $\alpha_i$ and are detected at

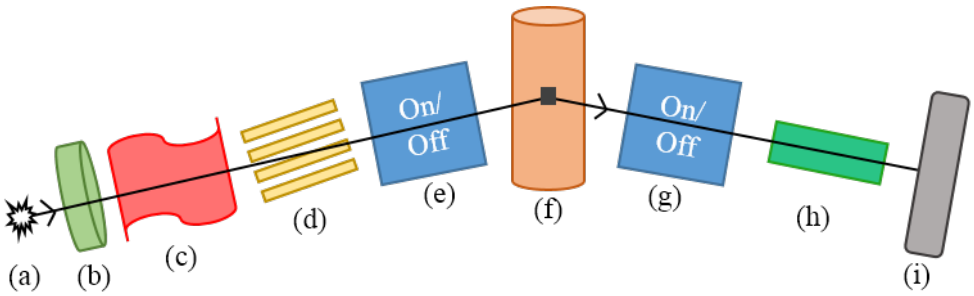


Figure 2.2: Equipment needed for the different PNR experimental configurations for monochromatic/TOF and NSF/SF [32]. (a) is the white neutron beam, (b) is the chopper, (c) is the polarising s-bender, (d) is the polarising monochromator, (e) is the incident spin-flipper , (f) is the sample environment, (g) is the diffracted spin-flipper, (h) is the supermirror/analyser and (i) is the detector. Note that all equipment is not used in conjunction, different configurations are needed as explained in the text and Table 2.1.

Table 2.1: List of the required equipment from Figure 2.2 to create the desired experimental set ups. All examples are of polarised neutron beams and include a,f and i.

| Set up | Configuration | Equipment names |
|---|---|---|
| Monochromatic NSF | d,e | Monochromator, incident SF. |
| Monochromatic SF | d,e,g,h | Monochromator, incident SF, diffracted SF, analyser. |
| TOF NSF | b,c,e | Choppers, polarising s-bender, incident SF. |
| TOF SF | b,c,e,g,h | Choppers, polarising s-bender, incident SF, diffracted SF, analyser. |

$\alpha_f = \alpha_i/2$, using the same geometries as XRR. Labels are as in Figure 2.1 with the addition of $\mathbf{H}_{ext}$ which is the externally applied magnetic field. $\boldsymbol{Q_z}$ is perpendicular to the thin film surface.

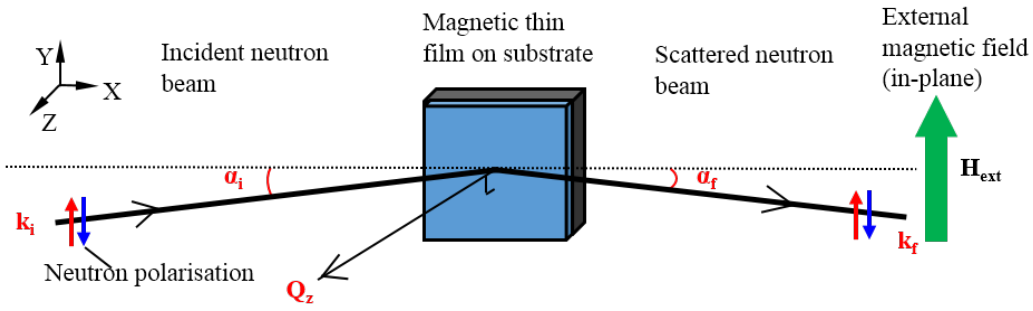


Figure 2.3: Polarised neutron reflectivity experimental setup in vertical alignment. Neutrons are polarised either 'u' or 'd' before interaction with the sample, and either 'u' or 'd' is detected after scattering. $\mathbf{H}_{ext}$ is the external magnetic field applied to the sample parallel to the neutron spin 'u'.

### 2.4.1 Complementary Techniques Summary

Although reflectivity fits can be robustly modelled without the use of any other complementary experiments, the final model may never be truly believed unless there is other evidence to support it. Often there are unusual sample features that would never be found by trial and error reflectivity fitting. Table 2.2 is a summary of the different techniques used in this thesis, and the corresponding parameters that can be extracted in order to help support reflectivity fitting.

Table 2.2: Complementary techniques used in this thesis, and their contribution to aid fitting reflectivity data and characterising samples.

| Technique | Extracted information |
|---|---|
| TEM | Crystal quality, interfacial roughness, thickness. |
| HAADF | Elemental $Z$ contrast, atomic ordering. |
| EELS | Compositional profile. |
| XRD | Averaged lattice constants, crystal orientation, grain size. |
| XRR | Averaged electron density depth profile, layer structure, film thickness, roughness |
| Magnetometry | Average magnetisation within the sample, hard and easy axis, shape of hysterisis loop. |

# Chapter 3

# Reflectivity Theory

X-ray and neutron reflectivity are techniques that complement each other as they both give depth dependent structural information about a sample, perpendicular to the surface. The technique excels in the observation of interfaces due to the distortion of the wave field near surfaces where changes in composition, density or magnetism are observed [33]. Both XRR and PNR (or NR) are often fitted simultaneously due to their differences in sensitivity as well as the additional neutron interaction with depth dependent magnetisation vectors. Their sensitivities differ due to their primary interaction with matter. X-rays interact with the electrons of the atom, therefore increasing linearly with $Z$, the atomic number. Neutrons interact with elements in a more randomised fashion [34], scattering from the atomic nuclei as well as any unpaired electrons in the shells due to it having its own inherent magnetic moment, resulting in coupled nuclear and magnetic information. XRR therefore probes the electron density perpendicular to the surfaces and interfaces where NR probes the nuclear density profile. PNR probes the magnetisation profile in addition to the nuclear [35].

Fitting X-ray and PNR data simultaneously allows for decoupling of nuclear and magnetic properties, while obtaining more reliable profiles from the limiting nature of the data sets. Interestingly, due to the spin of the neutron $\mu = -9.6624 \times 10^{-27}\,\mathrm{J/T}$ [28] (see reference for more neutron properties), neutrons can give absolute magnetic moment of a material where other techniques only give relative magnetic moments when calibrated. Calibration requires exact knowledge of the magnetisation of a certain calibration sample as well as the exact molecular weight. Referencing techniques increase margins for error and lower certainty of results.

In this chapter the fundamental principles of reflectivity are explained. As

reflectivity is an optical technique [36], this will start with generalised equations for electromagnetic waves (such as visible light) interacting with a single layer, focus will then be moved to the reflectance of X-rays and neutrons on multiple layers of material. For reflectivity scattering at very low angles (between 0.2° and 5°), larger than atomic distances are probed due to the small wave vector transfer, and the Snell-Descarte law describes the reflectance and transmittance of waves interacting with multiple layers of materials with different refractive indexes. The scattering length density (SLD) profile will be explained and shown how it relates to the sample structure, along with explanations specific to the GenX fitting software.

The equations stated in this chapter have been robustly published by many authors. Here the important equations are stated and have been taken and manipulated from sources [1, 28, 33, 36–51] in order to coherently combine them. The reader is directed to these references for more in depth derivations.

## 3.1 Optical Reflectivity

Optical formalism describes the refractive index of a material when interacted with by propagating electromagnetic radiation. The Snell-Descartes' law describes the interaction at this interface and from this, the Fresnel coefficients for reflectance and transmission can be calculated [37].

The Snell-Descartes' law is given by

$$n_j \cos\theta_j = n_{j-1} \cos\theta_t \tag{3.1}$$

which describes the interaction of electromagnetic radiation upon an interface of different refractive medium. Figure 3.1 depicts this. An incident wave in a refractive index of $n_j$, passes into a medium with different refractive index $n_{j-1}$, with an angle $\theta_j$ parallel to the medium (subscript defined by the angle made with the new lower layer). Some of the wave is transmitted into the layer at an angle $\theta_t$ and the remainder is reflected at an angle $\theta_r$.

Elastic scattering for specular non-diffuse scattering gives $\theta_j = \theta_r$, the specular wavevector $\boldsymbol{Q_z}$ is then perpendicular to the surface/refractive boundary with

$$\mathbf{Q_z} = \mathbf{k_r} - \mathbf{k_j} = 2k_0 \sin\theta_j = \frac{4\pi \sin(\theta_j)}{\lambda} \tag{3.2}$$

There is total external reflection of the wave below a certain angle $\theta_c$ (critical angle)

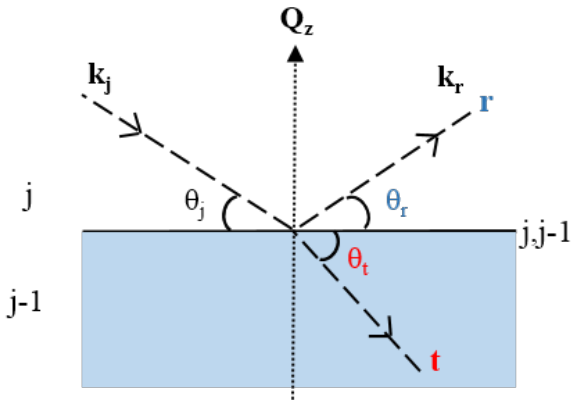


Figure 3.1: Snell's law showing the refraction of an electromagnetic wave after hitting an interface with two different refractive indexes of $j$ and $j-1$ where $n_j \neq n_{j-1}$, and $j, j-1$ is the boundary name.

which depends on the ratio of the refractive indices

$$\theta_c = \theta_j = \sin^{-1}\left(\frac{n_{j-1}}{n_j}\right) \tag{3.3}$$

where a more detailed description is given in [48]. For materials where the boundary changes from a low to higher refractive index, no total external reflection is observed [52].

Above this critical angle, the reflectance and transmission laws across an interface are given by the Fresnel equations. Reflection, $r$ and transmission, $t$ assuming the small angle approximation, are given as

$$r = \frac{I_r}{I_j} = \frac{\theta_j - \theta_t}{\theta_j + \theta_t} \tag{3.4}$$

$$t = \frac{I_t}{I_j} = \frac{2\theta_j}{\theta_j + \theta_t} \tag{3.5}$$

where $I$ is the amplitude of the corresponding wave and $j$ represents the intensity of the initial medium. The resulting intensity for reflectivity is then

$$R = r^2 = \left(\frac{\theta_j - \theta_t}{\theta_j + \theta_t}\right)^2 \tag{3.6}$$

where $|r|^2$ would be the complex conjugate if using $k$ or $Q$ vectors for the reflection equation. The transmission intensity $T$ is given as $|t|^2$, and describes the transmission of the wave into the next layer.

For multilayers (Figure 3.2), the Fresnel reflectivity generalises the reflectance for any interface within the sample as:

$$F^R_{j,j+1} = \frac{\theta_j - \theta_{j,j+1}}{\theta_j + \theta_{j,j+1}} \tag{3.7}$$

where $j$ is the layer of interest and $j+1$ is the layer above, from where the wave originates. As the substrate is modelled as a semi-infinite layer with no lower boundary, the substrate reflection $R_J \to 0$.

Parrat's recursive formula [33, 38, 39] uses the interface interactions described by Fresnel, to calculate the final reflected beam after multiple interactions with multiple interfaces. The reflected beam is given by

$$R_{j-1,j} = {a_{j-1}}^4 \left[ \frac{R_{j,j+1} + F^R_{j-1,j}}{R_{j,j+1} F_{j-1,j} + 1} \right] \tag{3.8}$$

where

$$R_{j,j+1} = {a_j}^2 F^R_{j,j+1} \tag{3.9}$$

and

$$a_j = \exp(-i\frac{\pi}{\lambda} n_j d_j) \tag{3.10}$$

Electromagnetic waves within the sample interfere when the reflected and transmitted waves propagate through the layers of different thickness $d$ and refractive index $n$. Multiple layers cause multiple reflections which interfere with each other, where the equation relating to constructive interference is:

$$m\lambda = 2 n_j d_j \sin\theta_j \tag{3.11}$$

where $m$ is an integer and for destructive interference [40]:

$$(m - \frac{1}{2})\lambda = 2 n_j d_j \sin\theta_j \tag{3.12}$$

The above equations can be implemented in XRR by the modification of the coefficients, as shown in the next section.

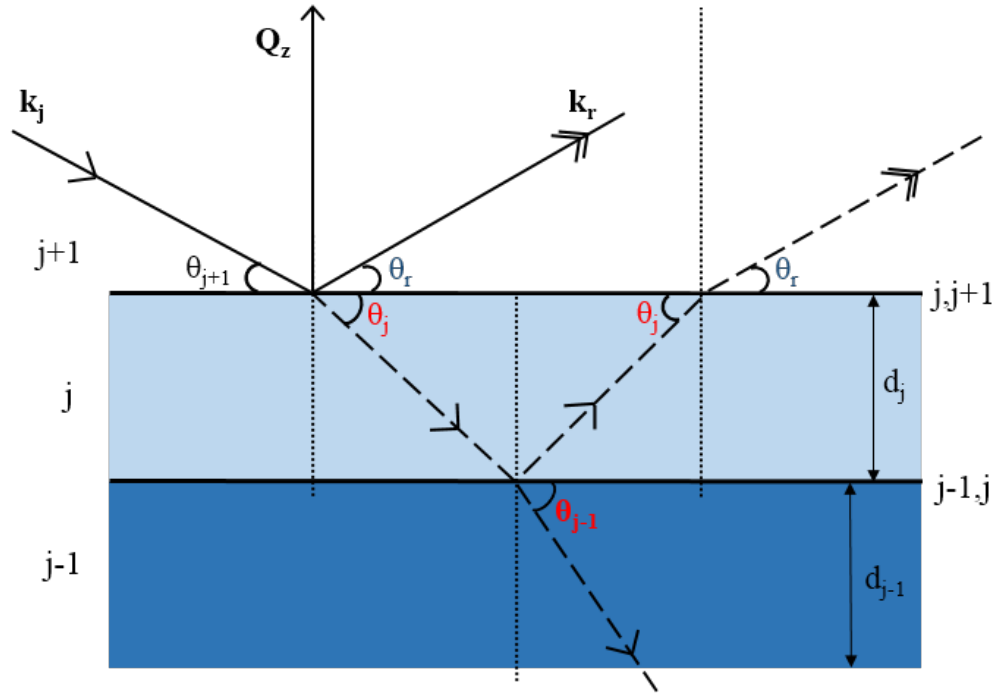


Figure 3.2: Reflection and transmission at interfaces using Fresnel's coefficients where j=J would be the substrate layer with no reflection and J,J-1 would be the lowest interface. Dotted lines are to show the surface normal and dashed lines represent beam paths.

## 3.2 X-ray Reflectivity

Using X-rays as a reflectance probe into materials can reveal features such as depth dependent changes in composition and electron density. For thin films, interfacial layers caused by diffusion and growth stoichiometry can be studied, where other surface dominant techniques would fail for reasons such as lower penetration depths, larger wavelengths, lower flux and different atomic interactions. This reveals the possibility to characterise depth dependent properties of different films, and enable comparisons when performing growth studies which are necessary for quality controlled growth of crystals for device applications.

At high X-ray energies only interactions with electrons need to be considered, therefore previously stated equations need to be modified to represent this interaction [37]. Repeating the equations for reflectivity of generalised electomagnetic waves and applying high energy X-rays, the following equations are obtained.

The refractive index for materials using X-ray radiation is

$$n = 1 - \delta - i\beta \tag{3.13}$$

where $\delta$ is the dispersion related to the real part of the scattering, and $\beta$ is the positive absorption coefficient related to the imaginary part. $\delta$ is on the order of $10^{-5}$ in solids and only around $10^{-8}$ in air [53]. It can be seen that the refractive index for materials under X-ray radiation is less than unity, where materials under photon radiation have $n > 1$. This phenomena implies that X-rays in materials have a faster phase velocity than the speed of light, $v_p = c/n$. This is not the case as the law of relativity states only signals carrying 'information' do not travel faster than $c$, known as group velocity $v_g$, which can be proven to be less than $c$. This occurs because the X-ray spectrum generally lies to the high-frequency side of various resonances associated with the binding of electrons [53].

$$\delta = \frac{\lambda^2}{2\pi} r_e \rho_e = \frac{\lambda^2}{2\pi} r_e N (f_0 + f') \tag{3.14}$$

where $r_e = 2.818 \times 10^{-15}\,\text{m}$ is the classical radius of the electron, $\rho_e$ is the electron density of the material, $f_0$ is the atomic scattering coefficient which tends to $Z$ (atomic number) at low angles [54], $f'$ is the dispersion correction related to the number of electrons per atom, and $N$ is the number density is given as

$$N = \frac{\rho N_A}{A} \tag{3.15}$$

where $\rho$ is mass density, $N_A$ is Avogadro's number and $A$ is the atomic weight [41].

$$\beta = \frac{\lambda}{4\pi} \mu_x = \frac{\lambda^2}{2\pi} r_e N f'' \tag{3.16}$$

where and $\mu_x$ is the absorption coefficient and $f''$ is the anomalous dispersion factor. The wavelength dependent dispersion corrections can be found for different energies of X-ray at URL: [55], where $f1 = Z + f'$ and $f2 = f''$. The full atomic scattering length / X-ray form factor is commonly shown as

$$f = f_0 + f' + f''. \tag{3.17}$$

These equations can be manipulated in order to consider layers of alloyed materials

with $x_i$ number of atoms per $\rho$:

$$\delta = \frac{\lambda^2}{2\pi} r_e \rho N_A \frac{\sum_i x_i \left(\frac{Z_i + f_i^{'}}{A_i}\right)}{\sum_i x_i} \tag{3.18}$$

and

$$\beta = \frac{\lambda^2}{2\pi} r_e \rho N_A \frac{\sum_i x_i \left(\frac{f_i^{''}}{A_i}\right)}{\sum_i x_i}. \tag{3.19}$$

The change in refractive index over a boundary is equivalent to a potential barrier height change that causes a scattering of the initial wavevector $k_j$ (shown later in Section 3.3.4). The change in profile through the sample depth is known as the SLD which has both real and imaginary parts as previously demonstrated in Equation 3.13. The corresponding reflected interference waves, called "Kiessig fringes"[56], change if the SLD is modified. For X-rays the real part of scattering length density is

$$ReSLD = \frac{2\pi}{\lambda^2}\delta = r_e N(Z + f') \tag{3.20}$$

and the imaginary part of the SLD is

$$ImSLD = \frac{2\pi}{\lambda^2}\beta = N f''. \tag{3.21}$$

The critical angle for total external reflection, assuming there is no absorption and the small angle approximation,

$$\theta_c = \sqrt{2\delta} = \frac{\lambda^2}{\pi} r_e \rho_e \tag{3.22}$$

and when calculated for wavevector $\boldsymbol{Q_z}$,

$$Q_c = \sqrt{16\pi N r_e}. \tag{3.23}$$

### 3.2.1 X-ray Fresnel and Parratt Equations

At angles higher than $\theta_c$ the Fresnel equations represent the reflectivity for >1 layer (assuming no roughness). For X-rays, using the refractive index Equation 3.13 and Equation 3.22, is

$$R = \left|\frac{I_R}{I_0}\right| = \left|\frac{\theta - \sqrt{\theta^2 - \theta_c^2 - 2i\beta}}{\theta + \sqrt{\theta^2 - \theta_c^2 - 2i\beta}}\right|^2 \tag{3.24}$$

[29] or as the wave-vector transfer

$$R = \left| \frac{Q_z - \sqrt{Q_z^2 - Q_c^2 - \frac{32i\pi^2\beta}{\lambda^2}}}{Q_z + \sqrt{Q_z^2 - Q_c^2 - \frac{32i\pi^2\beta}{\lambda^2}}} \right|^2 \tag{3.25}$$

as shown by Gibaud, Chapter 3 [42]. At values of $Q \gtrsim 3Q_c$ for smooth interfaces, the reflectivity falls as

$$R = \frac{Q_c^4}{16Q^4} \tag{3.26}$$

called the Porod region [29]. The electron density can be experimentally determined, assuming no absorption, using the equation [42]

$$Q_c = 3.75 \times 10^{-2}\sqrt{\rho_e} \tag{3.27}$$

where $\rho_e$ is in $e^-/\text{Å}^3$. A cautionary note is that this is for a single layer or change in refractive index. Additional layers within a sample can cause movement of the critical edge.

For X-rays within multilayers the Parratt equation for the middle layer $j$ becomes

$$R_{j-1,j} = {a_{j-1}}^4 \left[ \frac{R_{j,j+1} + F^R_{j-1,j}}{R_{j,j+1}F_{j-1,j} + 1} \right] \tag{3.28}$$

where

$$R_{j,j+1} = {a_j}^2 F^R_{j,j+1}, \tag{3.29}$$

$$F^R_{j,j+1} = \frac{f_j - f_{j+1}}{f_j + f_{j+1}}, \tag{3.30}$$

$$a_j = \exp(-i\frac{\pi}{\lambda} f_j d_j), \tag{3.31}$$

and

$$f_j = \sqrt{\theta^2 - \theta_c^2 - 2i\beta_j} = \sqrt{\theta^2 - 2\delta_n - 2i\beta_j} \tag{3.32}$$

or

$$f_j = \sqrt{Q_z^2 - Q_c^2 - \frac{32i\pi^2\beta}{\lambda^2}} = \sqrt{Q_z^2 - 16\pi N r_e - \frac{32i\pi^2\beta}{\lambda^2}} \tag{3.33}$$

Again for the substrate layer, $R = 0$ as it is assumed to be infinite. The top layer can then be simplified to $f_j = \theta_j$ and $a_j = 1$. [42]

An example of a reflectivity curve for a 200 Å Fe thin film on a Si substrate with no roughness is shown in Figure 3.3 where interference fringes due to the layer thickness, Kiessig fringes, are seen to be superimposed onto the Fresnel reflectivity.

The critical edge and fringe spacing is highlighted, in this case $Q_c \approx 0.065$ Å$^{-1}$, and Bragg's Law gives the fringe spacing at higher angle as [43]

$$\Delta 2\theta = \lambda/2d. \tag{3.34}$$

where $2\theta$ and is the fringe spacing in radians, $\lambda$ is wavelength and d is the thickness of the film, or

$$\Delta Q = 2\pi/d. \tag{3.35}$$

where Q is the fringe spacing [29].

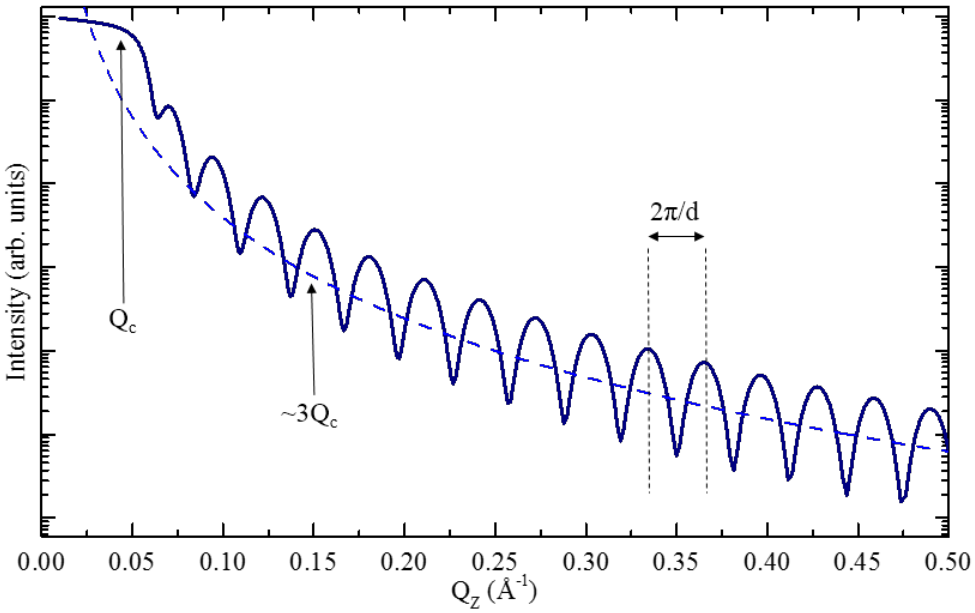


Figure 3.3: Interference patterns are shown corresponding to Fresnel's coefficients of reflectivity and transmission coinciding for a refractive index system of substrate, single layer, and air. $Q_c$ and Porod's $Q^4$ intensity drop off (dashed line) is shown.

## 3.3 Neutron Reflectivity

Neutron reflectivity is used as a contrasting, but complementary technique to XRR. Similar information is obtained from both techniques, due to the experiment probing the same sample features, but neutrons interact with the elements differently to that of X-rays. NR is a non destructive technique where neutrons scatter from the nucleus of the atom by the nuclear strong force, and have different sensitivities to isotopes of the same element.

### 3.3.1 Unpolarised Neutrons

The refractive index, $n$, shown in Equation 3.13 can again be applied to unpolarised neutrons where [41]

$$\delta_N = \frac{\lambda^2}{2\pi} N(b_0 + b') \tag{3.36}$$

$$\beta_N = \frac{\lambda^2}{2\pi} N|b''| \tag{3.37}$$

where $N$ is the number density (Equation 3.15), $b_0$ is the bound coherent scattering length, $b'$ is the bound incoherent scattering length and $b''$ is the absorption cross section where

$$b = b_0 + b' + b'' \tag{3.38}$$

In most cases both $b'$ and $b''$ are negligible, and therefore $b \simeq b_0$, where all values can be found at [57, 58]. The neutron scattering length $b$ are values experimentally determined due to the somewhat randomised interaction [34].

Continuing by ignoring negative neutron scattering materials and absorption, the neutron refractive index is

$$n = \sqrt{1 - \frac{\lambda^2}{2\pi} Nb} \tag{3.39}$$

[28, 44]. $Nb$ here is the scattering length density for a single element material. For further calculations considering absorption please see Reference [45]. To modify this equation for a mixed element material, replace $b$ with $\bar{b}$, the average neutron scattering length and adjust $N$ to represent the number density of the alloy.

$$NSLD = N\bar{b}. \tag{3.40}$$

The critical wavevector for the neutron total external reflection is then

$$Q_c = \sqrt{16\pi N\bar{b}}. \tag{3.41}$$

When compared to Equation 3.23 it can be seen that the critical edge calculations are equivalent.

$$R = \left| \frac{Q_z - \sqrt{Q_z^2 - Q_c^2}}{Q_z + \sqrt{Q_z^2 - Q_c^2}} \right|^2 = \left| \frac{Q_z - \sqrt{Q_z^2 - 16\pi N\bar{b}}}{Q_z + \sqrt{Q_z^2 - 16\pi N\bar{b}}} \right|^2 \tag{3.42}$$

For neutrons the Parratt recursive formula remains the same as Equation

3.28, with a change in the Fresnel coefficient Equation 3.31, where

$$f_j = \sqrt{Q_z^2 - Q_c^2} \tag{3.43}$$

replaces X-ray Equation 3.32 when neglecting absorption.

The X-ray and unpolarised neutron reflectivity essentially both probe the atomic structure of the sample. The scattering cross section of neutrons is different to the Z contrast of the X-rays, and therefore elemental sensitivity is enhanced differently in both techniques. Due to the interactions with nuclei being less probable, neutrons probe deeper into the sample but lose intensity quickly due to less flux from the source. X-rays are less penetrating, but due to very high flux, are able to retain good intensities at higher Q and from deeper into the sample.

### 3.3.2 Polarised Neutrons

Neutron reflectivity comes into its element due to the inherent magnetic moment of the neutron, which allows the measurement of the depth dependent averaged in-plane magnetic flux density/induction $\boldsymbol{B}$ within the sample. In this thesis all samples are fully saturated, and precession of neutrons due to their interaction with non parallel/anti parallel magnetic moments within the sample, such as magnetic domains, are not accounted for. To understand how the neutron beam is affected in these situations, the reader is advised to read references for the coherence length [1, 33] and the technique of spin-flip scattering [33, 36].

Polarised neutrons interacting with a medium of no magnetism retains the same properties of unpolarised neutrons. For the case of polarised neutrons interacting with a magnetic layer and ignoring absorption, the refractive index is modified to be [28]

$$n^{\pm} = \sqrt{1 - \frac{\lambda^2}{\pi}(\delta_N \pm \delta_M)} \tag{3.44}$$

where

$$\delta_M = \mp \frac{m\lambda^2}{h^2}\mu\mathbf{B} = \mp \frac{\lambda^2}{2\pi} N b_m \tag{3.45}$$

$m$ is the neutron mass, $h$ is Planck's constant, $\mu$ is the neutron magnetic moment, $\mathbf{B} = \mu_0(\mathbf{H} + \mathbf{M})$ is the magnetic induction inside the thin film (where $\mu_0$ is the permeability of free space) and $b_m$ is the magnetic scattering length. The sign is important as '+' is used for neutrons with spins parallel to the external magnetic field $\mathbf{H}$ and '−' for neutrons antiparallel to $\mathbf{H}$, but the neutron polarisation is antiparallel to its magnetic moment. The magnetic scattering length density (MSLD) is then

given as

$$MSLD = Nb_m = \mp \frac{m}{2\pi\hbar}\mu\mathbf{B} \tag{3.46}$$

and the SLD becomes

$$SLD^{\pm} = N(\bar{b} \pm b_m). \tag{3.47}$$

The magnetism also effects the total external reflection of the different neutron polarisations where

$$Q_c^{\pm} = \sqrt{16\pi N(\bar{b} \pm b_m)}. \tag{3.48}$$

where this is shown in Figure 3.4 for a splitting of $2\,\mu_B$/f.u. for 200 Å of Fe. The bulk magnetism in the sample can be measured by calculating the split reflectivity curves. Experimentally, for samples saturated by an external magnetic field $\boldsymbol{H}$, the electron spins align with the + neutron spin, therefore there is a higher scattering probability. This is seen in Figure 3.4 represented by PNR + having more intensity and the critical edge being at higher Q.

The Fresnel reflection amplitude for neutrons (Equation 3.42) is modified to account for the splitting in the reflectivity and the critical edge due to magnetism

$$R = \left| \frac{Q_z - \sqrt{Q_z^2 - Q_{c\pm}^2}}{Q_z + \sqrt{Q_z^2 - Q_{c\pm}^2}} \right|^2 = \left| \frac{Q_z - \sqrt{Q_z^2 - 16\pi N(\bar{b} \pm b_m)}}{Q_z + \sqrt{Q_z^2 - 16\pi N(\bar{b} \pm b_m)}} \right|^2. \tag{3.49}$$

The Fresnel coefficient is modified for polarised neutrons similarly

$$f_j = \sqrt{Q_z^2 - 16\pi N(\bar{b} \pm b_m)}. \tag{3.50}$$

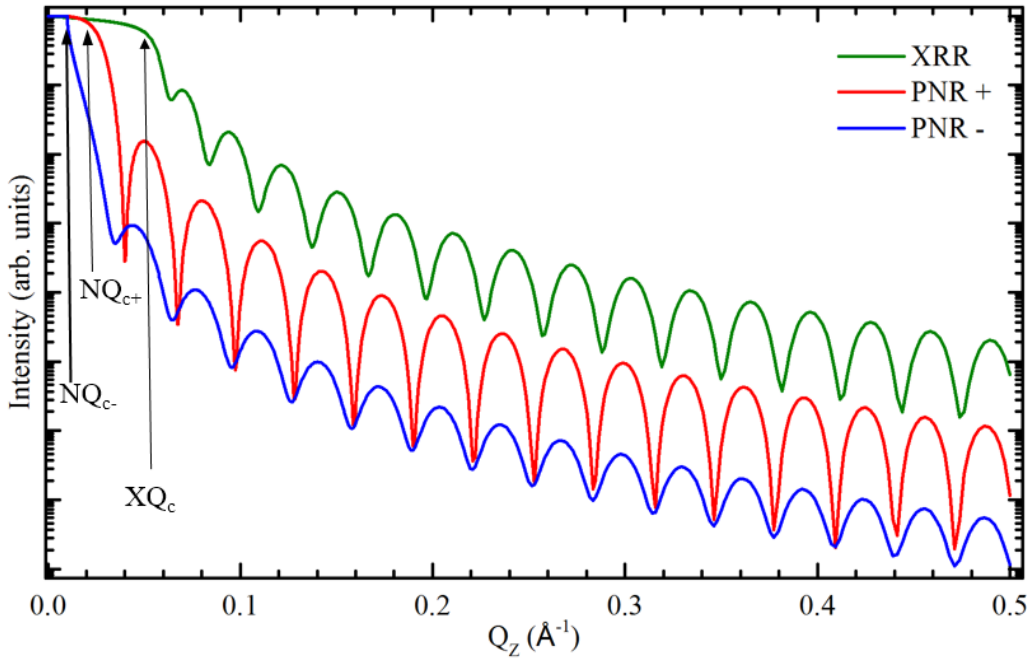


Figure 3.4: Reflectivity interference fringes (Kiessig fringes) for X-rays and neutrons for a 200 Å Fe layer on top of a Si substrate with a magnetic moment of 2 $\mu_B$/f.u. and substrate and surface roughness of 1 Å. $NQ_{c+}$ and $NQ_{c-}$ represent the PNR + and PNR − critical edge respectively. $XQ_c$ represents the XRR critical edge.

### 3.3.3 Roughness

In the perfect scenario, thin film crystals would be grown epitaxially onto a substrate without roughness, intermixing or defects. Real world examples have roughnesses and interdiffusion at interfaces which cause the electromagnetic wave to deviate away from the Fresnel refractive index model (with a perfect boundary between mediums), causing diffuse scattering and lowering the reflective intensity and changing the $1/Q^4$ [59] drop off. There is a need to adapt the Fresnel equations to account for the roughness, $\sigma$ (the root mean square roughness (rms)). In this thesis we only fit specular reflectivity, where the Nevot-Croce model is valid [60]. The deviation from the specular is given as

$$R = F_j^R \exp\left(-\frac{k_{j-1}k_j\sigma_j^2}{2}\right). \tag{3.51}$$

When modified for the Parratt formula, the Fresnel coefficient as seen in Equation 3.30 becomes

$$F^R_{j-1,j} = \frac{f_{j-1} - f_j}{f_{j-1} + f_j} \exp\left( - \frac{k_{j-1} k_j \sigma_j^2}{2} \right). \tag{3.52}$$

For diffuse scattering, other approximations are needed to model the roughness. The Born approximation and the distorted wave Born approximation (DWBA) are calculated by Sinha et al [61], and the reader is directed to the article for further information.

Experimentally, large roughnesses cause ill defined interfaces for the reflectance of X-rays and neutrons and have large effects on the corresponding Kiessig fringes, shown in Figures 3.5, 3.6, 3.7 and 3.8, where different combinations of roughness are compared to a substrate roughness of 1 Å and a surface roughness of 1 Å on the previously shown simulation of 200 Å of Fe on a Si substrate (Figure 3.4). Images have the same scaling for comparison purposes. Roughness at the substrate has a different effect than at the surface, and different roughness weightings between these two also change the reflectivity.

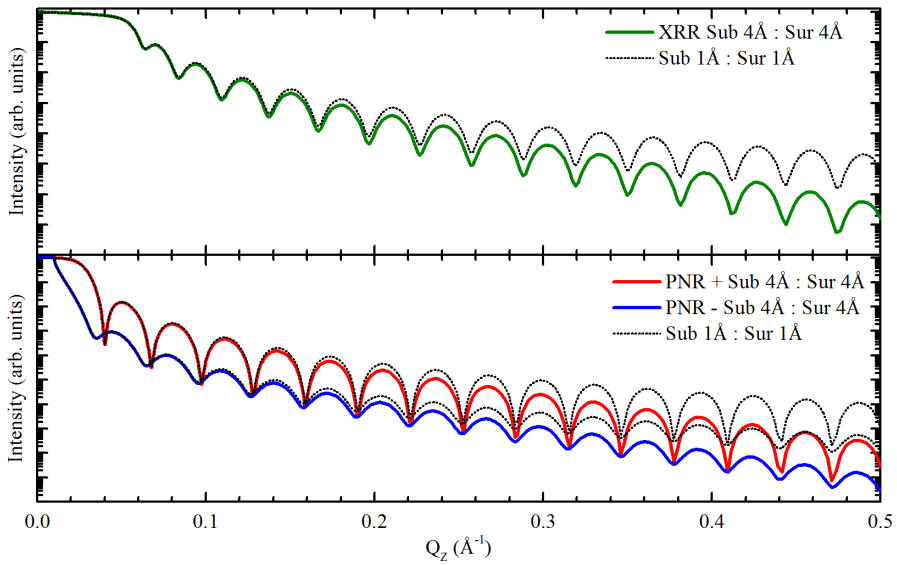


Figure 3.5: Comparison of roughness Sub 1 Å:Sur 1 Å to Sub 4 Å:Sur 4 Å for 200 Å Fe layer with 2 $\mu_B$/f.u. on Si substrate.

Figure 3.5 shows that increasing both substrate and surface roughness by equal amounts creates a faster drop off in the intensity, more noticeable at higher Q but equal for both XRR and PNR. Figure 3.6 shows that increasing the substrate roughness and leaving the surface roughness at a low value decreases the depth of

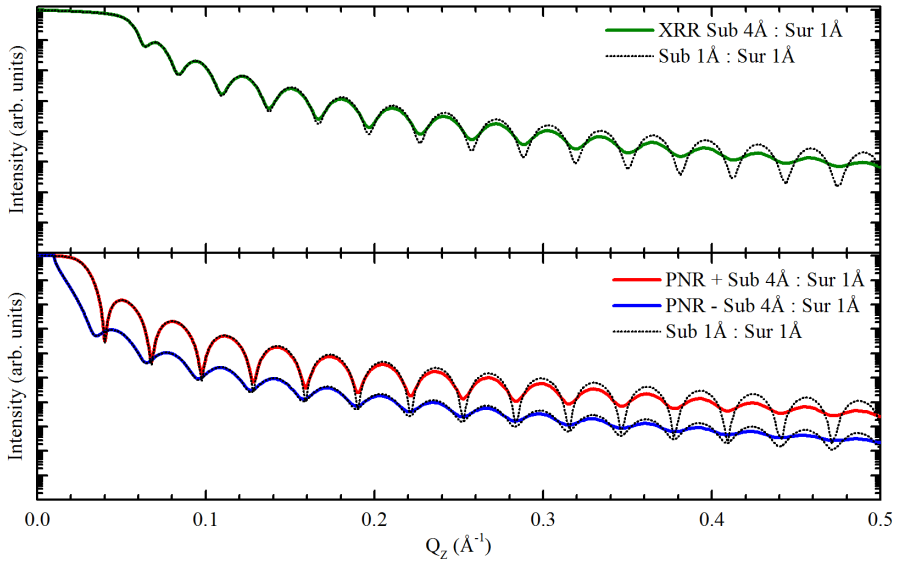


Figure 3.6: Comparison of roughness Sub 1 Å:Sur 1 Å to Sub 4 Å:Sur 1 Å for 200 Å Fe layer with 2 $\mu_B$/f.u. on Si substrate.

the fringes but maintains the same intensity drop off.

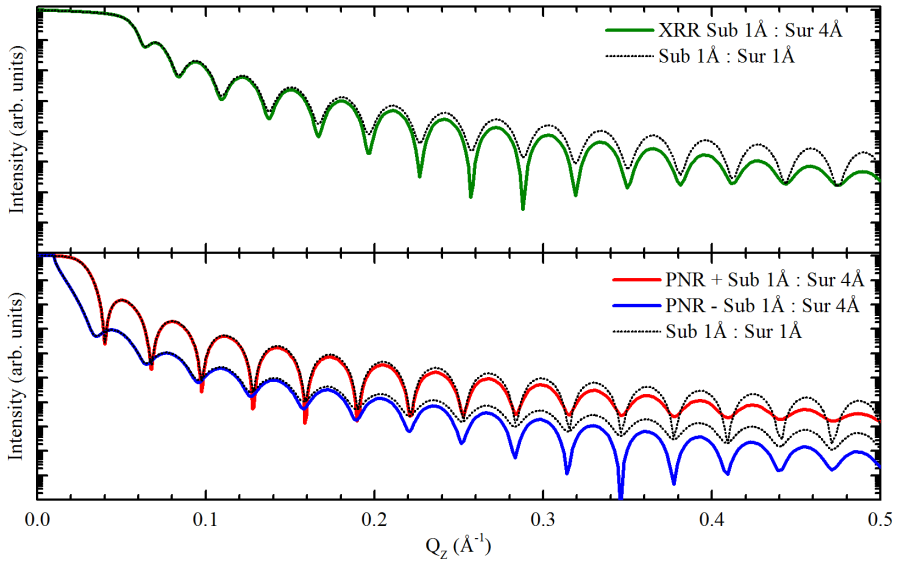


Figure 3.7: Comparison of roughness Sub 1 Å:Sur 1 Å to Sub 1 Å:Sur 4 Å for 200 Å Fe layer with 2 $\mu_B$/f.u. on Si substrate.

An increase in surface roughness (Figure 3.7) causes interference in the fringes and creates variations in the fringe depth throughout $Q_z$. Increasing the surface

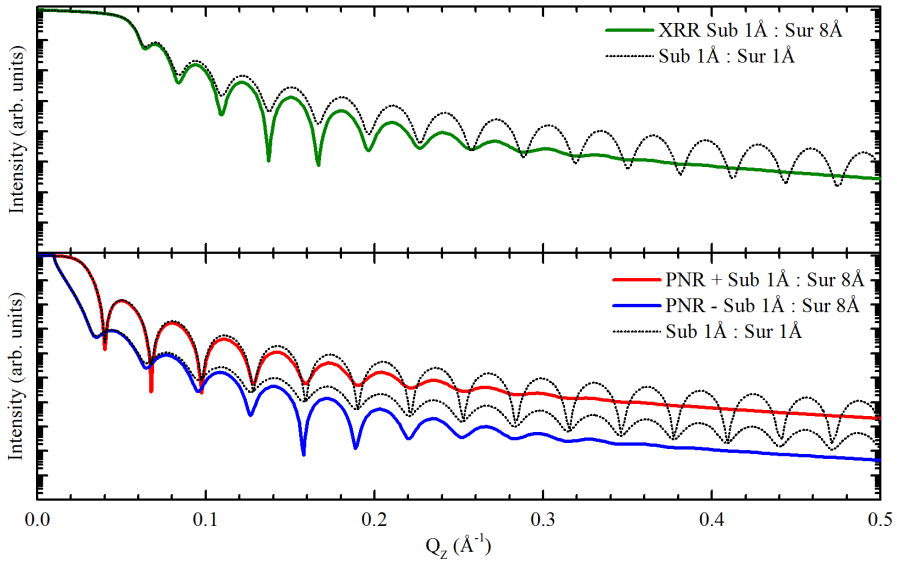


Figure 3.8: Comparison of roughness Sub 1 Å:Sur 1 Å to Sub 1 Å:Sur 8 Å for 200 Å Fe layer with 2 $\mu_B$/f.u. on Si substrate.

roughness further (Figure 3.8) changes the Q position of the deepest fringes and flattens fringes at high Q. For the XRR at low Q, the first fringe, deviations in intensity can be seen for high surface roughness. For even higher roughness, this would begin to change $Q_c$.

Given that $Q_c$ is around 0.046 Å$^{-1}$, deviations in the fringes appear at around $Q$ =0.14 Å$^{-1}$, demonstrating the reasoning to measure fringe thicknesses above $3Q_c$.

### 3.3.4 GenX Reflectivity Package

The GenX reflectivity package is a program coded using the Python language utilising a differential evolution algorithm for fitting X-ray and Neutron Reflectivity data along with Parratt's algorithm as described in the previous sections in this chapter. A complete explanation of how the software works can be found at References [23, 35, 62] and an introduction on how to set up a model is given in Chapter 4.

#### Scattering Length Density Profile

The scattering length density profile (SLD), as previously mentioned in Equations 3.20, 3.21, 3.40 and 3.46, is a combination of the scattering length of the layer, multiplied by the corresponding number density (Equation 3.15). It represents the interaction potential barrier height of the layers, $V$, which is related to the refractive

index, Equation 3.36 or Equation 3.18 by

$$V = \frac{h^2}{m\lambda^2}\delta_N \tag{3.53}$$

not including factors for magnetic contributions [1]. To a first approximation, the specular reflectivity measures the Fourier transform of the interaction potential, $V(z)$ (or the refractive index profile $n(z)$). The different probes scatter from a change in barrier height. A higher barrier represents a higher SL and therefore more scattering.

An example of the SLD profile that simulates the corresponding XRR and PNR data for 200 Å Fe layer with 2 $\mu_B$/f.u. on a Si substrate with substrate roughness of 1 Å and surface roughness of 4 Å is shown in Figure 3.9. The lower panel

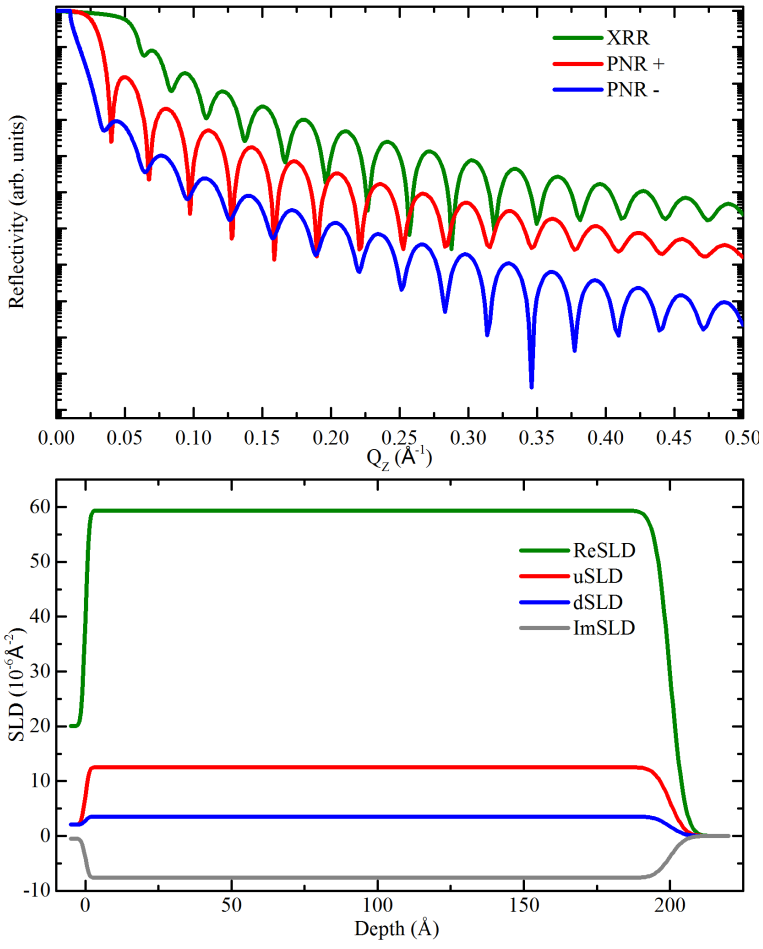


Figure 3.9: Simulated sample of 200 Å Fe layer with 2 $\mu_B$/f.u. on Si substrate with substrate roughness of 1 Å and surface roughness of 4 Å.

shows the SLDs that create the simulated reflectivity data in the upper panel. The SLD x-axis represents the depth from the sample surface (z) and using the equation above (Equation 3.53), can be converted into refractive index or interaction potential profiles. The green line "ReSLD" represents the real part of the X-ray SLD (XSLD Equation 3.20) and the grey line "ImSLD" (Equation 3.21) represents the imaginary part of the XSLD. "uSLD" is the neutron SLD + magnetic SLD = $SLD^{+}$ (Equation 3.47) and "dSLD" is the neutron SLD - magnetic SLD = $SLD^{-}$. The dSLD has a lower value for positively scattering materials, as neutrons scatter less and the intensity is lower, as seen by the intensity difference in the top panel. As there is only one layer, and the magnetism follows the same profile as the film and the uSLD and dSLD fringes are aligned. There is a slight offset at low Q due to the different gradient of roughness for the different NSLD. Experimentally, there are only four possible orders of magnitude for the neutron data before it is lost below background due to low neutron flux, causing higher Q roughness features to be lost. A comparison of SLD to sample construction is shown in Figure 3.10, where $n$ represents the refractive index of the layer and $j$ represents the Fresnel interfacial barriers. $n_1$ is air/vacuum and $n_5$ is the Si substrate. $n_2$ and $n_4$ are roughness layers which could represent either elemental mixing or structural roughness and $n_3$ is the Fe film.

### GenX Roughness Simulation

GenX models the roughness of a layer by applying a Gaussian distribution (with correction factors for the electric field amplitudes at interfaces) according to the Nevot-Croce model [23, 63]. Changes in the roughness also effect the PNR magnetic profile as the roughness is applied to the number density of the model which is common for all SLD. Roughness values that are larger than half the layer thickness are not valid. This is due to the Gaussian function being larger than that of the layer, where the roughness value states the full width half maximum (FWHM). If using the GenX mag_refl modelling with additional slicing, limiting the roughness is not as important, as the slices stop any problems caused by overlapping Gaussians due to small finite layer thicknesses. This allows further manipulation in the roughness profile enhanced by gradient variations. An example of the slicing (discrete steps) can be found on page 118 in the book by Y. Zhu [64].

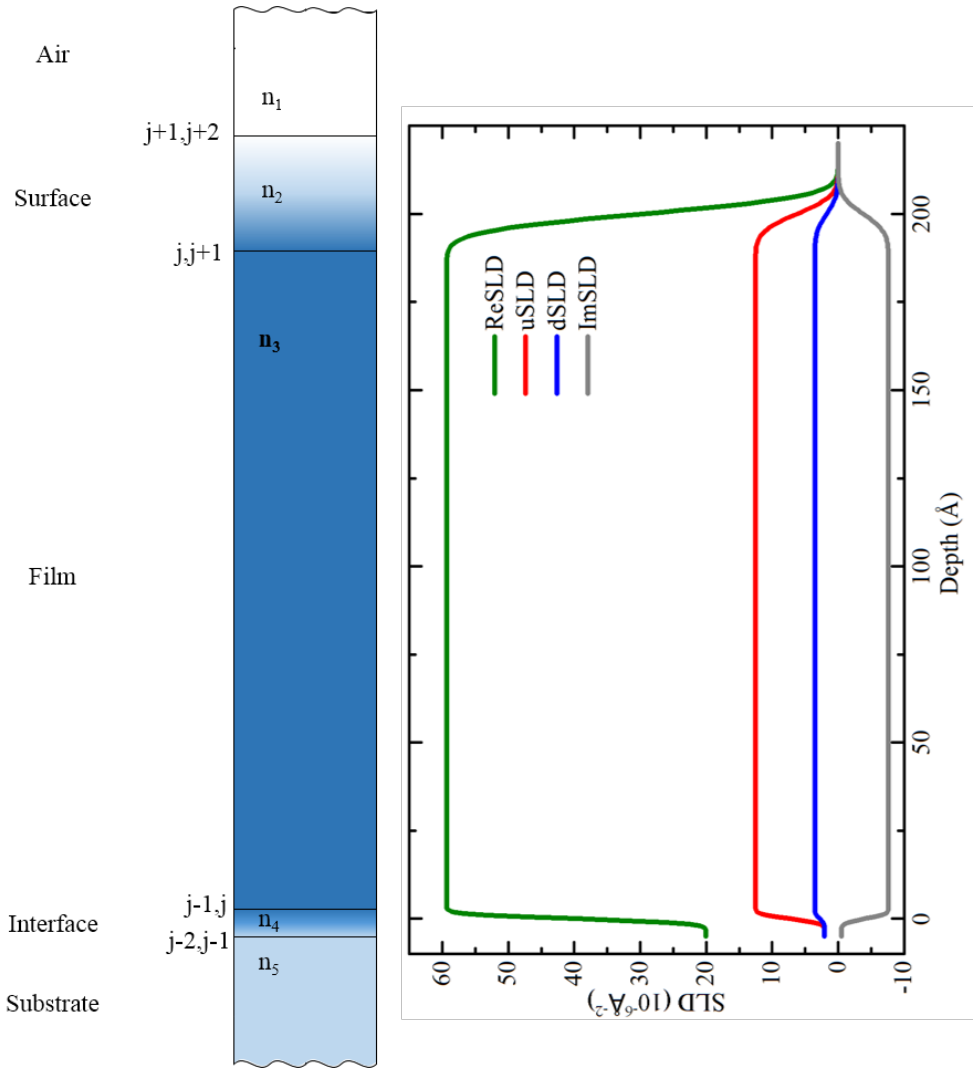


Figure 3.10: Representation of the sample structure in comparison to the SLD, showing the slab model is idealised.

### Footprint Calculation

PNR data is often corrected for illumination factors during the data reduction process before leaving the beamline. This is often not the case for XRR from lab based X-ray sources. A simple equation can be applied in order to correct for this intensity factor

$$F = \frac{T}{\sin\theta} \tag{3.54}$$

where $F$ is the beam footprint, $T$ is the beam height, and $\theta$ is the incident angle (Figure 3.11). Before running the XRR measurement the correct choice for front

slits can be found using

$$F = T/\sin(\theta) < L \qquad \theta \simeq \theta_c \tag{3.55}$$

where $L$ is the sample length and $\theta_c$ is the critical angle, as shown in Figure 3.11 [65].

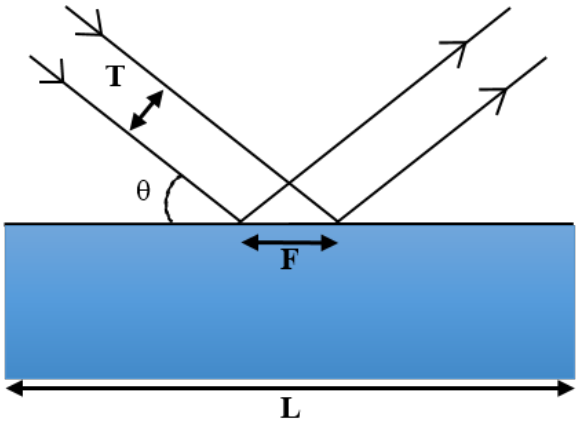


Figure 3.11: Footprint correction, $F$, of the beam depending on the beam height, $T$, the incident angle, $\theta$, and the sample width, $L$.

There is an option in the GenX software package that enables the simulated XRR data to be manipulated in order to fit the uncorrected experimental data. This requires the knowledge of the parameters discussed in Equation 3.54, the incident beam width and the sample length.

### Figure of Merit

The figure of merit (FOM) in GenX is a numerical value assigned to the quality of the fit. The further away the fit is from the data, the higher this number. Different FOM weight this calculation differently to different values (explained in the GenX Model help file). It is important to choose a FOM which focuses the fit where it is needed.

Standard GenX FOM weights data points equally. When simultaneously fitting XRR and PNR data, this weights towards the XRR as there are often many more data points due to higher flux from the source. To overcome this issue, a custom FOM can be applied in GenX to instead, weight the data sets equally. As PNR has two data sets, this does naturally weight the data but more evenly than with just the original FOM alone. Below is an example showing the custom FOMs created by manipulating the original "log" and "logR1" FOM from the software. The coding

language is Python (as the rest of GenX), the file is called "fom_funcs_custom.py" and is located in "C:\Program Files (x86)\GenX".

```
import numpy as np

def log_norm_dataset(simulations, data):
'''The absolute logarithmic difference normalised per dataset'''
N = len(data)
return [(np.log10(dataset.y) - np.log10(sim))/len(dataset.y)/N
for (dataset, sim) in zip(data, simulations)]

def logR1_norm_dataset(simulations, data):
'''The absolute logarithmic R1 difference normalised per dataset'''
N = len(data)
return [(np.log10(np.sqrt(dataset.y)) - np.log10(np.sqrt(sim)))/
np.sum(np.log10(np.sqrt(dataset.y)))/N
for (dataset, sim) in zip(data, simulations)]
}
```

It is possible to copy and paste this code and save it with the name and in the location above, to use it in GenX. Thanks go to Matts Björk for coding this.

A FOM scan can be performed in the software between a specified min and max value. An example is shown in Figure 3.12 and demonstrates how well defined a parameter is by the gradient either side of the minima peak where the gradient acts similar to an error. A large error and variation in value represents a less defined and less important parameter in the fit. Every parameter will have a different error, therefore individual perceived importance. FOM scans can also highlight other local minima nearby for the specified parameter, if they exist and the range is large enough. These scans are one dimensional and are dependent on the other parameters being in their fixed locations.

### Error Calculation

Parameter errors in this thesis extracted from the PNR data fitting, are obtained by judgement of the fitted data. An important parameter is chosen (possibly with a known larger error), such as the magnetism, and it is varied until there is an observable change in the fit. The change in parameter value is taken as the percentage error and all other parameters are varied by this same amount to obtain their error.

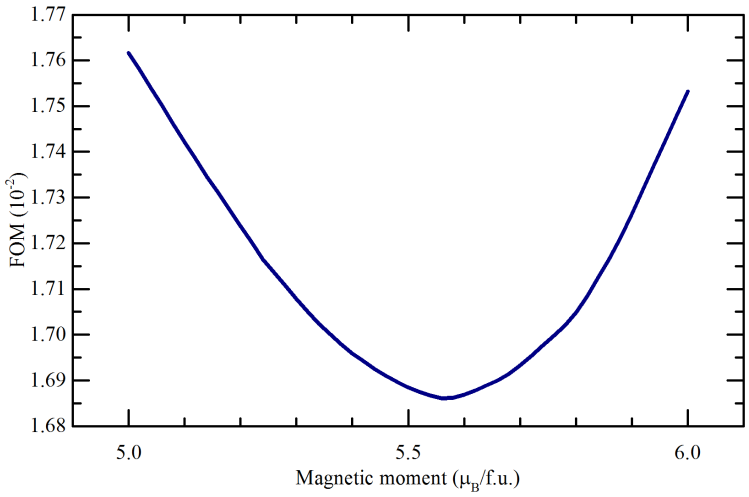


Figure 3.12: Figure of merit scan for the magnetic moment of experimental data discussed in Chapter 5.

Another error calculation method would be to move the parameter until there is a 5% difference in the optimal FOM, for example, and use this as the error.

### Conversions from GenX SLD Output to Conventional Units

When data has been successfully fitted using GenX, reflectivity data and SLD can be exported from the program. Conversions are needed in order to represent the data in conventional forms. Generally, SLD is in units of $10^{-6}$ Å$^{-2}$ and MSLD is often converted to $\mu_B$/f.u..

For spec_nx, X-ray SLDs

$$XSLD = \text{'GenX XSLD'} \times r_e \times (1 \times 10^6) \tag{3.56}$$

where $r_e$ is the classical electron radius in Å and neutron SLDs (including MSLD)

$$NSLD = \text{'GenX NSLD'} \times 10. \tag{3.57}$$

To convert from MSLD to $\mu_B$/f.u., Equation 3.23 from Y. Zhu [64] is used

$$MSLD = CN\mu \tag{3.58}$$

where MSLD is the value of the layer from GenX in units of $10^{-6}$ Å$^{-2}$, $C = 2.645 \times 10^{-5}$ Å$\mu_B^{-1}$, $N$ is the number density of the layer in units of Å$^{-3}$ and $\mu$ is the magnetic moment for specified density in units of $\mu_B$.

# Chapter 4

# Fitting of Reflectivity Data

Reflectivity fitting is known to be a complicated task due to the time, effort and the accuracy required to achieve an acceptable fit. The question of "is this fit good enough?" is dependent what information needs to be extracted from the model. In all cases, fitting of the critical edge and magnetic splitting (for PNR) is the most important. A perfect fit is not needed when trying to find film thickness or bulk film magnetism, as these features are easily extractable and the use of PNR is not even needed; XRR and VSM or SQUID measurements achieve these results. When buried interfaces or magnetic profiles are sought, the best possible fit is required with the best parameter minimisation (lowest FOM value Section 3.3.4) in order to trust the model information. Often this cannot be done by following a standard fitting procedure and requires further information about the sample. Some unusual sample features found using different techniques can change limitations of the fits and introduce a different style of modelling. The fitting procedure, when understood by manual manipulation, gives the user the feeling and understanding what SLD features are needed to fit the Kiessig fringes. Reflectivity fitting can be an art and It is always best to complete the data fitting process as quickly as possible, in order to understand the shape of the SLD profiles needed.

In this chapter the reflectivity fitting procedure of a single magnetic film grown on a substrate will be outlined, simultaneously fitting XRR and PNR as an average user of the software, not as an advanced user rewriting Python code. For more understanding of the software and coding used, the user is advised to read journal article [23], thesis [35] (page 59, Manual for GenX) and visit the webpages at [66], where the user can also download a copy of the software for Windows or Macintosh operating systems. This Chapter will also be loaded onto the GenX website so that it can be updated and improved for the needs of the users at ILL,

France and ISIS, RAL, UK.

## 4.1 GenX Setup

### 4.1.1 GenX Start-up Options

After installing the software, the next process is to set up the basics of the model. Before importing data, ensure it has been processed accordingly: illumination corrected (if not using this option in the GenX software), and normalised as shown in the previous Chapter 3.3.4.

- When starting GenX click to install the "Reflectivity" plug-in (if the option is given).
- Choose either "spec_nx" or "mag_refl" model (Figure 4.1). This thesis focuses on spec_nx, see 3.3.4 for a short description of the advantage of magrefl. More information can be found on the GenX website [66].
- Go to Settings>Plugins and ensure that "Reflectivity" is loaded by clicking the option if it is there. If the parameter tabs don't load (Figure 4.2 number 15), this will be the cause.

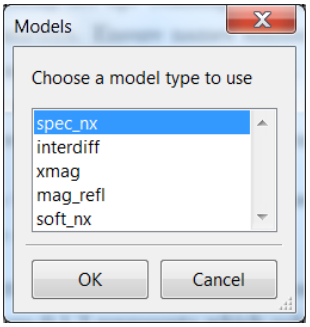


Figure 4.1: GenX pop up window showing model choices.

Figure 4.2 shows the initial GenX interface. Important buttons are numbered in order to help the reader find the correct button when mentioned in the text. A description of the button purposes are given in Table 4.1. Throughout fitting it is advisable to press the "simulate" button (lightening bolt or F9, number 4) after every change made to the model, in order to check the changes made and ensure there are no errors. Sometimes errors will occur until the model has been correctly set up. Naming conventions are also important when adding layers and parameters.

Ensure names similar to code words used by GenX are not used, as this can cause errors are not used. GenX has a help file located Help>Built-in Help>Models. You can also see here a help file for the FOM (Chapter 3.3.4).

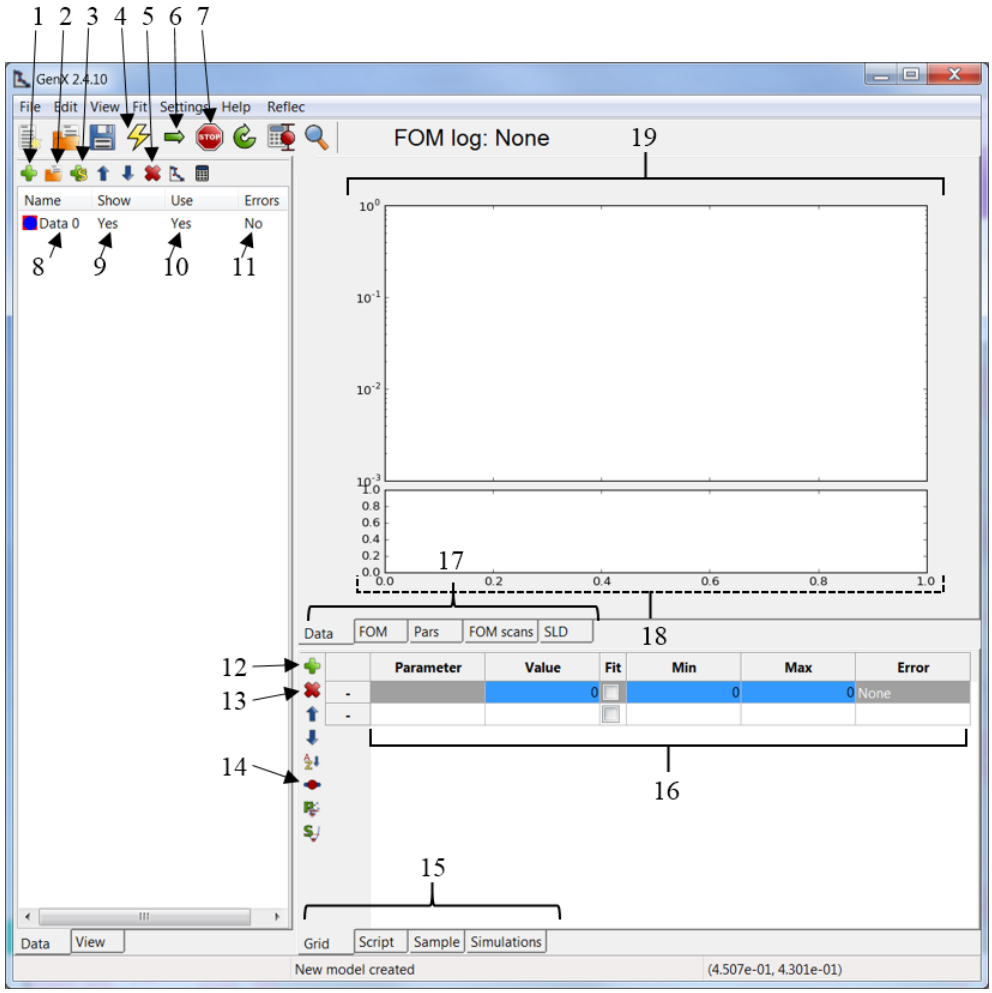


Figure 4.2: The initial GenX window with labels described in the text.

Table 4.1: List of GenX buttons and panels corresponding to Figure 4.2 from 1-19 and Figure 4.3.

| Number | Description |
|---|---|
| 1 | Add data sets |
| 2 | Open data file |
| 3 | Create simulated data |
| 4 | Simulate |
| 5 | Delete data set |
| 6 | Start fit |
| 7 | Stop fit |
| 8 | Data set name |
| 9 | View this data set on 19? |
| 10 | Fit this data set? |
| 11 | Include errors in fitting? |
| 12 | Add new Parameter |
| 13 | Delete parameter |
| 14 | Use visual sliders |
| 15 | Parameter tabs |
| 16 | Parameter grid |
| 17 | Visualisation tabs |
| 18 | FOM viewer |
| 19 | Data and simulation viewer |
| 20 | Sample tab |
| 21 | Add layer |
| 22 | Add stack |
| 23 | Delete Layer |
| 24 | Rename layer |
| 25 | Move layer arrows |
| 26 | Slicing options (mag_refl) |
| 27 | Instrument setup |

### 4.1.2 Inserting Data Sets

- Settings>Import defines the layout of the data to be loaded into the program where 0,1,2 represents which column the corresponding values are located in. Redefine if necessary.
- The green plus (button 1), allows more data set spaces, and the file button next to it (button 2) allows for the file loaded into the selected data space by searching its location.
- Simulate the data 'F9' to show it in the Data and simulation viewer (panel 19).

- The data sets can be renamed and colours changed using the small graphing icon (next to button 5).
- Data can be manipulated using the calculator button, but it is not advisable to change any of the experimental data without valid reason.

Figure 4.3 shows the sample tab and buttons 20-27.

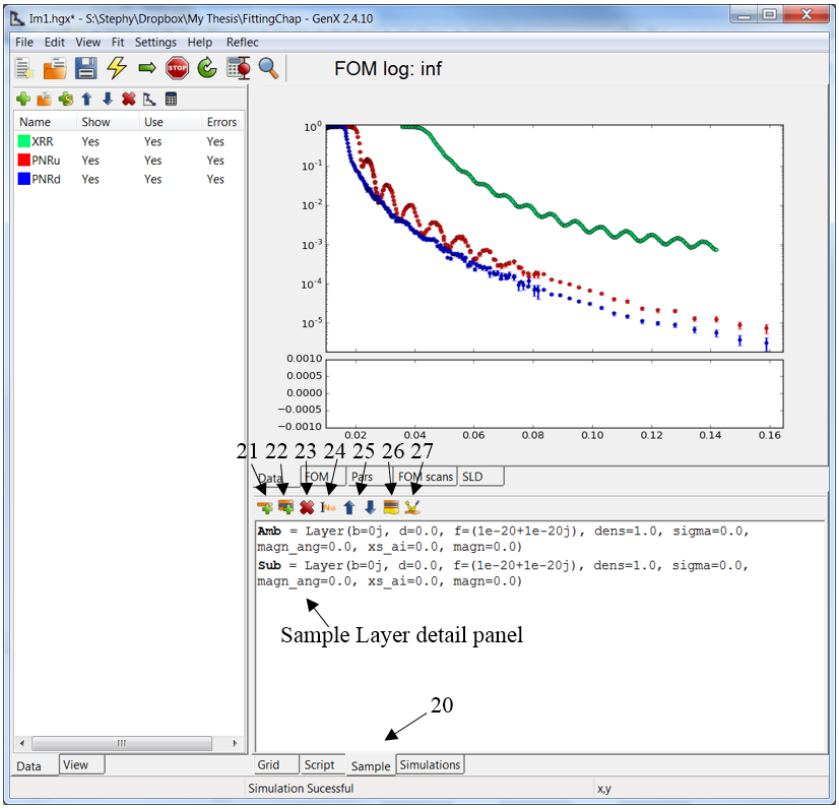


Figure 4.3: GenX model showing three data sets the Sample tab, buttons 20-27.

### 4.1.3 Defining Instrument Settings

- At the bottom, the "Sample" tab (button 20) contains information about the materials and layers in the model and contains the options to edit the probe.
- Clicking on the "instrument editor" (button 27) brings up a pop up box containing details about the instruments used (Figure 4.4). It is important to create a new instrument for each different experiment used. In this case, one will be created for the XRR (name kept as "inst") and another for the PNR (named "neut"). If there are new experimental parameters, start a new instrumental profile by clicking the green +.

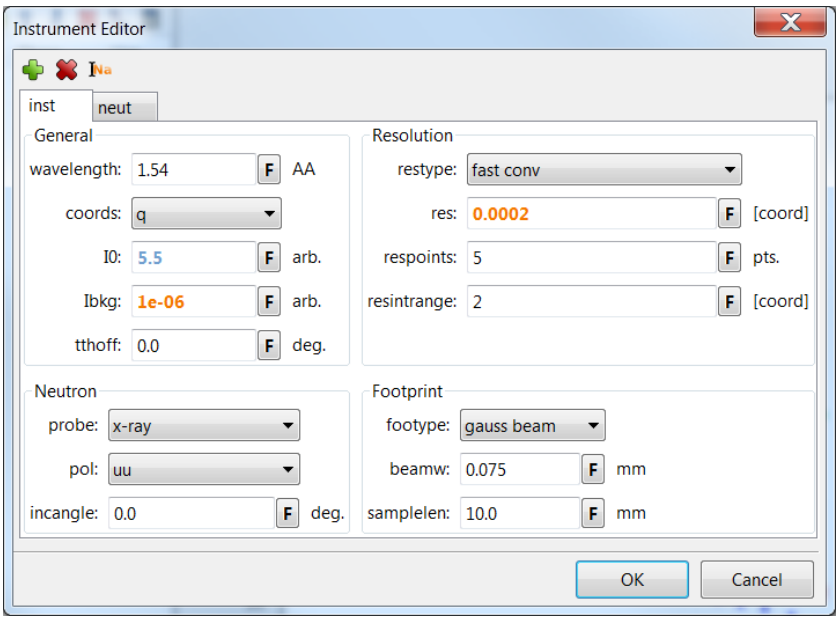


Figure 4.4: GenX model showing instrument editor window.

- Ensure the wavelength of your corresponding probe is correct and that your coordinates are either “tth” or “q”. Q is a better option as it is not dependant on wavelength or angle and is often the standard for neutron facilities. (Note: after finishing the set up, check that changing the wavelength doesn’t effect the simulation when in Q. An error sometimes occurs in the SL calculation if there are different wavelengths for different probes.)

- Resolution is instrument and experiment dependant, and ”varying res” is the option to choose when slit sizes change throughout the single reflectivity measurement, unless they were modified to maintain the same resolution. “full conv” values takes more points into account and calculates the resolution at each data point, making it run more slowly than “fast conv” which assumes equally spaced data points and integrates over the number of points which is needed to fill up the maximum encountered resolution. The resolution value is normally around 2%, but be aware that the methods of calculating the resolution means that this value can be 0.0002 for “fast conv” and 0.002 for “full conv and varying res”. The dx/x options are programmed for the POLREF neutron reflectometer at ISIS, RAL and are the relative resolution where again $2\% = 0.02$.

- The bottom right section holds the opportunity to add the illumination (footprint) correction to the data, if this was not done externally before importing

into GenX (parameters explained in Chapter 3.3.4).

- The bottom left sets up the probe used. In this case the options are “x-ray” and “ass” for XRR and “neutron pol” and “uu” for PNR.
- Press OK and return to the main window. Press the “Simulations” tab in the Parameter tabs (15).
- The tab should give a list of the data sets and corresponding instrument settings. Double click on a data set and change the instrument drop down box to match the corresponding set up (Figure 4.5).
- Click the “+” button to add a parameter rule. The instrument settings need to be defined for each data set. Possible error: if only the “cp” object is available, simulate the model. As the XRR is only one instrumental setting, further parameters should not need to be added here. For the PNRu choose Object: “neut”, Parameter: “setPol”, and Expression: ‘uu’.

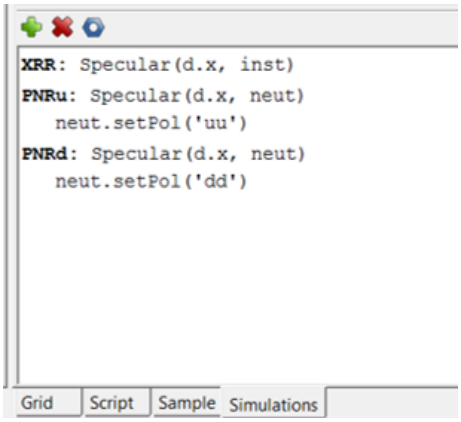


Figure 4.5: GenX model showing the simulations tab with instrument setup.

### 4.1.4 Setting the Sample

- Next head back to the “Sample” tab (button 20) and add a stack by clicking button 22, giving it a name (see Figure 4.6). Click the new stack in the panel and press button 21. In this example the layer is called “film”. Double click the new layer to bring up the layer editor.
- Enter information about the film. The “f” box represents the XSL where “fp.Fe*3+fp.O*4” can be typed in to automatically calculate the SL value of

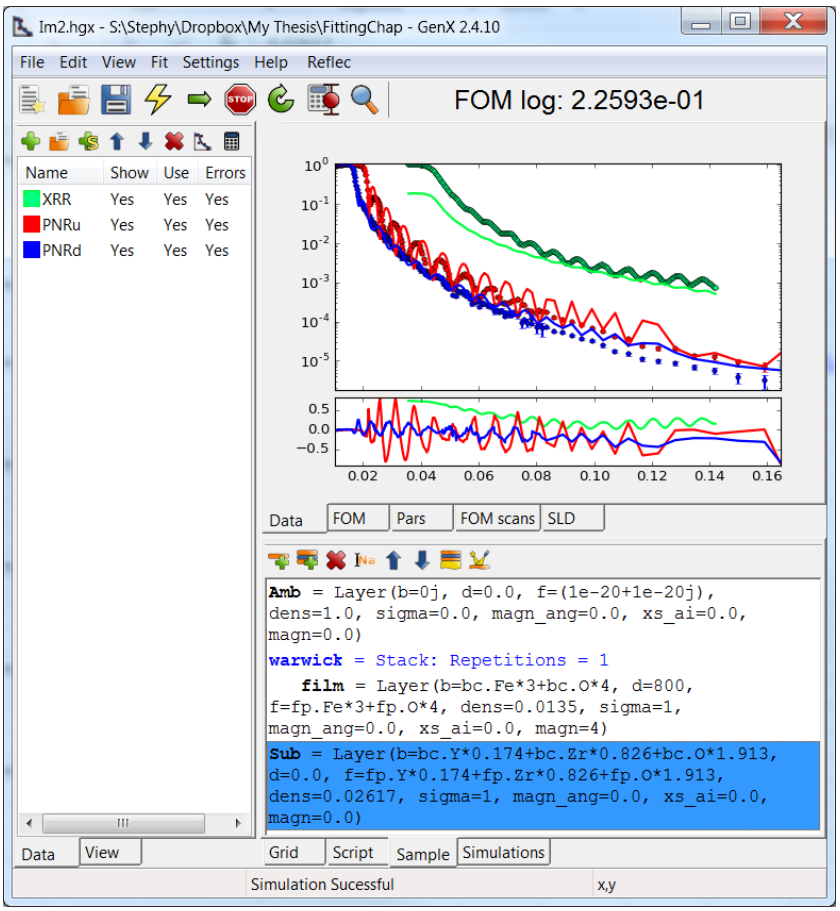


Figure 4.6: GenX model showing the sample tab with added layer details. The simulated data for the added layer information is also shown.

$Fe_3O_4$ (assuming the instrument editor wavelength is correct). The scattering length can also be added directly using the convention 'A−Bj' where A is the real part of the XSL and B is the imaginary (ensure to include 'j'). For $Fe_3O_4$ at $\lambda = 1.54$ Å this is (106.7817 - 9.7601j). The "b" box represents the neutron SL where bc.Fe*3+bc.O*4 can be used or 51.5620 typed. There is no need for the imaginary part of the neutron SL here as the absorption cross section is negligible in most cases (see [57, 58] for more information).

- "Dens" is the number density defined by Equation 3.15. Consistency is needed when defining the correct number of atoms per volume specified to be sure the parameters are logical.
- "d" is the thickness of the layer (to be left as 0.0 for the substrate).
- "sigma" is the RMS roughness of the layer which should be added as 1 for

now.

- "magn" is the expected magnetic value of the film in $\mu_B$ per volume to the same composition and density as previously used.
- Press OK and exit the layer editor.
- Enter the corresponding information for the substrate, by double clicking on the layer. The thickness, D should remain at 0.
- Press simulate (F9) to see the simulated reflectivity curves of the model inputted.

### 4.1.5 Setting the FOM and Computational Power

- Panel 18 is the representation of the FOM. To change the FOM click Settings >Optimizer (Figure 4.7), and choose a realistic FOM for the data press OK and simulate. For simultaneous fitting of XRR and PNR, logR1 is an option which appears to weight the data sets similarly. This is seen as the FOM plot shows the deviation from the fit. The FOM focusses the fitting to improve the largest deviations away from 0. FOM equations are show in the Help > Built-in Help > Models file.

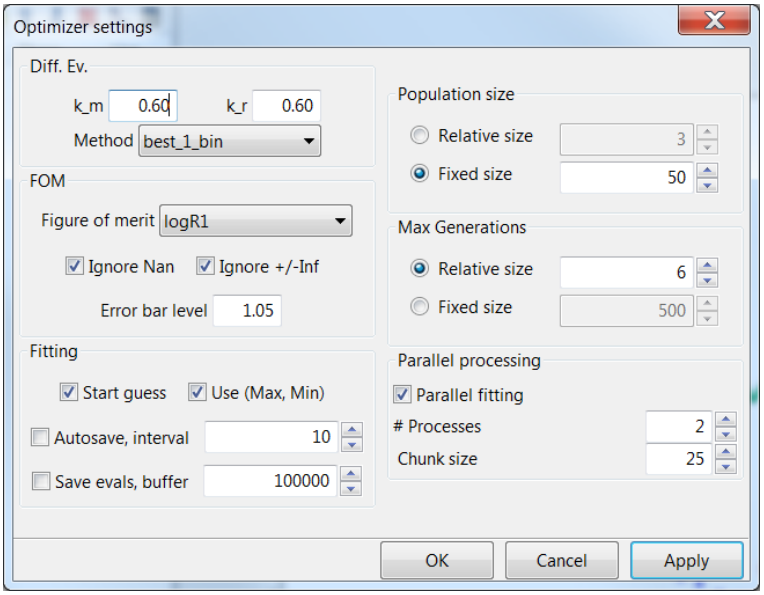


Figure 4.7: GenX model showing optimizer window with FOM options and iteration information.

- Also in the Optimizer window, are the options to ignore certain features of the data, such as negative values and 0s which are not processable by FOM with logs or error bars. Click these boxes to ignore them instead of removing them from the data set. The right hand side of this box represents changes in the way the processing of the fit works. A good set of options is Population size: Fixed size: 50, Max Generations: Relative Size 6, Parallel processing: # Processes 2, Chunk size: 25. Make sure to check the parallel fitting box. This will then use two computer cores to run 50 processes to a maximum number of iterations (generations) for a given population size [35]. The differential evaluation box is set up to be generalised for most uses of the software, but can be further explained in [62].

- The "Fitting" box takes into account the initial parameters and uses the max and min values as stated in the Parameter grid (16). There is an option to autosave the file after a set number of intervals and also to save evaluations for error processing.

### 4.1.6 Sample Parameter Grid Import.

The remaining task is to go to the "Grid" tab and input the parameters by right clicking the parameter box. More can be added with the "+" symbol. Input the Instrument settings, along with the layer parameters as shown in Figure 4.8. When adding the parameters, the min and max values are automatically set to ±10% of the current value. This is a good starting range and can be adjusted later to give the fit more room to adjust. Values in this table are specific to the data shown in the thesis, and must be changed for the individual data input.

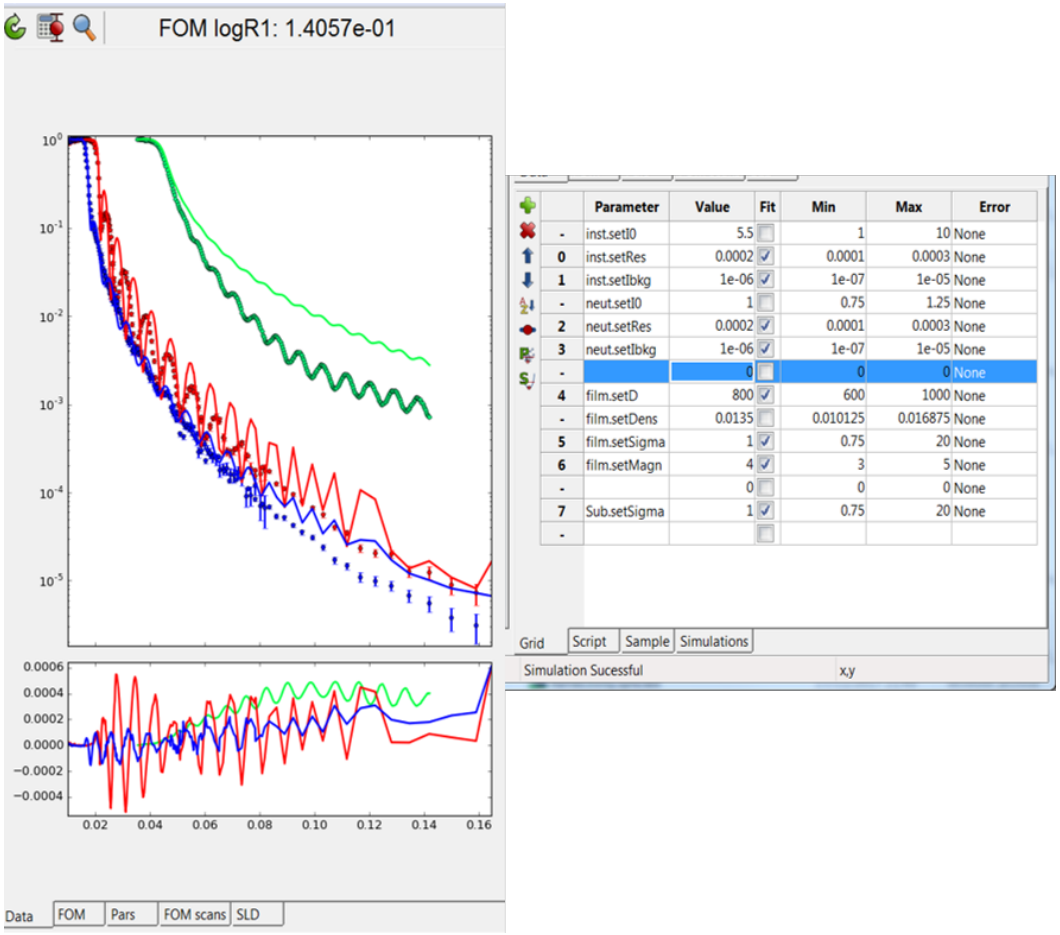


Figure 4.8: GenX model showing the grid with parameters added for the sample and the instrument.

## 4.2 Fitting the Data

The challenge now is to fit the data by hand. It is important to know how the parameters change the simulation, and also to set up certain parameters in order to limit the fit. By clicking Fit>Automatic simulation, enables the ability for the up and down arrows (that appear when changing the parameter value) to simulate the fit after every click which is useful when observing the changes that one parameter makes. Rather than changing the values, a slider option is also available by clicking View>Grid>View as slider or by pressing the slider button (14) to the left of the grid. By changing the thickness, we start to improve the fit (Figure 4.9). It is very crucial to pay attention to the critical edge of the neutrons. The position of $Q_{c+}$ is dominated by the film SLD and $Q_{c-}$ by the substrate SLD. It is a necessary starting point to align the simulation with the data in order to fix the dominant values of

SLD and MSLD. When making manual changes (and after fitting the data) always check the SLD as unusual (or non smooth) features in the SLD are often unrealistic and shouldn't be believed unless other experiments back up this characteristic.

### 4.2.1 Setting Custom Parameters

As neutrons are randomly sensitive to elements, it is better to choose to vary the composition of the materials vs the density, unless the composition of the film is very well known. Custom parameters are needed in order for the individual elemental contributions to vary, while remaining consistent between X-ray and neutron data sets.

- In the Simulations tab, click on the grey nut at the top of the panel. Parameters are created "NFe" with a value 3, and NO with a value 4. Click on the XRR data set and press the "+". Object: film, Parameter: setF, Expression: fp.Fe*cp.NFe+fp.O*cp.NO . For just one of the PNR data sets Object: film, Parameter: setB, Expression: bc.Fe*cp.NFe+bc.O*cp.NO. (Example can be seen in the final spec_nx fit Figure 4.16.) Pressing simulate shouldn't change the simulation as we have entered the same composition as previously applied. The option here was to add two user variables instead of Fe*x+O(1-x) due to wanting to allow for changes in density as well as composition (N*b). The current method allows for depletion of atoms within the density specified. Any custom parameters are read by the code in the order displayed in the simulations tab. Parameters are also carried though to other data sets, so ensure values are specified correctly and check they work as expected.

- Return to the parameter grid (16) and add the user variables. Modify them manually until they appear to fit the critical edge of the neutron data (zoom into the graph to check, right click the simulation viewer 19). As the YSZ substrate used here isn't very well characterised in terms of the density or SL, the choice to vary dens is much easier.

### 4.2.2 Data Fit Continuation

A better fit to the data is observed and updated parameters can be seen in Fig 4.9. neut.setRes min and max values must be changed in order to accommodate for the new value. As the expected value for this is 0.0002, caution should be taken that there isn't a missing parameter causing the decrease in fringe definition rather than a res change. It is clear from the X-ray fit that in order to curve the shape

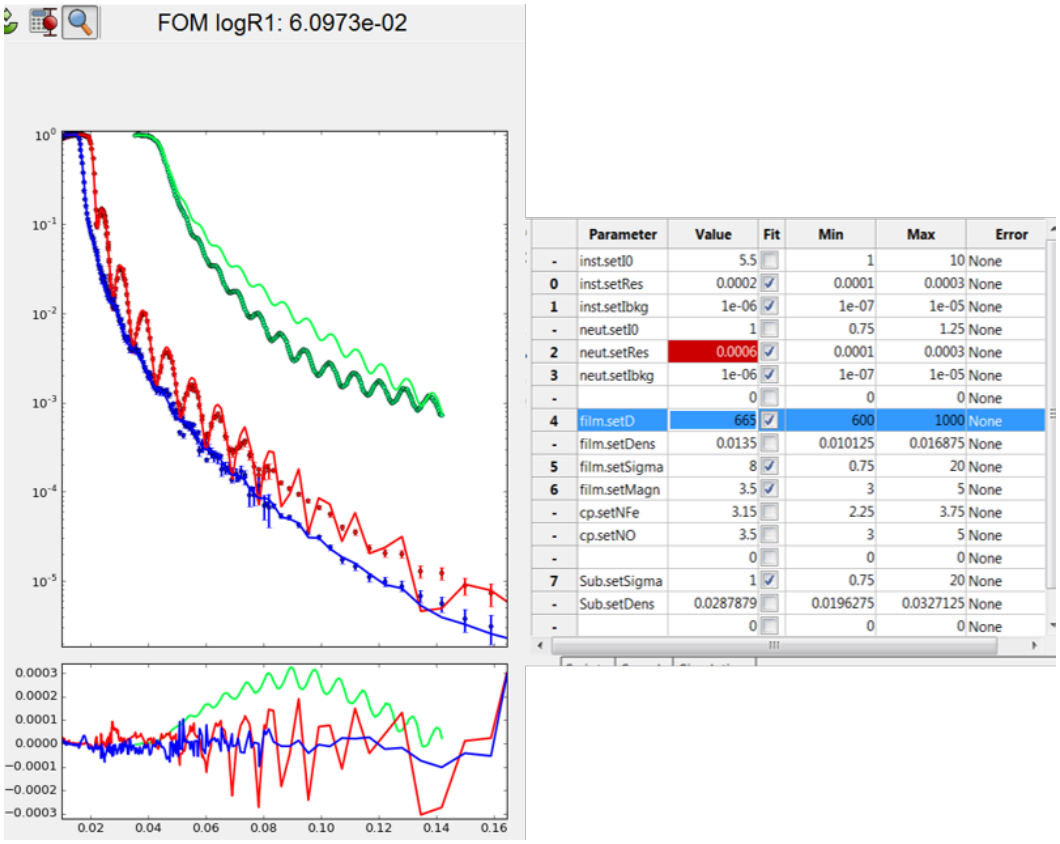


Figure 4.9: GenX model showing the grid and the first guess of the parameters after manual fitting of the critical edge and fringes by modifying the substrate dens, film composition, film thickness and roughness.

of the drop off, another layer is needed. To optimise parameters, a FOM taking into account the lower Q range should be found and the fit can be run. FOM:R1 is chosen with current value 6.2015e-02. I0 parameters are fixed as changes in SL and instrument settings can effect this height. Parameters can be allowed a larger range of adjustment when the simulation is closer to the data.

The fit minimises to FOM: R1=3.3108e-2 (Figure 4.10), but it is clear that some parameters are not representative of the data. The neutron res is too low as seen by the first PNR+ fringe so is raised to matched the data. The background values for the neutron data (as see as an increase in I0 at high Q) is also too high. This is also lowered and fixed. The roughness had increased in order to fit the X-ray data, so is lowered, which improves the neutron fit further. As the neutron data fits quite well, the sub density, neut res and neut bkg are fixed. Simulating the new parameters leads to a FOM that has increased to R1: 4.5240e-2 (Figure 4.11), but is more representative of the entire data set rather than just the low Q region. It is

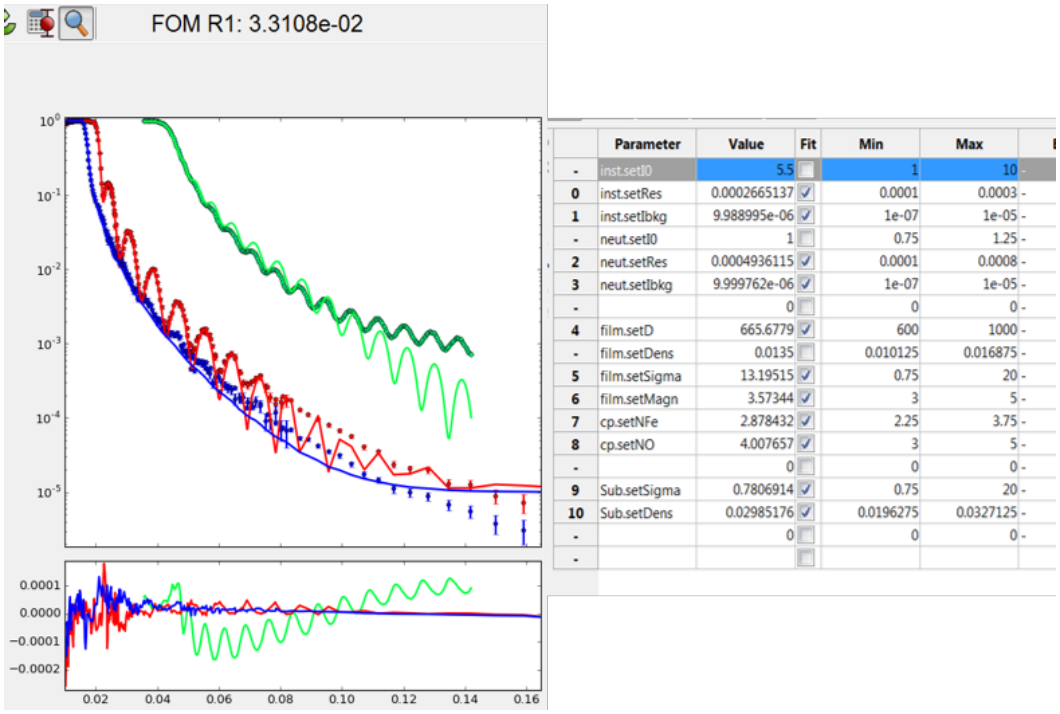


| | Parameter | Value | Fit | Min | Max |
|---|---|---|---|---|---|
| - | inst.setI0 | 5.5 | ☐ | 1 | 10 |
| 0 | inst.setRes | 0.0002665137 | ☑ | 0.0001 | 0.0003 |
| 1 | inst.setIbkg | 9.988995e-06 | ☑ | 1e-07 | 1e-05 |
| - | neut.setI0 | 1 | ☐ | 0.75 | 1.25 |
| 2 | neut.setRes | 0.0004936115 | ☑ | 0.0001 | 0.0008 |
| 3 | neut.setIbkg | 9.999762e-06 | ☑ | 1e-07 | 1e-05 |
| - | | 0 | ☐ | 0 | 0 |
| 4 | film.setD | 665.6779 | ☑ | 600 | 1000 |
| - | film.setDens | 0.0135 | ☐ | 0.010125 | 0.016875 |
| 5 | film.setSigma | 13.19515 | ☑ | 0.75 | 20 |
| 6 | film.setMagn | 3.57344 | ☑ | 3 | 5 |
| 7 | cp.setNFe | 2.878432 | ☑ | 2.25 | 3.75 |
| 8 | cp.setNO | 4.007657 | ☑ | 3 | 5 |
| - | | 0 | ☐ | 0 | 0 |
| 9 | Sub.setSigma | 0.7806914 | ☑ | 0.75 | 20 |
| 10 | Sub.setDens | 0.02985176 | ☑ | 0.0196275 | 0.0327125 |
| - | | 0 | ☐ | 0 | 0 |
| - | | | ☐ | | |

Figure 4.10: GenX model showing the first minimised fit with film layer and substrate.

often the nature of the XRR data to have a surface layer that the PNR doesn't see as it is more sensitive to the surface of the sample, and one will now be included, following the same process as before.

When fitting the new layer, it is again advisable to fit either dens or SL only. Keeping the dens the same as the film again allows more movement in the SLD, but as the surface SLD is expected to be lower than that of the film (due to more O and less Fe), more adjustment must be allowed in the min/max values. For thin layers it is also advisable to add a parameter which limits the available roughness.

- Make a new parameter "lay1sig = 0.4".
- In the top data set Object: lay1, Parameter: setSigma, Expression: "lay1.getD()*cp.lay1sig".
- Add to the grid and make min=0.01 and max=0.5.

The roughness limitation then takes the value of the layer thickness, and only allows the roughness to be a maximum of half the value. This then ensures the Gaussian isn't wider than the layer algorithm valid. If this were part of two smaller

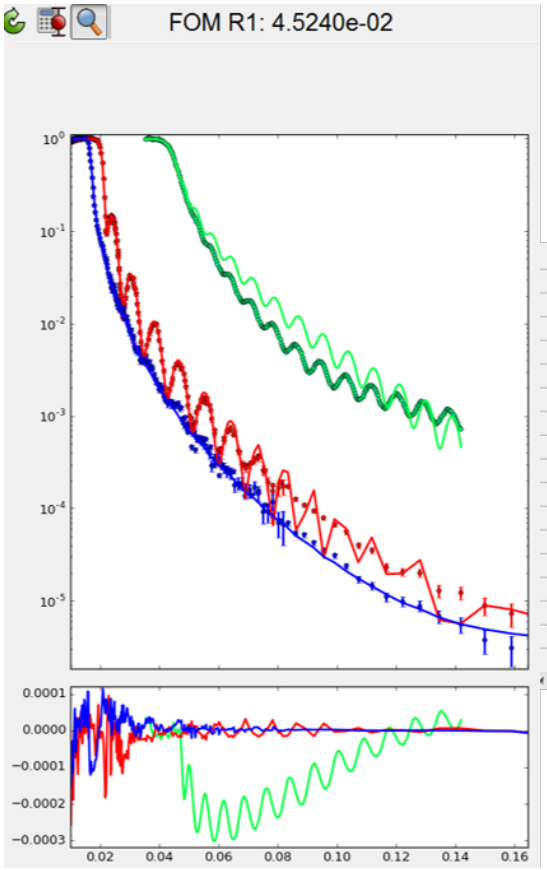


| | Parameter | Value | Fit | Min | Max | Error |
|---|---|---|---|---|---|---|
| - | inst.setI0 | 5.5 | ☐ | 1 | 10 | - |
| 0 | inst.setRes | 0.0002665137 | ☑ | 0.0001 | 0.0003 | - |
| 1 | inst.setIbkg | 6.535e-06 | ☑ | 1e-07 | 1e-05 | - |
| - | neut.setI0 | 1 | ☐ | 0.75 | 1.25 | - |
| - | neut.setRes | 0.00059 | ☐ | 0.0001 | 0.0008 | - |
| - | neut.setIbkg | 3.56476e-06 | ☐ | 1e-07 | 1e-05 | - |
| - | | 0 | ☐ | 0 | 0 | - |
| 2 | film.setD | 665.6779 | ☑ | 600 | 1000 | - |
| - | film.setDens | 0.0135 | ☐ | 0.010125 | 0.016875 | - |
| 3 | film.setSigma | 9.3452 | ☑ | 0.75 | 20 | - |
| 4 | film.setMagn | 3.57344 | ☑ | 3 | 5 | - |
| 5 | cp.setNFe | 2.878432 | ☑ | 2.25 | 3.75 | - |
| 6 | cp.setNO | 4.007657 | ☑ | 3 | 5 | - |
| - | | 0 | ☐ | 0 | 0 | - |
| 7 | Sub.setSigma | 0.7806914 | ☑ | 0.75 | 20 | - |
| - | Sub.setDens | 0.02985176 | ☐ | 0.0196275 | 0.0327125 | - |
| - | | 0 | ☐ | 0 | 0 | - |

Figure 4.11: GenX model showing manual modification after first fitting procedure.

layers, it is also important to set the roughness so that it doesn't exceed half the thickness of either layer (often viewed as a single resonance feature). This ensures the error function representing the roughness has finished varying before starting a new layer.

Again it is important to vary the model by hand to set a new starting point (Figure 4.12). When choosing a FOM and running the fit, not every available parameter has to be fitted. If the fit looks good, but optimisation needs to be on the composition, then just let these parameters fit. When fitting it is informant to look at the "Pars" tab. Here it shows where the parameter is positioned within its min/max values, and indicates the need for these boundaries to be moved. Change the FOMs in order to fit different parts of the data sets before adding any more layers. It is also beneficial to push the fit out of its minima by changing the thickness of a layer etc, and see if it minimises to the same place. This can be done by playing with parameters to see which ones improve the data set in the way you want. Pushing the fit out of possible local minima is important to find a more

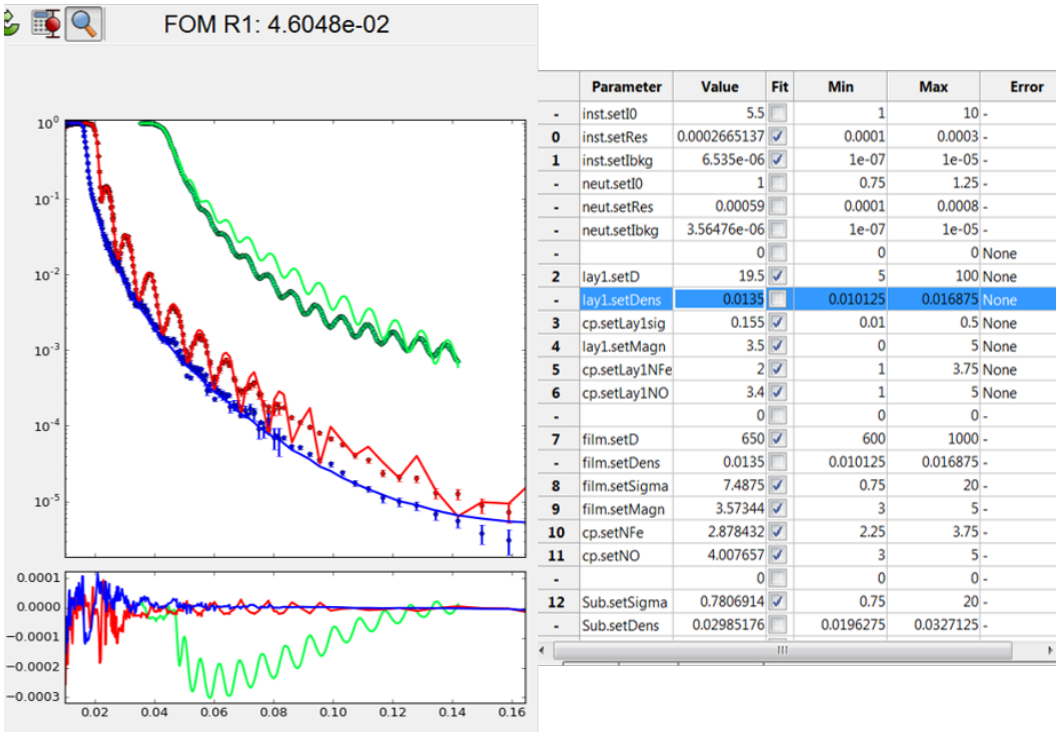


| | Parameter | Value | Fit | Min | Max | Error |
|---|---|---|---|---|---|---|
| - | inst.setI0 | 5.5 | ☐ | 1 | 10 | - |
| 0 | inst.setRes | 0.0002665137 | ☑ | 0.0001 | 0.0003 | - |
| 1 | inst.setIbkg | 6.535e-06 | ☑ | 1e-07 | 1e-05 | - |
| - | neut.setI0 | 1 | ☐ | 0.75 | 1.25 | - |
| - | neut.setRes | 0.00059 | ☐ | 0.0001 | 0.0008 | - |
| - | neut.setIbkg | 3.56476e-06 | ☐ | 1e-07 | 1e-05 | - |
| - | | 0 | ☐ | 0 | 0 | None |
| 2 | lay1.setD | 19.5 | ☑ | 5 | 100 | None |
| - | lay1.setDens | 0.0135 | ☐ | 0.010125 | 0.016875 | None |
| 3 | cp.setLay1sig | 0.155 | ☑ | 0.01 | 0.5 | None |
| 4 | lay1.setMagn | 3.5 | ☑ | 0 | 5 | None |
| 5 | cp.setLay1NFe | 2 | ☑ | 1 | 3.75 | None |
| 6 | cp.setLay1NO | 3.4 | ☑ | 1 | 5 | None |
| - | | 0 | ☐ | 0 | 0 | - |
| 7 | film.setD | 650 | ☑ | 600 | 1000 | - |
| - | film.setDens | 0.0135 | ☐ | 0.010125 | 0.016875 | - |
| 8 | film.setSigma | 7.4875 | ☑ | 0.75 | 20 | - |
| 9 | film.setMagn | 3.57344 | ☑ | 3 | 5 | - |
| 10 | cp.setNFe | 2.878432 | ☑ | 2.25 | 3.75 | - |
| 11 | cp.setNO | 4.007657 | ☑ | 3 | 5 | - |
| - | | 0 | ☐ | 0 | 0 | - |
| 12 | Sub.setSigma | 0.7806914 | ☑ | 0.75 | 20 | - |
| - | Sub.setDens | 0.02985176 | ☐ | 0.0196275 | 0.0327125 | - |

Figure 4.12: GenX model with substrate, film and surface after manual fitting.

global minima. Save models at regular intervals, with logical names in order to be able to retrieve models and fits if you prefer an older fit or the program shuts without saving. It is also easy to press save instead of simulate, always save before modifying a model.

Figure 4.13 shows the fitted data where the drop off in the XRR data is not fitted, but the neutrons are a good fit. An attempt of moving the surface layer to the interface, doesn't improve the XRR. There is the observable need for a rougher neutron interface due to the definition of the fringes being too large at high Q, but increases in this parameter lose all high Q definition in the X-ray data. To combat this issue an interfacial layer is added.

The thickness of the film has been very well defined from the beginning, so the new film thickness is set to be cp.thick-lay2.getD(). This allows one parameter to change two, making the model more efficient. Adding this interface layer allows a change in composition, density and magnetism near the substrate. The substrate roughness must be limited to half the thickness of the interfacial layer to stop overlapping of error functions. The first guess of fitting the interface should be that the SLD is the same as the film. This enables the possibility that a roughness or thickness change in the magnetism at the interface could cause the fringe effect.

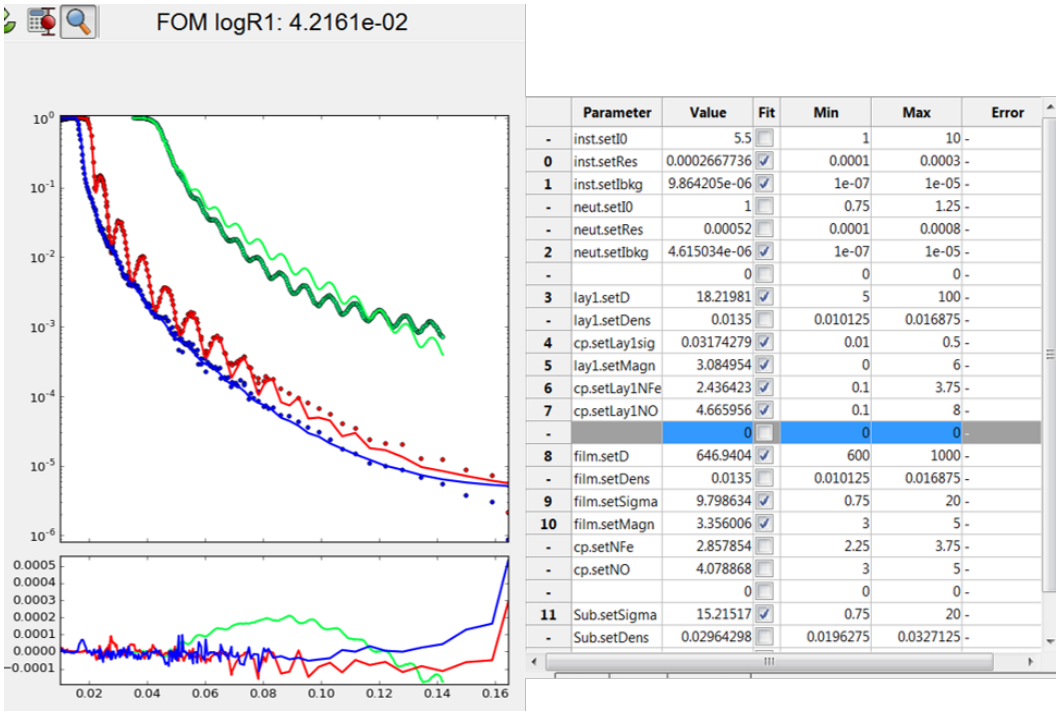


| | Parameter | Value | Fit | Min | Max | Error |
|---|---|---|---|---|---|---|
| - | inst.setI0 | 5.5 | ☐ | 1 | 10 | - |
| 0 | inst.setRes | 0.0002667736 | ☑ | 0.0001 | 0.0003 | - |
| 1 | inst.setIbkg | 9.864205e-06 | ☑ | 1e-07 | 1e-05 | - |
| - | neut.setI0 | 1 | ☐ | 0.75 | 1.25 | - |
| - | neut.setRes | 0.00052 | ☐ | 0.0001 | 0.0008 | - |
| 2 | neut.setIbkg | 4.615034e-06 | ☑ | 1e-07 | 1e-05 | - |
| - | | 0 | ☐ | 0 | 0 | - |
| 3 | lay1.setD | 18.21981 | ☑ | 5 | 100 | - |
| - | lay1.setDens | 0.0135 | ☐ | 0.010125 | 0.016875 | - |
| 4 | cp.setLay1sig | 0.03174279 | ☑ | 0.01 | 0.5 | - |
| 5 | lay1.setMagn | 3.084954 | ☑ | 0 | 6 | - |
| 6 | cp.setLay1NFe | 2.436423 | ☑ | 0.1 | 3.75 | - |
| 7 | cp.setLay1NO | 4.665956 | ☑ | 0.1 | 8 | - |
| - | | 0 | ☐ | 0 | 0 | - |
| 8 | film.setD | 646.9404 | ☑ | 600 | 1000 | - |
| - | film.setDens | 0.0135 | ☐ | 0.010125 | 0.016875 | - |
| 9 | film.setSigma | 9.798634 | ☑ | 0.75 | 20 | - |
| 10 | film.setMagn | 3.356006 | ☑ | 3 | 5 | - |
| - | cp.setNFe | 2.857854 | ☐ | 2.25 | 3.75 | - |
| - | cp.setNO | 4.078868 | ☐ | 3 | 5 | - |
| - | | 0 | ☐ | 0 | 0 | - |
| 11 | Sub.setSigma | 15.21517 | ☑ | 0.75 | 20 | - |
| - | Sub.setDens | 0.02964298 | ☐ | 0.0196275 | 0.0327125 | - |

Figure 4.13: GenX model with substrate, film and surface fitted using logR1.

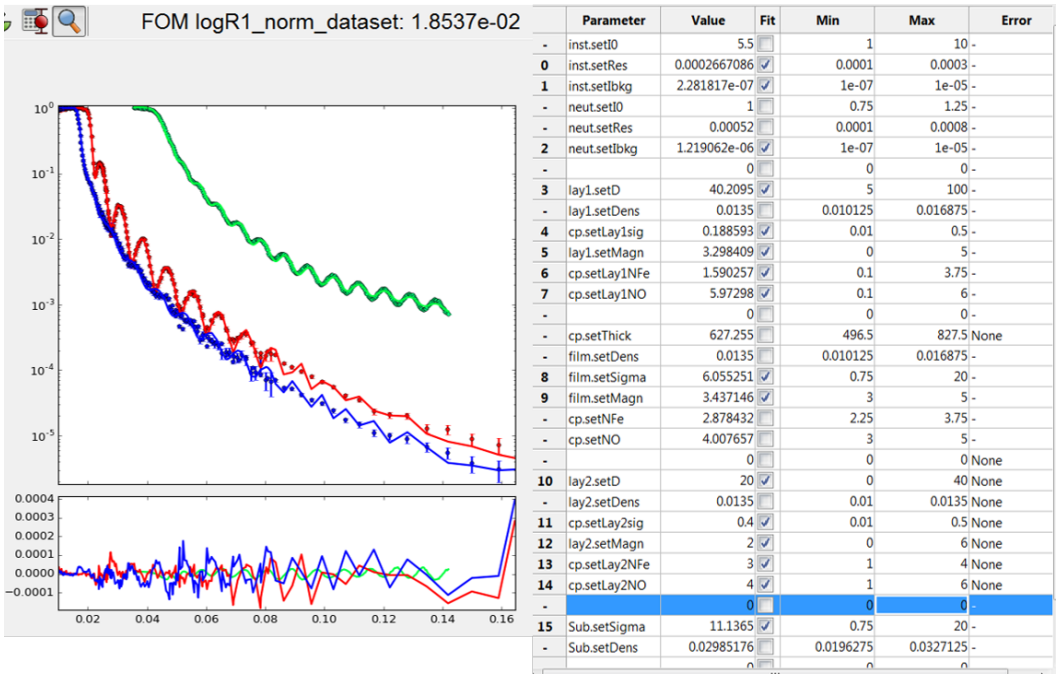


| | Parameter | Value | Fit | Min | Max | Error |
|---|---|---|---|---|---|---|
| - | inst.setI0 | 5.5 | ☐ | 1 | 10 | - |
| 0 | inst.setRes | 0.0002667086 | ☑ | 0.0001 | 0.0003 | - |
| 1 | inst.setIbkg | 2.281817e-07 | ☑ | 1e-07 | 1e-05 | - |
| - | neut.setI0 | 1 | ☐ | 0.75 | 1.25 | - |
| - | neut.setRes | 0.00052 | ☐ | 0.0001 | 0.0008 | - |
| 2 | neut.setIbkg | 1.219062e-06 | ☑ | 1e-07 | 1e-05 | - |
| - | | 0 | ☐ | 0 | 0 | - |
| 3 | lay1.setD | 40.2095 | ☑ | 5 | 100 | - |
| - | lay1.setDens | 0.0135 | ☐ | 0.010125 | 0.016875 | - |
| 4 | cp.setLay1sig | 0.188593 | ☑ | 0.01 | 0.5 | - |
| 5 | lay1.setMagn | 3.298409 | ☑ | 0 | 5 | - |
| 6 | cp.setLay1NFe | 1.590257 | ☑ | 0.1 | 3.75 | - |
| 7 | cp.setLay1NO | 5.97298 | ☑ | 0.1 | 6 | - |
| - | | 0 | ☐ | 0 | 0 | - |
| - | cp.setThick | 627.255 | ☐ | 496.5 | 827.5 | None |
| - | film.setDens | 0.0135 | ☐ | 0.010125 | 0.016875 | - |
| 8 | film.setSigma | 6.055251 | ☑ | 0.75 | 20 | - |
| 9 | film.setMagn | 3.437146 | ☑ | 3 | 5 | - |
| - | cp.setNFe | 2.878432 | ☐ | 2.25 | 3.75 | - |
| - | cp.setNO | 4.007657 | ☐ | 3 | 5 | - |
| - | | 0 | ☐ | 0 | 0 | None |
| 10 | lay2.setD | 20 | ☑ | 0 | 40 | None |
| - | lay2.setDens | 0.0135 | ☐ | 0.01 | 0.0135 | None |
| 11 | cp.setLay2sig | 0.4 | ☑ | 0.01 | 0.5 | None |
| 12 | lay2.setMagn | 2 | ☑ | 0 | 6 | None |
| 13 | cp.setLay2NFe | 3 | ☑ | 1 | 4 | None |
| 14 | cp.setLay2NO | 4 | ☑ | 1 | 6 | None |
| - | | 0 | ☐ | 0 | 0 | - |
| 15 | Sub.setSigma | 11.1365 | ☑ | 0.75 | 20 | - |
| - | Sub.setDens | 0.02985176 | ☐ | 0.0196275 | 0.0327125 | - |

Figure 4.14: Manually fitted GenX model with substrate, interface, film and surface.

A good fit to the data is observed with improved X-ray drop off, when manually adjusted. It is apparent in this fit (Figure 4.14, as previous fits), that the neutrons require a rougher interface or change in NSLD due to the definition of the fringes being too large at high Q. The composition of the interface is allowed to adjust and the program ran.

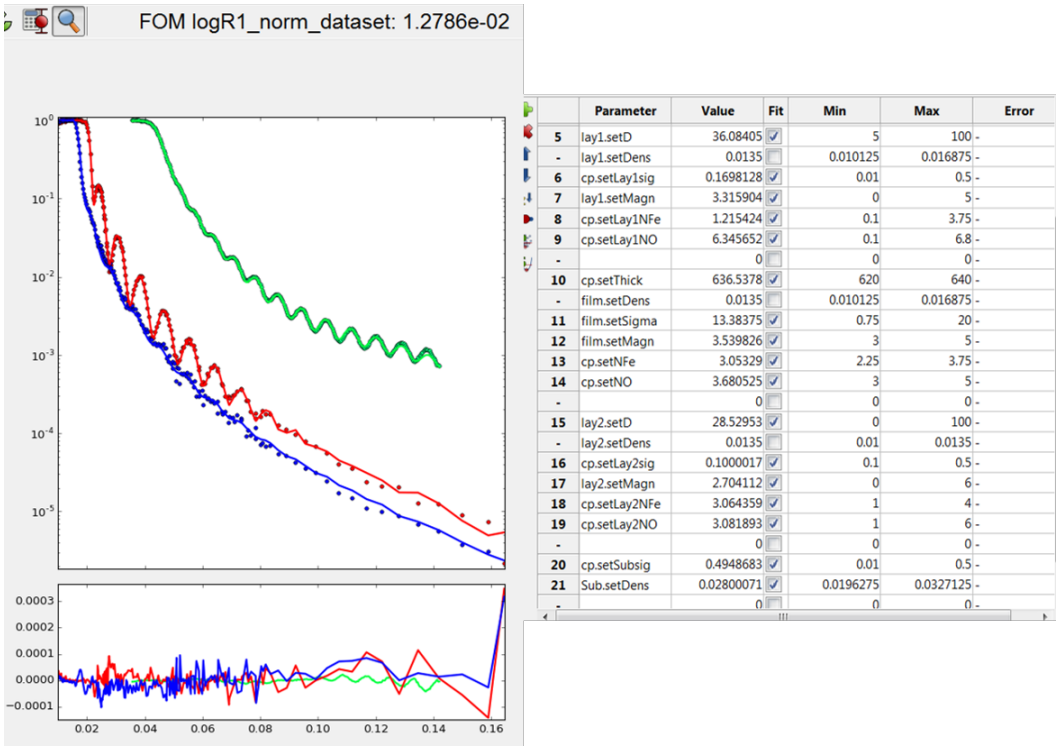


Figure 4.15: Final GenX model with substrate, interface, film and surface.

Figure 4.15 is a very good fit to the data, but parameters such as roughness of the substrate are limited and fit at a maximum value. There is also an unusual decrease in SLD in the XRR data at the interface (Figure 4.16). This could be explained by a depletion of atoms, or the lack of heavier scattering atoms being replaced by lower SL atoms, but without evidence from other complementary experiments, it can not be confirmed. One way to check the model is to add more layers and fit the data. It is possible that the addition of a layer could improve the fit, or enable the removal of the dip in SLD. It is often the case that the more parameters are added the appearances of errors in the SLD appear, and the model needs to be carefully limited. Check the fitting of the critical edge if substrate parameters were allowed to adjust. If the dens requires adjustment, fix it to the new value and reminimise the data. Another way to check the model is by transferring it into mag_refl

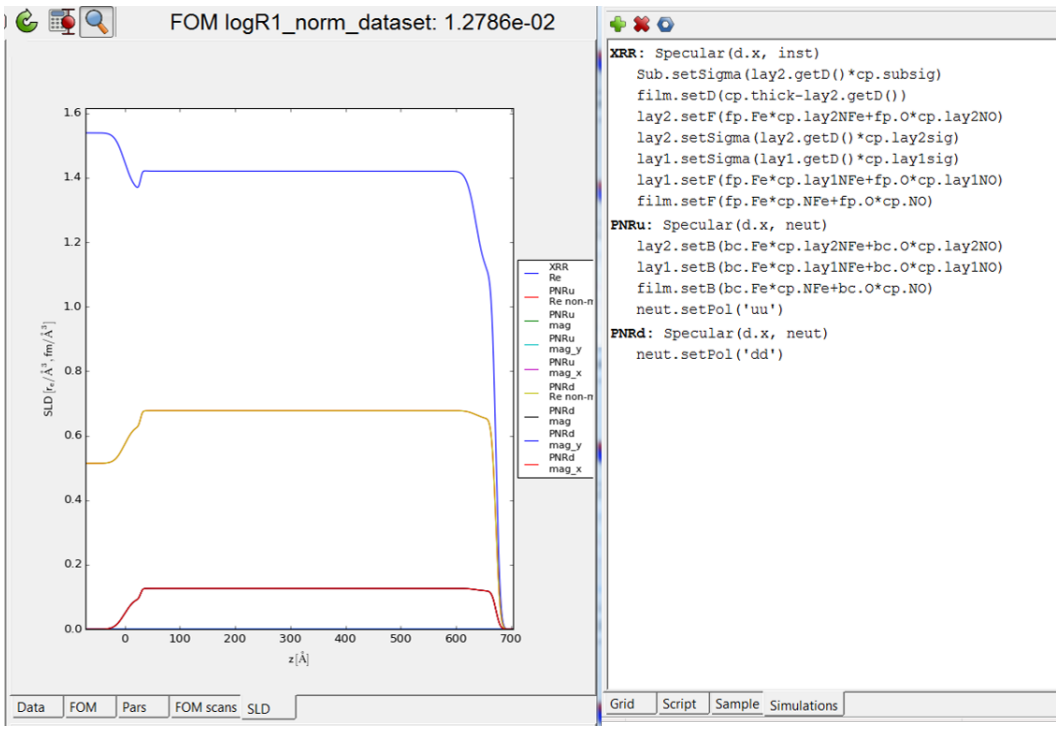


Figure 4.16: Corresponding SLD to Final GenX model with substrate, interface, film and surface.

where high roughnesses are allowed to vary the gradient of the layer transitions without causing errors due to incremental slicing. Slicing is also possible in spec_nx, but requires extra coding, and instructions are given in the GenX documentation [66]. When the fit is finalised, it is then possible to extract the parameters from the model and find errors using calculation examples in Chapter 3.3.4. As composition was varied in this model, the magnetic moment value can be scaled to the ratio of the totalnominalSL:totalfittedSL for direct comparison with theoretical values. The same adjustment can be applied if the dens was modified, instead by ratio of the dens.

# Chapter 5

# $Co_2FeAl_{0.5}Si_{0.5}$ grown on Si(111)

## 5.1 Introduction

Co-based Heusler alloys are an ideal candidate for many spintronic applications due to their theoretically predicted 100% spin-polarisation at the Fermi level (at 0 K) and high Curie temperatures >1000 K [7]. The full Heusler materials consist of $X_2YZ$ where $X$ and $Y$ are transition metals and $Z$ are main group elements. In this thesis, a quaternary Heusler thin film $Co_2FeAl_{0.5}Si_{0.5}$ (CFAS) is grown with the elements $X$ = Co, $Y$ = Fe and $Z$ = Al/Si. This material is chosen over CFA or CFS due to the DOS minority spin gap placement being equally distributed around the Fermi level, as opposed to shifted [5, 67]. The mid-gap Fermi level protects the spin-polarisation from thermal effects, where as CFA and CFS are more sensitive to this [68].

The lattice can be considered as four inter-penetrating face-centred cubic (FCC) structures (Figure 5.1) and a more detailed description is given by Fecher and Felser [7] along with the corresponding Wyckoff positions. The Figure shows the unit cell, which contains 8 f.u.. Different phases of the material exist related to the disorder of the elements in the structure. $L2_1$ is fully ordered, where $B2$ has an intermixing on both $Y$ and $Z$ sites. There exists an $A2$ phase where all lattice sites intermix, but this is not discussed in this thesis.

Theoretical DOS calculations of CFAS (Figure 5.2) predict that the material is half-metallic with a band gap in the minority spin states [5]. The Figure shows the DOS for both $L2_1$ (a) and $B2$ (b) phases where a small number of states are seen in the vicinity of the Fermi-level for (b), but maintains a very high SP. Shan et. al.

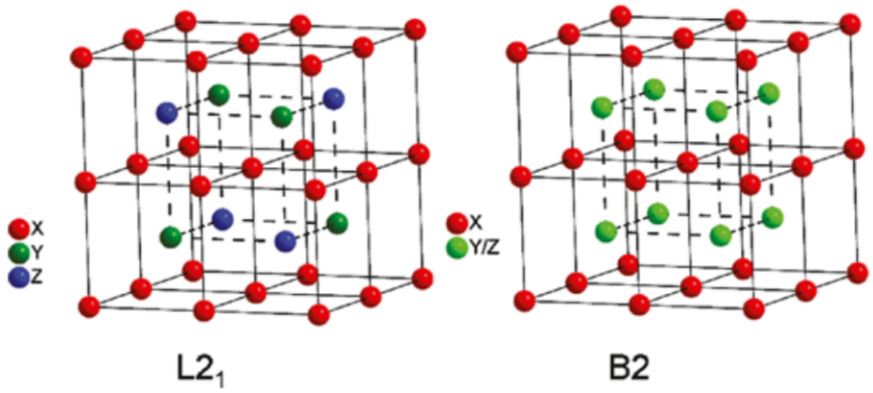


Figure 5.1: CFAS Heusler unit cell crystal structures in both $L2_1$ and $B2$ phases where the difference is disorder. $L2_1$ is fully ordered and $B$ has intermixing of Y and Z atoms. X = Co, Y = Fe and Z = Al/Si. Taken from [7].

[69] have demonstrated a SP of >90 % for CFAS $B2$ at 300 K when grown on MgO substrates as a MTJ, highlighting the potential for this material to be experimentally confirmed as HM. Other SP values for MTJs are 80 % at 4.2 K in the $L2_1$ phase [70] and 71 % at 7 K for partially $B2$ phase [71]. Measurements of SP of CFAS in thin film form have been reported by Tezuka et al as 70 % at 5 K for a $B2$ structure [72]. Bulk alloys have been experimentally shown by Nakatani et al to have 60 % at 4.2 K in an $L2_1$ phase with additional $B2$ and $A2$ disorder [68]. It is difficult to directly compare these values due the materials being part of a multilayered devices, thin films or bulk materials. There are also drastic differences between sample growth conditions, measurement techniques and reported experimental conditions.

Another indication of the half-metallicity is the total $\mu_B$/f.u.. The predicted total spin magnetic moment of a full Heusler material can be calculated by the Slater-Pauling rule

$$M_t = Z_t - 24 \tag{5.1}$$

where $M_t$ is the total magnetisation and $Z_t$ is the total number of valence electrons. For CFAS this gives a total magnetic moment of 5.5 $\mu_B$/f.u. [73]. It has been theoretically calculated that the less ordered phase, $B2$ does not reduce the magnetic moment [74]. A variety of experimental values of the magnetic moment, measured by VSM, have been reported as 6 $\mu_B$/f.u. for a multilayered device at 4.2 K in the $L2_1$ phase [70], 5.61 $\mu_B$/f.u. for a 200 nm thin film at 5 K with 81 % $L2_1$ phase [75], 4.8 $\mu_B$/f.u. for a 30 nm thin film at room temperature in the $L2_1$ phase [76] and 5.29 $\mu_B$/f.u. for bulk alloys at 10 K in an $L2_1$ phase with additional $B2$ and $A2$ disorder [68]. Again it is difficult to compare these results when the experimental

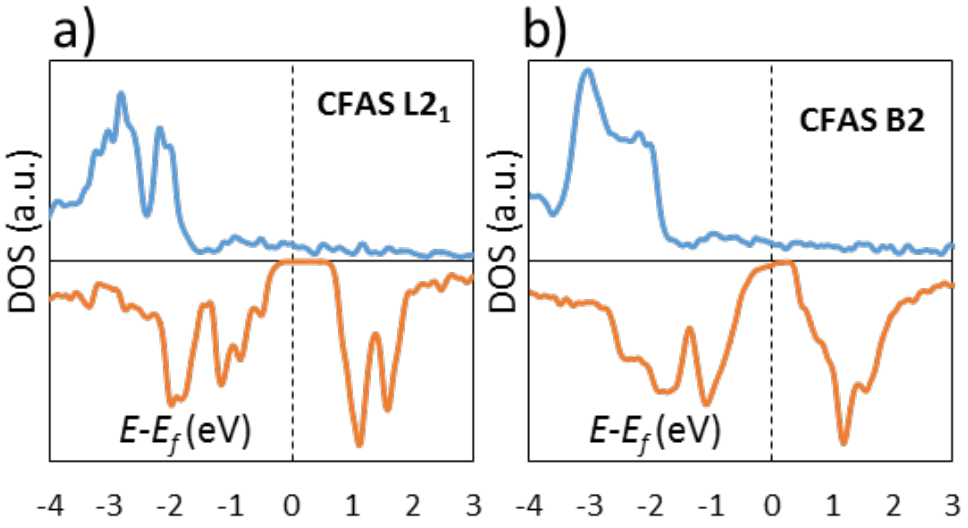


Figure 5.2: Spin polarised DOS for a) $L2_1$ and b) $B2$ ordered CFAS. The DOS spin up is in the top half of the diagram, while spin down is in the bottom [5].

details are not consistent. As VSM is an averaging technique, the quality of the film at the interfaces and surfaces plays a big role in the extracted magnetic moment value and would be considerably different for bulk materials.

For use as spintronic materials the CFAS crystal needs to be optimised in thin film form. As thin films are thinner than critical thicknesses [77], where after materials stabilise, they are known for defects and non-bulk like properties. Growth complications such as interfacial mixing between film and substrate, compositional variations, mixed phases and crystal deformations, change the properties of the material sometimes destroying or reversing SP. Careful choice of substrate is also crucial as the first few layers of thin film can underpin the entire growth quality. Poor choice of substrate can cause strain due to lattice mismatch, where the crystal has to compensate, or unwanted interfacial regions caused by elemental diffusion.

Si is chosen as a substrate due to its broad uses in current electronic device technologies, with spin-diffusion lengths of ∼350 µm into the material [19]. If successfully grown as a confirmed HM with polarisation maintained up to the substrate and a limited or no interfacial layer, it would work as a spin-injector into Si-based devices. The challenge with the growth is due to the lattice mismatch of ∼4 %.

The individual elemental SL of the materials used in this chapter can be seen in Figure 5.3 in order to highlight how simultaneous fitting of XRR and PNR gives varied sensitivity to the same atomic compositions. A small change in Fe would

have a large effect on the neutron SL, but could be mistaken for Co in the X-rays. A comparison of material properties is given in Table 5.1 where large differences in total SL is observed for the different probes used.

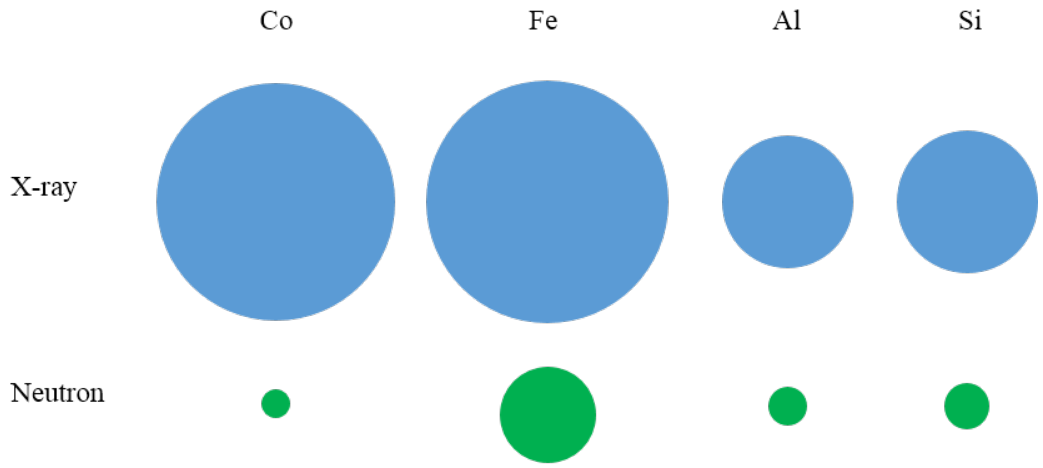


Figure 5.3: Visual representation of the difference in SL of X-rays and neutrons from elements in the chapter: Co, Fe Al and Si.

Table 5.1: Nominal properties and parameters of materials used in the chapter for comparative purposes. Both X-ray and neutron SL are shown along with $N$, the number density of the material.

| Parameter | Value |
|---|---|
| Lattice constant - Si (Å) | 5.43 |
| Lattice constant - CFAS (Å) | 5.68 |
| Mismatch (%) | 4.6 |
| XSL - Si (e-/atom) | 14.25 - 0.33j |
| NSL - Si (fm/atom) | 4.15 |
| XSL - CFAS (e-/atom) | 87.12 - 10.73j |
| NSL - CFAS (fm/atom) | 18.23 |
| $N$ - Si Å$^{-3}$ | 0.0499 |
| $N$ - CFAS Å$^{-3}$ | 0.0218 |

The experiments in this chapter characterise the structure and composition of the CFAS thin film grown on Si(111). Results are combined in order to assist the building of a model to fit PNR data, obtaining structural and magnetic depth profiles. Modelling of the quaternary Heusler alloys is complicated and leads to non-unique solutions due to many parameter couplings. Validity and choice of final model is discussed.

## 5.2 Complementary Techniques

A range of experimental techniques are shown below in order to characterise the samples, both structurally and magnetically. Quality growth is important to create thin films optimised for devices and to ensure properties are reproducible.

### 5.2.1 Growth

The sample was prepared by co-deposition of Co, Fe, Si, Al using low-temperature molecular beam epitaxy [78, 79]. A 25 nm-thick CFAS film was deposited on a pre-cleaned $10 \times 10\,\mathrm{mm}^2$ Si(111) substrate at room temperature. Prior to loading Si(111) substrates into the chamber, their surfaces were chemically cleaned with an aqueous 1% HF solution to remove native oxide and contamination. In-situ energy-dispersive X-ray spectroscopy (EDS), similar to EELS, confirmed that the CFAS films were stoichiometric.

### 5.2.2 Microscopy

The scanning transmission electron microscopy (STEM), high angle annular dark field (HAADF) and EELS images presented below (Figures 5.4, 5.5, 5.6), show atomic resolution images of the $Co_2FeAl_{0.5}Si_{0.5}$ thin film. Experimental configurations are described in Kuerbanjiang et al. [80].

These techniques are useful in order to determine the surface and interface morphologies and chemical intermixing in the films. These characteristics are important as they modify properties which are particularly relevant for technological advancement in spintronic devices.

#### Scanning Transmission Electron Microscopy

Film thickness uniformity is confirmed by low magnification STEM (Figure 5.4) and demonstrates a sample of the proposed thickness. There are no visible steps of varied composition or density at either the surface or interface. Any waves or terraces seen on a larger scale would have to be accounted for in the reflectivity modelling.

Looking more closely at the sample interface (Figure 5.5), intermixing of the substrate and film is observed on the order of 8 nm causing crystal deformations. This demonstrates the requirement of at least one interfacial layer in the reflectivity model due to need for variation in the composition and density towards the substrate. If this region were smaller, it could be modelled as roughness.

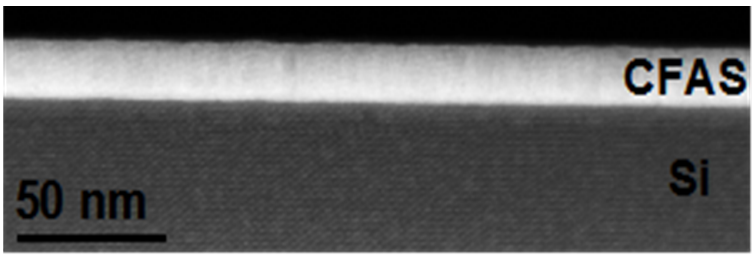


Figure 5.4: Low magnification HAADF STEM confirming the sample thickness and uniformity of the thin film.

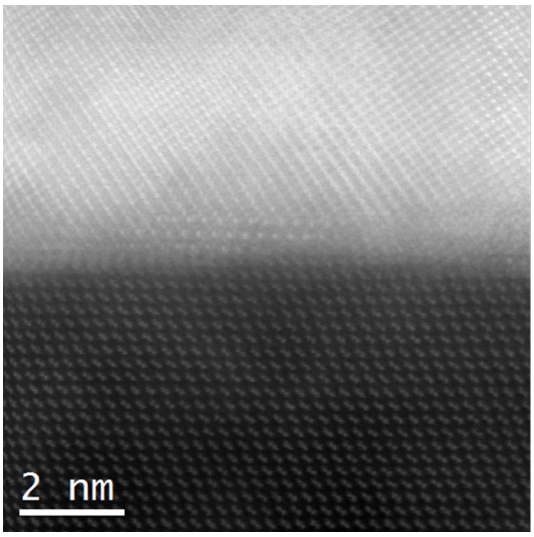


Figure 5.5: STEM from a section of CFAS/Si interface 2 nm.

### High Angle Annular Dark Field Imaging

The phase of the Heusler alloy is important as chemical intermixing can change the magnetic and electronic properties of the material, even when the crystal structure remains the same. Figure 5.6 compares the CFAS HAADF image alongside two QSTEM simulated models [81]. The $[1\bar{1}0]$ crystallographic orientation is chosen in order to observe the high-low Z contrast between the two columns, Co and Fe/Al/Si. This is possible because in the $[1\bar{1}0]$ projection, each visible atom (in the $L2_1$ phase) represents either individual $X$, $Y$ or $Z$ elements. The two theorized models represent the the $L2_1$ and the $B2$ phase of the Heusler alloy. Due to the intensity difference of the line profile pattern observed, the experimental data more closely matches that of the $B2$ phase, showing an intermixing of Fe, Al and Si atoms on the non-Co situated lattice sites. Figure 5.7 shows SAD recorded from a region containing both substrate and thin film confirming the CFAS to be a single crystal due to clear

spots and the orientation of the film with respects to the substrate. Simulating diffraction patterns confirms that the epitaxial relationship is Si(111)‖CFAS(111) and Si(1$\bar{1}$0)‖CFAS($\bar{1}$10) [80]. As the $B2$ phase is expected to retain half-metallicity for the bulk of the material [74], 5.5 $\mu_B$/f.u. is expected to be extracted from the PNR data.

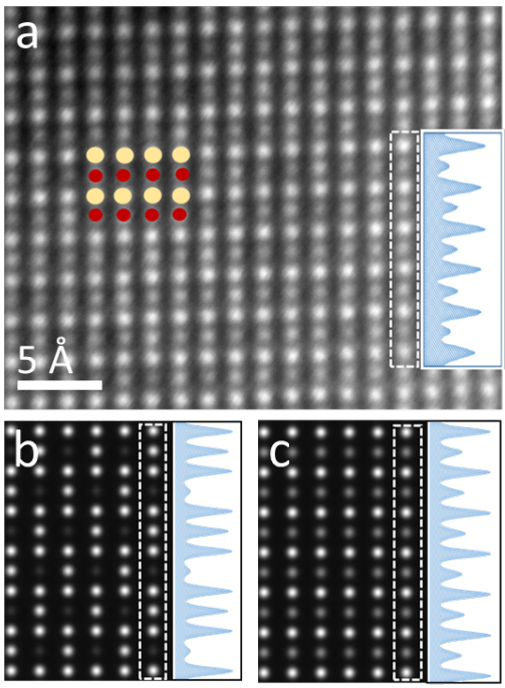


Figure 5.6: HAADF STEM images of the CFAS sample looking along the [1-10] crystallographic direction. (a) is the experimental HAADF image and (b)(c) are theoretical examples of what would be seen if the $L_{21}$ or $B2$ Heusler phase was observed, respectively. Yellow and smaller red circles represents a Co and intermixed Fe/Si/Al site respectively [80].

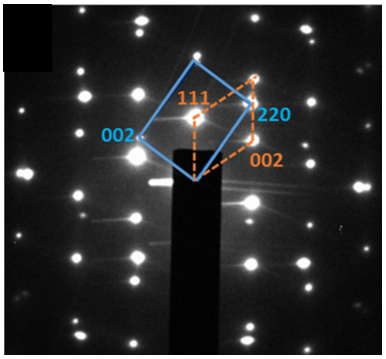


Figure 5.7: SAD taken along the $[1\bar{1}0]$ zone axis from an area covering both the film and substrate. The unit cell of the diffraction pattern is depicted with a blue solid line for the film and orange dashed rectangle for the Si substrate. Simulations confirm Si(111)‖CFAS(111) and Si$(1\bar{1}0)$‖CFAS$(\bar{1}10)$ twinning [80].

### Electron Energy Loss Spectroscopy

While HAADF can give structural information, EELS can simultaneously be implemented to give a compositional profile over the same region (Figure 5.2.2) by tuning the electron energy to that of Co $L_{2,3}$, Fe $L_{2,3}$, Al $K$ and Si $K$ to give sensitivity to the specific elements. A large interface region of ∼120 Å is observed with a continuously changing compositional profile. This is larger than the data previously shown (Figure 5.5), but specific compositional variation is more difficult to observe in transmission electron microscopy (TEM) images.

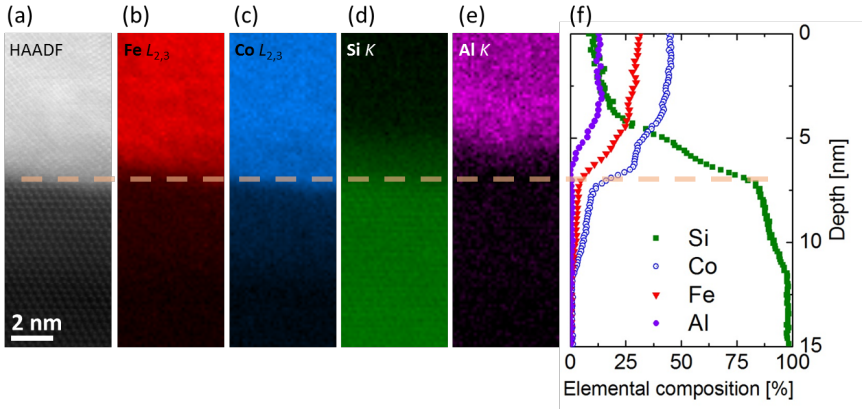


Figure 5.8: Interfacial STEM EELS where (a) is a HAADF produced simultaneously with the EELS acquisition. (b)(c)(d)(e) are spatially resolved EELS at edges as labelled in image. (f) is an intensity profile of the different atomic species over the same interface region. The dotted line is to guide the eye at a possible substrate position [80].

### Density Functional Theory

Possible values for the SP and magnetism at the interface of CFAS and Si can be theoretically calculated by density functional theory (DFT) using the CASTEP software [80]. The results are shown in Table 5.2 where the CFS conventional f.u. is chosen for reference due to the lack of Al at the interface as seen by the EELS data (Figure 5.8). $C_{Co} = 100\%$ would be equal to 2 atoms per f.u. and $C_{Fe} = 100\%$ would be equal to 1 atom per f.u.. Any missing atoms from a total of 4 atoms per f.u. are Si. It is clear from the Table that variations in composition within the f.u. have a large effect on both the magnetisation and SP of the thin film. At the interface over a small region, this effect could be negligible. Over the lengths suggested by TEM and EELS, this is a drastic change that could damage the possibility of this material-substrate combination being used in spintronic devices.

Table 5.2: Influence of structural disorder on the magnetic moment and spin-polarization at the Fermi level. The CFS conventional f.u. is chosen for reference with 4 atoms per cubic unit cell. CFe and CCo, refer to the relative (compared to the number of atoms in the CFS unit cell) number of atoms per formula unit [80].

| Label | $C_{Fe}$ (%) | $C_{Co}$ (%) | Magnetic moment ($\mu_B$/f.u.) | SP (%) |
|---|---|---|---|---|
| CFS | 100.0 | 100.0 | 6.0 | 100 |
| c1 | 75.0 | 100.0 | 5.0 | 100 |
| c2 | 50.0 | 100.0 | 4.0 | 89 |
| c3 | 25.0 | 100.0 | 2.9 | 41 |
| c4 | 0.0 | 100.0 | 1.8 | -22 |
| c5 | 0.0 | 87.5 | 1.2 | 4 |
| c6 | 0.0 | 75.0 | 0.7 | -17 |
| c7 | 0.0 | 62.5 | 0.4 | -75 |
| c8 | 0.0 | 50.0 | 0.0 | 0 |

## 5.2.3 X-ray Diffraction

XRD measurements probe larger length scales of sample due to larger beam sizes (mm vs nm from microscopy). Larger length scales are beneficial as they are more representative of the parameters used to fit PNR data due to the lateral layer averaging sensitivity. Parameters found using techniques such as XRD are therefore more heavily relied on. Experimental set up alignment details are described in Figure 2.1.

The different Heusler phases have different structure factors due to disorder, as demonstrated by Felser and Fecher [7], where only certain reflection peaks are observed. For $L2_1$ both CFAS(111) and (200) family of reflections can be observed in XRD measurements. In contrast, only the CFAS(200) family are available in the

$B2$ phase. For the $A2$ phase where atoms are completely disordered across lattice sites, neither family of reflections are observed. Further information on structure factor calculation can be found in References [27, 28]. Observable reflections are important to understand in order to indicate Heusler phase, but also to check film orientation and measure lattice constants.

The HAADF experiments demonstrate the film exhibits the $B2$ disordered phase, and due to structure factor rules, means that the (hhh) peaks are absent. Only the even reflections from the (100) family of peaks for the CFAS should be visible [7]. The odd Si(111) family of reflections are expected along with the (400) peak. Si(200) and (222) are basis-forbidden reflections.

A $\theta - 2\theta$ scan aligned to the Si(111) (Figure 5.9) reveals no CFAS(111) peaks out of plane. The Si(222) reflection is observed here and is a can be a common occurrence due to multiple diffraction [82]. Setting diffraction conditions to that of CFAS(111) and running a $\chi - \phi$ mesh ($\Delta\chi$ =30°; $\Delta\phi$ =360°), reveals no intensity. If the peak were off in alignment, it would be revealed in such a scan. In order to confirm $B2$ disorder and measure a lattice constant, we scan for the CFAS(200).

It is possible to reach CFAS(200) by firstly aligning to Si(111) reflection to establish a reference position, moving to the correct $2\theta$ position of the CFAS peak, rotating the $\chi$ angle by 54.74° and scanning $\phi$ over 360°. Aligning to the peak and completing a broad $\omega - 2\theta$ scan will then show both (200) and (400) peaks (Figure 5.10). No Si(400) peak is seen here due to the twinning of the CFAS with respects to the substrate, which causes an offset in $\phi$. Hence, when moving to the diffraction conditions for Si(400) and rotating $\phi$ about 360°, the substrate peak can be found.

Fitting the centre position of the CFAS reflections (Figure 5.10) gives an averaged lattice constant of 5.68(1) Å [80], which agrees with the predicted value of the thin film as stated by Nakatani et al [68]. The number density, $N$, of the cubic CFAS film can be calculated as 183.25 Å$^3$.

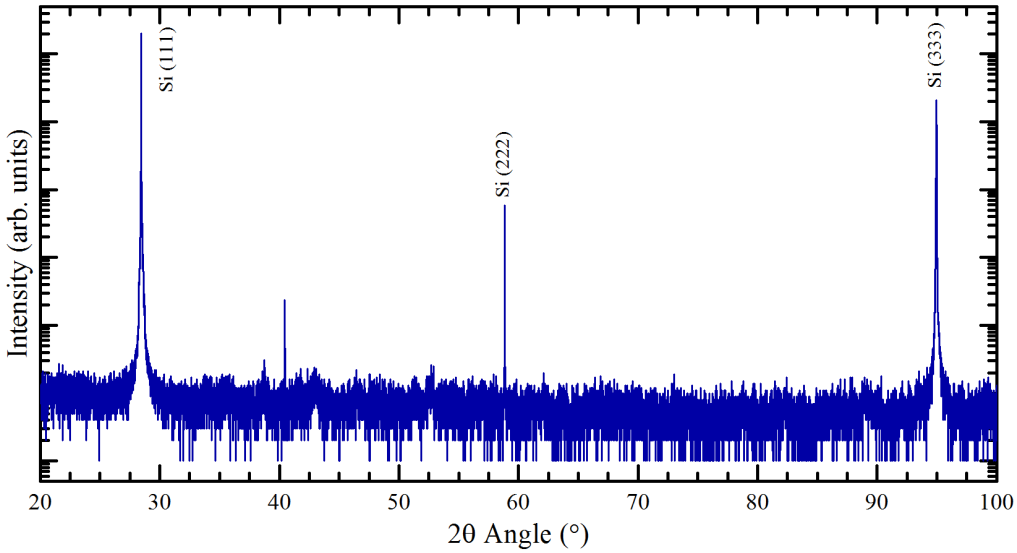


Figure 5.9: CFAS/Si(111) $\theta - 2\theta$ scan aligned to the Si(111) substrate peak.

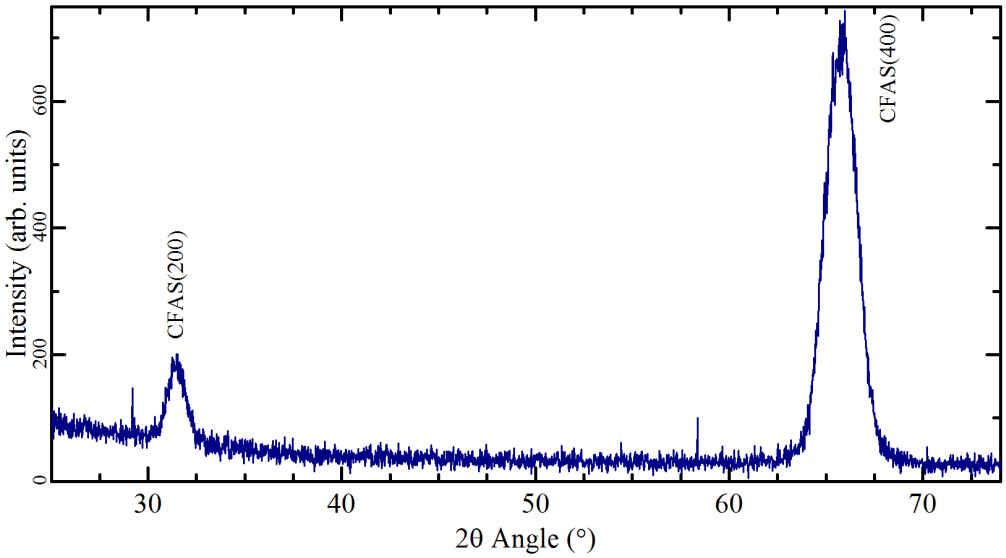


Figure 5.10: $\omega - 2\theta$ scan aligned to the CFAS(200) film peak where $\chi = 54.7°$. Data taken on Rigaku SmartLab, University of York.

### 5.2.4 X-ray Reflectivity

XRR is performed in order to observe the reflection from layers using the same physics as PNR, described in Chapter 3. The same experiment, using a different probe enables simultaneous fitting with the PNR data. Both on and off axis (specular and off-specular) scans (Figure 5.11) are measured in order to subtract

background and any diffuse scattering. The off-axis scan is performed at $\Delta\omega = -0.1°$. The off-axis reflectivity measurement is 4 orders of magnitude lower than the specular scan, showing very little background, and fringes are not seen, demonstrating that there is no correlated roughness. The fringe separation suggests a film thickness of 210 Å in agreement with the TEM. This value is used to give an estimate of the VSM magnetic moment. A full fit of the data is shown in Figure 5.14 where simultaneous fitting is preferred in conjunction with PNR.

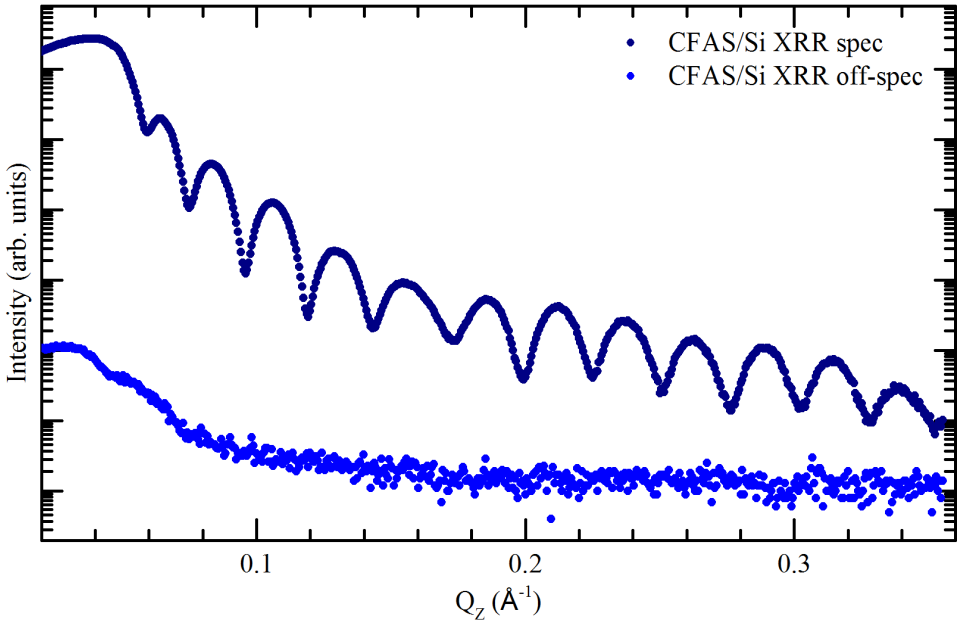


Figure 5.11: XRR of CFAS/Si(111) sample. Both specular and off-specular data ($\Delta\omega = -0.1°$) is shown.

### 5.2.5 Magnetometry

To investigate the magnetic properties of this CFAS thin film, we firstly check the thin film average moment using VSM (Figure 5.12). We expect to obtain a magnetic moment that agrees with the theoretical value 5.5 $\mu_B$/f.u., which is the ideal value at absolute zero temperature for CFAS according to the Slater-Pauling rule [67]. Due to a large intermixed interface (shown in EELS Figure 5.2.2), we assume the bulk like magnetism does not continue through this region causing a drop in magnetic moment towards the substrate, therefore lowering the average value.

Taking the VSM data calibrated to a value of $5.73 \times 10^{-4}$ emu (using a well known Pd sample), the measured density of 5.68 Å and a uniform film thickness

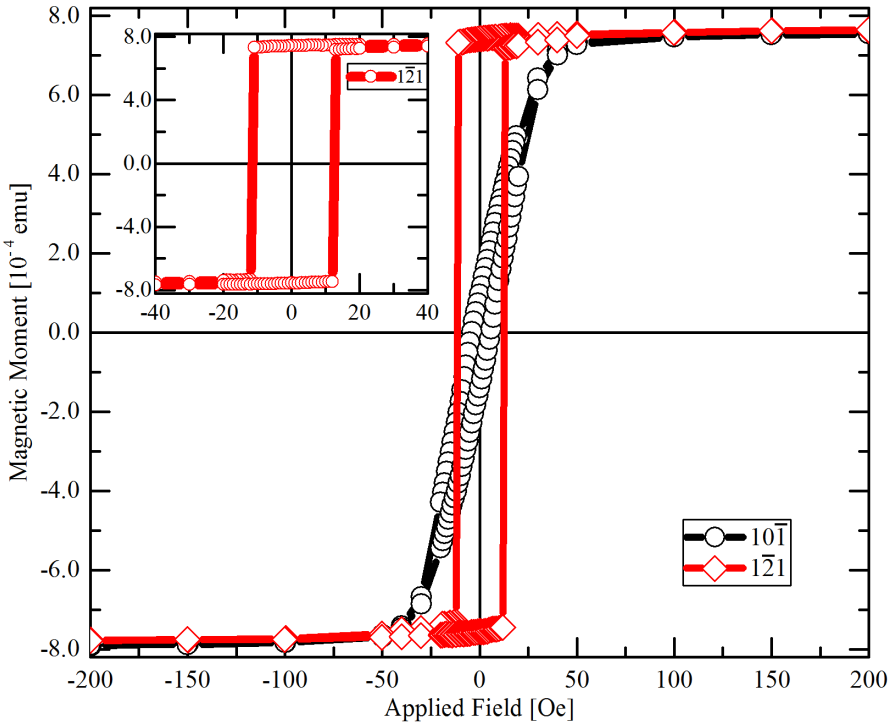


Figure 5.12: Magnetometry data for CFAS film on Si(111) aligned along the easy axis ($1\bar{2}1$) in red, and along the hard axis ($10\bar{1}$) in black. $M_S = 7.53 \times 10^{-4}$ emu. The inset shows data along the ($1\bar{2}1$) direction, focussed to show the square hysteresis loop and low coercivity $H_C = 14.0$ Oe. [83]

of 210 Å (taken from fitting of XRR data) a magnetic moment of 5.2(4) $\mu_B$/f u is obtained, in agreement with theory but on the lower side of the error. This could be due to a lower than theorised bulk-film magnetic moment, an over estimate of the thickness of the main film or additional non magnetic or lower moment layers. To gain a more accurate magnetic moment and magnetic profile of the sample, we look to PNR.

### 5.2.6 Polarised Neutron Reflectivity

Both PNR and XRR reflectivity data is shown in Figure 5.13, normalised to unity. The PNR experiment was performed in a 1T external magnetic field, applied perpendicular to the sample normal during the measurement to ensure full saturation and removing the possibility of spin-flip scattering due to misalignment from the easy axis. Noticeable differences are observed in both $Q$ range and error bars when comparing the sample data due to flux of the probes used. If the sample size,

$10 \times 10\,\mathrm{mm}^2$, were larger, the intensity of the neutron data would be greater, and more orders of magnitude and higher ranges of $Q$ would be possible.

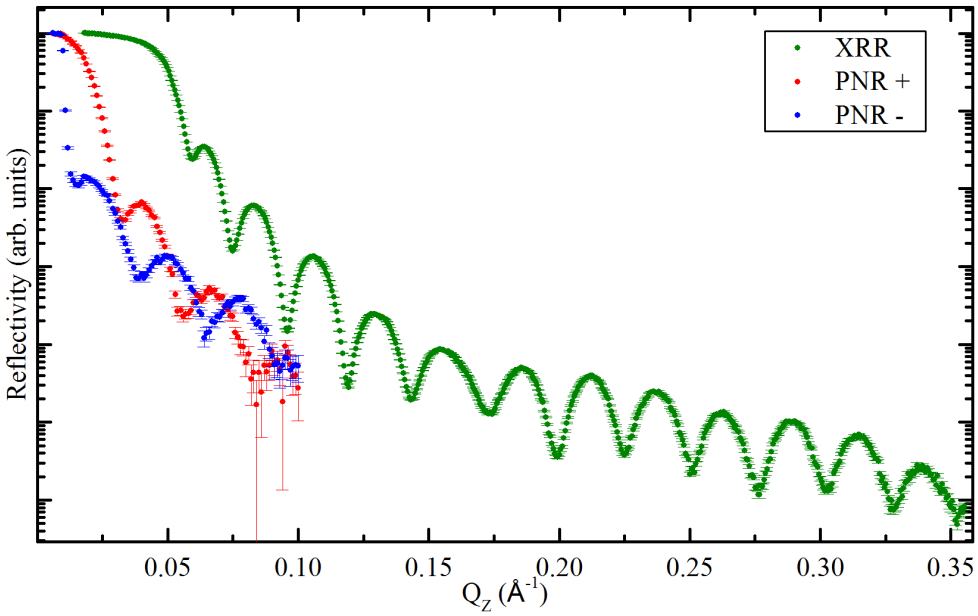


Figure 5.13: PNR and XRR data for the CFAS film grown on Si(111). Error bars are in the Y-axis.

## 5.3 Reflectivity Data Fitting

This chapter does not go into details about the initial modelling procedure of a single film on a substrate as shown later in Chapter 6. It does however show how different models can fit the reflectivity data equally well even though the SLDs are quite different. In combination with the complementary experimental data, the final choice of model is validated.

Initially it is important to fix as many parameters as possible using the information extracted from earlier characterisation experiments in order to limit the fits to realistic models. In this case of models in this chapter, the composition of the film remains fixed (details given per model description), and the Si substrate is fixed to all bulk Si values. As the molecular weight of the CFAS is unknown, we represent the density of this CFAS cubic material using (lattice constant)$^3$. Models are built up layer by layer, simultaneously fitting XRR and PNR data. They are adjusted accordingly and refitted for every change in model until a low FOM value is achieved with realistic values for all parameters.

For this CFAS dataset we obtain three models, where the fits to the data can be seen in Figure 5.14 to highlight the equivalent fit quality. The evolution of the fitting comes from questioning the legitimacy of the first model and creating another using more specific information obtained from other techniques. A description of each model will be made followed by a comparison to other models. It is important to note that due to the complicated nature of this quaternary full-Heusler alloy, fitting becomes extremely challenging due to strong correlations between many parameters. Standard methods of fitting have proven ineffective which highlights many discrepancies in the way reflectivity fitting is traditionally completed. SLDs corresponding to the very similar fits are show in Figure 5.15, where clear differences can be seen.

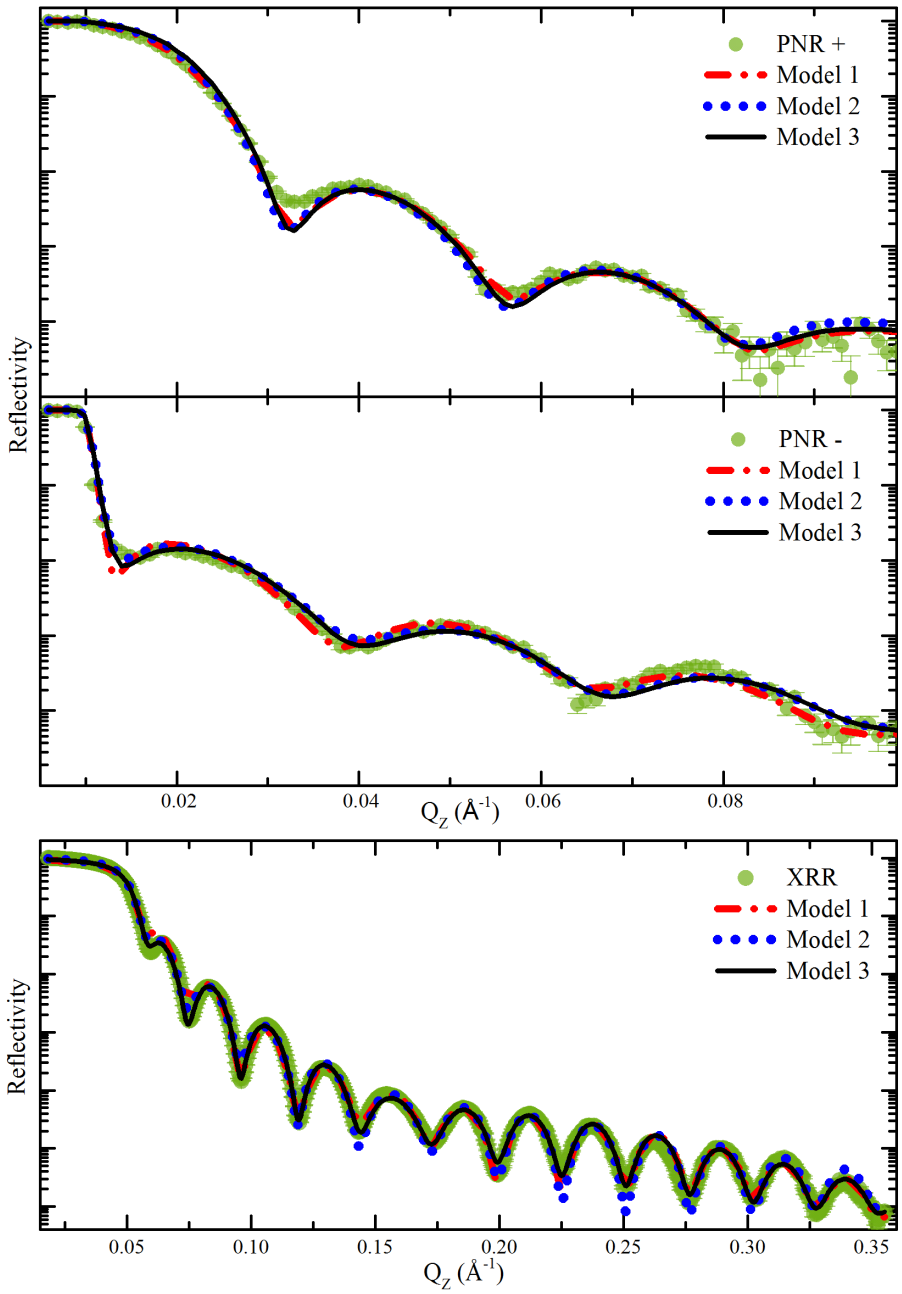


Figure 5.14: PNR and XRR data with the corresponding Kiessig fringes from three SLD models overlayed. Data: Large green circles, Model 1: red dashed dotted line, Model 2: blue dotted line and Model 3: solid black line.

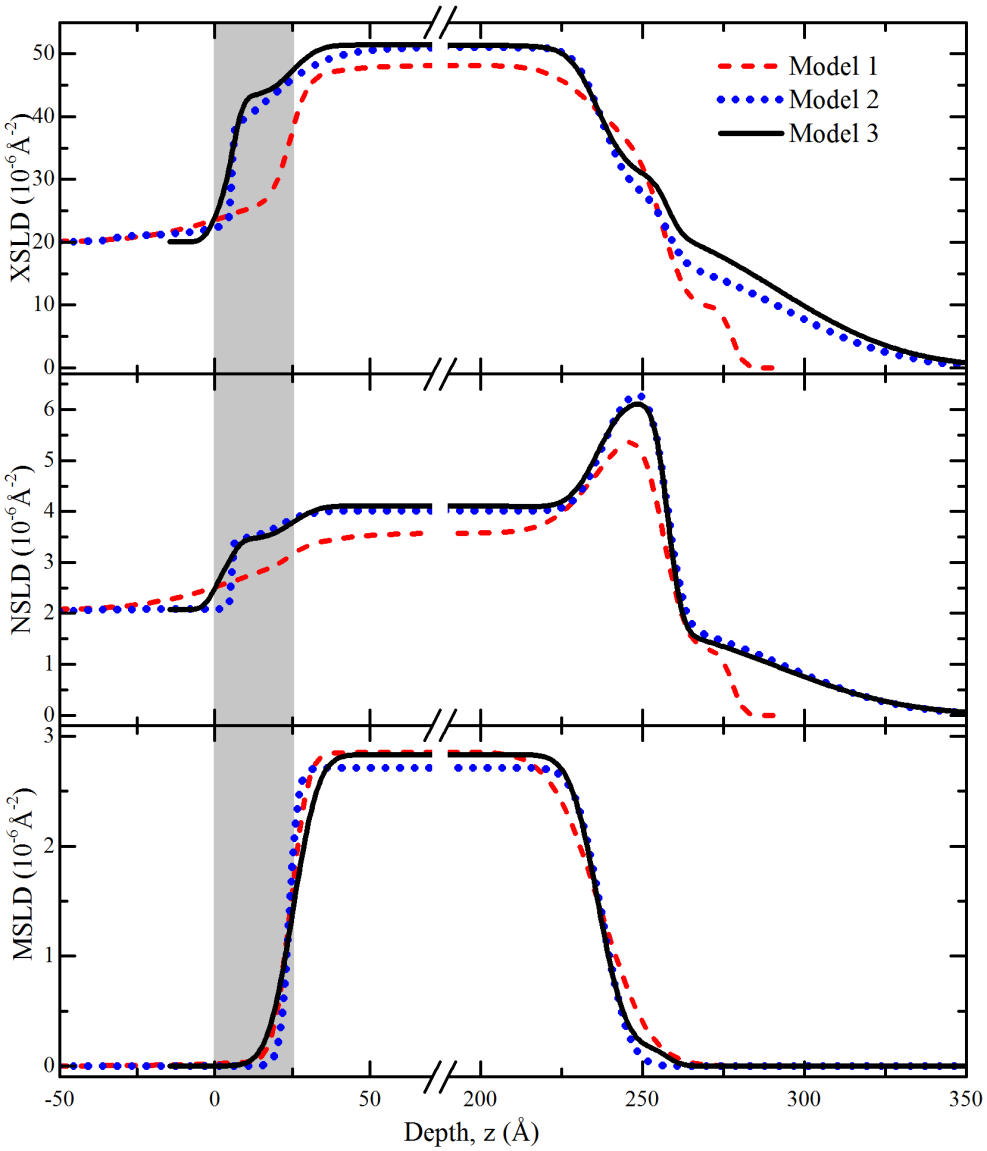


Figure 5.15: SLD profiles for Model 1, Model 2 and Model 3 overlayed. Depth (x-axis) for all models aligned by taking the centre point of the MSLD. Grey box highlights the interface region as defined by the centre of the magnetic profile gradient and where it reaches 0 [83].

### 5.3.1 Model 1 with Nominal Composition

Model 1 was created using the standard slab model stated in Section 3.3.4 which contains layered materials simulating multiple reflections which creates the SLD. Fitted using mainly FOM: log R1, the model is minimised keeping the composition of the film nominal ($Co_2FeAl_{0.5}Si_{0.5}$) with the addition of two surface layers and an interface layer. In Figure 5.15 attention is drawn to the rough interface which lacks definition, and the observed decrease in SLD between z = 50 Å and z = 250 Å due to an increase in fitted density, which in Model 1 represents modifications of composition and number density, $N$. The large change in $N$ is a suggestion that the model, while being a good fit, isn't an accurate representation of the sample structure. Due to the low $Q$ range in the neutron data, there is also difficult obtaining resolution further towards the substrate at high $Q$, so the fit will not be weighted towards this region. Creating a new model is therefore an appropriate way to test Model 1. Both a better defined interface and a better guess of film composition, may change the fitted properties of the main film and surface.

### 5.3.2 Model 2 with EELS compositional interface profile

Compositional EELS data reported previously in section 5.2.2 and published in [80] was used for Model 2. EELS (shown again at the bottom of Figure 5.16) is taken and converted into a format which could be programmed into GenX in order to directly replicate the interfacial SL. The point by point percentage composition in the data for a specific depth (z), is taken and multiplied by the elemental SL of the corresponding probe. Adding calculated SL and dividing by 100 gives the SL at each z position (as plotted in Figure 5.16). It is assumed, with respects to the EELS data, that z = 0 Å and z = 170 Å is the substrate and film position respectively.

For simple coding of the SL profile into GenX, the data plotted is fitted using a double Boltzmann function (Equation 5.2, where the fits are shown by solid lines in Figure 5.16). The double Boltzmann equation and fitted parameters are transferred into the GenX code. Non-fixed profiles for both density and magnetism are represented by a single Boltzmann function (Equation 5.3). A double Boltzmann function was robustly later tested, but did not improve the fit.

Double Boltzmann function [84]:

$$y = y_0 + A[(p/1 + e^{z-z_1/k_1}) + (1-p)/(1 + e^{z-z_2/k_2})] \tag{5.2}$$

where all parameters are fitted to the EELS data except for z which is dependent on the position with respects to the depth axis, z, of the model.

Single Boltzmann function [84]:

$$y = [(A_1 - A_2)/(1 + e^{x - x_0/dx})] + A_2 \tag{5.3}$$

where $A_2, x_0$ and $dx$ are parameters within the model allowed to adjust position (with respects to depth axis, z, and magnitude of the functions).

The SL of the main film is assumed by the average SL of the final 10 Å of the interface EELS data (as shown in Figure 5.16 by the grey shaded region) and corresponds to a composition similar to Co 46%, Fe 30%, Al 14%, Si 10% with an error of 5%, but exact values are used in the modelling. To complete the film, the density and magnetism in the model is allowed to freely fit. To complete the SLD, the two surface layers likened to Model 1, are replicated and allowed to freely adjust. Using FOM:logR1 leads to the minimised SLD solution shown in Figure 5.15. It profiles a more defined interface region, visible by steps in the profile with higher SLD for the main film and a rougher surface, bringing $N$ closer to the theoretical value. Although a good fit to the data is found, the FOM for this model is higher than that of Model 1 and could be a result of the limiting nature of the modelling. As this second model created doubt in the SLD profiles rather than confirm them, a third model is created.

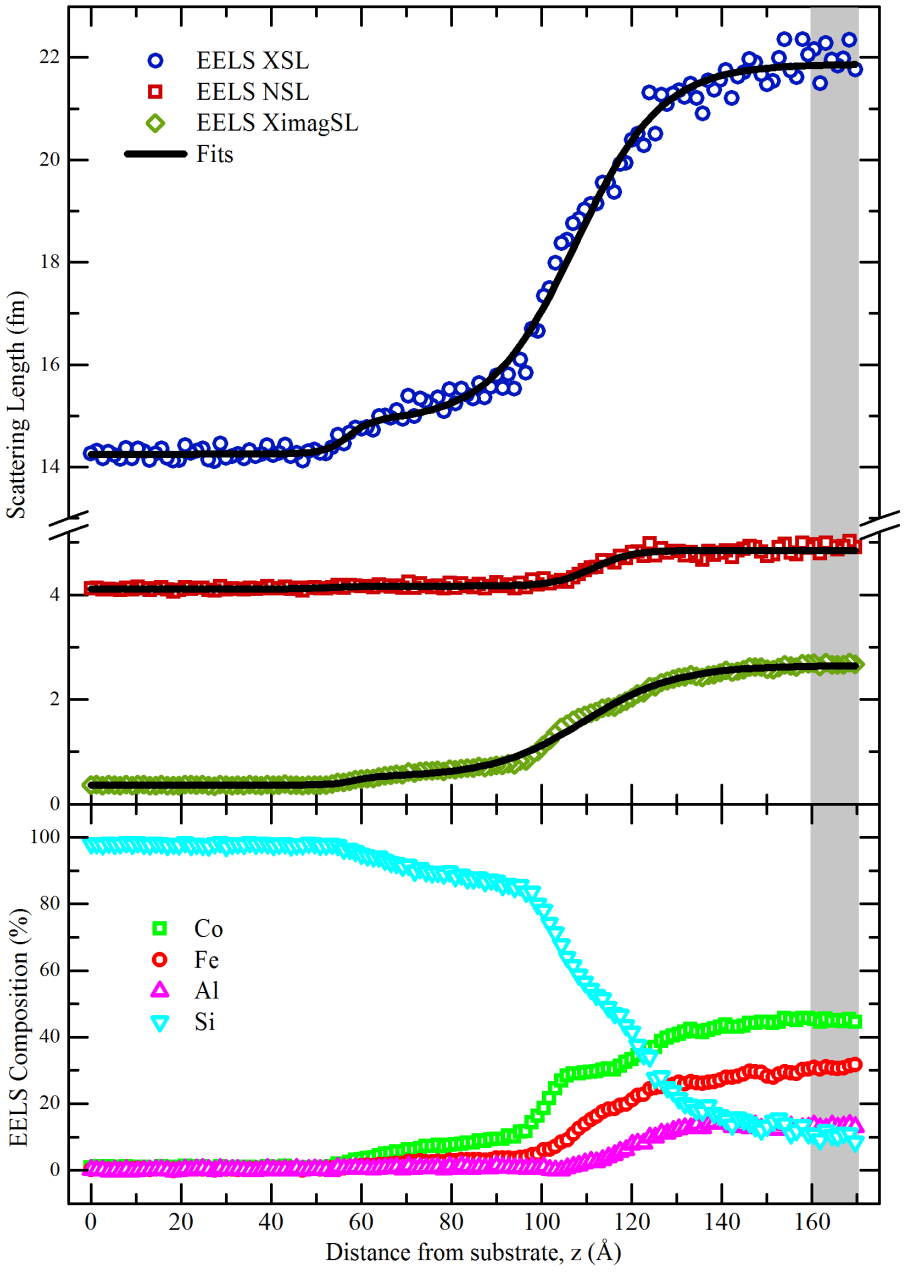


Figure 5.16: Neutron and X-ray scattering lengths across interface region, converted to EELS data (shown in the lower panel) and fitted using double Boltzmann functions (black line). Fitted SL profiles are used to create interface region in Model 2 (seen in Figure 5.14). [83]

### 5.3.3 Model 3 with EELS film composition

Model 3 is created as a "hybrid" style model. Where the standard slab model is taken, but is also strongly based on Model 2 in order to make it more freely fitting. The parameters and layers from Model 2 are taken and put into a new model with the exception of the interface region, which is modelled by two layers, closely mimicking the double Boltzmann interface profile in Model 2. The parameters for these two layers are fitted while keeping the film and surface fixed in order to recreate the interface of Model 2, which is successful. Next all parameters, except film composition and substrate values, are freed. The resulting model is Model 3 (Figure 5.15), which produces a FOM lower than that of the previous two models.

### 5.3.4 $Co_2FeAl_{0.5}Si_{0.5}$ Model comparison

All models are plotted together for comparison: the reflectivity fits in Figure 5.14, corresponding SLDs in Figure 5.15 and a summary of specified parameters in Table 5.3. It is important to note that due to the differences in model setup, it was necessary to find a way to calibrate the z position of all models. Normally defined as the location of the substrate position, here this is z not '0' due to the differences in roughness (Gaussian width) and the modelling of Model 2. As the magnetic thickness is the parameter with the least coupling due to it being based on the splitting and offset of the neutron spins, the centre point of all models was aligned for the MSLD by differentiating and fitting the peak. Layer thicknesses can be defined by differentiating the SLD and fitting the centre point of the peak or taking values directly from GenX. The FWHM of these peaks is large due to the error function either side representing the roughness of the layer. If there was no roughness these peaks would be infinitely thin. Adding together the FWHM then gives the thickness of the total roughness, as a change in the SLD represents a deviation from the main film (values shown in Table 5.3 as "Thickness + Sigma").

As hybrid Model 3 was created in order to improve the fitting of Model 2, it is logical to compare them to confirm the benefit of the less limiting model (Figure 5.17). The FOM plots below each data set represents the deviation of the fit away from the data where '0' is a perfect match. It is clearly seen that both models are very similar where most improvements to the fit are emphasised in the XRR data set through the reduction of dips in the FOM. In PNR+ it is also seen that high $Q$ has a better fitting to the data. The SLDs in Figure 5.18 are again very similar, but lifting the restraints on the model causes a thinner interface with less roughness, and a magnetic moment in the main film which has increased.

Table 5.3: Comparison of important values and parameters extracted from the fitted SLD models. Composition 1 is $Co_2FeAl_{0.5}Si_{0.5}$ and composition 2 is $Co_{1.84}Fe_{1.2}Al_{0.56}Si_{0.4}$.

| Model | Nominal | 1 | 2 | 3 |
|---|---|---|---|---|
| Composition | 1 | 1 | 2 | 2 |
| FOM ($10^{-2}$) | - | 1.69 | 2.19 | 1.57 |
| Equiv. Unit Cell Volume ($Å^3$) | 183 | 204 | 193 | 192 |
| Film Thickness (Å) | 210 | 212 | 216 | 211 |
| Total Interface Thickness (Å) | 0 | 16 | 58 | 25 |
| Interface Thickness + Sigma (Å) | - | 113 | 72 | 56 |
| Magnetic Moment ($\mu_B$/f.u.) | 5.5 | 4.9 | 4.7 | 4.9 |
| MSLD ($10^{-6}Å^{-2}$) | 3.17 | 2.86 | 2.72 | 2.84 |
| Surface Thickness (Å) | - | 41 | 57 | 56 |
| Surface Thickness + Sigma (Å) | - | 96 | 130 | 146 |

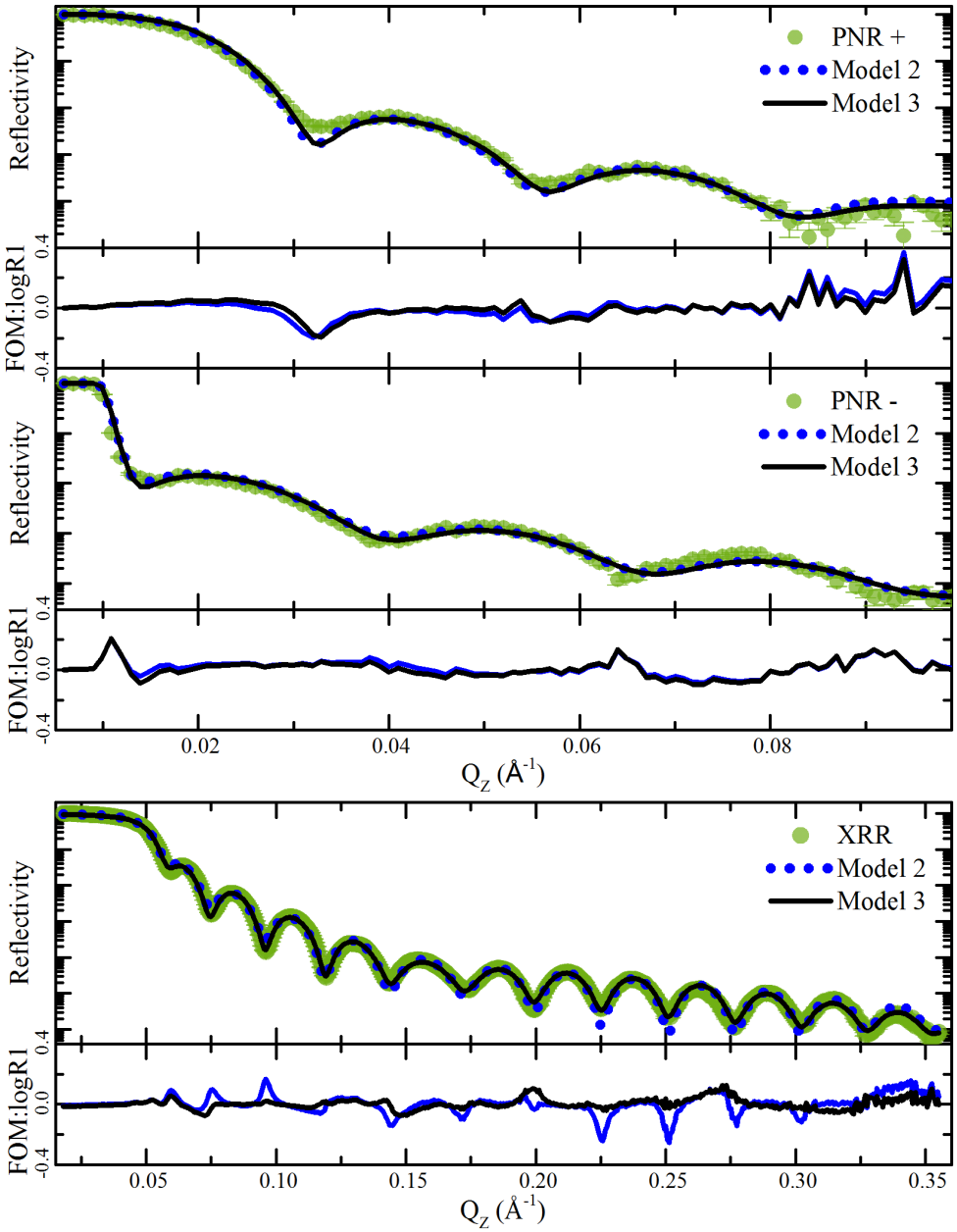


Figure 5.17: PNR and XRR data with the corresponding Kiessig fringes from Model 2 and Model 3. Data: Large green circles, Model 2: blue dotted line, Model 3: black solid line. FOM is plotted in colours corresponding to the model to highlight differences in fit.

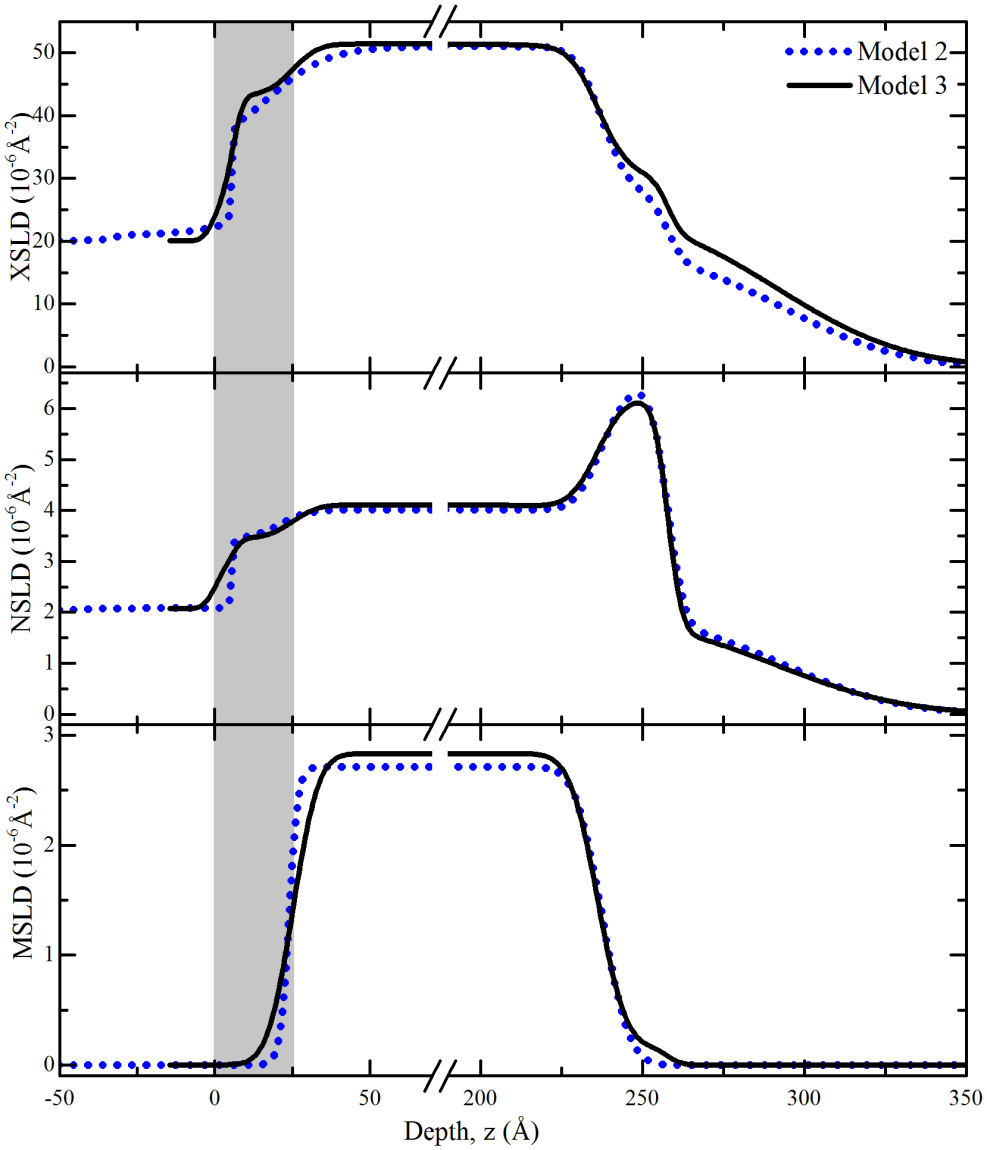


Figure 5.18: SLD profiles for Model 2 and Model 3 overlayed. Grey box highlights the interface region as defined by the centre of the magnetic profile gradient and where it reaches 0. Both models are very similar due as Model 3 is a more freely fitting Model 2.

Model 1 and 3 are compared in Figure 5.19. Discrepancies in fit are again highlighted by FOM plots underneath the data. It is important to remember that the data is fitted simultaneously, so compromises and loss of sensitivity in certain areas such as low $Q$ ($\sim Q_c$) are made in order to fit the data over the entire data sets within the weighting of the FOM:logR1 where XRR > PNR+ > PNR−.

For PNR+, there is a good fit to the data for both models. There is a small disagreement in the curvature of the first fringe due to the differences in SL for the film, but an agreement in the phase of the fringes at the converging point $Q \sim 0.032\,\text{Å}^{-1}$. In PNR− the fringes are out of phase throughout the entire fitting, possibly caused by a small disagreement in MSLD thickness due to best fitting the magnetism for different SLD. In the XRR, the phase difference is not observed and suggests the increased number of fringes, due to the extended $Q$-range, creates more sensitivity to interference of the layer thicknesses and naturally weights the fit causing the neutron data to compensate.

The FOM graph for PNR− highlights a small discrepancy in the gradient of the first fringe for both data at $Q \sim 0.01\,\text{Å}^{-1}$. The reason for this could be a combination of parameters including roughness, surface profile, density, composition and magnetism. It is most likely due to an inaccurate averaging of the film composition, which is the chosen to be fixed in all models. A slight variation in this composition can have a large effect on the SLs for the different probes due to the different sensitivities to the elements and the critical edge is most sensitive to main film composition and density. This theory is supported by the good fit to the XRR data at $Q \sim 0.05\,\text{Å}^{-1}$, showing the density has adjusted to find the best fit for the fixed composition but is again weighted by the high statistics of the X-rays. The first two fringes of Model 1 XRR have higher FOM than Model 3, and as low $Q$ is mostly sensitive to surface parameters, the better fit in Model 3 strongly suggests that the X-rays require this extended surface region in order to fit these fringes, and the roughness gradient towards high $Q$.

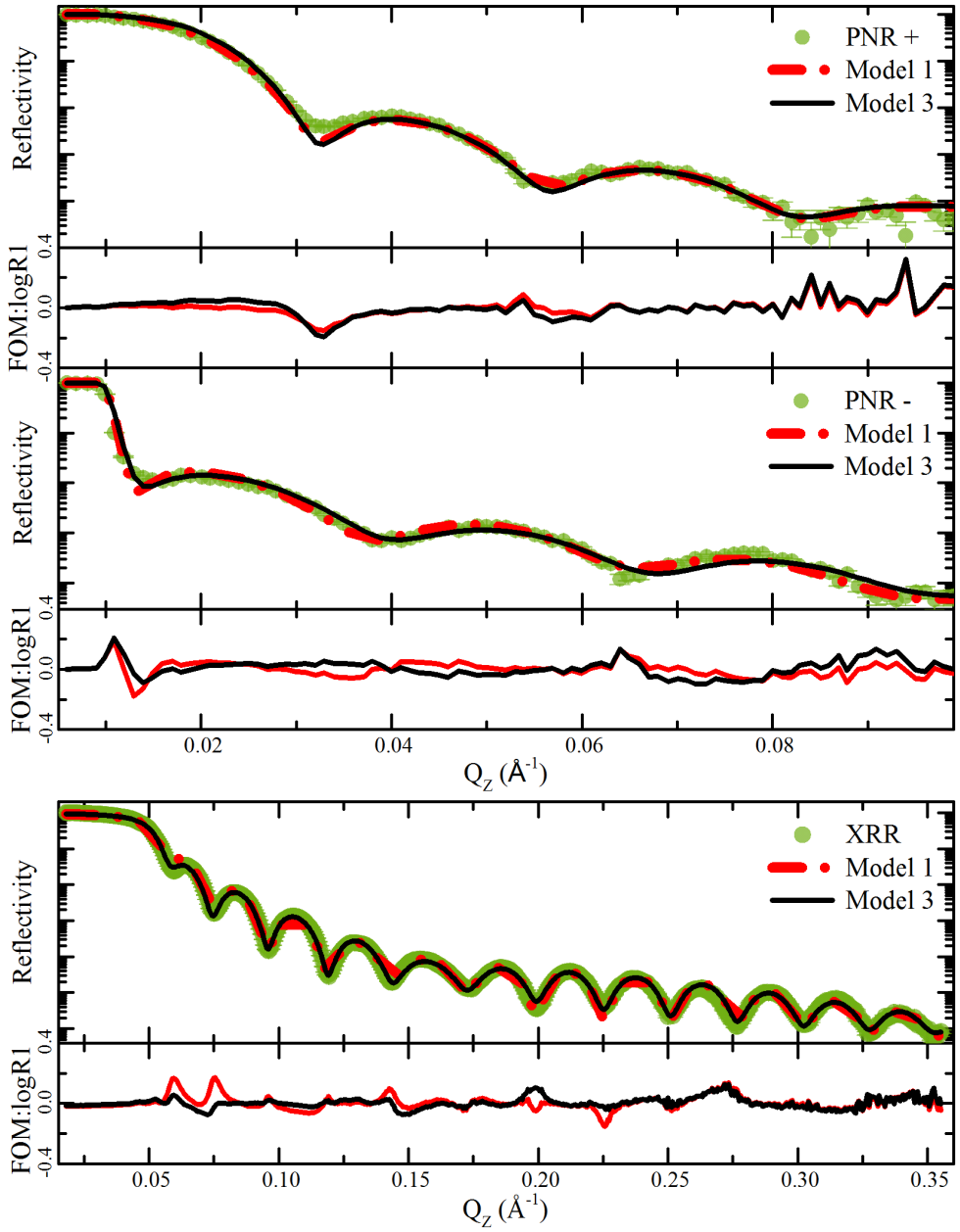


Figure 5.19: PNR and XRR data with the corresponding Kiessig fringes from Model 1 and Model 3. Data: Large green circles, Model 1: red dashed dotted line, Model 3: black solid line. FOM is plotted in colours corresponding to the model to highlight differences in fit.

Focussing now on the features of the SLD (Figure 5.20) and the possible reasons for the variations in profile. The surface is very contrasting for these two models. The long surface tail of Model 3 is likely due to an artefact of the fitting

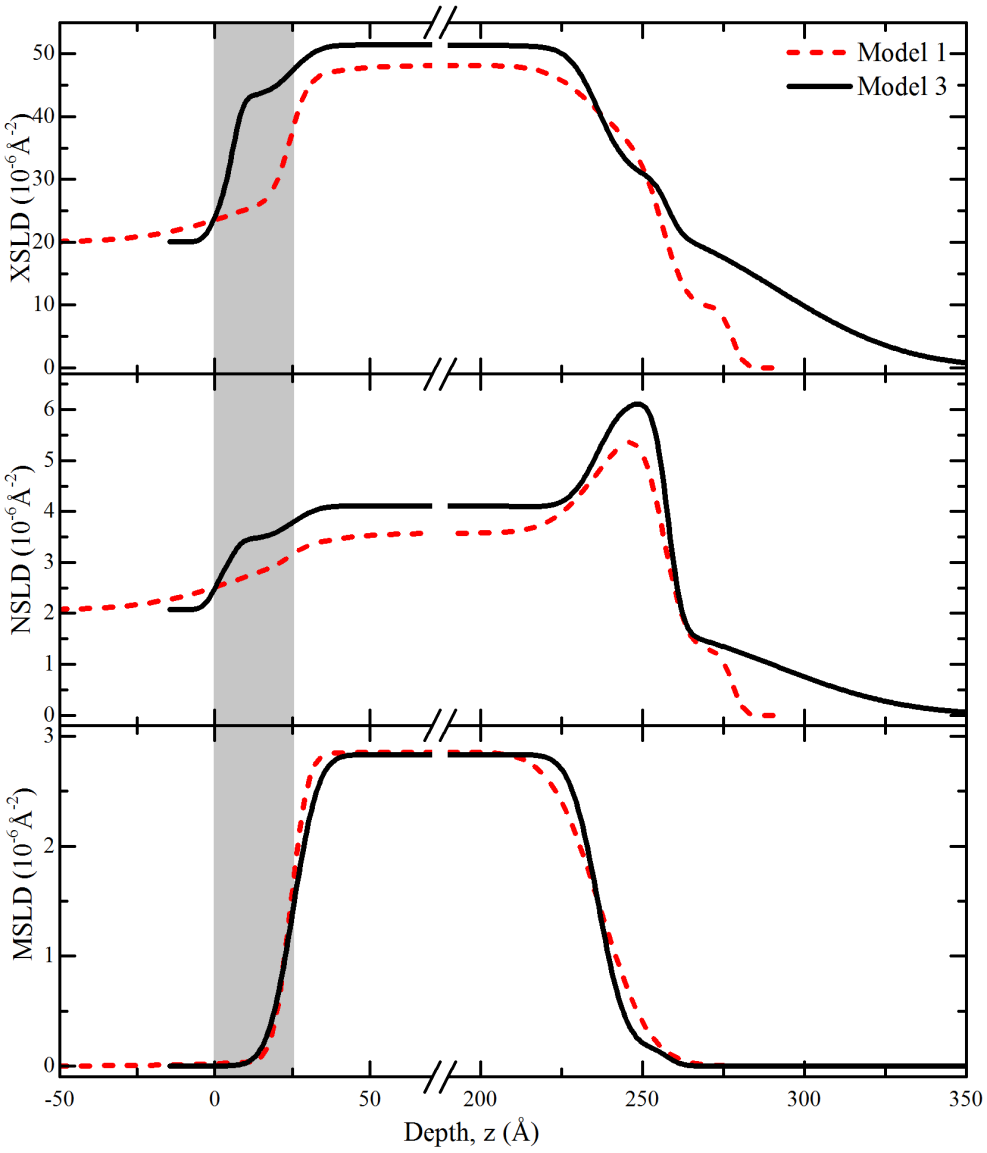


Figure 5.20: SLD profiles for Model 2 and Model 3 overlayed. Grey box highlights the interface region as defined by the centre of the magnetic profile gradient and where it reaches 0.

where the X-rays are sensitive to macroscopic surface roughnesses on a large length scale. A reason for Model 1 not having the tails could either be the composition/film SLD value forcing the roughness to be at the interface instead of the surface causing the correct barrier height variation, or the fitting formalism taking a different minimisation route by fitting with a large substrate roughness instead of a small one as can be compared in Table 5.3. It also introduces the idea that the roughness

and height of the SLD layers can be conserved within the SLD, creating a similar Kiessig fringe pattern.

The overall surface thickness given by Models 1 and 3 is between 41 Å and 56 Å, summarised per model in Table 5.3, and agrees with the varying composition seen in the EELS surface map (Figure 5.21). The surface EELS map shows the intensity of each element when the electrons are tuned to the corresponding elemental energy. The colour is added to show different regions where yellow has more of the specified element, and black the least. When accounting for the roughness in the surface layer of the SLD models, by taking into account the error function width, these total surface thicknesses increase to 96 Å and 146 Å. This definition cannot be interpreted from the EELS surface map due to lack of sensitivity and extremely small length scales when compared to the mm size beam footprint on the sample from reflectivity.

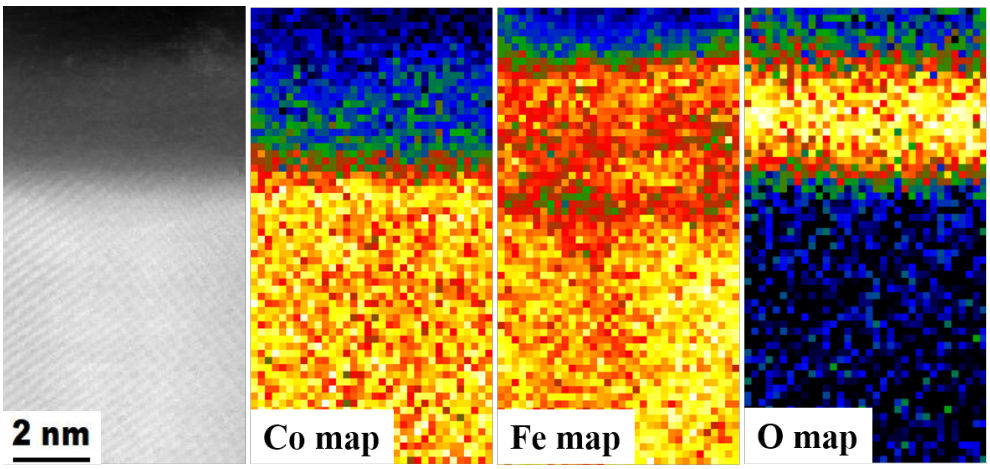


Figure 5.21: AC-STEM HAADF image and Co, Fe and O EELS maps of the near-surface region of a CFAS film. Yellow-red shows high intensity, blue-green low intensity. [83]

A large peak can be seen in all neutron SLD models (Figure 5.15) in the lower surface layer at z ∼ 250 Å. This is an uncommon feature to see in the SLD for reflectivity, but can easily be explained by analysing the EELS map. The Co map shows a depletion of Co in the uppermost 50 Å of the image. These Co lattice sites are either to be filled by Al, Si or O. They are not seen to be filled by Fe due to ∼10 Å of the Fe layer being diffused over the entire 60 Å surface. It is important to note that the surface of the sample does not have to be confined to the region which is oxidised and varying composition at the surface also requires a new layer. Co is the lowest scatter of all the considerable elements and therefore any exchange of

atom will be more highly scattering in the neutrons causing the peak in the NSLD. Al and Si EELS surface maps were not taken.

It can be seen that the two models, even though their differences in SLD (Figure 5.20), produce interference fringes of similar merit. This similarity suggests a type of conservation of features in the SLD due to the Kiessig fringes being Fourier transform of the differential of the SLD. These features could be roughness profiles, thickness of layers and magnitudes of scattering barriers. Due to the large interface and surface regions in this sample, it enables these features to be located in different places in the SLD and cause a similar interference pattern. The Kiessig fringes show a larger oscillation every $Q \sim 0.125\,\text{Å}^{-1}$ corresponding to $\sim$30 Å. In Model 1 this comes from the surface steps and in Model 3 from the interface steps.

The MSLD is in agreement between all models, more specifically it is the same for freely fitting Models 1 and 3. The agreement strongly suggests a successful decoupling of the magnetism despite SLD differences. The common thickness of the CFAS magnetic layer is $212 \pm 1$ Å, with an approximate non magnetic interface layer of 25 Å (highlighted by the grey shaded region in Figure 5.20). This interface length scale is in agreement with the microscopy Section 5.2.2 and also agrees with the theoretical model that the intermixing causes a progressive decrease in magnetic moment as Si replaces Fe and Co in the unit cell as simulated in Table 5.2 [80]. In the table, CFS is used due to the lack of Al in the interface region as shown in the EELS data (Section 5.2.2), and the simplification of modelling without the extra element. The magnetic moment mentioned is per f.u., which is four times smaller than the formula unit cell, and suggests that the most possibly configurations reduces the magnetism as confirmed by the reflectivity fitting.

The precise value of the magnetic moment is difficult to extract for this particular sample, due to the coupling of parameters as previously mentioned. The best estimate for the moment from the different models, is found by taking the MSLD, and using the XRD measured (lattice constant)$^3$ as the common density, to extract the moment. For Model 1 and Model 3 we obtain a moment of $4.9(2)\,\mu_B$/f.u., which are in agreement with the VSM data taken earlier (Figure 5.12), but lower than expected when compared to the theoretical value of $5.5\,\mu_B$/f.u.. This value is extracted under the assumption that the film thickness as defined by the SLD is correct, and that the entire of this thickness is of the same density and composition without intermixing or defects. Looking back at the SLD (Figure 5.15) and observing the difficulty of defining the precise z of the layers, especially for the surface and interface, this value is not well defined. But taking the magnetic thickness, but is in agreement with the VSM value of $5.2(4)\,\mu_B$/f.u. and close to the predicted value.

Model 2 produces a magnetic moment of 4.7(1) $\mu_B$/f.u., in agreement with the VSM value but at the lower boundary of error margin and validating the choice of Model 3.

It is interesting to try and understand the reason for differences in main film SLD value, as it is very unlikely the two models should both produce reflectivity fringes which fit the data. While adjusting the data in order to find this link, it is found that by modifying a small selection of parameters, a fit can be obtained which is similar to the data but has different SLD (Figure 5.22) This new model would then need to be minimised, but it is interesting to see how easily it can be done and to see which parameters are strongly linked. All the adjustment of models is done within the limits of the original models; the entire substrate and the main film composition remains static. Model 3 is plotted to give visualisation of the SLD differences. Starting with Model 1, reducing the substrate roughness to 10% of the value, increasing the density of the film to that of Model 3 and reducing the magnetism, finds an alternative way of reproducing similar neutron Kiessig fringes. There are still some features missing, and by coarsely adjusting several other parameters, the fit can be refined by hand. If the first surface layer SL value is increased by 10%, the X-ray features at low $Q$ begin to refit and increasing the roughness of the surface improves this. The first fringe of the neutron data fits well, but the X-ray first fringe doesn't fit. There are still errors in the scattering length used here that cannot be easily fixed using density. It seems that a conservation of features in the SLD is a way of finding multiple solutions to create similar interference fringes. It also reinforces the coupling of parameters, especially that of substrate roughness and main SLDs. Dependent on which data set is more strongly weighted, and the path of the minimisation, depends on whether this is due to surface sensitivity or the main film height and exists when there are large interfaces, surfaces and roughnesses. The low $Q$ range of the neutrons is a limiting feature due to the lack of fringes, causing less sensitivity at the interface. Even though the X-rays are less sensitive to layers lower in the sample due to penetration depths, the high $Q$ data gives guidance and weighing to the fits.

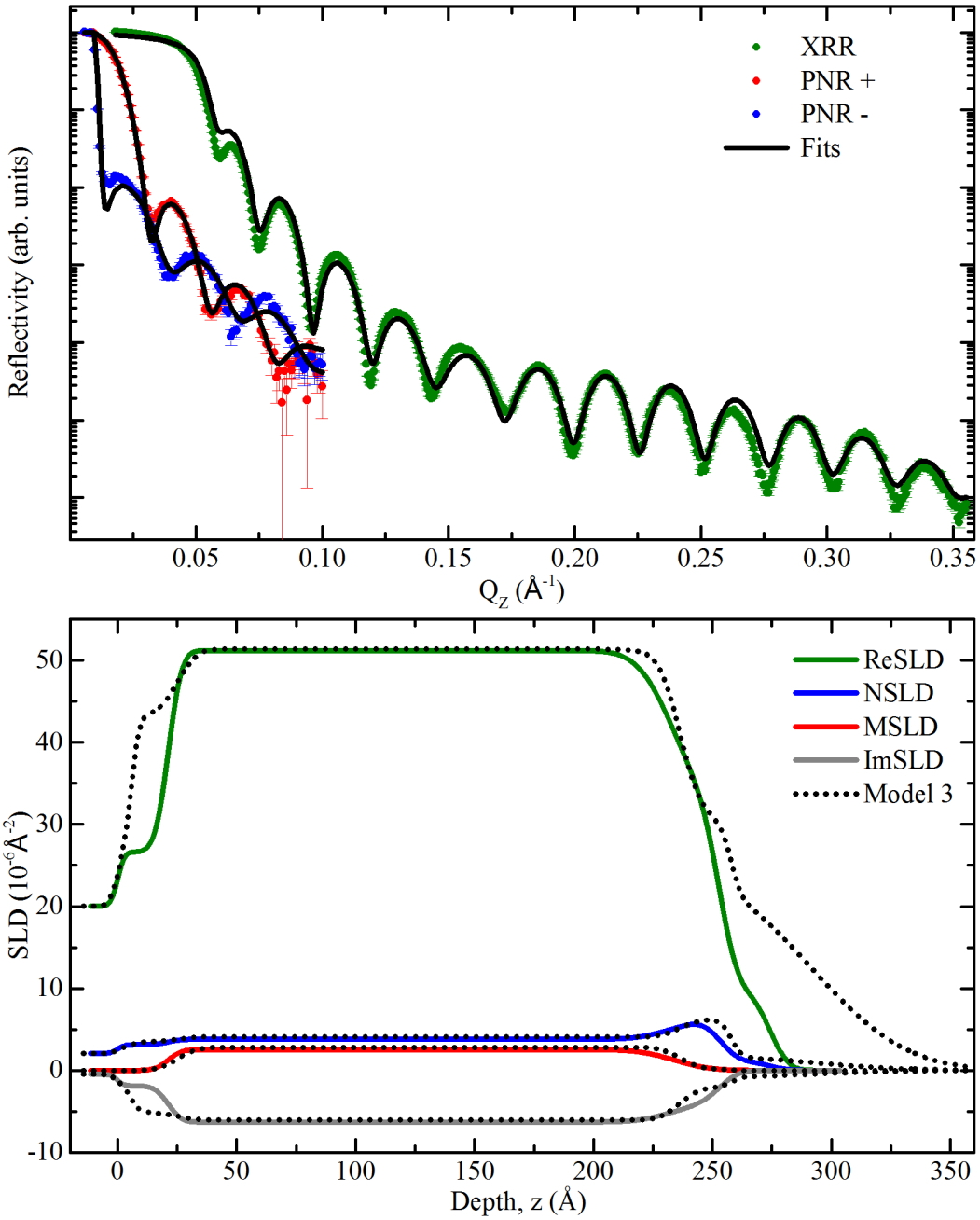


Figure 5.22: Fits and corresponding SLD for manually edited Model 1, changing parameters as described in the text. This Model has not been minimised using GenX, only modelled.

## 5.4 Conclusions

The work in this chapter has brought attention to the fact that different reflectivity models can equally describe the CFAS thin film layer on Si(111). This is mainly due to the complexity of the full-Heusler alloy with non-ideal composition and density. Large surface and interfacial layers, when grown on Si, cause the ability for different features with the same SLD potential difference and thickness, to be interchanged in the model to produce similar Kiessig fringes. This leads to many of the parameters being strongly coupled and unique SLD are not discovered. A unique magnetic profile is extracted, however, and emphasises the strength of this technique.

Using a hybrid model, where by the SLD was rigidly fitted to other data obtained, then relaxed, was found the best method of modelling the data. It is important to note, that this was only confirmed when comparing this hybrid model to a standard freely fitting model. It was discovered while pushing the limits of the data and understanding what could be extracted, that choosing to fix the composition of the complex Heusler alloy. Acommon practice in reflectivity fitting, was not the best choice for this sample. Due to the sensitivity of the probes to the different elements, linear adjustment of the film SLD by adjusting density is not a good method, but does bring the data closer to a minima due to only having one parameter to change instead of four. For example, an increase of one Fe atom per unit cell, replacing Co, is an increase of 4 times in the neutron SL, where it is not an observable difference in the X-rays. The SLD needs to be more freely adjustable. It is also a disadvantage that the composition and density of the layer are also coupled to any defects or changes in crystallographic structure over the entire layer to which it represents. This indicates that any composition or density can only be taken as an indication of atomic and structural information of the sample. This is acceptable if we are looking to discover the magnetic profile of the thin film only, but does cause discrepancies when attempting to extract an exact magnetic moment of the sample.

To further decouple a precise magnetic moment value from the models, it is important to carefully limit parameters such as density and composition. A possible solution for this would be to perform such measurements as energy-dependent XRR as this would more carefully define the critical edge which is strongly dependent on the density and composition of the film. It is also a good idea to take XRR measurements of the sample at different points in time, as the surface can modify but the majority of the sample will remain the same. It is possible to allow the model to vary at the surface for the different data sets, while retaining the same

layer structure and parameters underneath. It is then easier to obtain a fit which is more unique and can account for time dependent oxidation.

A way of preserving the film quality would be to add a capping layer to the surface of the sample. This would preserve magnetic profiles throughout the sample and limit the thick, rough, layers at the surface. The ability of the SLD features interchanging between surface and interface would then be diminished. It is then also sensible to find a different semiconductor material for the substrate which is epitaxially compatible with the CFAS thin film, in order to reduce the amount of diffusion at the interface and also limiting large undefined regions, while retaining specific spintronic properties.

# Chapter 6

# $Co_2FeAl_{0.5}Si_{0.5}$ grown on Ge(111)

## 6.1 Introduction

The quaternary full Heusler thin film alloy $Co_2FeAl_{0.5}Si_{0.5}$ has previously been grown on Si substrates (Chapter 5). It was found that diffusion of Si into the film created a large 150 Å interfacial layer. This compositional change induced a large decrease in magnetism over this interfacial region with 25 Å magnetic dead layer next to the substrate. The majority of the film exhibited a magnetic moment of 4.9 $\mu_B$/f.u. which is lower than theoretically expected from this material [67], possibly caused by the larger interfacial region where magnetism doesn't recover. Using Ge as the substrate for the CFAS layer is expected to minimise the diffusion region at the interface, and also reduce strain related to the mismatch of the two materials being 0.4% instead of 4.6% for Si. Like Si, Ge is also well known for its long range spin-diffusion length $\sim$10 $\mu$m [20]. Table 6.1 shows all the properties of Ge and CFAS needed for this chapter.

This chapter focuses on how fitting reflectivity data should be approached and robustly modelled. Complementary techniques are used to corroborate the fit achieved. A second Ge sample "Ge2" is introduced in order to realise whether sample reproducibility is possible for this specific growth method, necessary for device fabrication.

Table 6.1: Nominal properties and parameters of materials used in the chapter, for comparative purposes.

| Parameter | Value |
|---|---|
| Lattice constant - Ge (Å) | 5.66 |
| Lattice constant - CFAS (Å) | 5.68 |
| Mismatch (%) | 0.4 |
| XSL - Ge (e-/atom) | 30.92 - 0.88j |
| NSL - Ge (fm/atom) | 8.19 |
| XSL - CFAS (e-/atom) | 87.12 - 10.73j |
| NSL - CFAS (fm/atom) | 18.23 |
| $N$ - Ge $Å^{-3}$ | 0.0442 |
| $N$ - CFAS $Å^{-3}$ | 0.0218 |

## 6.2 $Co_2FeAl_{0.5}Si_{0.5}$ grown on Ge(111)

### 6.2.1 Transmission Electron Microscopy

Film uniformity and a thickness of ∼180 Å can be seen in the TEM image in Figure 6.1(a) with a sharp interface between the CFAS film and Ge substrate. Figure 6.1(b) shows the experimental SAD pattern where compared with simulated diffraction patterns Figure 6.1(c), confirms that even though the CFAS and Ge are lattice matched and one would expect an over lapping cube on cube epitaxy, that the CFAS preferentially grows twinned with respect to the Ge substrate with the epitaxial relationships: CFAS(111) ∥ Ge(111) and CFAS($1\bar{1}0$) ∥ Ge($\bar{1}10$). Twinning is a feature on too small a length scale to be seen by the averaging nature of reflectivity, but is important to be aware of the crystal structure, atomic ordering due to possible effects on the magnetism.

### 6.2.2 High Angular Annular Dark Field and Electron Energy Loss Spectroscopy

Looking more closely at the interface using HAADF STEM (Figure 6.2), at low magnification (a) there is an intermixing layer of ∼10 Å. As this figure is orientated along the ($1\bar{1}0$) direction, it is possible to see down the atomic columns where most Z contrast is available. In the bulk of the film (Figure 6.2(b)), a line profile is produced in the vicinity of the boxed region and the corresponding line profile Figure 6.2(d) shows a large contrast between regions of Co and other elements. For the interface in Figure 6.2(c), there is less contrast between the peaks in the line profile (Figure 6.2(e)), which represents intermixing in this region. Due to the similarities in peak

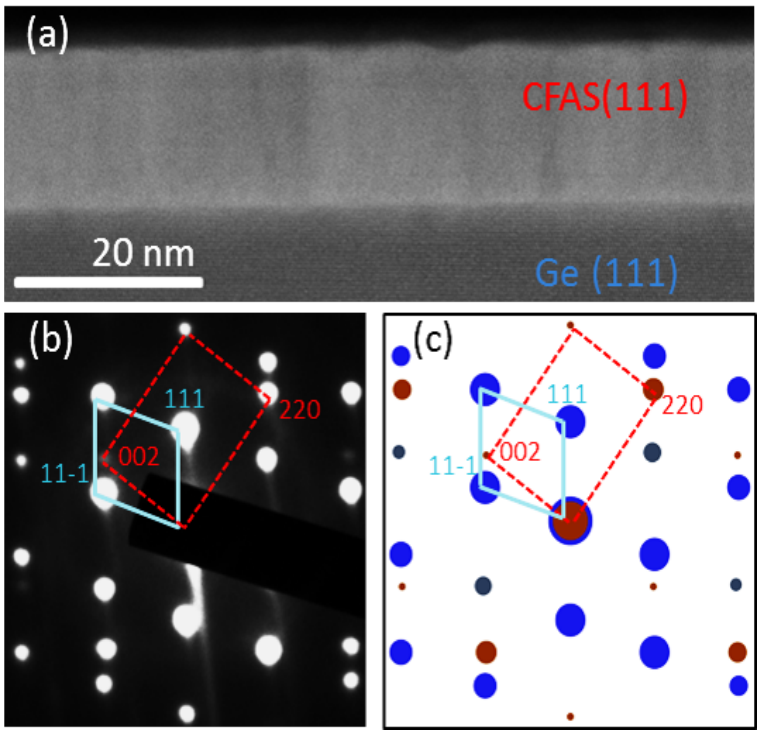


Figure 6.1: (a) Low magnification overview HAADF STEM image showing that the film is uniform with a thickness of ∼180 Å. (b) SAD pattern from an area that includes both film and substrate, showing the single crystal nature of the grown film and the epitaxial relationship with the substrate. The motifs are labelled with the red dashed rectangle for the film and blue solid rhombus for the Ge substrate. (c) Simulated SAED diffraction pattern assuming twinned epitaxy with respect to the substrate which shows excellent agreement with the observations. The reflections labelled in red are from the film; in blue from the substrate. The reflections in grey appear due to double diffraction in the substrate [85].

heights, it is suggested that Ge, the higher Z element, is replacing the Fe-Al/Si sites. Atomic composition is determined by EELS mapping across the interface along the white line identified in Figure 6.3(f). Figure 6.3(g) represents the corresponding averaged elemental composition where Ge is seen to diffuse into the film over ∼10 Å.

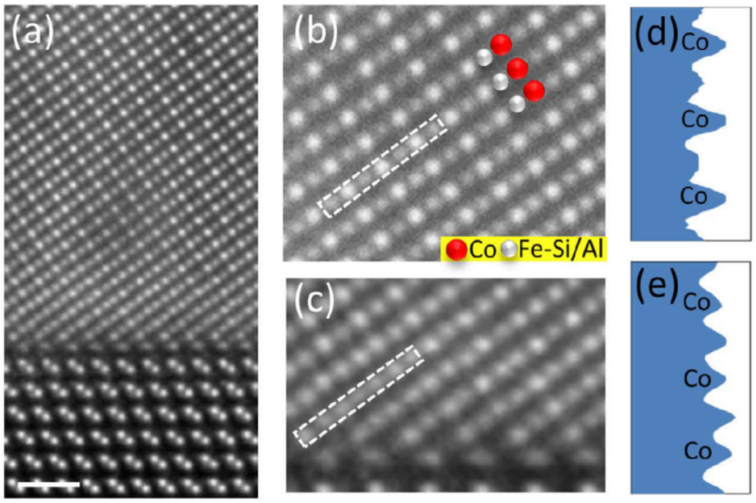


Figure 6.2: (a) Higher magnification HAADF STEM image along the [1$\bar{1}$0] direction showing the CFAS/Ge interfacial region. The white scale bar corresponds to 0.7nm. (b) Atomic resolution HAADF STEM image from a section of the main film showing planes of atoms along the [001] direction, (d) shows the corresponding line profile in the dashed white box. (c) Atomic resolution HAADF STEM of the interface region along the [001] direction, (e) shows the corresponding line profile [85].

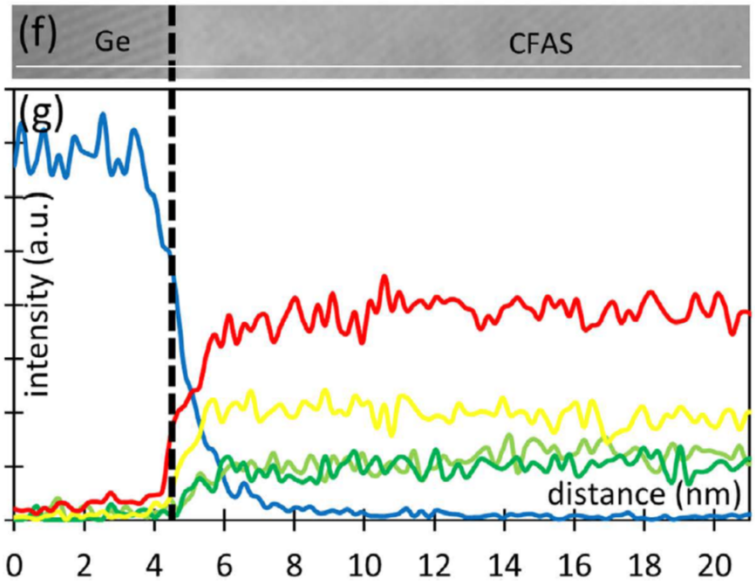


Figure 6.3: (f) STEM image of the substrate/interface region where the white line represents the location of the EELS intensity mapping in (f) where Ge-blue, Co-red, Fe-yellow, Al-light green and Si-dark green. [85].

### 6.2.3 Partial Density of States

Further chemical mapping (not shown in this thesis [85]) shows that the Ge diffuses into the CFAS film by moving and replacing along the Fe-Al/Si planes. The Co remains on its original lattice site, maintaining the same CFAS crystal structure. Using this information, partial density of states (PDOS) has been calculated for the different compositions and structures across the interface [85]. Table 6.2 shows the change in SP for different theoretical compositions where Ge replaces Fe or Al/Si in the typical CFAS formula unit. There are only three of these configurations where the SP decreases, but half metallicity is only observed in two configurations where Ge is equal to 0 or 0.25. PDOS in Figure 6.4 shows a more detailed picture of the polarisation at the Fermi level. In the figure, (b) (i) - (v) represent different sections of the interfacial transition with different configurations of elements and lattice structures. This replicates the few layers of atoms across the interface in Figure 6.2 where (c) represents the corresponding DOS showing the change in spin polarisation. It is observed that the band gap is not as large as for CFAS-$B2$ as $L2_1$ (Figure 5.2), but due to the region of diffusion being so small with structural retention, the electronic properties are retained across the interface showing potential of this material grown on Ge(111) for spintronic devices. All of the compositional variations shown in Table 6.2 retain some magnetism and therefore it is expected that there is magnetism within the sample up to the substrate even if the profile decreases through a possible interfacial layer.

Table 6.2: Magnetic moment $\mu_B$/f.u. and spin-polarization values (%) of configurations c1-c8 obtained when Ge atoms gradually substitute the Fe-Al/Si atoms in the bulk CFAS unit cell. n stands for the number of atoms per formula unit for each of the atomic species, where the number of Co atoms in the f.u. is always 2 [85].

| Label | CFAS | c1 | c2 | c3 | c4 | c5 | c6 | c7 | c8 |
|---|---|---|---|---|---|---|---|---|---|
| n(Fe) | 1 | 1 | 1 | 1 | 1 | 0.75 | 0.5 | 0.25 | 0 |
| n(Si/Al) | 1 | 0.75 | 0.5 | 0.25 | 0 | 0 | 0 | 0 | 0 |
| n(Ge) | 0 | 0.25 | 0.5 | 0.75 | 1 | 1.25 | 1.5 | 1.75 | 2 |
| Magnetic moment ($\mu_B$/f.u.) | 5.5 | 5.5 | 5.75 | 6 | 6 | 5 | 3.95 | 2.8 | 1.75 |
| SP (%) | 100 | 100 | 100 | 100 | 100 | 100 | 69 | 88 | 24 |

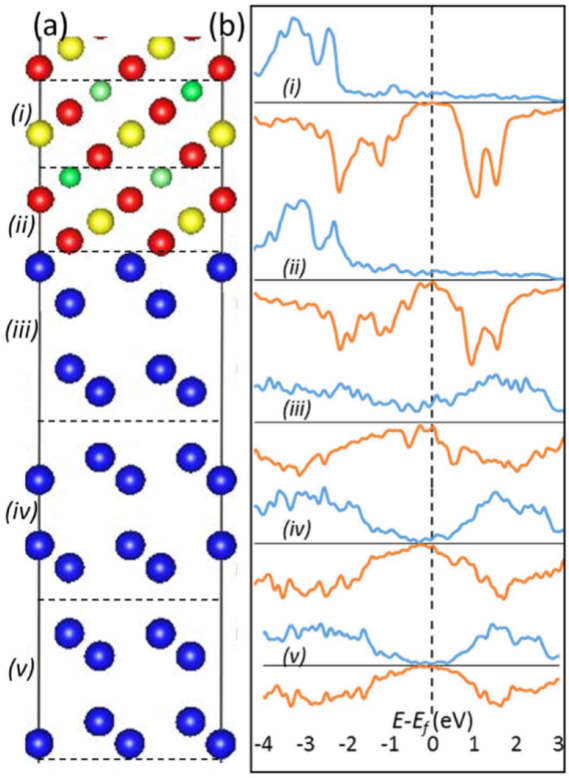


Figure 6.4: (a) Structural model of the CFAS/Ge interface viewed along the $[1\bar{1}0]$ crystallographic direction where (b) shows the corresponding PDOS for the different elemental configurations (i)-(v) through the intermixing process. Blue represents spin up PDOS in the upper half of the graphs and the orange represents spin down PDOS in the lower parts of the graphs [85].

### 6.2.4 X-ray Diffraction

To check the structural Heusler phase of the CFAS material over a larger length scale, a simple out of plane $\theta - 2\theta$ scan is performed on the sample aligned to the Ge(111) reflection (Figure 6.5). From this we observe the Ge(111) and (333) peaks, but no peaks from the CFAS. This is to be expected for $B2$ phase full-Heusler alloys. We do observe a small Ge(222) peak which should be suppressed due to structure factor rules ([27]) as in the case of Si (222), but is due to multiple scattering as determined by the small FWHM.

Figure 6.6 shows both CFAS(200) and (400), aligned by setting the correct $2\theta$ position, rotating $\chi$ by 54.74° and scanning in $\phi$ (see Figure 2.1 for rotation directions). As structure factor rules forbid Ge(200) reflections, it is best to align to the CFAS(200) as we can be sure that it cannot be confused with the substrate

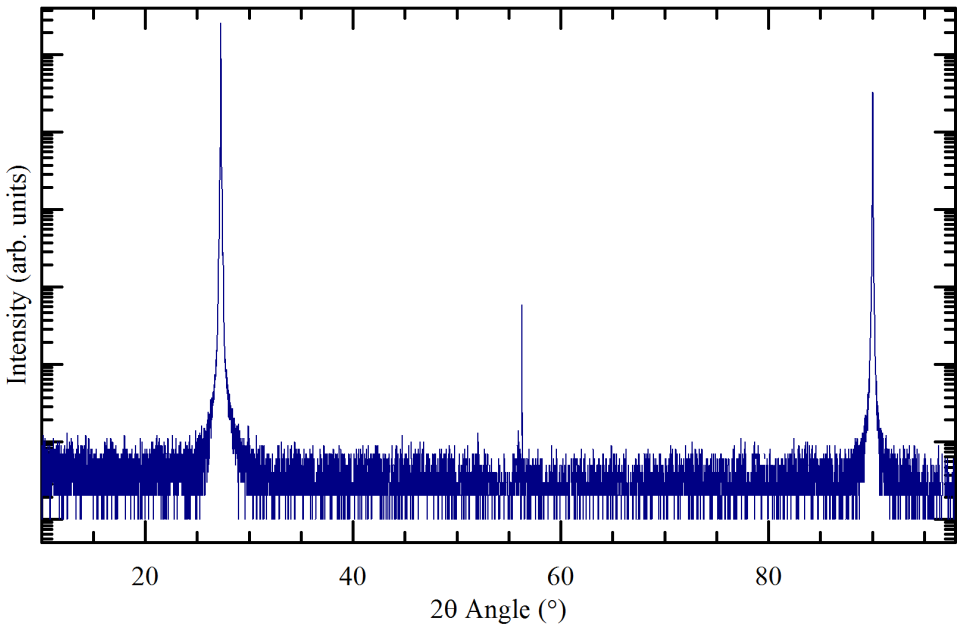


Figure 6.5: $\theta - 2\theta$ scan of the CFAS/Ge(111) sample aligned to the Ge(111) out of plane reflection. There is no observation of any CFAS peak, therefore suggesting the film is in the $B2$ phase.

peak. Aligning then to CFAS(400), a 360° $\phi$ scan locates the positions of the Ge(400) reflections. The CFAS is rotated 60° with respect to the film. Fitting the centre point of the peaks and using Equation 2.1, gives an average lattice constant of a = 5.67 Å. This is within error, but the slight value deviation can be due to factors such as alignment errors of the XRD instrument, or crystallographic defects changing the averaged lattice constant of the crystal such as distortion.

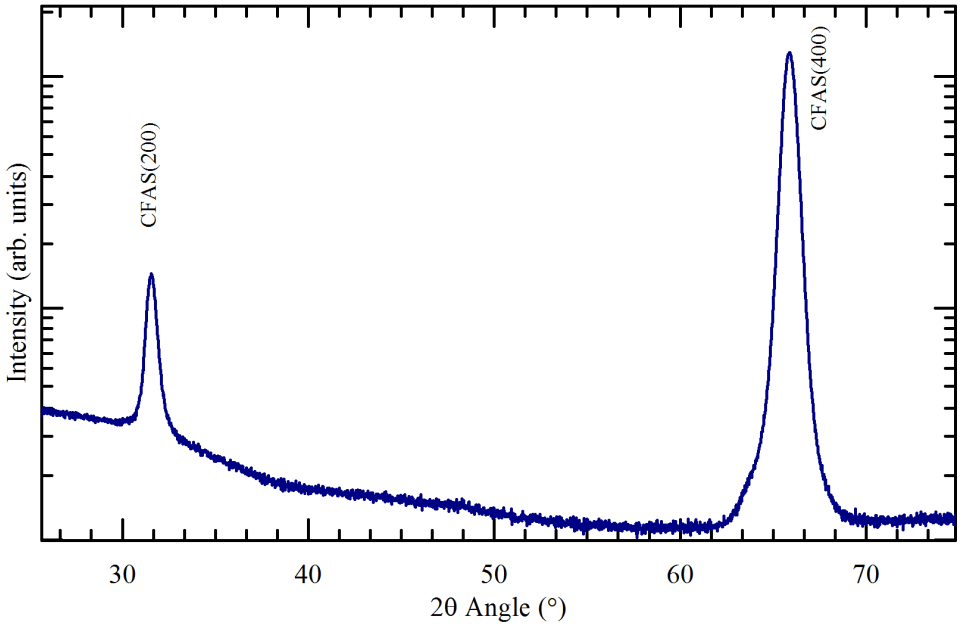


Figure 6.6: In plane $\omega - 2\theta$ scan aligned to the CFAS(200) peak where $\chi = 54.7°$, showing $B2$ crystallographic phases. Data taken on Rigaku SmartLab, University of York.

### 6.2.5 X-ray Reflectivity

Correlated roughness is seen in Figure 6.7, indicating that roughness at the interface propagates to the surface. This will need to be allowed for in the model but due to the off-specular being orders of magnitude lower than the specular, the suggestion is that this roughness is small. Figure 6.7 is the on and off specular reflectivity for the Ge sample. The large drop in intensity between specular and off-specular reflections suggests low diffuse scattering from roughness in the sample, but there is correlated roughness.

### 6.2.6 Fitting

Previous techniques suggest sample properties that may be observable in reflectivity, and help to suggest profile features when struggling to fit data, and or confirm validity of fits. It is important to remember that due to the different sensitivities of the other experiments, caused by probe type and effective sample size, these features may not be seen in the much larger averaging reflectivity data. A summary of techniques and the sample features extracted from the data, is shown in Table 6.3.

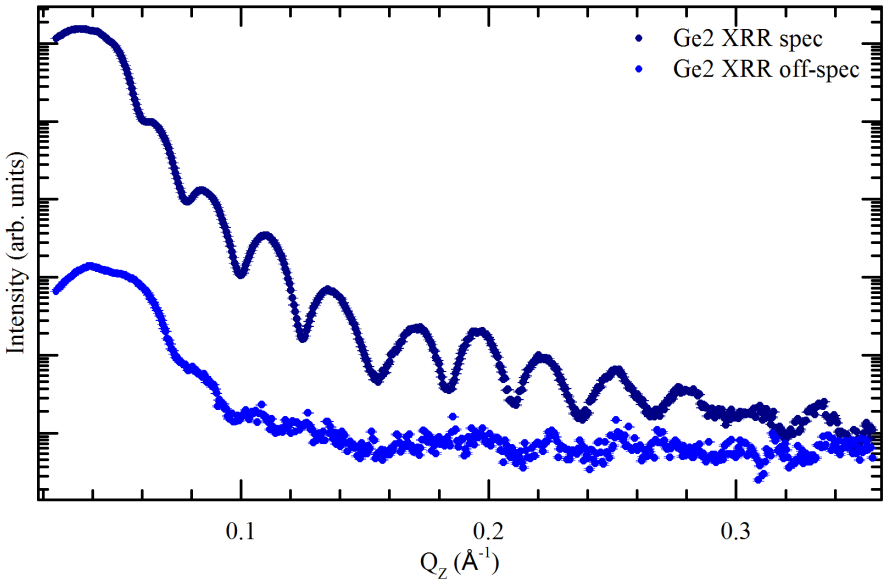


Figure 6.7: XRR specular and off-specular ($\omega$ = -0.1°) scan of CFAS/Ge(111) sample.

It is interesting, and also useful, to compare the reflectivity data to the Si(111) sample from the previous chapter (Figure 6.8). The comparison suggests how the two models should differ. If the reflectivity model fits the data using parameters shown in Table 6.3, this gives confidence in the fits. The model for the Si sample had both large interfacial and surface regions, where SLD features could be interchanged between the two while maintaining a good fit to the data assuming SLD barrier heights were conserved. Due to lattice matching and minimal diffusion, as shown in Figure 6.3, the Ge sample is expected to have zero to minimal interface layers, and due to the assumption of a similar oxidation process, a surface profile resembling that of the Si sample.

The fringes are very similar for both samples with the XRR data suggesting a slightly higher Ge surface roughness which creates a faster drop-off of the data. In the XRR data at low $Q$, there is an obvious thickness difference between the samples shown by the larger Ge fringes, but they become of similar width at higher $Q$. This suggests a thinner Ge sample surface, but similar film thickness. This is also seen in the PNR+ data. The critical edge for both the XRR and PNR+ is in the same location indicating a similar film composition, but PNR− critical edge has a dramatic shift which is due to the difference in substrate SLD. The "M" feature seen previously in the Si sample between XRR $Q = 0.15\,\text{Å}^{-1}$ and $0.2\,\text{Å}^{-1}$, owing to a layer thickness of ∼30 Å, is also observed in the Ge XRR, this time between

Table 6.3: List of all the observable parameters taken from previous characterisation techniques, helping to aid and confirm the model used to fit the data.

| Technique | Feature observed |
|---|---|
| HAADF STEM | 180 Å; Good quality; Consistent film; Diffusion at Interface $\sim$ 1 nm |
| EELS | Interface $\sim$ 2 nm |
| XRD | $B2$ phase; 5.67 Å measured lattice constant |
| XRR Ge vs Si | Increase in sub:sur roughness; Similar film thickness; Thinner surface; Same film XSLD; 20 Å vs 30 Å layer |
| PNR+ Ge vs Si | Similar film thickness; Thinner surface; Similar MSLD; Similar uSLD |
| PNR− Ge vs Si | Different substrate; Similar NSLD; Different dSLD |

$0.125\,\text{Å}^{-1}$ and $0.18\,\text{Å}^{-1}$ representing a layer thickness of $\sim$20 Å. In the Si, this feature was positioned at the interface for Model 3, but shows the need for at least one extra layer in the model.

Table 6.3 combines the features extracted from the previous experiments and the Si(111) sample comparison. It is good practice to build the model slowly and fit after the addition of each layer in order to be sure that a more simple model is not the best fit. It can be easy to over complicate a model due to lack of robust fitting (pushing the parameters out of their minima and allowing to refit), and also difficult to fit data accurately where the starting parameters are too far away from that of the global minima. It is beneficial to compare the final model with these parameters to confirm the accuracy of the best fit model (as will be seen later in the chapter), but these extracted characteristics can aid model fitting when in difficulty.

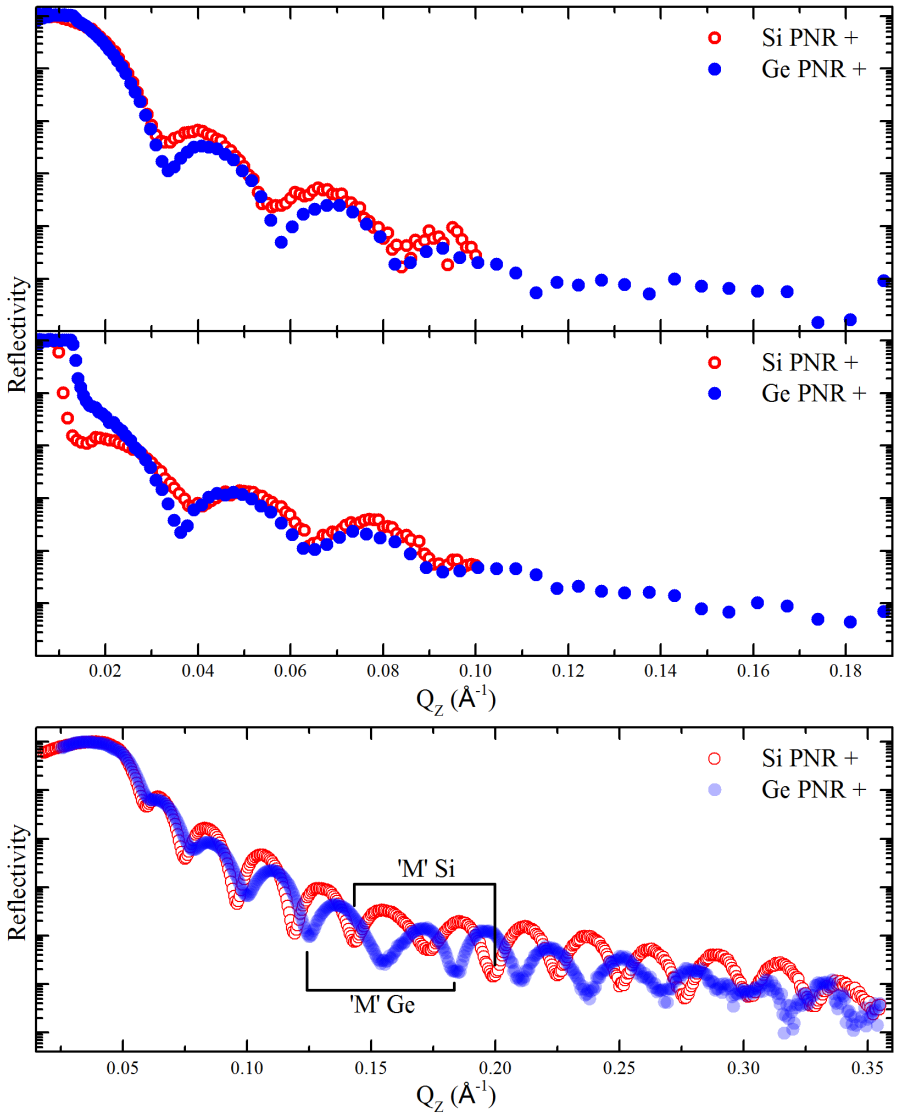


Figure 6.8: Reflectivity data for PNR+, PNR− and XRR for both Si(111) and Ge(111) samples for comparison purposes in order to confirm Ge model validity. Square brackets indicate 'M' feature described in the text.

Data from Figures 6.9 to 6.14 build and fit the model layer by layer until a best fit is obtained. Chapter 5 (CFAS/Si) was fitting by modifying the density of the main film. As it was discovered that this method limited the movement of the SLD, this chapter utilises the ability to change composition while keeping the CFAS number density constant nominal value $1/5.68^3$. Changes in composition are programmed by allowing the number of atoms to adjust for each of the different elements. The X-rays and neutrons are therefore fitted to the same composition, while allowing for non linear changes in SL. It must be made clear that the change in composition does not represent the exact composition of the layer, as these modifications also account for changes in density, defects, and other anomalies in the layer. The composition is not kept at a constant 4 atoms/f.u. but allowed to adjust within ± 10% for each element. The main FOM used in this chapter is custom logR1 (Section 3.3.4), where each data point on each data set is weighted equally. This enables the software to more fairly weight the data sets, in fact it is slightly skewed towards the PNR as there are two data sets for the one experiment which is useful for giving sensitivity to the magnetic profile. FOM values are summarised in Table 6.4 in order to give numerical values to the quality of the fit. FOMN (neutron only FOM) and FOMX (X-ray only FOM) are shown to give insight on where the newer model makes an improvement to the fit.

Table 6.4: Comparison of FOM values for the different CFAS/Ge(111) models. The layers column defines the layers included in the model, where 'I' is an interfacial layer, 'F' is the film and 'S' represents a surface layer. All values are to the power of $10^{-2}$.

| Model | Layers | FOM | FOMN | FOMX |
|---|---|---|---|---|
| 1 | 0I - F - 0S | 4.50 | 3.05 | 1.45 |
| 2 | 0I - F - 1S | 2.61 | 1.65 | 0.96 |
| 3 | 1I - F - 0S | 3.85 | 2.46 | 1.39 |
| 4 | 1I - F - 1S | 2.42 | 1.47 | 0.94 |
| 5 | 0I - F - 2S | 2.19 | 1.51 | 0.69 |
| 6 | 1I - F - 2S | 1.91 | 1.31 | 0.61 |

The modelling process will now be discussed step by step in order to fit the Ge sample data. Model 1 (Figure 6.9) has one CFAS layer on top of the substrate. At first glance it is apparent that more layers are needed due to the missing fringes in XRR and PNR−. The surface of the XRR data seems to fit sensibly but more layers must be included to fit fringes at higher $Q$. A CFAS film thickness is found to be ∼225 Å. This is thicker than both Si data and the microscopy images but could be compensating for the thickness of a missing layer.

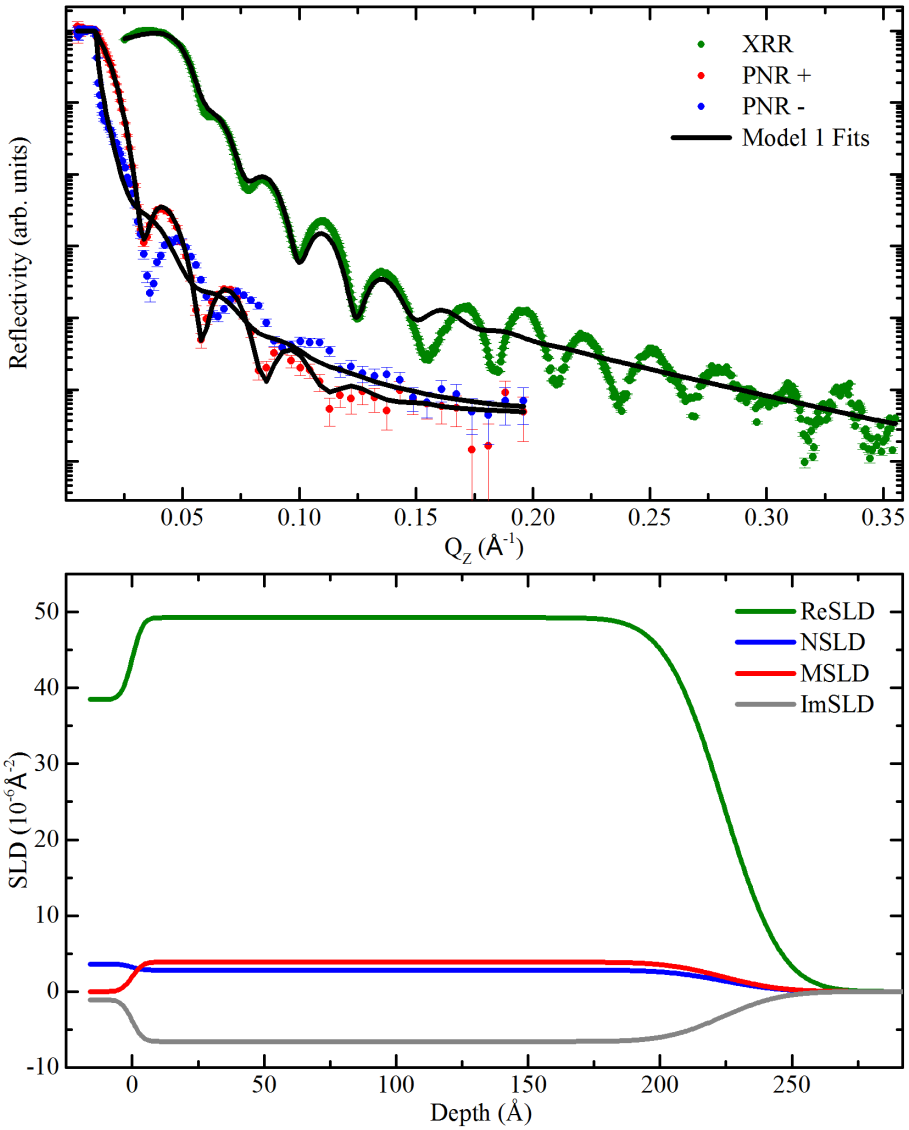


Figure 6.9: Model 1 with substrate and one CFAS layer, fitted simultaneously; custom logR1 = $4.50 \times 10^{-2}$.

Model 2 (Figure 6.10) incorporates one additional layer which is positioned at the surface and is a good fit to the data. More definition is needed at the XRR surface as the fringes at low $Q$ are not representative of the data. The neutrons are a better fit to the data as they are less surface sensitive. There is a slight shift in the simulated fit directly after $Q_{c-}$ for PNR−, which could be due to an inaccuracy of the instrument resolution, the magnetic moment of the film not being high enough, or a discrepancy in the substrate parameters.

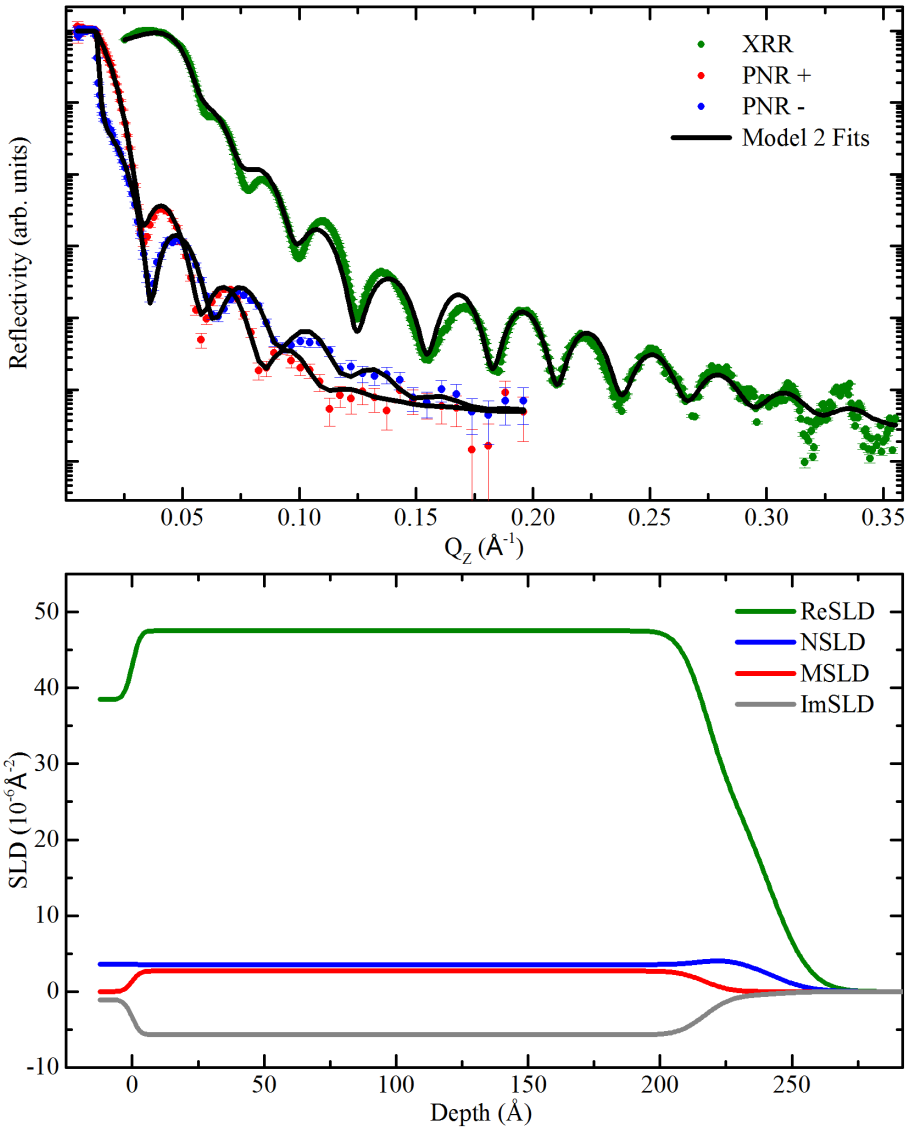


Figure 6.10: Model 2 with substrate, a CFAS layer and one surface layer. Fitted simultaneously; custom logR1 = $2.61 \times 10^{-2}$.

The one additional layer in Model 3 (Figure 6.11) is positioned this time, at

the interface. After re-fitting it leads to a fit similar to that of Model 1 and is not a viable option due to disappearing higher $Q$ fringes in addition to the increase in FOM when compared to Model 2 and unrealistic increases of SLD at the interface.

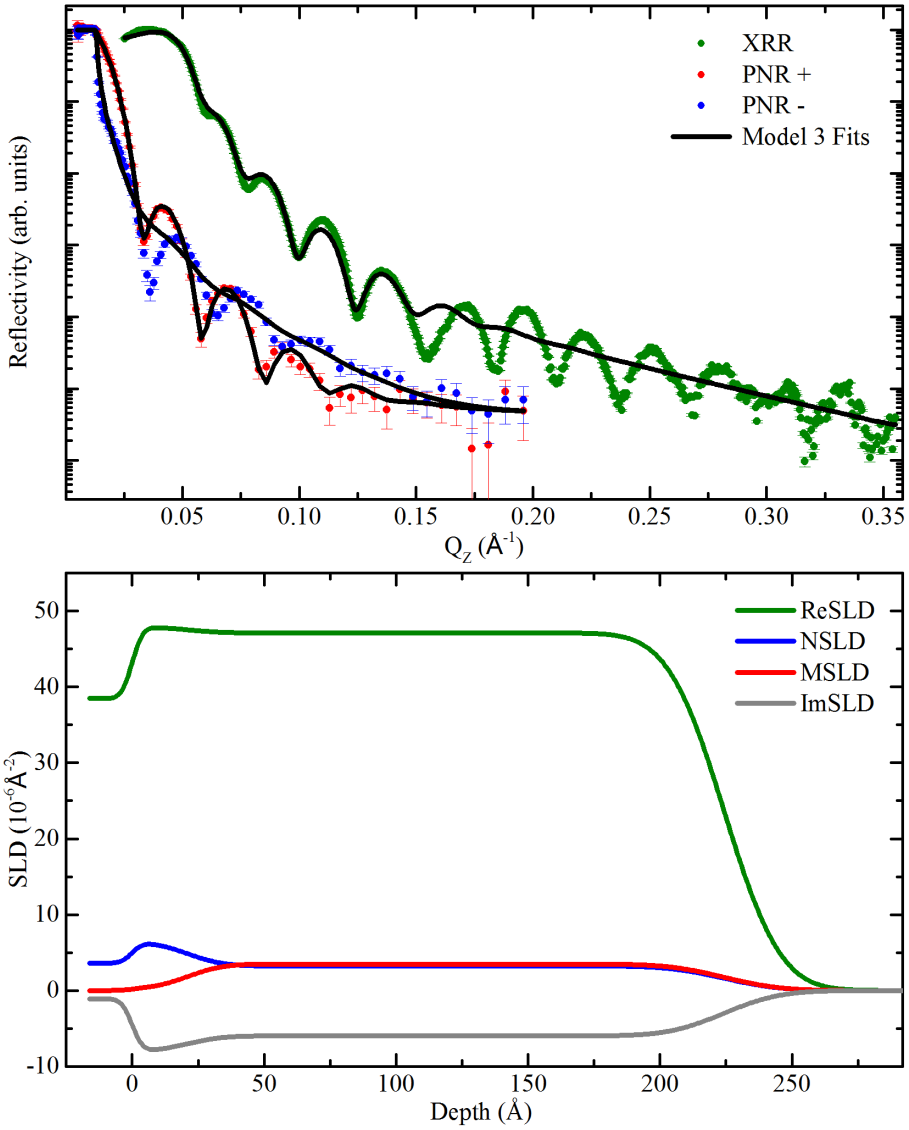


Figure 6.11: Model 3 with substrate, one interface layer and a CFAS layer. Fitted simultaneously; custom logR1 = $3.85 \times 10^{-2}$.

Model 4 (Figure 6.12) has the addition of two layers, one placed at the surface and the other at the interface. When compared to Model 2, there is a small improvement of the combined FOM with the noticeable difference being $\Delta$ FOM$_N$= $-0.1755 \times 10^{-2}$ , suggesting a decrease in the magnetism at the interface is a property desired by the neutron data. An interfacial layer is also consistent with mi-

croscopy data (Figure 6.3). The improvement is observed in the PNR− just after $Q_{c-}$ and in PNR+ at high $Q$. The XRR data still requires more surface features as also suggested by Model 2 as there was no visible decrease in the fit, verified by the FOM.

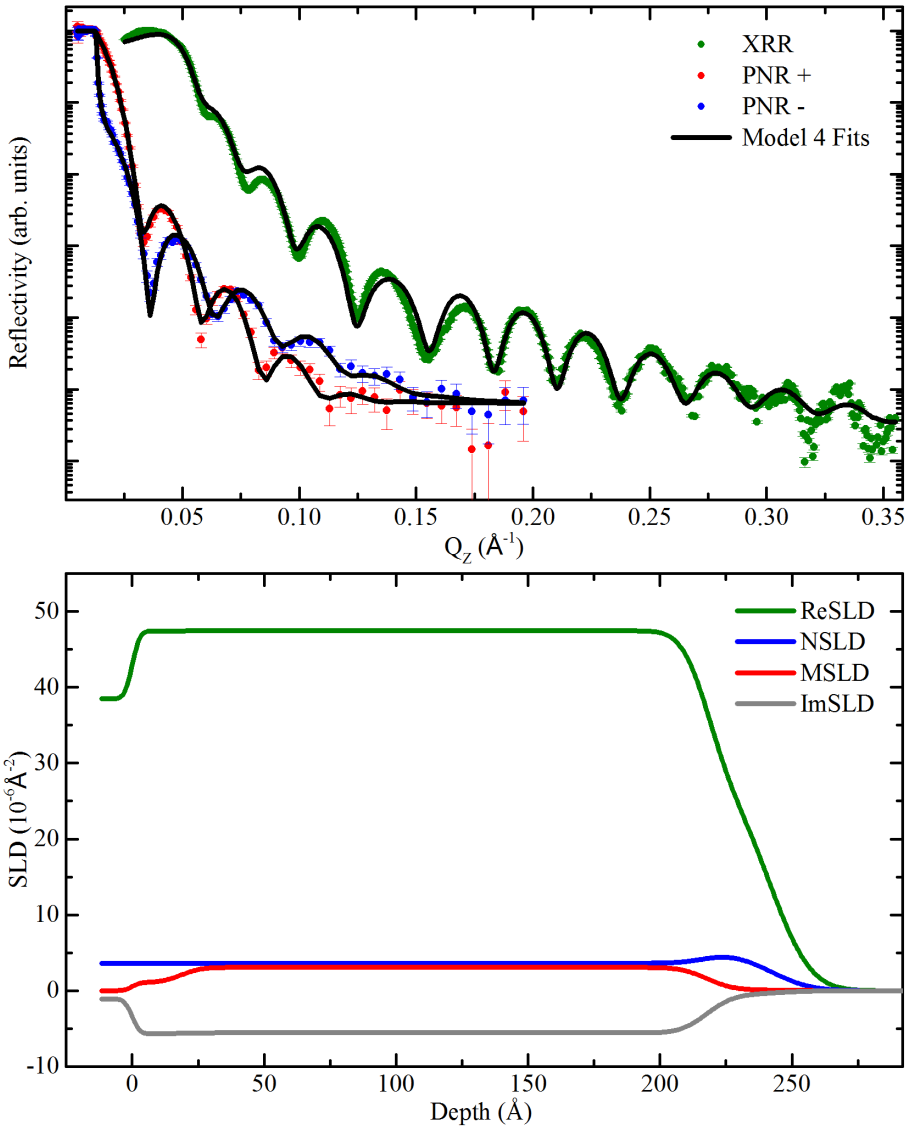


Figure 6.12: Model 4 with substrate, one interface layer, CFAS layer and a surface layer. Fitted simultaneously; custom logR1 = $2.42 \times 10^{-2}$ .

Both additional layers are placed at the surface in Model 5 (Figure 6.13), and a dramatic improvement to the XRR data is observed, with $\Delta\text{FOM}_X = -2.5963 \times 10^{-3}$. In this case $\Delta\text{FOM}_N = +3.58 \times 10^{-4}$ , strongly suggesting that the neutrons needed an interfacial layer with decreased magnetism as in Model 4.

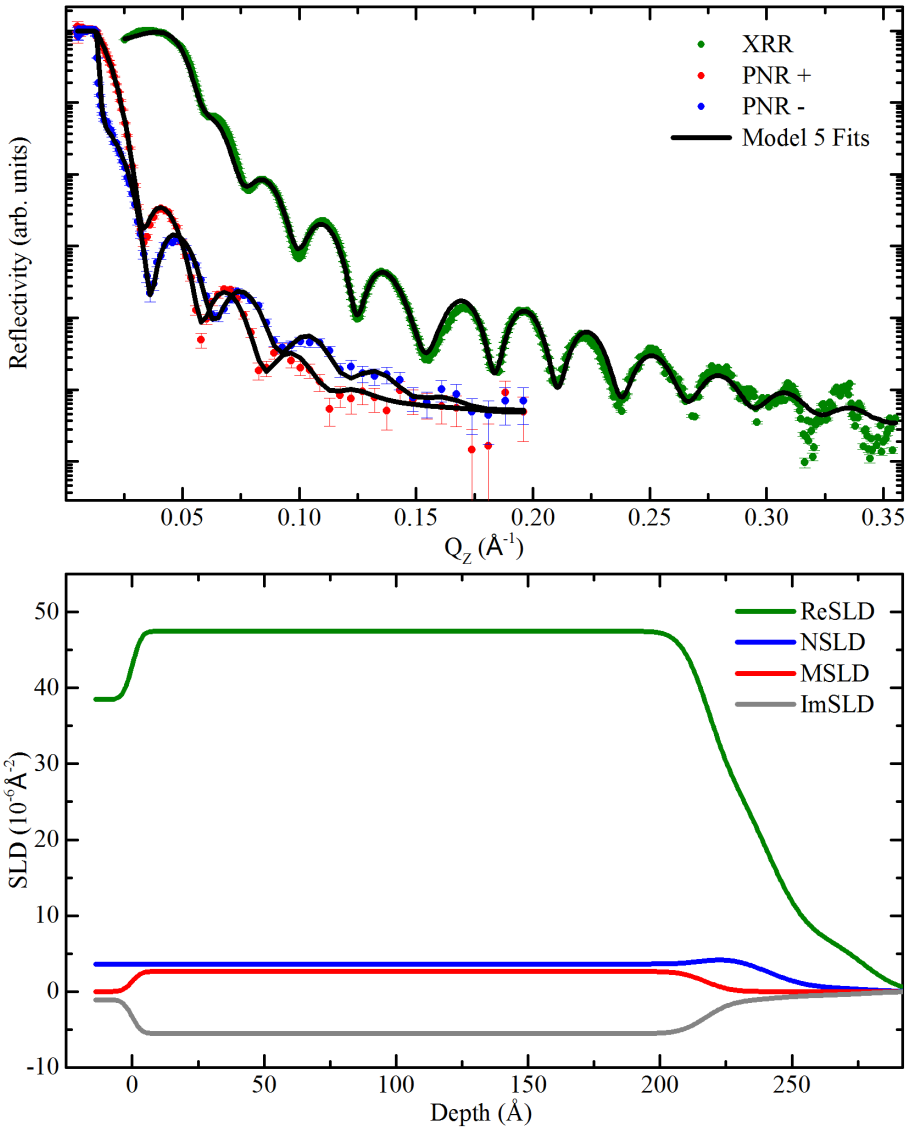


Figure 6.13: Model 5 with substrate, CFAS layer and two surface layers. Fitted simultaneously; custom logR1 = $2.19 \times 10^{-2}$.

Model 6 (Figure 6.14) has an interfacial layer, CFAS film, and two surface layers. The decrease in SLD through the interfacial layer, seen easily in the XRR due to larger change in the SLD, can be explained by the STEM EELS data shown previously. If the accuracy of the EELS is to be trusted (around 5%), elemental mixing at the interface causes a slight depletion in Co atoms towards the substrate without replacement of other atoms (seen in Figure 6.3 between $\sim$ 8 and 12 nm). Interface regions are also non-uniform over large length scales, therefore small changes in compositions and densities are likely, especially when averaged with other features such as defects. Model 6 is the best model where all FOM values are lowest.

Referring back to the table of observed features (Table 6.3), we can compare the SLDs to the values we expected. The SLD (Figure 6.14) can be differentiated and the peaks fitted to find exact values of the layer thicknesses. This technique is useful when wanting to find the roughness values. It is also a good technique to check error functions from large roughnesses aren't overlapping as this invalidates the formulas used to create the SLD and the corresponding Kiessig fringes. If all values of roughness are <50 % of the layer (including the layer either side), the SLDs are valid.

Model 6 fitted with a main film thickness of 199(1) Å, an interface layer of 18(1) Å agreeing with both EELS and the XRR Si comparison, and two surface layers of 24 Å and 36 Å. Due to changes in composition, we have to manipulate the magnetic moment value extracted from the MSLD in order to successfully compare it with that of the nominal value we expect. The definition of the f.u. is $Co_2FeAl_{0.5}Si_{0.5}$ per density $= 5.68^3 = 183.25\,\text{Å}^3$. The ratio of the nominal and fitted scattering length is used to adjust the $\mu_B$. The magnetic moment extracted from the fitted MSLD for Model 6 is $5.13\,\mu_B$/f.u., and when using a ratio of $NSLD_{Nom} : NSLD_{Ge} = 1 : 0.93$, we find the magnetic moment for the bulk of the thin film to be $5.5(2)\,\mu_B$/f.u. over the uniform 200 Å layer. The interface decreases in magnetism over 18 Å towards the substrate, and shows that the change in composition at the interface lowers the magnetic moment, even when PDOS suggests the preservation of SP over such a small region.

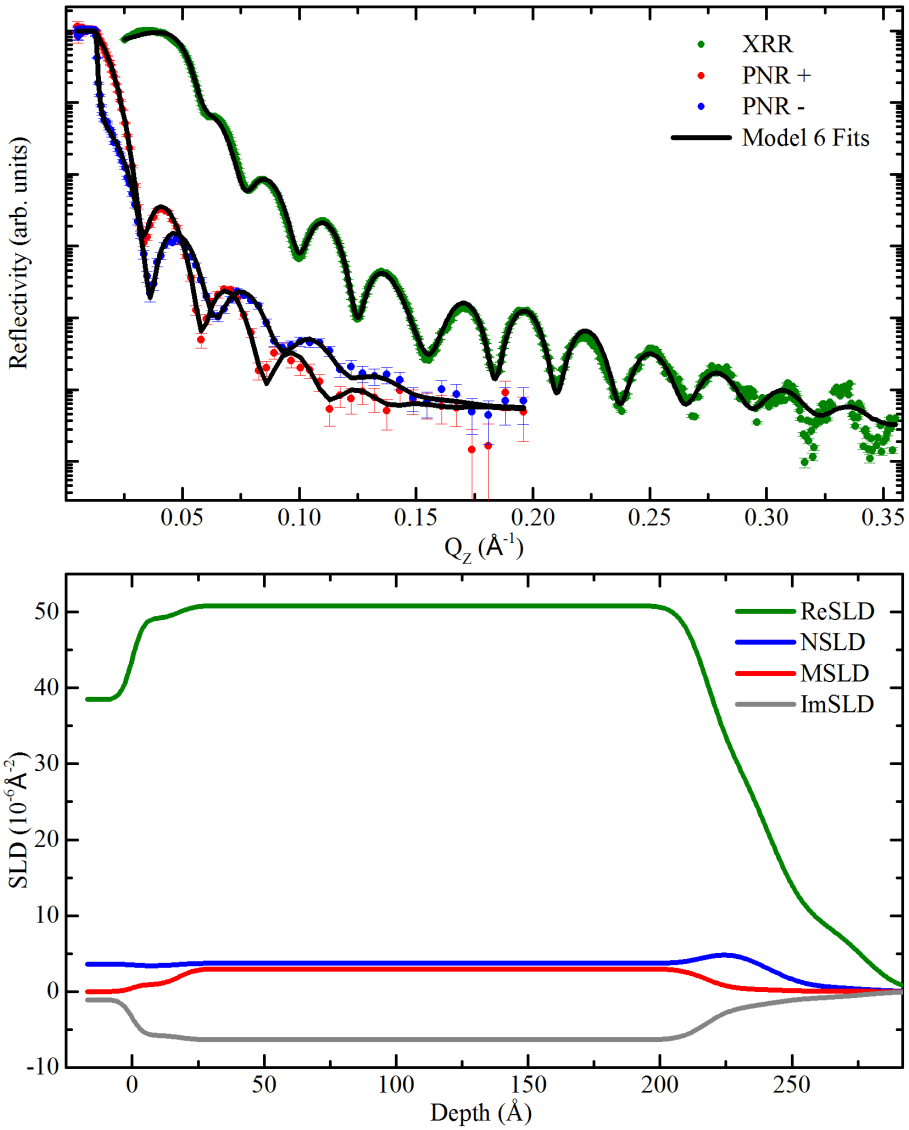


Figure 6.14: Model 6 with substrate, one interface layer, CFAS layer and two surface layers. Fitted simultaneously; custom logR1 = $1.91 \times 10^{-2}$.

It has been observed through the model fitting shown, that the second surface layer is needed in order to fit the XRR data, as this probe is more sensitive to surfaces. Comparing the SLD of both Si(111) and Ge(111) samples (Figure 6.15) confirms that comparisons of two similar samples helps to model the fit. It also gives confidence in both fits as two separate samples grown in the same way, agree with each other and confirms the quality of the growth recipe.

Discussing Figure 6.15, the Si/Ge SLD comparison, the XSLD of the film is very similar for both samples where the difference is likely to be caused by the change in the average film density as measured from the XRD $a_{CFAS/Si} = 5.68\,\text{Å}$ and $a_{CFAS/Ge} = 5.67\,\text{Å}$, where the model used the nominal 5.68 Å value. The interface step is again the cause of the 'M' feature which represents a layer of 20 Å for Ge and a layer of 30 Å for the Si. As predicted, the surface of the Ge sample is smaller due to the lengthened fringes at low $Q$ and the surface roughness is larger. The overall thickness of the main layer is similar, at ∼200 Å compared to ∼211 Å for the Si. There is a difference in NSLD value for the layer, drawing attention to the preferences of fitting SL for more complex films instead of varying density, as the XSLD fits equivalently. The surface exhibits a similar increase in SLD as the Si, indicating a similar oxidation where Co ceases and is replaces by other elements. The magnitude discrepancy is likely due to the difference in film NSLD, or a variation in oxidation.

The uSLD and dSLD is also plotted in order to observe the splitting of the neutron spins for both models. They can then be directly related to features in reflectivity data. A x-axis offset in the dips of the reflectivity fringes for the PNR is easily explained by the NSLD. For the Si sample, at ∼200 Å to 250 Å, the first surface layer creates an effective thickening of the layer in the uSLD which is not seen for dSLD. For the Ge, the lower SL of the first surface layer causes both u and d to have a similar film thickness, changing where the dips are positioned at low $Q$ (more surface sensitive) and making the fringes for PNR+ and PNR− more aligned.

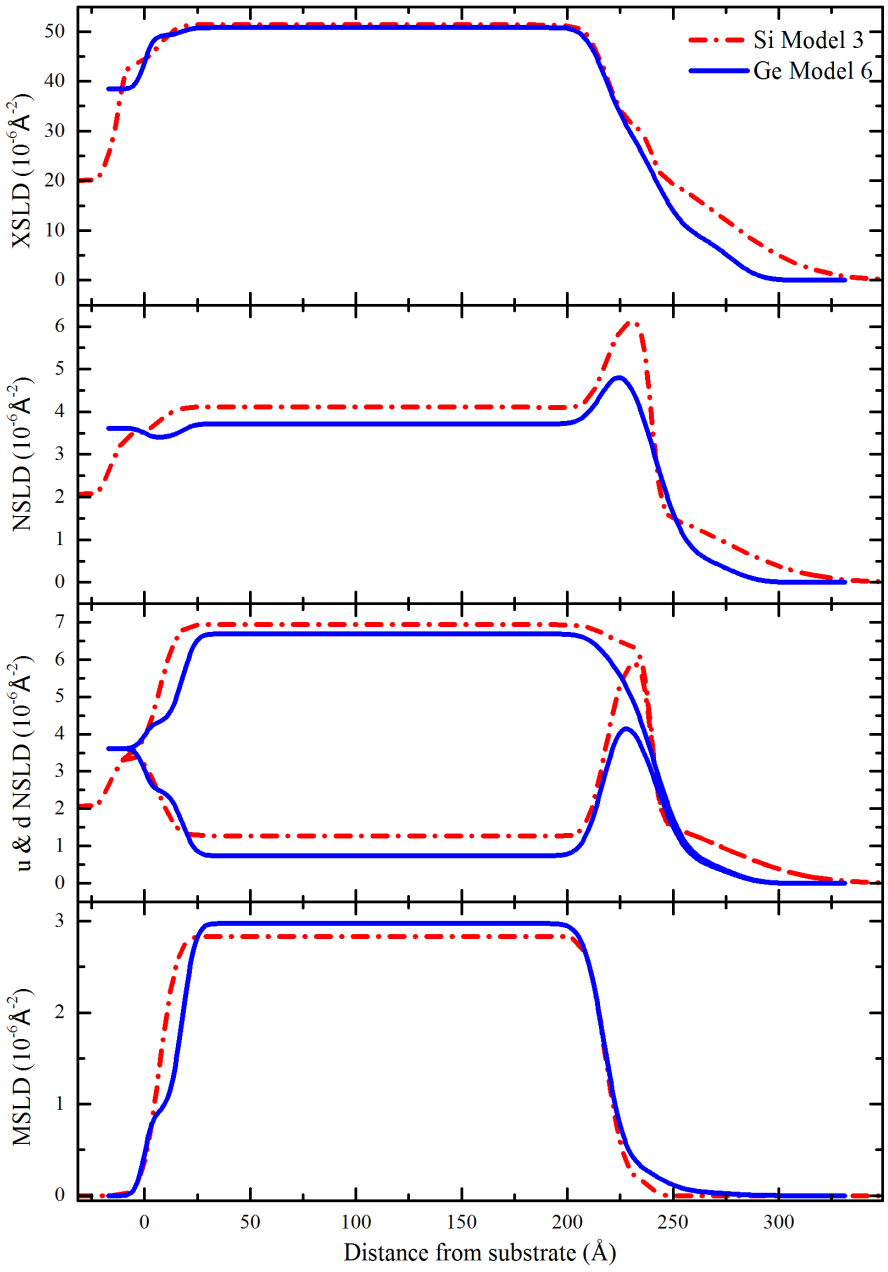


Figure 6.15: A comparison of the SLDs from CFAS/Si(111) and Ge(111) best fit models. The Z axis is again somewhat arbitrary, but has been adjusted so that the main films in the XSLD start at the same value. u & d NSLD represents the uSLD = NSLD + MSLD and dSLD = NSLD - MSLD, respectively.

Comparing the two better fit Models 4 and 6 (Figure 6.16), highlights the change in SLD when all three additional layers are introduced. From Figure 6.12 it was clear that the XRR needed additional surface features in order to fit low $Q$, whereas the neutron NSLD was already a good fit to the data. This is clear in the comparison as there is little change in the NSLD and a large change in the XSLD when looking at the fit, and the corresponding FOM. The modification in the surface of Model 6 allows the film XSLD to increase and as seen in Figure 6.8, which is also supported by the similarity in XSLD value to the Si sample. It is apparent that the XSLD is very sensitive to changes in roughness i.e. a larger roughness creates a lower XSLD. This is difficult to quantify whether Model 6 has more or less roughness due to the addition of layers. It is evident that the increase in surface SLD for both XSLD and NSLD allows for the same potential value to be removed from the interface through SLD conservation as seen in Chapter 5.

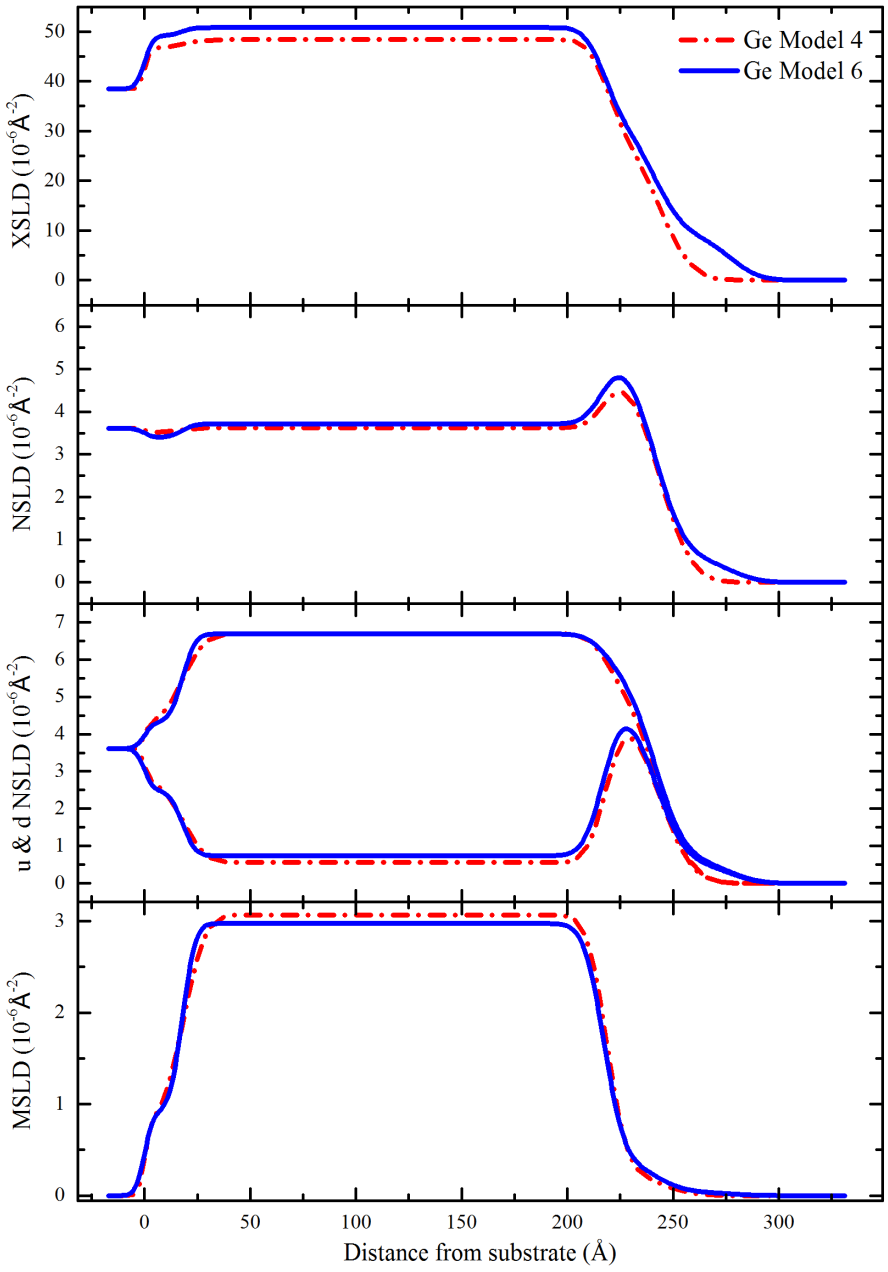


Figure 6.16: CFAS/Ge(111) Model 4 and Model 6 SLD comparison. Neutron u & d represents the uSLD = NSLD + MSLD and dSLD = NSLD - MSLD, respectively.

### 6.2.7 Conclusion

Allowing $b$ and $f$ to vary instead of density only allows more freedom in simultaneous fitting of X-ray and neutron reflectivity data. This is observed throughout the chapter via the different models as the SLD are allowed to adjust in SL, accounting for different sensitivities in elemental composition. A direct comparison with the Si sample from the previous chapter, reveals a similar film with a slightly different surface and interface profile. It is unknown whether the change between samples in NSLD and MSLD, is due to the effect the large Si diffusion layer has on the film, or the limitations in modelling where only density was allowed to vary. The similarity in the XSLD suggests a more adjustable model was needed. The Ge sample yields an interface region, as suggested by microscopy, where the magnetism decreases through it, reaching zero at the substrate. Despite this, the main film of 200 Å, exhibits a magnetic moment of $5.5(2)\,\mu_B$/f.u. in agreement with the theoretical value [67, 74]. $Co_2FeAl_{0.5}Si_{0.5}$ grown on Ge(111) therefore shows promise as a half metallic material, where next steps are to check SP and begin to test its ability in multi-layered devices.

## 6.3 $Co_2FeAl_{0.5}Si_{0.5}$ grown Ge(111) - "Ge2"

For materials to be used in devices, it is important to be able to reproduce the same crystals every growth. Small deviations in crystal quality can leave a device unusable due to causing changes in important characteristics such as electronic and magnetic properties. A second sample of composition $Co_2FeAl_{0.5}Si_{0.5}$ grown on Ge(111) ("Ge2") was subjected to the same XRR and PNR measurements as the Ge sample mentioned previously in order to check the differences between two samples of the same growth recipe. Due to reliable growth methods, Ge2 is expected to be of the same composition, thickness and magnetic moment value as Ge seen in the previous section.

Unfortunately, no microscopy was performed on this sample and fitting is relied on by robust modelling and comparisons to the first Ge sample. The open question is whether reflectivity fitting can be executed robustly enough in order for reliable fits to be obtained without complementary data corroborating certain parameters.

### 6.3.1 X-ray Diffraction and X-ray Reflectivity

An out of plane $\theta - 2\theta$ shows the lack of CFAS peaks in the (hhh) crystallographic direction. From the previous Ge sample, this indicates that the material is similarly in the $B2$ Heusler phase (Figure 6.17). The multiple scattering peak Ge(222) is again observed alongside the expected substrate reflections. Some roughness correlation is seen in the off-specular scan as was seen for the Ge sample.

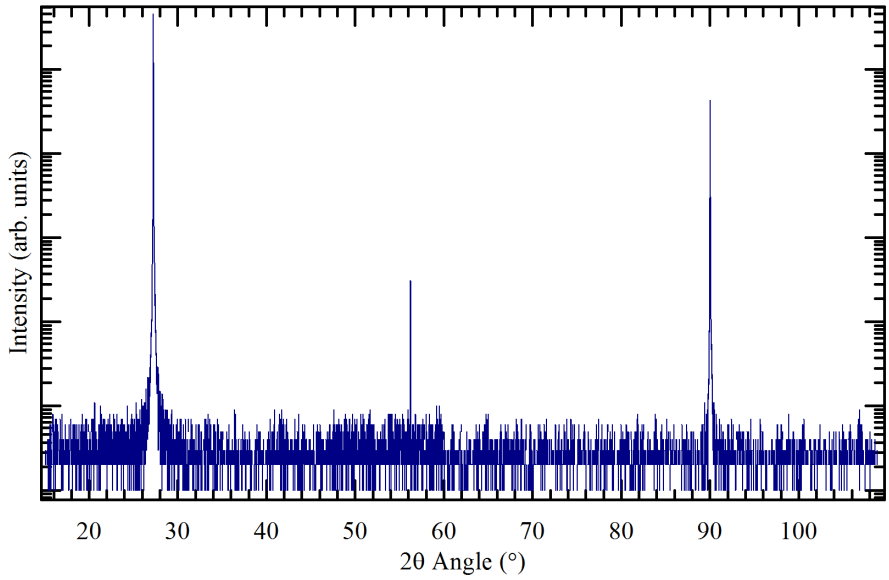


Figure 6.17: $\theta - 2\theta$ out of plane scan of Ge2 aligned to the Ge(111) peak showing no evidence of CFAS reflections.

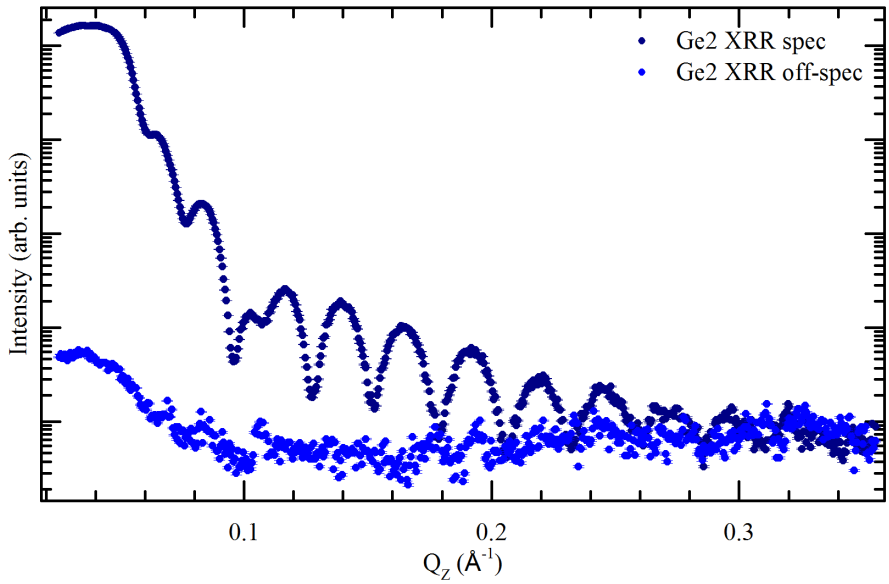


Figure 6.18: XRR specular and offspecular ($\omega$ = -0.1°) scan of Ge2 sample.

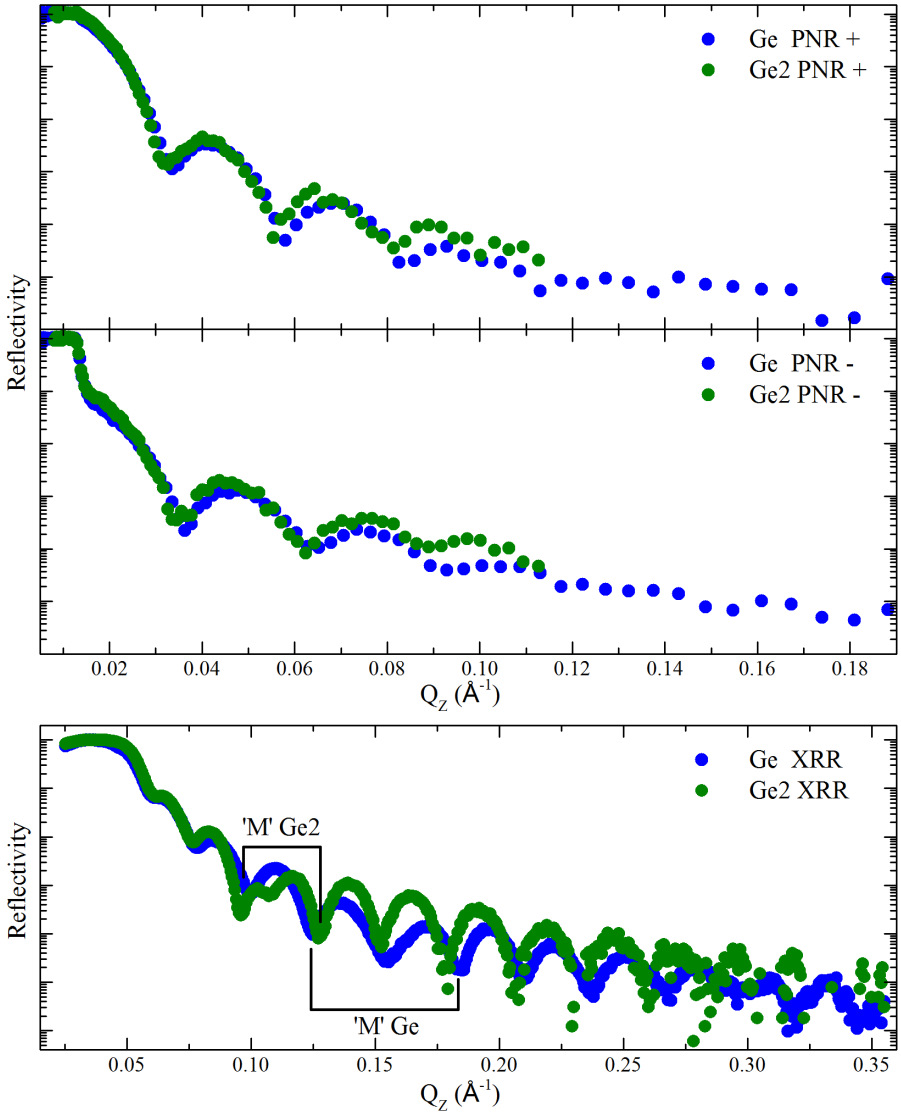


Figure 6.19: A comparison of the reflectivity data from CFAS/Ge(111) and the second Ge(111) best fit models. Brackets highlight ‘M’ feature described in the text.

### 6.3.2 Reflectivity fitting

Comparing sample Ge reflectivity curves with that of Ge2 (Figure 6.19), there is only a small observable difference in the thickness of the PNR fringes. In the XRR the similar ‘M’ feature observed in both Ge and Si samples isn’t there, but instead there is a different feature at $Q \sim 0.1\,\text{Å}^{-1}$ which doesn’t have apparent effect on the fringes at higher $Q$ and gives an indication of a surface feature of layer thickness

$\sim$21 Å. A higher surface roughness is expected than the Ge sample due to the increase in fringe depth at $Q \sim 0.175$. Noisier data at high $Q$ is due to background noise.

The models are set up in the same way as for the previous Ge sample, while composition is allowed to vary, keeping density constant. This seems logical due to the similarities between samples. Models are developed in the same way, where each model adds or moves a layer and a robust minimisation is performed. A comparison of the improvements in FOM is seen in Table 6.5. Models without improvement or validity aren't shown.

Table 6.5: Comparison of FOM values for the different CFAS/Ge(111) 2 models. All values are to the power of $10^{-2}$. The layers column identifies which layers are in the model where I = interface, F = film and S = surface, and the number represents the number of these layers.

| Model | Layers | FOM | FOMN | FOMX |
|---|---|---|---|---|
| 1 | 0I-F-1S | 4.14 | 2.62 | 1.52 |
| 2 | 0I-F-2S | 3.62 | 2.15 | 1.48 |
| 3 | 1I-F-2S | 2.92 | 1.66 | 1.25 |

Model 1 (Figure 6.20) has one additional surface layer with a good fit to the data. The thickness of the main layer agrees with the majority of fringes in both XRR and PNR data. The fit to the PNR data seems good but closer fits are needed to the first fringe in both + and −, suggesting a requirement for surface modification. This is also observed in the XRR where the first fringe isn't deep enough, and the prominent reflectivity feature is not fitted.

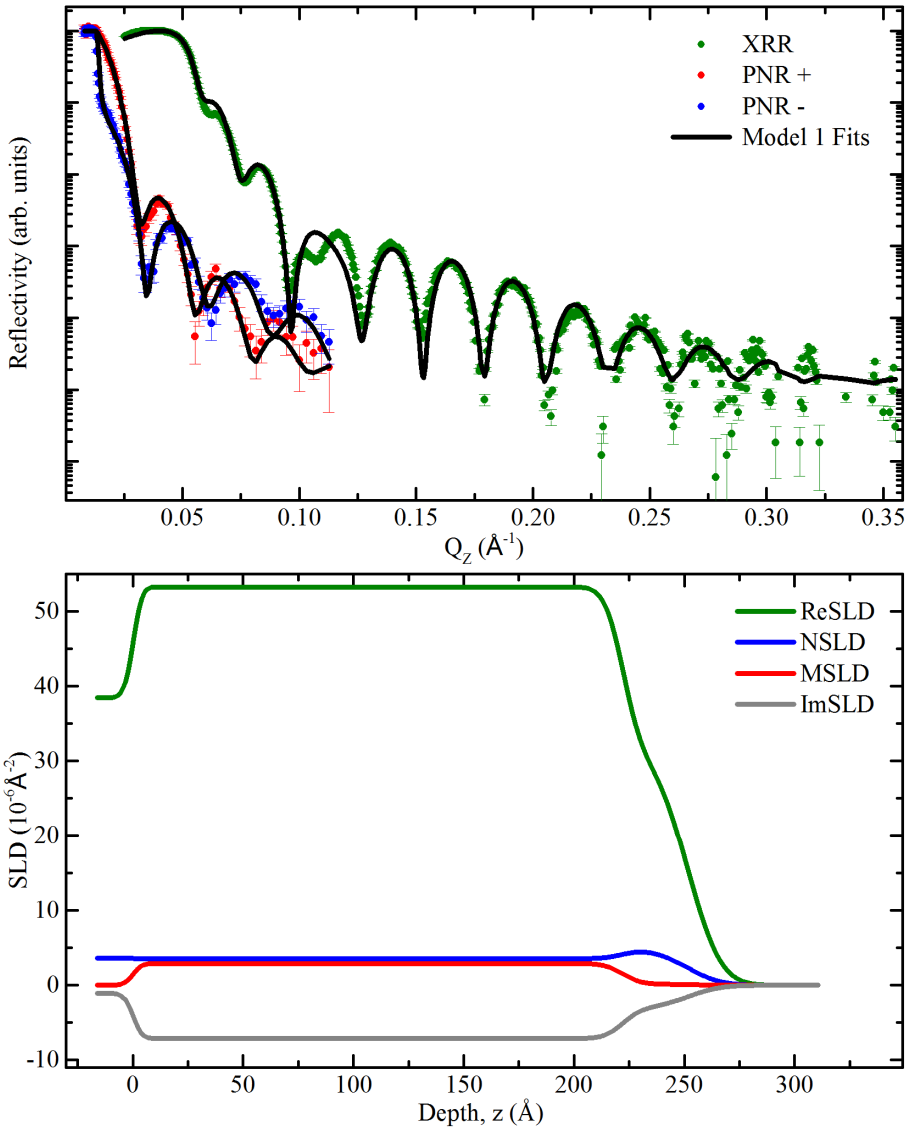


Figure 6.20: Model 1 with substrate, CFAS layer and one surface layer. Fitted simultaneously; custom logR1 = $4.14 \times 10^{-2}$.

Model 2 has the main CFAS layer, plus two surface layers (Figure 6.21). There is an improvement in the FOM for both data sets, where the addition of a second surface layer brings in the feature at $Q \sim 0.1\,\text{Å}^{-1}$. The XRR fringe depths are too exaggerated at low $Q$, suggesting a roughness discrepancy at the surface which should be decreased. The opposite is observed for the fringe depth at higher $Q$.

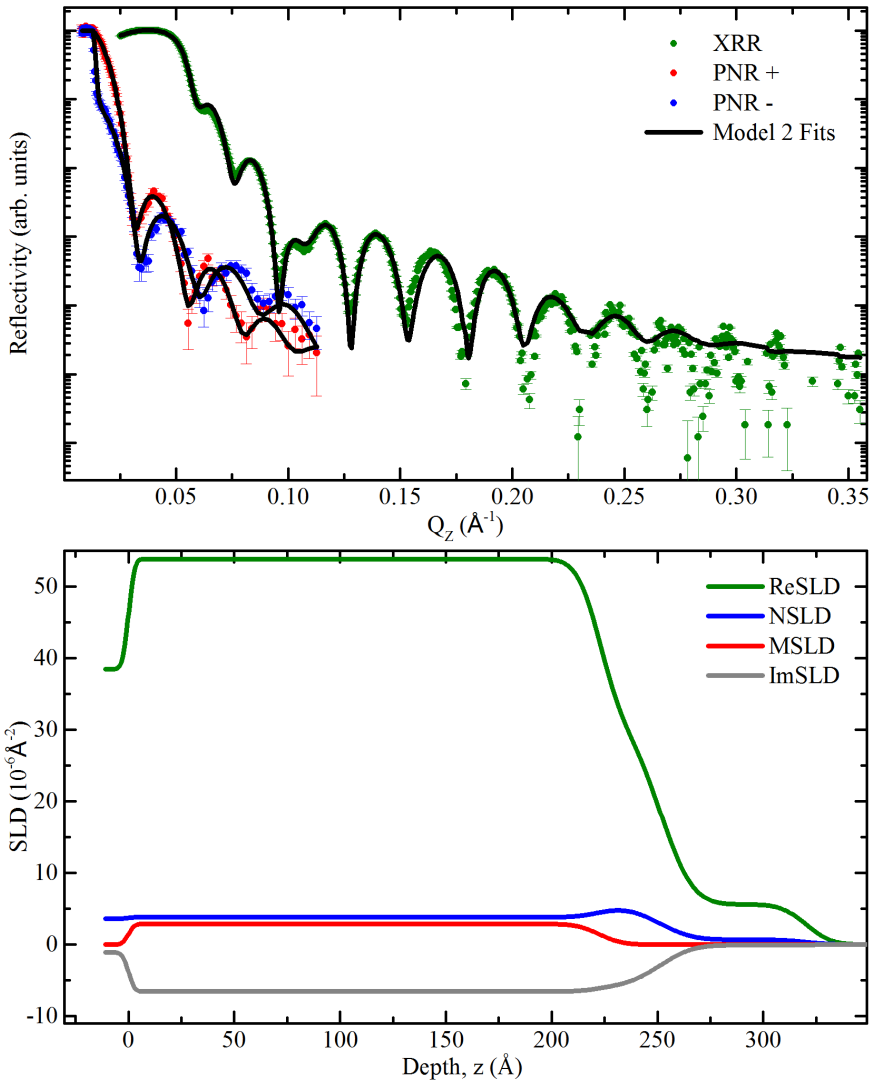


Figure 6.21: Model 2 with substrate, CFAS layer and two surface layers. Fitted simultaneously; custom logR1 $= 3.62 \times 10^{-2}$.

Model 3 (Figure 6.22) adds an interface layer to Model 2. This then refits to have a decrease in SLD through the interface and a drop of magnetism over this region, as in the Ge sample. The first fringe in the XRR is too low, suggesting there

is an error in modelling the surface.

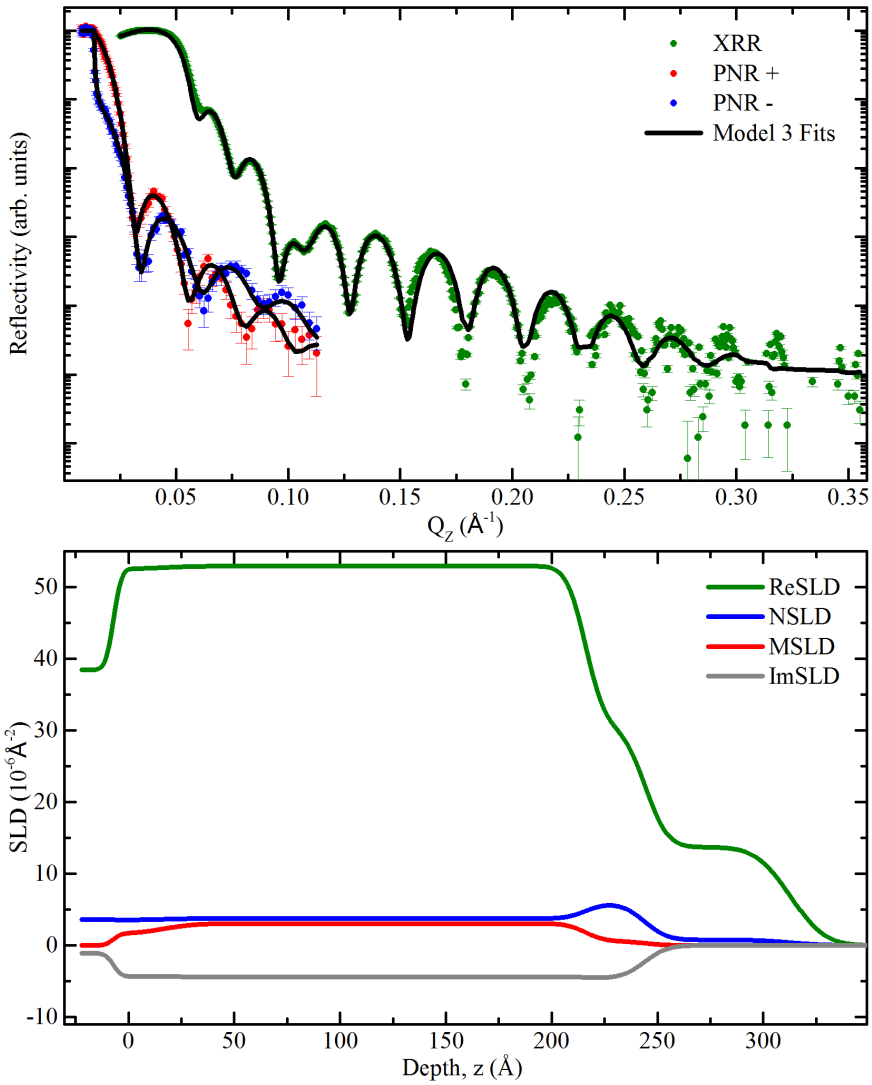


Figure 6.22: Model 3 with substrate, one interface layer, CFAS layer and two surface layers. Fitted simultaneously; custom logR1 = $2.92 \times 10^{-2}$.

Currently Model 3 is the best fit model. It fits with a main CFAS layer of ∼199 Å, the same as Ge, but with a different surface thickness. Using the same technique to extract the magnetic moment as in the previous Ge section, we extract a magnetic moment of 5.5(2) $\mu_B$/f u. A stepped decrease in magnetism is seen again over the interface region. When comparing SLDs for both models (Figure 6.23) it becomes clear that the layer has higher magnetism over the interface, and is observed to penetrate further towards the substrate due to a rougher interface without lowered SLD.

There are features in Model 3 that suggest this is still not the best fit to the data. The critical edge and first fringe of the XRR data is too steep and deep, there is a thickness offset at $Q \sim 0.15\,\text{Å}^{-1}$ and the fringes at high Q seem to be too shallow. It is also very unlikely that the surface should have this large a profile, which in turn, could be the cause of the discrepancy between the two XSLDs. The neutrons are a good fit to the data, where small improvements could be made such as the second PNR+ fringe could be deepened with a change such as an increase in surface roughness. In this case it is important to remember that replicating the delicate feature in X-rays is constraining the neutron fit, and the drop in magnetism at the interface or other features may not be real. Increasing the number of parameters in this model does not improve the fit.

The fringe feature at $Q \sim 0.1\,\text{Å}^{-1}$ is due to a complex combination of surface profile parameters. It is also strongly affected by the SLD value of the interface layer, where changing this parameter mimics a roughness effect by increasing of decreasing the drop-off of the fringes. The surface has to have both the correct barrier heights, gradients of roughness, and thickness of layers in order to fit. Without the large top surface layer, the first fringe in the XRR also doesn't fit. It is surprisingly difficult to find a combination of parameters to fit this feature, where the solutions found are somewhat unrealistic. The neutrons aren't sensitive to the details of these features, and only require the peak in NSLD at the surface and the decrease in magnetism at the interface.

Comparing the SLDs of the best fit models for Ge and Ge2 (Figure 6.23), the fitted features can be related back to the reflectivity data. The PNR profiles have very similar NSLD and MSLD values with slight differences at the interface and surface. The dSLD for Ge2 is higher than in Ge and this can be seen at low $Q$ in the PNR− data as the intensity here is higher. There is a decrease in fringe spacing for Ge2 at higher $Q$ and this is observed in the SLD at the interface where the it is lengthened due to a larger layer. For the XRR data, if the feature at $Q \sim 0.1\,\text{Å}^{-1}$ is represented by the surface layer in the model, then the XSLD also agrees with the data. The fringes are of similar thickness with an offset due to a change in surface profile.

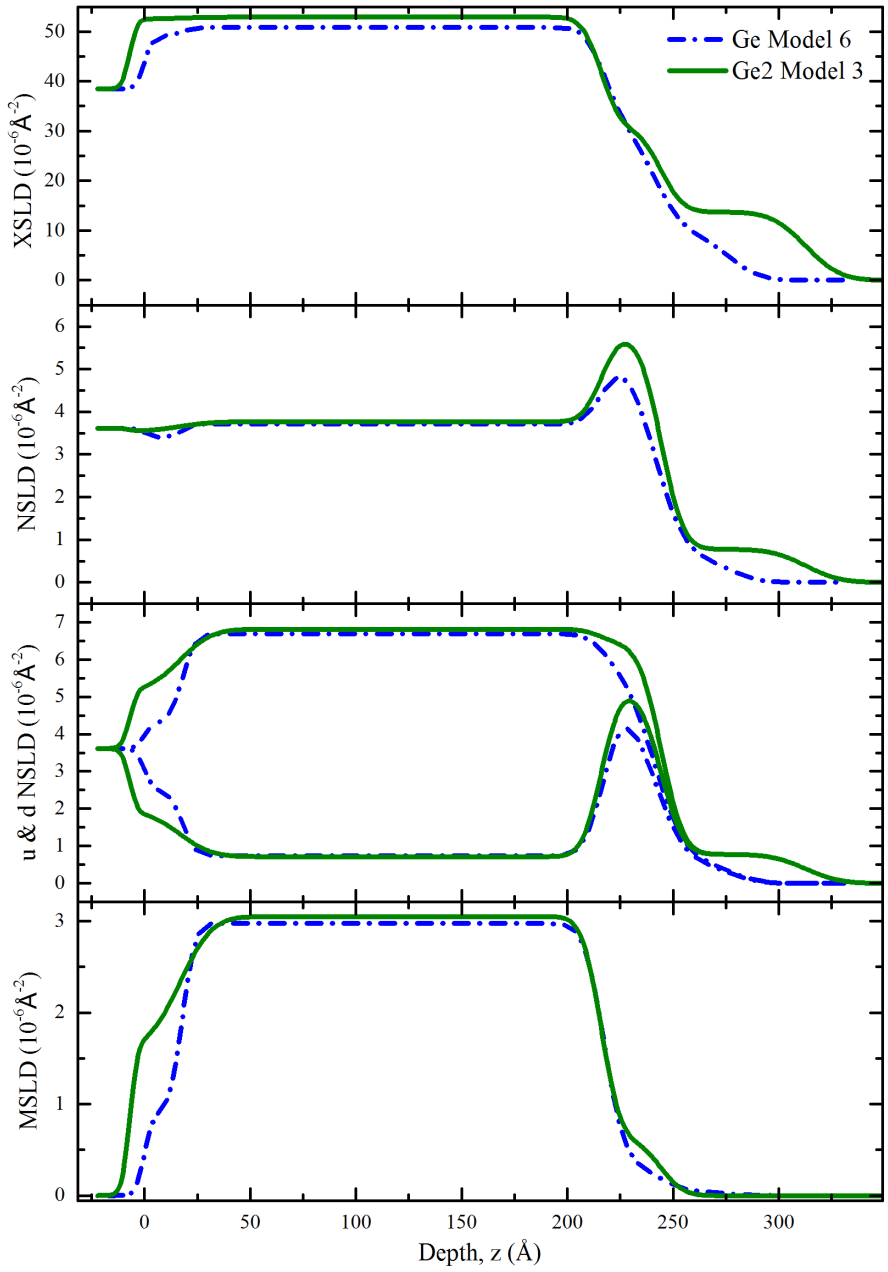


Figure 6.23: A comparison of the SLDs from CFAS/Ge(111) and Ge(111) 2 best fit models. The x-axis (depth) is again somewhat arbitrary, but has been adjusted so that the main films in the XSLD start at the same value. Neutron u & d represents the uSLD = NSLD + MSLD and dSLD = NSLD - MSLD, respectively.

An additional model is shown in Figure 6.24 labelled Model 0, to draw attention to the observation of imaginary part of the X-ray data ($f_{imag}$) if fitting using f and b instead of an atomic composition. This model has a FOM value smaller than that of Model 3, (custom logR1 : $2.89 \times 10^{-2}$) and always fits similarly when allowing $f_{real}$ and $f_{imag}$ to vary independently. Ge2 Model 3 is plotted in black dots to show the difference in SLD. It is interesting to see that the neutron data remains mostly unchanged by modification in the XRR and suggests a continued SLD across the interface, but with a reduction in the magnetism. As Co and Fe have the largest imaginary scattering length for the available elements used, $f_{imag}$ max is $f_{real}/8$, with the assumption the layer is entirely Co. Unless there is an absorption coming from elsewhere in the sample due to contamination etc, this feature isn't realistic and must be limited.

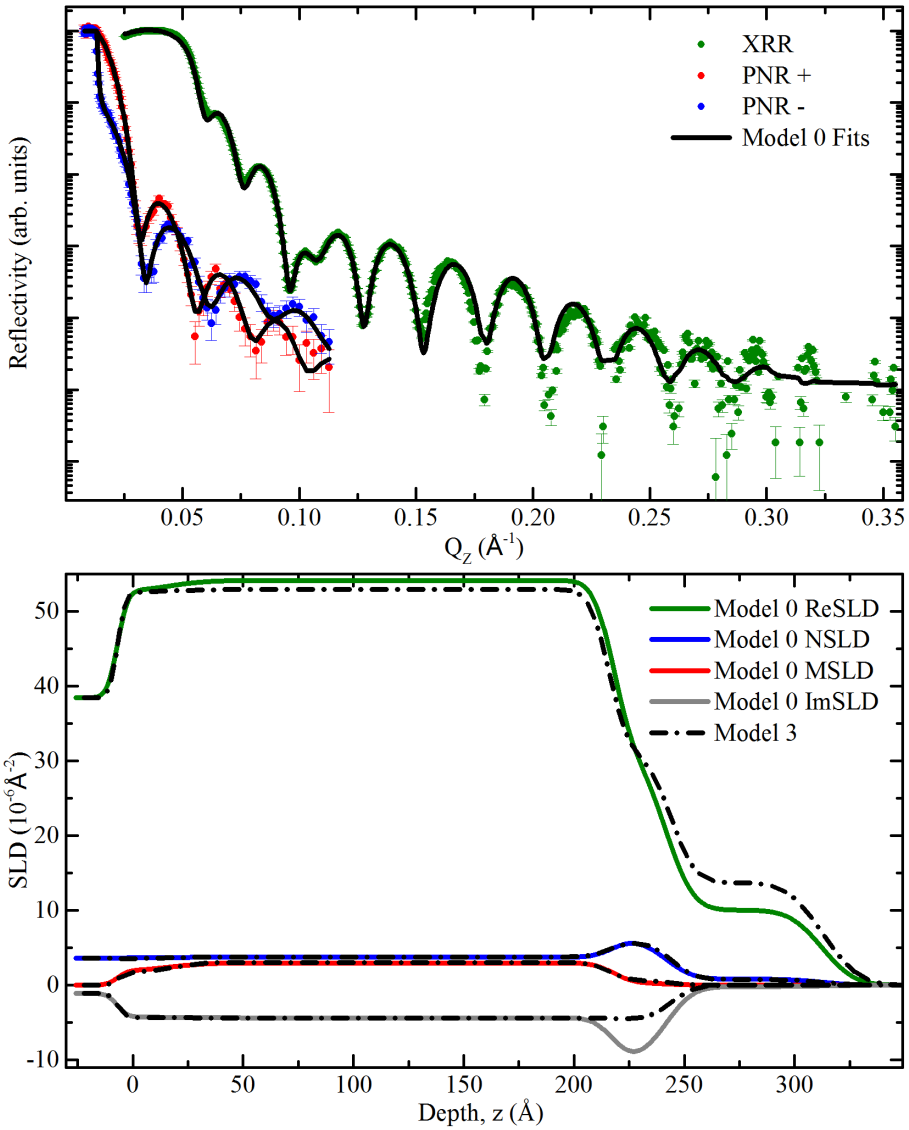


Figure 6.24: Model 0 reflectivity fit and corresponding SLDs. Model 3 is added to the SLD as a dotted black line to highlight the differences in a comparable model. Custom logR1 : $2.89 \times 10^{-2}$.

### 6.3.3 Conclusion

As the history of this Ge2 sample is unknown post growth, it is difficult to have faith in this final model due to observed inaccuracies of the fit to the data. Initial modelling suggests that the growth is good and replicable between samples. Without the large unknown surface feature, the samples would be similar and both have the same thickness and MSLD. The similarities in samples gives confidence in the growth recipe of the material and the ability to be able to reproduce films of the same quality.

There is a possibility that the 'M' feature see in Ge2 (Figure 6.18) is due to sample slipping during the experiment (vertically orientated setup) or there is a misalignment as suggested by an order of magnitude drop in intensity when compared with the Ge sample. If this were true, the surface feature may not exist and the samples could be near identical. The main differences in the current model are in the surface and interface features. If the surface is incorrect, switching of interfacial and surface features (as already demonstrated) may occur and the data sets could be the same. A secondary XRR measurement is needed along with further characterisation experiments. Parameters will then limit the model and confirm the interfacial magnetic profile. From the current fitting parameters, the material is reproducible for each sample, maintaining magnetic moments in the film of $\sim 5.5\,\mu_B$/f.u. with minimal interfacial diffusion roughness due to structural defects.

# Chapter 7

# $Fe_3O_4$ grown on MgO(111)

## 7.1 Introduction

$Fe_3O_4$, also known as magnetite, is a naturally occurring ferromagnetic material which is a predicted half metal as shown by DOS as calculated by Zhang and Satpathy [86], and has a high Curie temperature $T_C \sim 858\,\mathrm{K}$ [87]. Although the material has been rigorously studied, its properties such as crystal and electronic structure, transport and magnetic properties and phase transformations are not fully understood. Magnetite has a complex $FCC$ cubic spinel crystal structure at room temperature, better described by Fong et al [2] and Gilks [88], with a primitive cell lattice constant of 8.396 Å where Figure 7.1 shows the fully occupied O sublattice and two Fe sublattices. Two different valences exist for $Fe_3O_4$ and are situated in different places in the crystal structure where $Fe^{2+}$ are represented on the Figure by the yellow spheres, $Fe^{3+}$ are represented by red spheres and O atoms are blue. The $Fe^{2+}$ are on tetrahedral sites (A) and $Fe^{3+}$ are at the octahedral (B) sites.

Experimentally, 100 % SP has not yet been realised and there are varied reported values ranging from40 % [89] and 80 % SP [90], for this reason, amongst other results they observed, Tobin et al [91] argue that $Fe_3O_4$ is not half-metallic. Theoretically the magnetic moment for $Fe_3O_4$ is $4\,\mu_B$/f.u. [16, 86, 90] due to contributions from $Fe_A$ site having $5\,\mu_B$/f.u. and $Fe_B$ site contributing both $-5\,\mu_B$/f.u. and $4\,\mu_B$/f.u.. Experimentally, magnetic moments in $Fe_3O_4$ materials have been reported as $3.68\,\mu_B$/f.u. [92], $4\,\mu_B$/f.u. [16] and $3.32\,\mu_B$/f.u. [93]. Again these measurements are not consistent and it is well known that bulk properties can be very different from surface and interface properties [94].

The material is complicated further due to a transition at the Verwey temperature, $T_V \sim 120\,\mathrm{K}$ [95]. Below this transition there is a decrease in conductivity

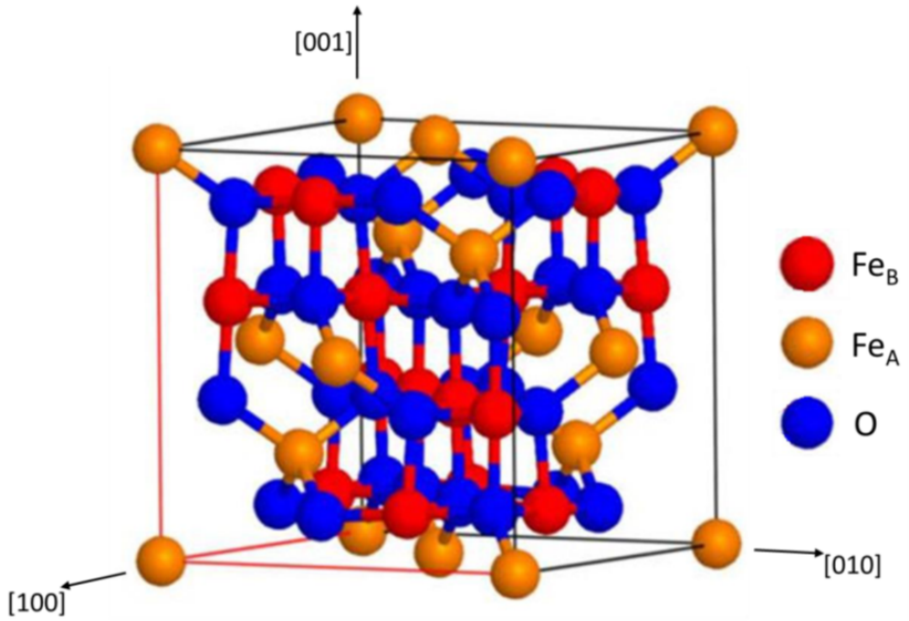


Figure 7.1: Cubic unit cell of $Fe_3O_4$ composed of 56 atoms representing 8 $Fe_3O_4$ chemical units. $Fe_B$ is represented by red spheres, $Fe_A$ by yellow and O by blue [88]

due to disorder in the $Fe^{3+}$ on the (B) sublattice which distorts the crystal, making it monoclinic [2]. This material feature will be discussed further in Section 7.3.

Growth of $Fe_3O_4$ is particularly difficult due to defects such as antiphase domain boundaries (APBs) as a result of growth nucleation sites between film and substrate [96, 97]. In previous works [88, 98, 99] it was found that post-annealing $Fe_3O_4$ films in a $CO/CO_2$ gas mixture, achieved stable crystal structures in accordance to the equilibrium phase diagram [100] with control over stoichiometry and structural defects in the thin films. Previous work [101] has also demonstrated switching in magneto-resistance (MR) from positive to negative over $T_V$, showing bulk-like $Fe_3O_4$ properties and therefore demonstrating good quality films. Understanding and perfecting the growth of half-metallic materials is very important if they are to be used in devices for spintronic applications.

Furthering the study of $Fe_3O_4$, it is grown in thin film form on MgO, as it has been proven to be a successful tunnel barrier material [102] and has a good mismatch (half the $Fe_3O_4$ unit cell) to $Fe_3O_4$. Previous work has shown that the MgO(111) polar oxide surface reduces faceting and interfacial mixing with the $Fe_3O_4$(111) polar film and creates abrupt interfaces in comparison to classic electrostatic models that require atomic mixing at polar interfaces [103]. Three samples are grown with different post-annealing temperatures where the structural and magnetic properties

are characterised using microscopy (TEM), XRD, magnetometry and PNR.

Figure 7.2 is a visual representation of SLs for the different elements in the material composition with respects to neutron and X-ray sensitivity. Specific material parameters are shown in Table 7.1.

Further study of the material is shown in Section 7.3, where the Verwey transition of the $Fe_3O_4$ is exploited by temperature dependent PNR in order to observe the effect the different growth methods have on the layer averaged atomic and magnetic properties at lower temperatures.

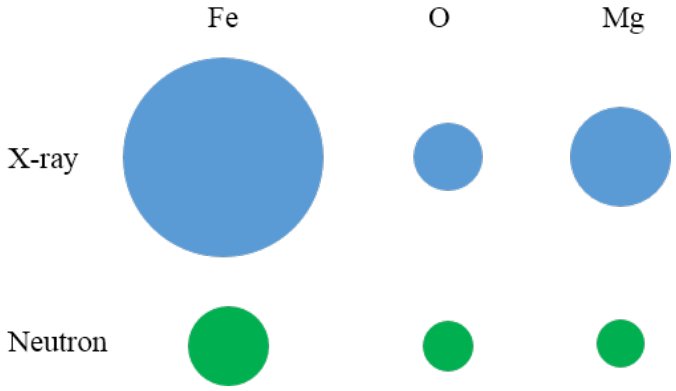


Figure 7.2: Visual representation of the difference in SL magnitude of X-rays and neutrons from elements in the chapter: Fe, O and Mg.

Table 7.1: Nominal properties and parameters of materials used in the chapter for comparative purposes. Mismatch relate to the same orientation of substrate and film.

| Parameter | Value |
|---|---|
| Lattice constant - MgO (Å) | 4.21 |
| Lattice constant - $Fe_3O_4$ (Å) | 8.39 |
| Mismatch (%) | 0.99 |
| XSL - MgO (e-/atom) | 30.91471 - 0.88018018j |
| NSL - MgO (fm/atom) | 8.19 |
| XSL - $Fe_3O_4$ (e-/atom) | 106.78 - 9.76j |
| NSL - $Fe_3O_4$ (fm/atom) | 51.562 |
| $N$ - MgO ($Å^{-3}$) | 0.0535 |
| $N$ - $Fe_3O_4$ ($Å^{-3}$) | 0.0135 |

## 7.2 MgO Structural Study

### Sample information

Detailed sample growth information can be found in the thesis of D. Gilks [88]. Briefly, nominally 80 nm $Fe_3O_4$ thin films have been grown on $10\times10\,mm^2$ MgO(111) substrates using molecular beam epitaxy (MBE) in ultra high vacuum (UHV) by use of simultaneous deposition of Fe and O onto the MgO substrate held at 300 °C in an O partial pressure of $5 \times 10^{-6}$ mbar. Post-annealing of the samples was performed at 950 °C, 400 °C and 350 °C in a $CO/CO_2$ atmosphere. The annealing temperatures give the samples their naming suffixes. Unfortunately, specific substrate surface preparation data is unknown for these samples.

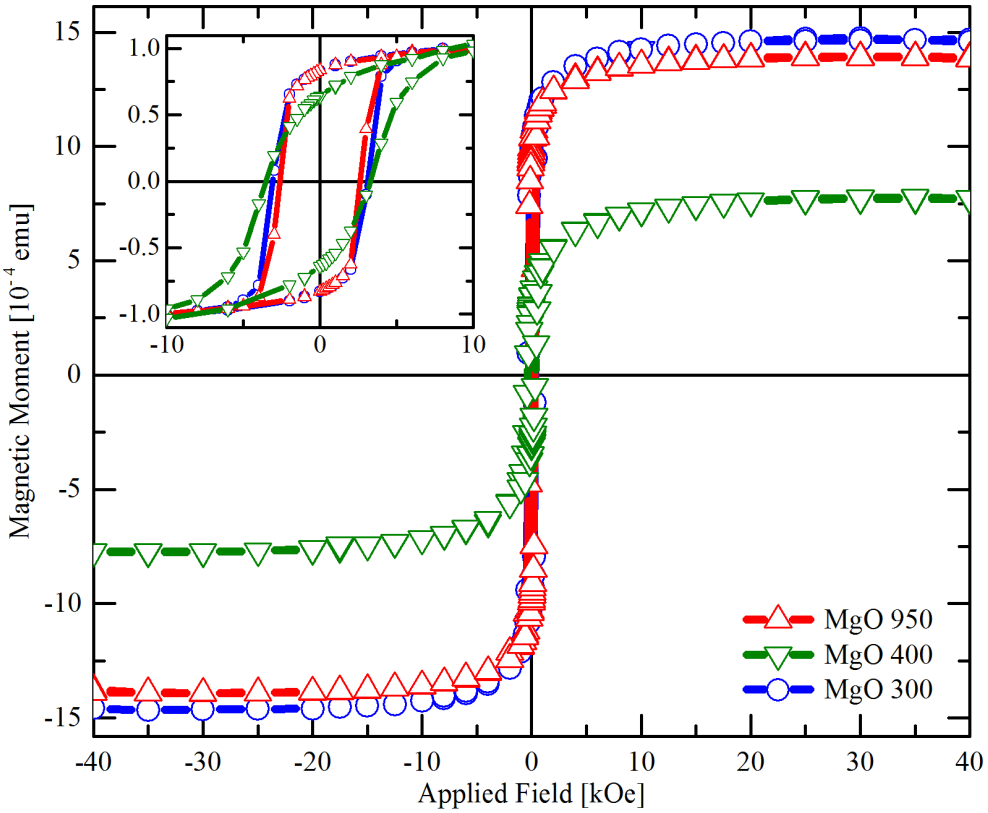


Figure 7.3: SQUID measurements of average magnetic moment for all MgO samples at room temperature. The inset is the moment normalised for all the samples in order to directly compare the shape of the hysterisis loop. Differences in saturation magnetisation and coercivity between samples are clear.

### Magnetometry

Magnetometry (SQUID data in Figure 7.3) gives a basic comparison between the samples. Samples were cut from nominal $10\times10\,\mathrm{mm}^2$ before the measurements were taken, creating volume discrepancies between samples. Diamagnetic background was removed from the raw data by fitting a straight line to the data at both high and low fields, averaging this value and removing the gradient from the data set. The main section of the Figure suggests that MgO 300 and 950 are very similar samples, with slight differences in thickness or magnetism. MgO 400 is either much thinner, or has a substantial decrease in magnetism with respects to the other films. Focussing on the inset, where values have been scaled to match each other, the shape of the hysteresis loop can be observed. MgO 300 and 950 are again very similar where the shape is very square, suggesting ease of magnetisation flipping when an external field is applied. MgO 400 has a less square loop, suggesting a film that has more growth defects causing pinning of magnetic domains. The origin of the defects are unknown from the analysis of this technique due to SQUID data being the induced magnetisation from the entire sample, and its purely magnetic nature. Possible causes of the pinning include interfacial or surface diffusion, roughnesses at interfaces (including the surface), strains from epitaxial growth on the substrate, grain boundaries and crystal mosaics. The only known differences between the samples is the post-annealing temperature. MgO 400 is considerably different, therefore some error must have occurred during sample preparation.

### Reflectivity

As previously with magnetometry, reflectivity data is a simple way of comparing basic differences between films. Table 7.2 gives a comparison of sample thicknesses taken from the experimental data in this chapter, and will be referred to where appropriate. Figure 7.4 shows the XRR of the samples where differences in fringe spacing related to sample thickness, and drop off in intensity showing different surface roughnesses, are clearly seen. The inset shows that each sample has the same critical edge $Q_c$ representing the same film composition. After $Q_c$ the drop off are different for each sample showing the difference in surface roughnesses for each sample. MgO 400 appears to have a larger surface roughness than the other samples, seen as a slightly faster drop off in intensity, and larger spaced fringes suggesting a smaller film. A smaller film thickness would have a large contribution to the decreased saturation magnetisation seen earlier. The high-$Q$ fringes of MgO 300 are more shallow than the other two samples suggesting a larger substrate or interface

roughness.

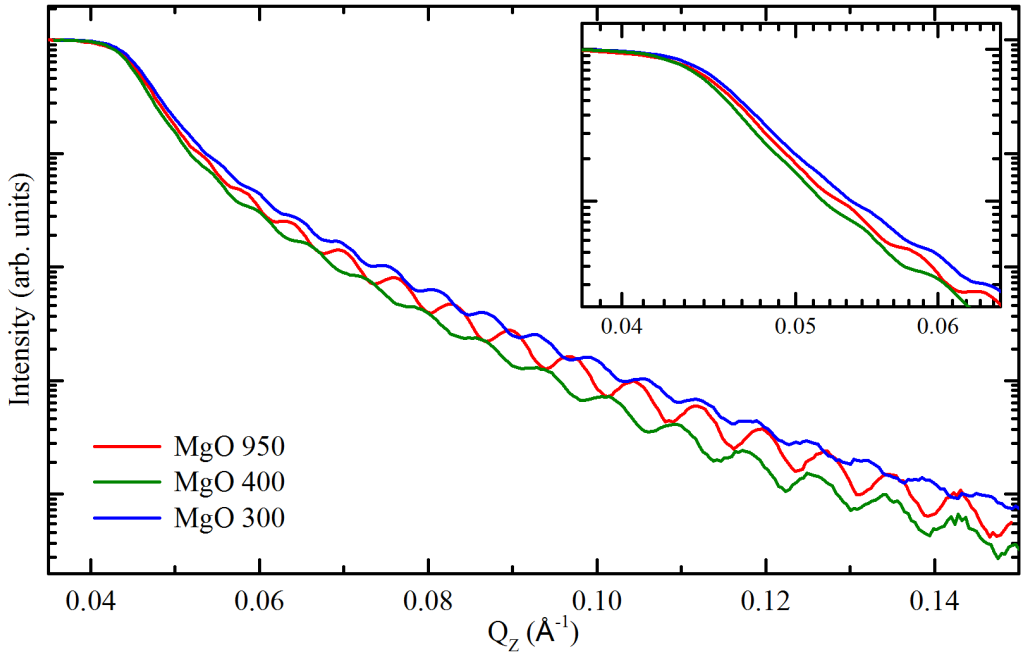


Figure 7.4: Comparison of XRR for all MgO samples. Inset focuses on the critical edge.

PNR measurements were taken on the D17 reflectometer in time of flight (TOF) mode at the Institut Laue-Langevin in Grenoble, France. A superconducting cryomagnet provided a 2 T external magnetic field to ensure sample saturation along with the ability to change sample temperature to specific values around $T_V$ (as discussed in Section 7.3). Noise in the data at $Q \sim 0.028\,\text{Å}^{-1}$ is due to stitching of the data when changing angle and slit sizes in TOF mode.

Figure 7.5 shows the PNR of all MgO samples, where the higher fringes represent PNR+ and the lower represent PNR− for each data set. Sample data is split for clarity with 300 and 950 in the top panel and 400 in the bottom. The inset again highlights the critical edge via log scaling in both axes and smaller viewing area. Fringe characteristics in the PNR are in agreement with the XRR (Figure 7.4). MgO 300 and 950 are very similar samples with differences in thickness and roughness, where thickness variances could account for small discrepancy in the SQUID saturation magnetism (Figure 7.3). In contrast, PNR confirms that MgO 400 has a different film thickness, roughness and suggests a lower magnetism as seen by the smaller splitting after the critical edge. This magnetic information coincides with the details from the magnetometry, where the decreasing magnetism due to

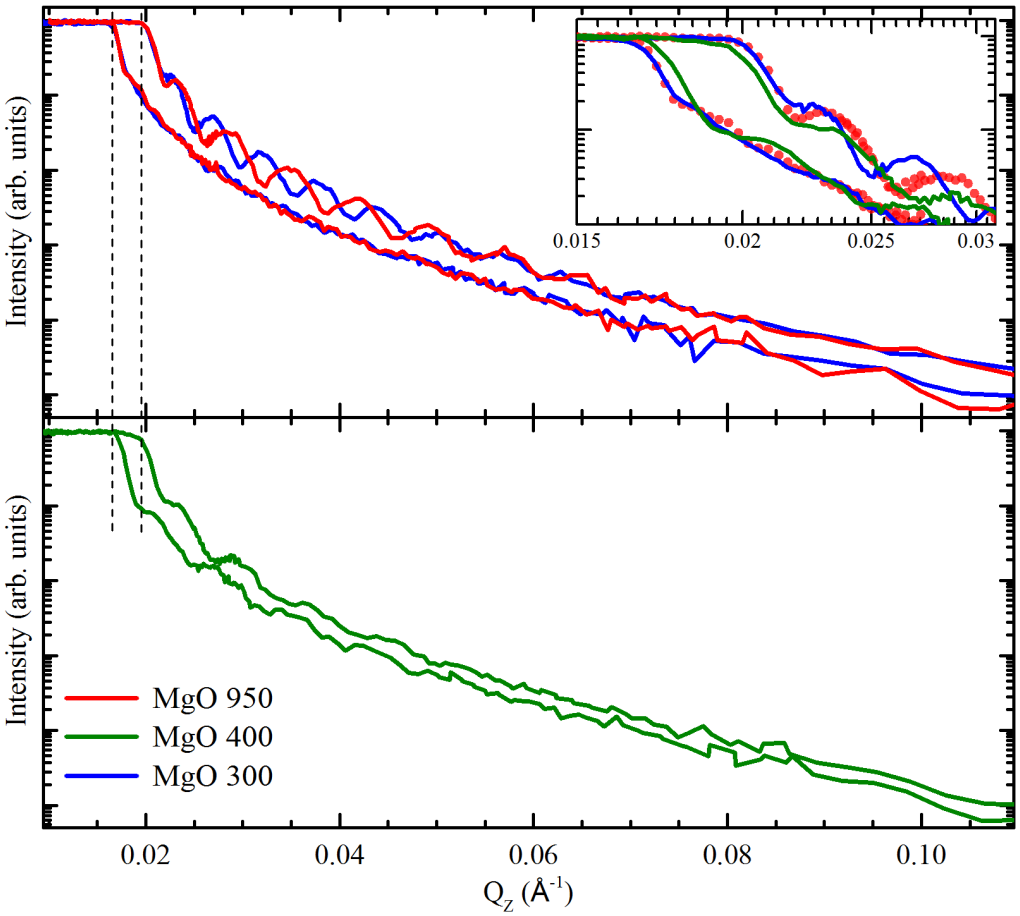


Figure 7.5: Room temperature PNR data for all MgO samples where the top panel shows MgO 300 and 950 and the bottom shows MgO 400, split for clarity and comparison purposes with the same graph scales. The inset shows a magnified low-$Q$ region, including the critical edge. Changes in the film composition/density and magnetism is observed, as well as differences in the magnetic profile throughout the films. Vertical dotted lines are a guide for the eye to compare the position of the critical edges.

roughness or diffusion could be the reason for a less square hysteresis loop and lowered saturation magnetisation.

Samples will now be considered individually to try and tease out the differences between sample growths. A comparison and summary will be made at the end of the chapter. All models are built using the method in Chapter 4 and minimised fully using a combination of applicable FOM.

Table 7.2: Comparison of film thicknesses obtained using different techniques as indicated in the table. Grain size found by XRD is for $Fe_3O_4(400)$ peaks in all cases. All values are in Å.

| Sample | TEM | XRD | XRR | Fitted Reflectivity |
|---|---|---|---|---|
| MgO 300 | - | 450 | 963 | 932 |
| MgO 400 | 720 | 234 | 768 | 771 |
| MgO 950 | 800 | 234 | 831 | 820 |

### 7.2.1 MgO 950

From the above experiments and previously published work [88, 98, 99] where the post-annealing temperature was 1100 °C, the expectation is that MgO 950 will be the best quality film of the growth study. The complementary techniques will be ordered from larger scale analysis of the sample down to small scale, starting with reflectivity and ending in microscopy.

#### MgO 950 XRR

XRR measurements (Figure 7.6) show correlated roughness between substrate and film by the observation of fringes in the off-axis scan where $\Delta\omega = -0.1$. Correlated roughness demonstrates a structural style roughness in the sample, as compositional diffusion remains specular. Structural roughness in this case, due to the high annealing temperature, is likely to do with mosaic features from the substrate propagating through to the surface of the film. Mosaic features can be determined by XRD measurements as the high incident angle and small wavelength probes the crystal on atomic length scales. Here the beam footprint is small but still averages over mm of sample. An averaged film thickness can be calculated from Figure 7.6 using Equation 3.35 of 831 Å.

For later fitting of the XRR data it is important to subtract the off-axis measurement from the background of the specular (on-axis) reflectivity measurement. This removes the background to the specular measurement which is needed in order to fit the data, as fitting packages cannot account for the addition of diffuse scattering.

#### MgO 950 XRD

To begin to understand the crystallographic origins in the variations between the samples it is important to understand the out of plane film crystal orientation with respects to the film. As one of the more simple scans, it gives insight into the strain

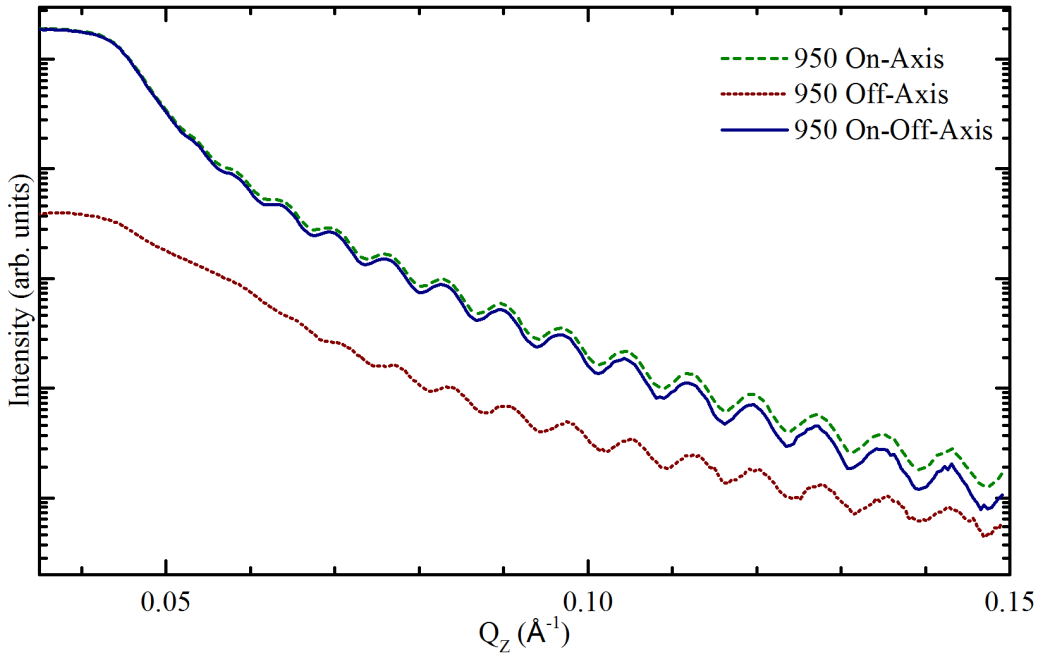


Figure 7.6: On-axis and off-axis XRR measurements for the 950 sample where the On-Off axis data represents the specular only contribution. Correlated roughness is observed from the Off/diffuse scattering measurement of $\Delta\omega = -0.1$.

on the sample from mismatch. XRD $\theta - 2\theta$ scans (Figure 7.7) reveal that the film out of plane orientation is in the (100) direction with the presence of (400) and (800) crystallographic peaks, in agreement with $FCC$ structure factor rules. No (111) family reflections are observed out of plane, when a $\chi - \phi$ scan is performed at the (111) $2\theta$ position, aligned to the $Fe_3O_4$(400) peak to check for tilted crystal structures suggesting there is only one orientation of crystal in the out of plane direction. The expected epitaxial relationship is MgO(111)$\|$$Fe_3O_4$(111) due to lattice matching of 99% (1.7%) for the same orientations. This MgO(111)$\|$$Fe_3O_4$(100) relationship has a mismatch of 40% and must not be a simple epitaxial relationship where stoichiometry may be the cause.

Fitting the film peaks in Figure 7.7, reveals an average lattice constant of 8.43 Å which is higher than the nominal $Fe_3O_4$ lattice constant of 8.39 Å, suggesting a change in nominal stoichiometry or residual strain. The Scherrer equation can be used in order to calculate the grain sizes of the corresponding crystal orientations within the sample [27]

$$t = \frac{0.9\lambda}{B\cos\theta_B} \tag{7.1}$$

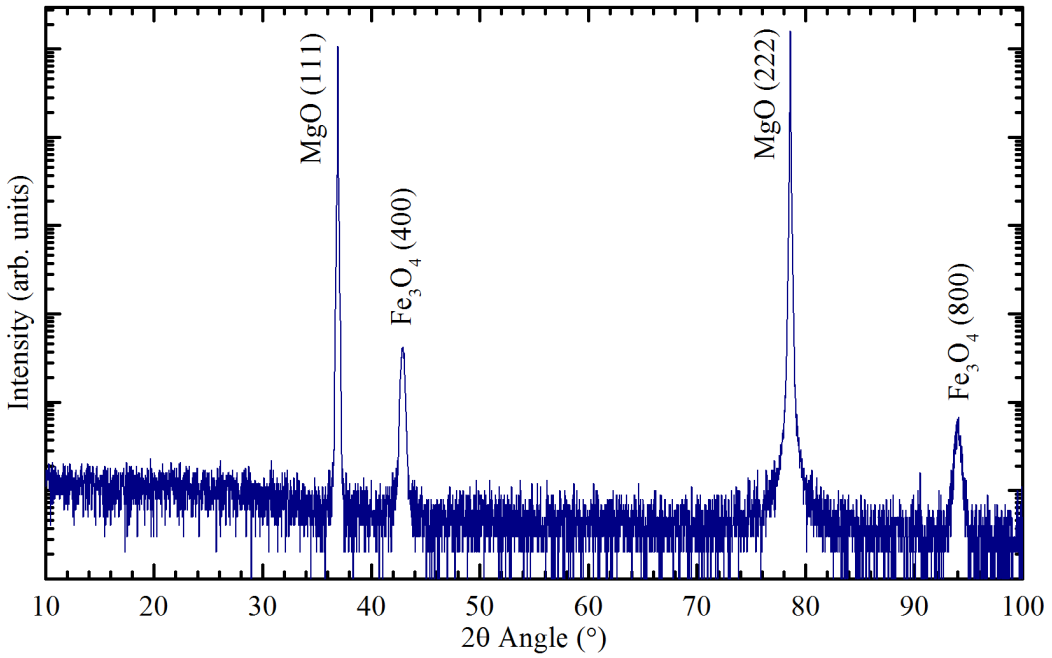


Figure 7.7: Out of plane $\theta - 2\theta$ scan of MgO 950 aligned to the MgO(111) substrate showing only $Fe_3O_4$(400) and (800) film peaks.

where $t$ is the grain size, $B$ is $\Delta 2\theta$ the FWHM in radians and $\theta_B$ is the peak position $2\theta/2$ in radians. If the crystal structure extends throughout the z direction in the film, then $t$ should be on the order of the film thickness. By fitting the out of plane ($Q_z$) $2\theta$ film peaks, it is possible to interpret the grain sizes of the corresponding crystallographic orientations within the sample. For MgO 950 a thickness of 234 Å is calculated, much lower than the XRR fringe thickness of 831 Å.

Rocking curves ($\omega$ rocks) about a peak give information about the tilting of a crystal into slightly different directions away from the surface plane. Mosaics cause peaks to be at diffraction angles where $\omega \neq 2\theta/2$. In the rocking curve this would be observed as multiple peaks if the resolution of the instrument is lower than that of the width of the peak as shown in Figure 7.8.

To retrieve a better understanding of the mosaics, a $\chi - \phi$ scan can be performed (known as a texture map/pole figure/mesh), where the sample is tilted in both directions and the incident beam and detector remain stationary at a set $2\theta$ peak diffraction condition. Figure 7.9 shows the mesh aligned to the substrate out of plane MgO(111) peak. It shows intensity in multiple different directions, creating mosaics in the film and at the surface. The mosaic surface may be the cause of the $Fe_3O_4$(400) family of reflections where the (111) was originally expected.

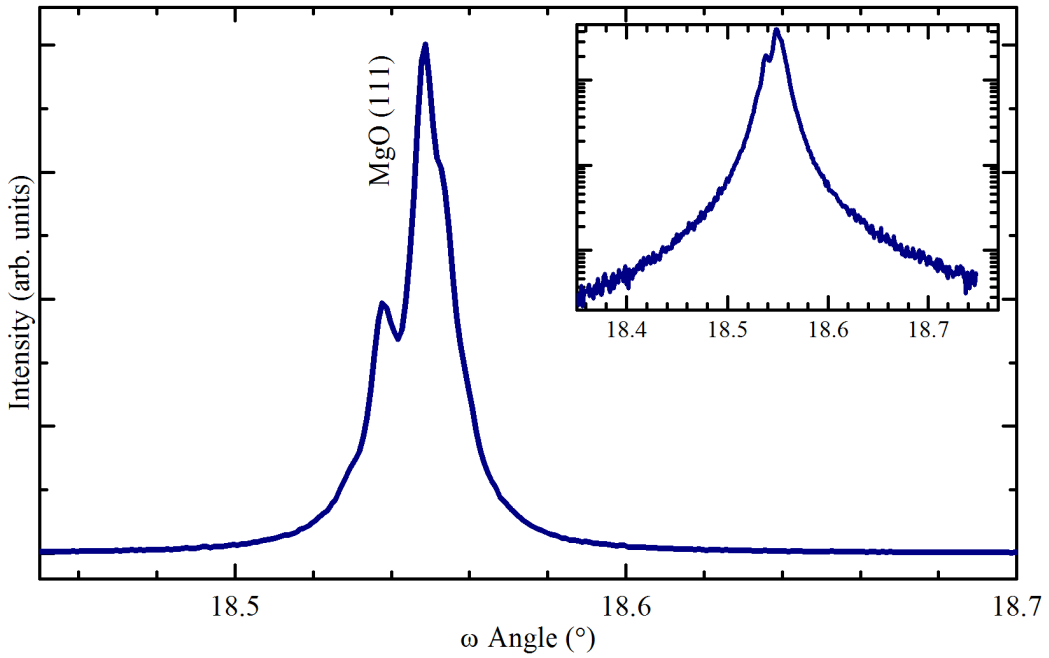


Figure 7.8: MgO 950 $\omega$-rock about aligned MgO(111) out of plane substrate peak. Inset shows broadness of peak on a y-axis log scale.

Observing the film peak at the same alignment as the substrate peak, now gives the correlation of the crystal orientation with respects to the substrate it is grown on. Figure 7.10 shows that the film grows in a single domain at an orientation between $\Delta\phi = 90°$ and 150° away from the substrate, also with an offset in $\chi$ between 4° and 6°. The high annealing temperature and the ability for the atoms to move more freely suggests that this epitaxial relationship is the most relaxed. The film peak is very broad when compared to the substrate peak and could be caused by the $Fe_3O_4$ needing to fill the gaps between the mosaic regions creating crystal orientations facing in different ways.

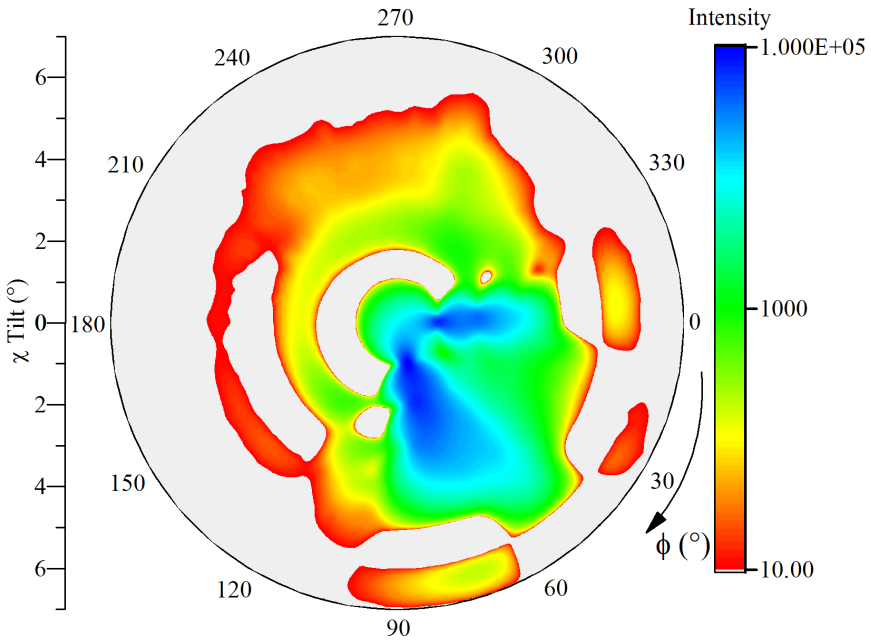


Figure 7.9: MgO 950 $\chi - \phi$ mesh aligned to MgO(111) peak. The substrate peaks are seen to be rotated 60° in phi with respects to each other and are very broad in chi, suggesting mosaics.

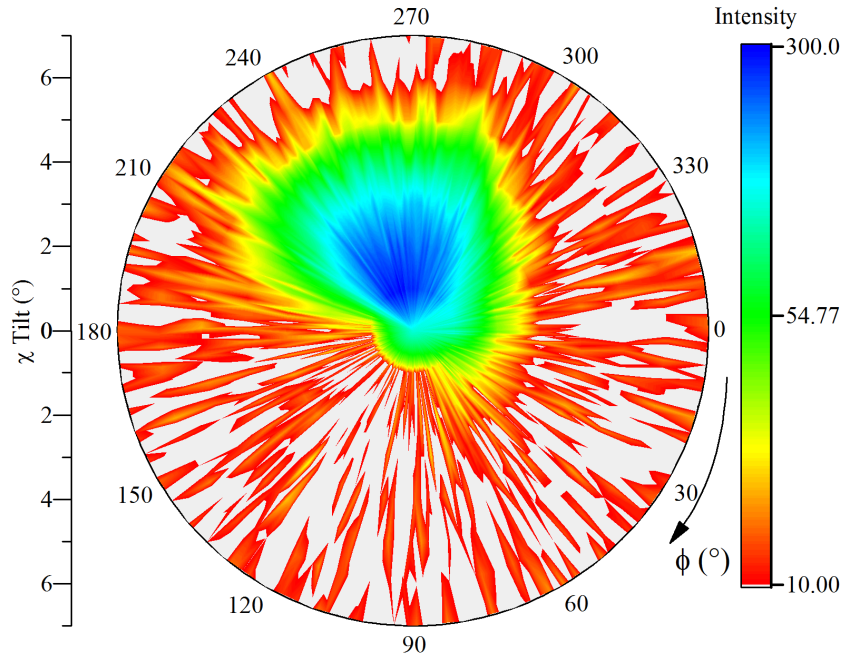


Figure 7.10: MgO 950 $\chi - \phi$ mesh about $Fe_3O_4(400)$, aligned to MgO(111) peak.

### MgO 950 Microscopy

TEM images (Figure 7.11), show a crystalline film with some defects (seen by changes in contrast and 'line' type features). Firstly the substrate quality is low with many defects over the order of 100 nm, which will also propagate through to the film. It has already been shown that roughness from the substrate is correlated to the surface in XRR measurements. Changes in film crystal structure can be seen in the 2 nm image at domain/grain boundaries (highlighted by vertical lines), agreeing with the findings from the XRD. The annealing helps recrystallisation and recovery of stoichiometry after growth where the strain is quite small. There are some sections of film that are very well ordered irrespective of the MgO quality underneath. This could be due to the high annealing temperature allowing the crystal to reorder itself and recover after strain at the interface. Additional information obtained shows a total film thickness of ∼800 Å and an interface thickness of ∼20 Å.

As in previous chapters, these values are to be taken with caution due to the size of the sample used in comparison to the area that PNR averages over. The images are yet to be analysed fully, which limits the information available for use in the model, and unlike previous chapters, there is no EELS data across the interface to guide the structural profile.

### MgO 950 Room Temperature Reflectivity

Combining all results found from the data mentioned previously, allows the reflectivity model to be built by creating a standard slab model (Chapter 3) where the choice to vary composition and fix density to the nominal $Fe_3O_4$ value is made. The XRR data (Figure 7.6) showing diffuse scattering from structural roughness propagating through to the surface, is a clear indication of the need for both an additional interfacial and surface layer, which is also confirmed by the TEM data. Note that structural roughness and diffusion are modelled in reflectivity packages as the same Gaussian distribution function. Care will need to be taken with respects to the placement of layers within the model, as similar features in SLD corresponding to certain potential barrier heights, can be shifted from interface to surface as seen in Chapter 5.

Simultaneous fits to both XRR and PNR data, along with the corresponding SLD are shown in Figure 7.12. Three additional layers were needed to obtain this fit, two surface and one interfacial layer in addition to the film. The structural SLDs show a continuous thin film with variations from this at the surface and interface layer. The main film has a thickness of 680 Å with an interface of 50.5 Å

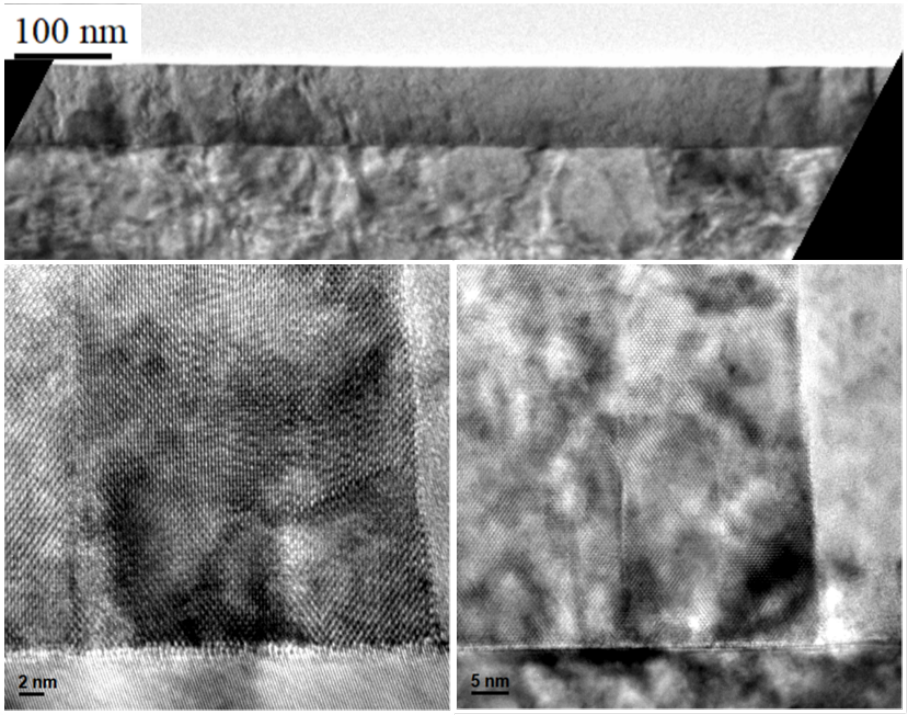


Figure 7.11: TEM images of MgO 950 at three different magnifications: 100 nm, 5 nm and 2 nm. The image direction is looking along the substrate $(1\bar{1}0)$ zone axis perpendicular to the substrate surface. The substrate is at the bottom in all images, and the $Fe_3O_4$ film above this.

and a total surface thickness of 88 Å (55 Å and 33 Å). As in other chapters, a small increase in the NSLD near the surface is observed, which could be a region of increased Fe due to the post-annealing of the film in a $CO/CO_2$ gas mix, where CO could strip O atoms from the top layer of the film in order to become $CO_2$. Without further complementary techniques, such as EELS, or X-ray photoelectron spectroscopy which are all element and surface sensitive, this cannot be confirmed. Taking the averaged magnetic moment in the layer from GenX, and manipulating the magnetism value in order to find the ratio between the nominal SL and the fitted film, we obtain 3.4(2) $\mu_B$/f.u..

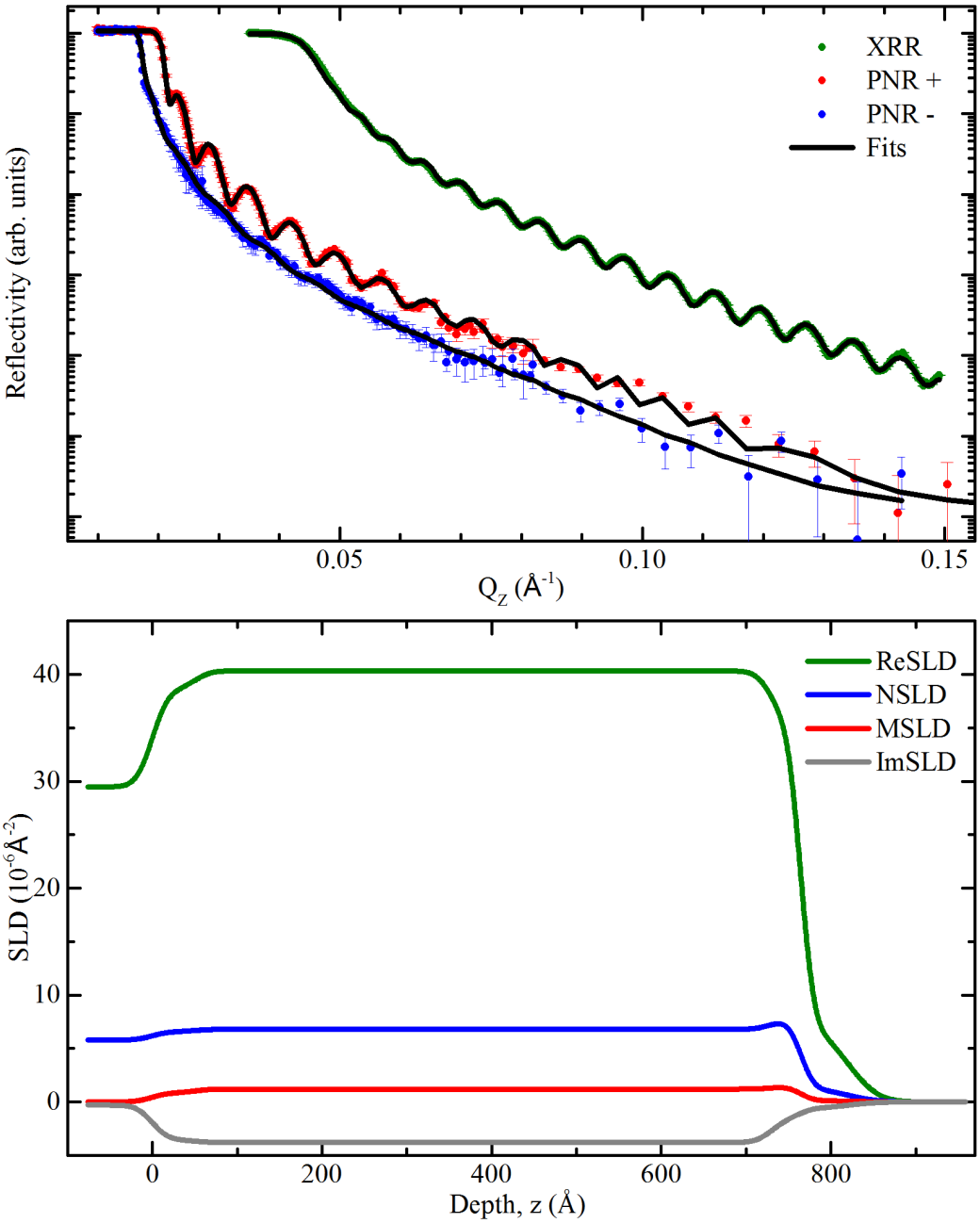


Figure 7.12: MgO 950 fitted reflectivity curves and the corresponding SLDs showing uniform film composition throughout most of the sample with interfacial and surface regions.

### 7.2.2 MgO 400

Before any more experimental data is analysed for MgO 400, it is already apparent that there has been an issue with sample growth as there should only be slight variation between MgO 300 and 400, and this is not the case. This could be due to an error during the growth, influence of treatment post growth, or a defective substrate. This section will try to analyse the possible cause. The same logical ordering of the previous section will be followed for the MgO 400 sample. XRR again shows diffuse scattering in from the thin film, demonstrating structural roughness and the need for both surface and interface regions (Figure 7.13).

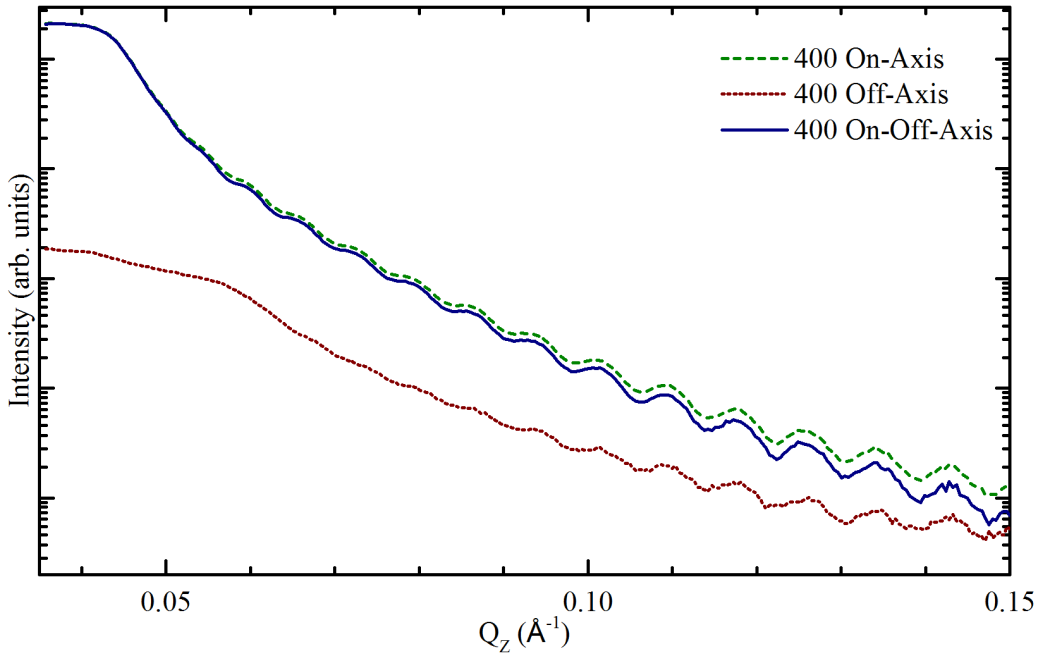


Figure 7.13: On axis and off axis XRR measurements for the 400 sample where the On-Off axis data represents the specular only contribution. Correlated roughness is observed from the Off/diffuse scattering measurement of $\Delta\omega = -0.1$.

#### MgO 400 XRD

The $Fe_3O_4(400)$ family of reflections (Figure 7.14) is again observed in the $\theta - 2\theta$ out of plane scan of the sample with no evidence of the (111) orientation. The measured lattice constant of the MgO(111) is 4.217 Å and $Fe_3O_4(400)$ is 8.416 Å. This lattice constant is closer to that of bulk $Fe_3O_4$. The grain size of the film is 243 Å, which is the same as the value calculated for MgO 950.

Figure 7.15 shows the substrate $\chi - \phi$ rock where the variation in mosaic directions of the substrate crystals are orientated away from each other, but this time at a smaller separation angle $\Delta\phi = 80°$. There is the suggestion that the higher annealing temperature also affects the mosaic nature of the substrate. Previously the film intensity was projected away from the intensity of the substrate, where as in this case, the film crystallography is directed in the direction of one of the substrate directions but is still very broad. Figure 7.16) shows that the film is split, tilted in two different directions creating a twinning type effect at $\Delta\phi = 150°$.

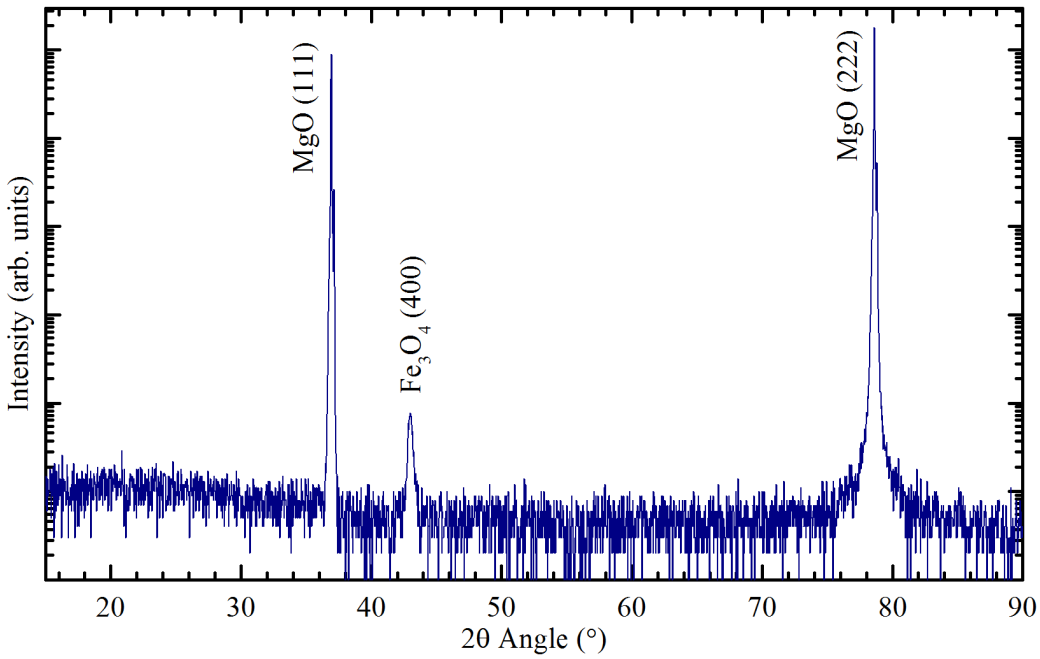


Figure 7.14: MgO 400 $\theta-2\theta$ scan between $2\theta = 15°$ and 90°, aligned to the MgO(111) substrate peak revealing only the $Fe_3O_4$(400) reflection as seen in MgO 950.

### MgO 400 Microscopy

The TEM images from MgO 400 (Figure 7.17) show many more grain boundaries within the thin film crystal when compared with MgO 950 (Figure 7.11). Crystallographic defects in the substrate towards the left of the 50 nm image show the film quality is directly effected and creates a grain boundary with respects to the film crystal on the more ordered MgO. Due to the lower annealing temperature, the film is not able to recover by creating more a more ordered film. The varying structural defects could cause effects on the magnetic and behaviour of the sample. A larger

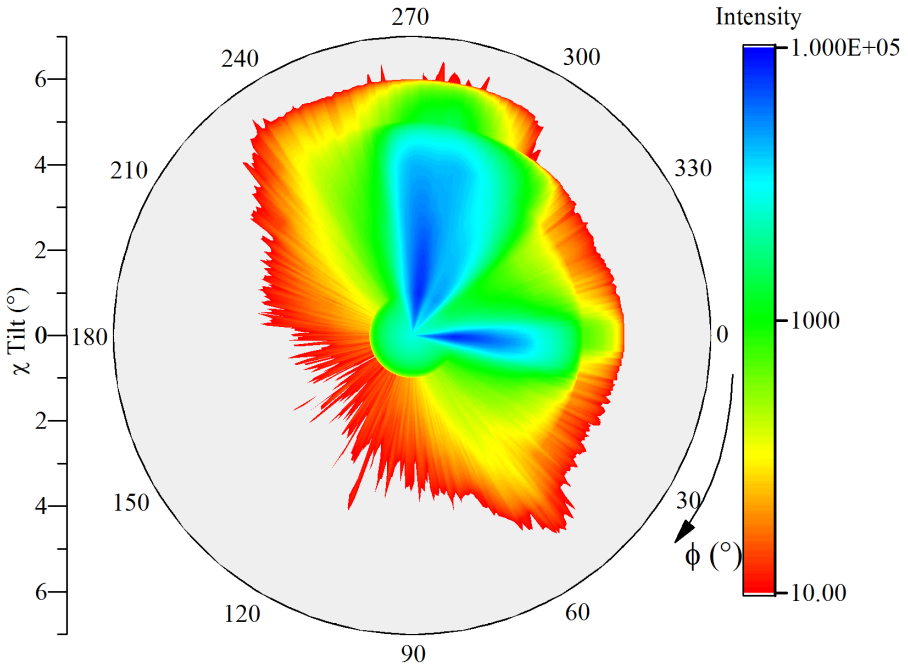


Figure 7.15: MgO 400 $\chi-\phi$ mesh scan aligned to MgO(111) peak. The two substrate peaks are separated by $\Delta\phi = 80°$.

interfacial region of ∼100 Å is observed along with a film thickness of ∼720 Å.

### MgO 400 Room Temperature Reflectivity

As MgO 400 is considerably different to both MgO 950 and 300, it is expected that the model used for 950, does not fit this data set. The model is rebuilt layer by layer, fitting at each instance where Figure 7.18 is the final model with four additional layers to the film. There are two interfacial layers and two surface layers, where one of the layers acts as a split film SLD. The surface layers appear to have fitted similarly to that of MgO 950, including the increase in Fe with thicknesses of 83.5 Å (50.4 Å and 33 Å respectively). The film is split into two layers; a layer of constant SLD near the surface of 487 Å and a layer of continually varying composition of 200 Å. There is an additional interfacial layer of 54.5 Å before the substrate. The varying SLD can be more clearly seen in the X-ray ReSLD of Figure 7.18. The NSLD is less sensitive to the change in SL as the variation here comes from the MSLD, which decreases throughout these varying layers towards the substrate. The magnetism increases slightly at the surface with the increase in Fe, and then drops to zero. The continuous part of the film has an adjusted moment of 2.6(1) $\mu_B$/f.u.

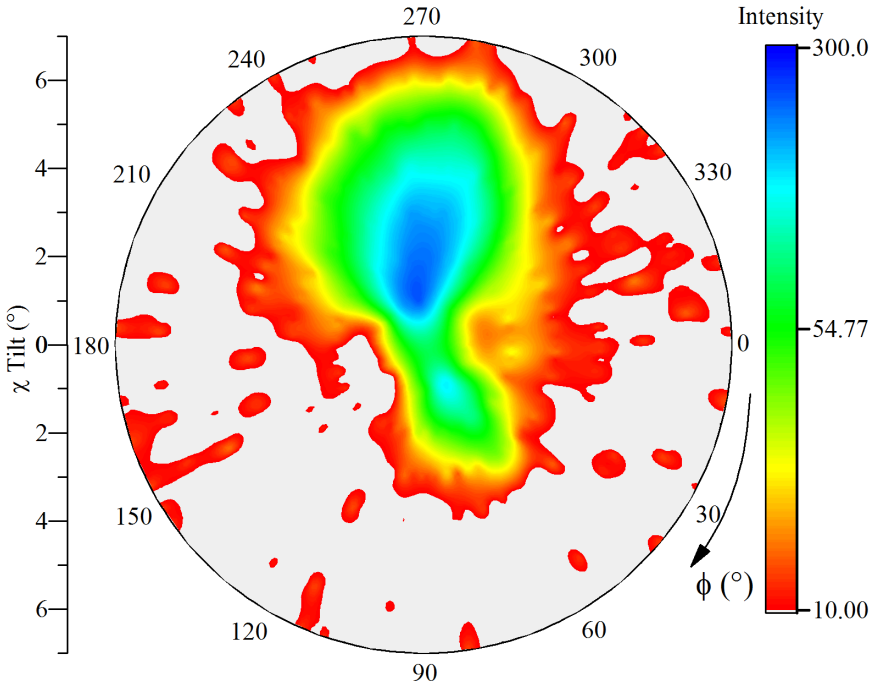


Figure 7.16: MgO 400 $\chi - \phi$ mesh about $Fe_3O_4(400)$, aligned to MgO(111) peak. The film peaks are separated by $\Delta\phi = 150°$.

which is considerably lower than that of MgO 950, as predicted by the reduced splitting in the PNR. Overall the thickness of both MgO 400 and 950 are the same, but there is a varying composition over $\sim$200 Å which reduces the magnetism and does not recover in the upper part of the film.

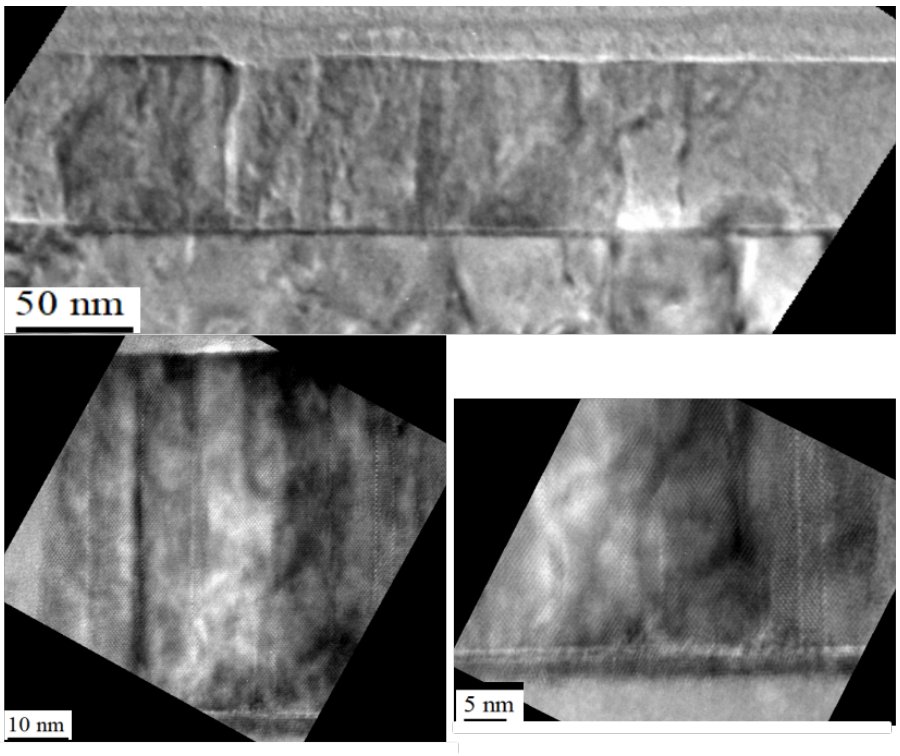


Figure 7.17: TEM images of MgO 400 at three different magnifications: 50 nm, 10 nm and 5 nm. The image direction is looking along the substrate $(1\bar{1}0)$ zone axis perpendicular to the substrate surface. The substrate is at the bottom in all images, and the $Fe_3O_4$ film above this. Many defects are seen propagating vertically through the film and a large interface region ∼100 Å is observed in image 5 nm.

### 7.2.3 MgO 300

MgO 300 is the sample with the lowest post-annealing temperature. Ordering of the film is often found at higher temperatures, therefore this sample is expected to have more defects (not considering MgO 400 with suspected complications in growth). Previous comparative data of reflectivity suggests that both MgO 300 and 950 are very similar in composition and magnetism, but have different thicknesses. Analysis of the data will reveal the effect of higher annealing temperatures.

Unfortunately at the time of writing this chapter, there are no microscopy images for MgO 300 due to issues with TEM preparation of the sample. For MgO 300, the complementary techniques are therefore limited to XRD, magnetometry and the similarities seen between MgO 950.

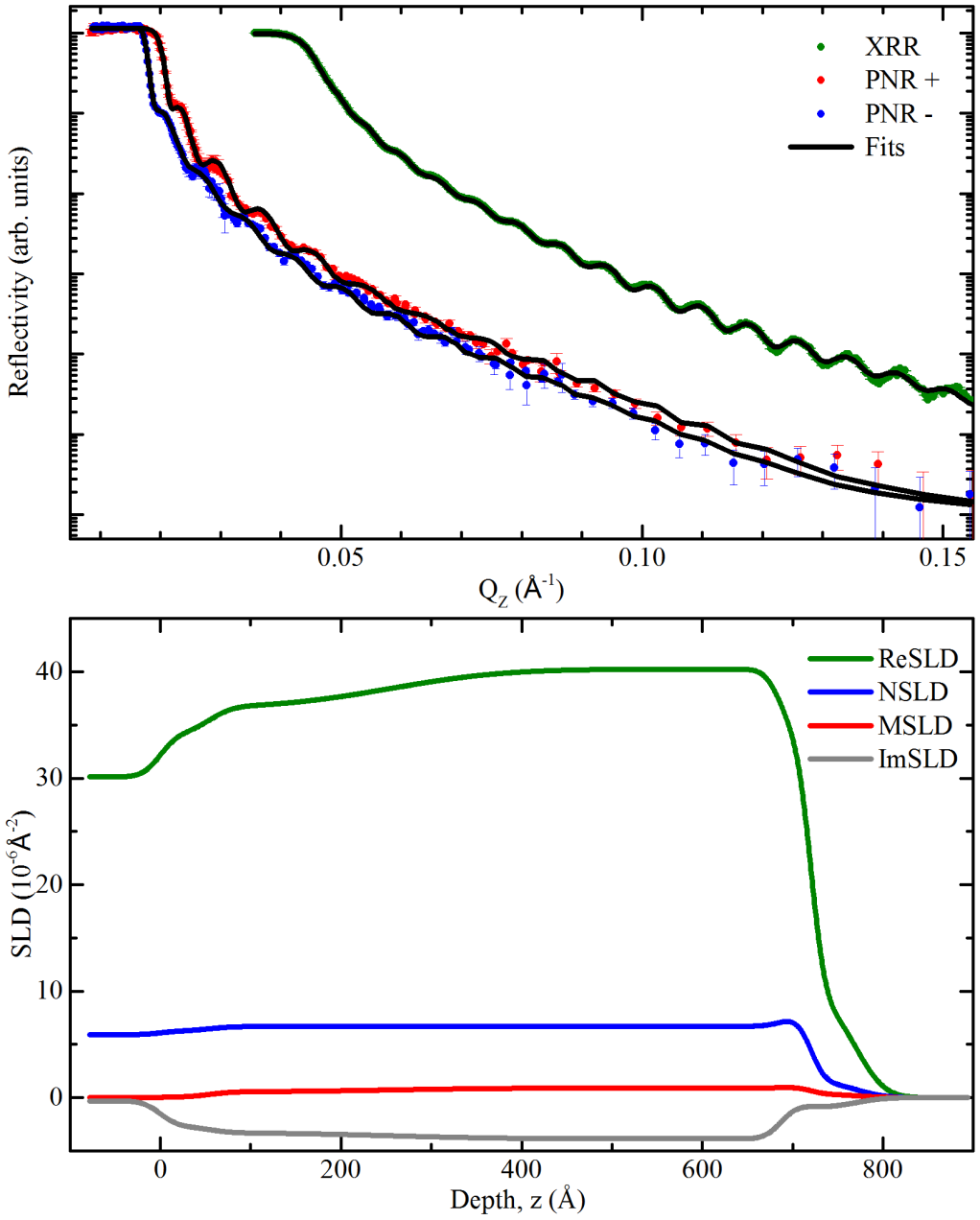


Figure 7.18: MgO 400 fitted reflectivity curves and the corresponding SLDs showing a thin region of stoichiometric film ∼160 Å towards the surface before the SLD gradually decreases towards the substrate.

### MgO 300 XRR

Likened to the other MgO samples, MgO 300 has correlated roughness as shown in Figure 7.19 and this will need to be modelled effectively.

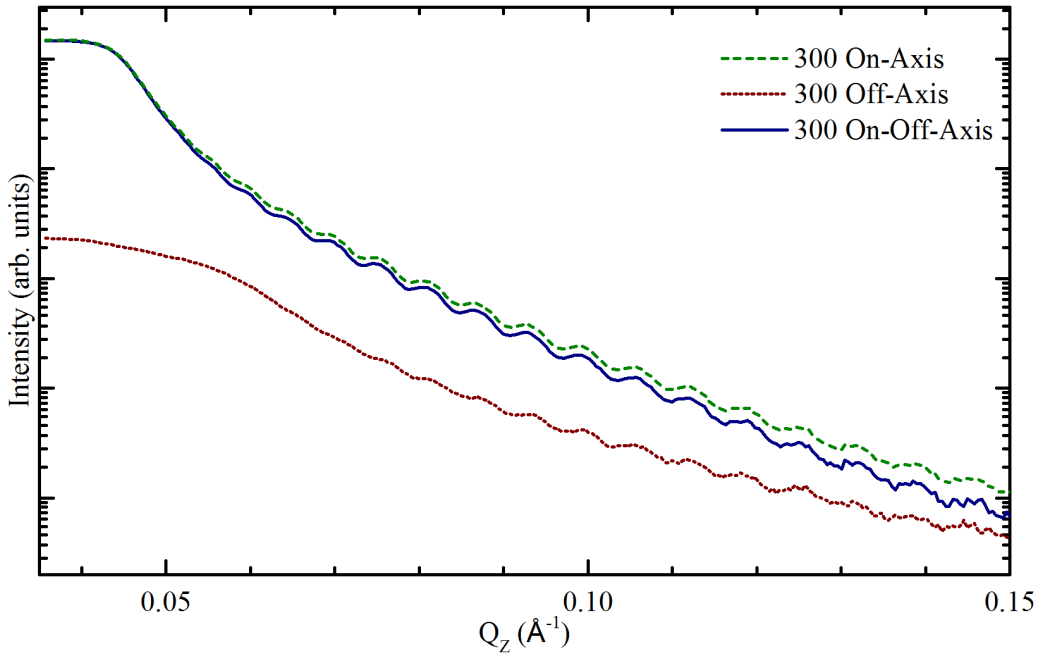


Figure 7.19: On axis and off axis XRR measurements for the 300 sample where the On-Off axis data represents the specular only contribution.

### MgO 300 XRD

Unlike other samples, the $\theta - 2\theta$ scans shown in Figures 7.20 and 7.21 reveal that MgO 300 has both $Fe_3O_4$(400) and (111) reflections out of plane. Only when aligning to the $Fe_3O_4$(111) reflection, is the (333) peak is also revealed. The measured lattice constant of the MgO(111) is 4.217 Å, $Fe_3O_4$(400) is 8.430 Å and $Fe_3O_4$(111) is 8.405 Å. The (400) reflection lattice constant is in agreement with the MgO 950 sample with a larger than nominal lattice size, where the (111) reflection is smaller, closer to nominal. A grain size calculation for this sample gives thickness of 450 Å for both (100) and (111) directions, suggesting that in the area of the footprint of the beam, there are large grains of both crystal orientations.

The texture scan around the substrate peak in Figure 7.22 shows minimal mosaics, suggesting the lower annealing temperature has caused the MgO substrate to maintain a more orientated crystallographic direction, or the substrate chosen randomly is of better quality. In turn this causes the $Fe_3O_4$ to be mainly single domain where the $Fe_3O_4$(400) peak is sharper than other samples (Figure 7.23) with a change in $\phi$ of between 100° and 130° with respects to the substrate (Figure 7.22).

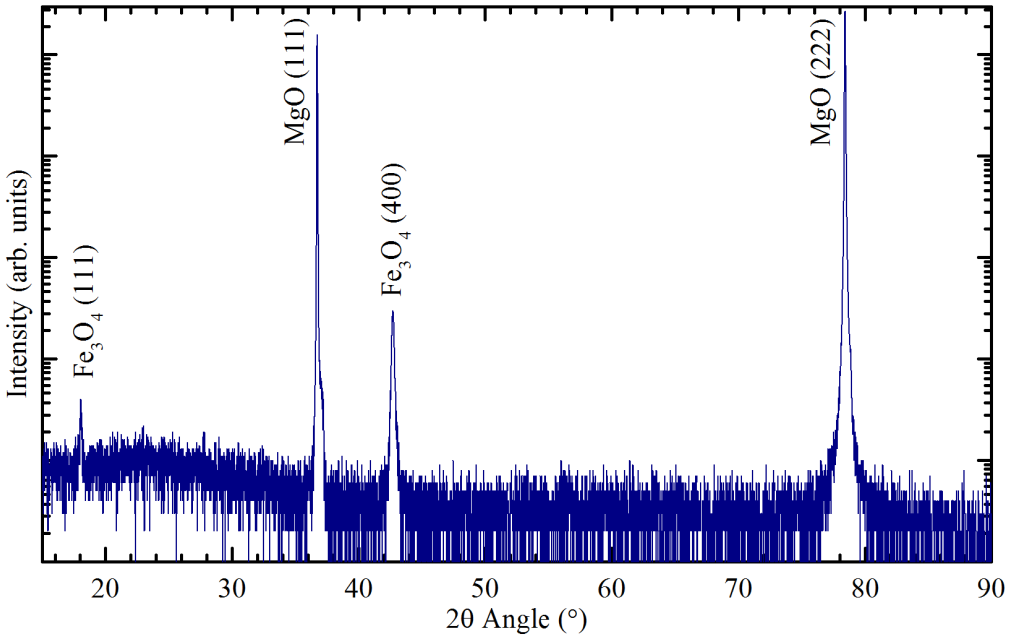


Figure 7.20: MgO 300 $\theta - 2\theta$ scan aligned to the substrate (111) reflection. Both $Fe_3O_4$(400) and (111) peaks are visible

A pole figure is performed at the $Fe_3O_4$(333) reflection, in order to check the alignment with respect to the substrate. The substrate peak is aligned, and $2\theta$ is set to the (333) $Fe_3O_4$ reflection ($\theta$ is half of $2\theta$). At this position in $2\theta$ only film peaks are possible due to structure factor rules and Figure 7.24 shows the observed reflections. They are symmetric around the (333) reflection, ignoring the slight offset due to the misalignment with the substrate. The reflections are highlighted by the black arrows. Indexing the peaks; the arrow closest to the centre shows the (511) reflection related to the (400) at $\chi \sim 15.8°$, the middle arrow shows the (511) with respects to the (333) at $\chi \sim 35.3°$ which has twelve reflections and appears to be in three domains equally spaces in $\phi$, and the furthest from the centre is the (333) related to the (400) orientation at $\chi \sim 54.7°$. There are also peaks to the very edge of the scan which have not yet been identified. The $Fe_3O_4$ thin film has at least two orientations within the sample, yet the magnetometry data suggests the retention of magnetism equivalent to MgO 950.

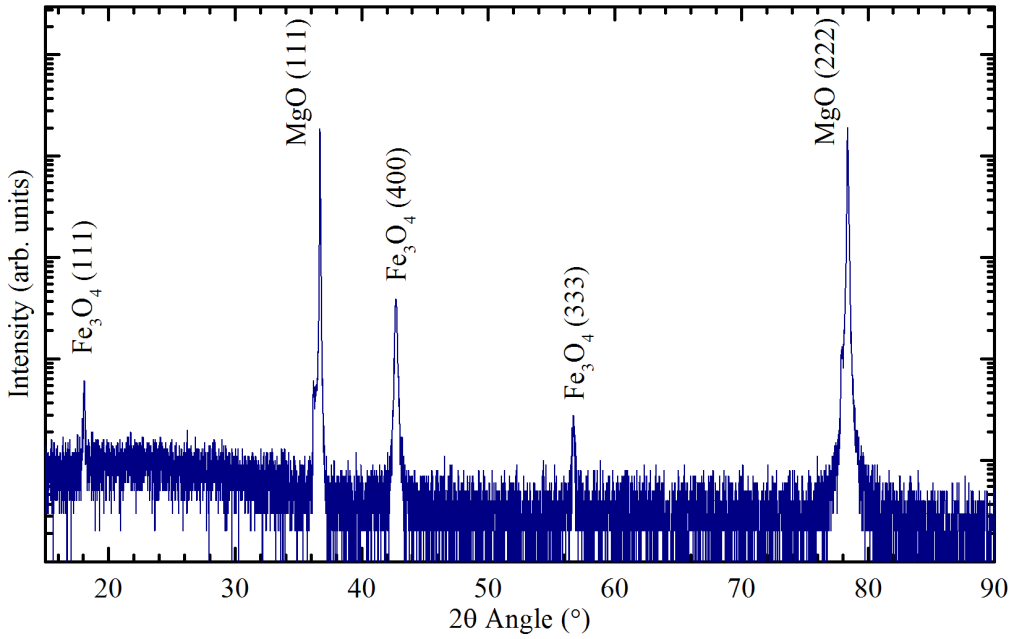


Figure 7.21: MgO 300 $\theta - 2\theta$ scan aligned to the $Fe_3O_4(111)$ peak revealing the $Fe_3O_4(333)$, and confirming several orientations of film on the MgO(111) substrate.

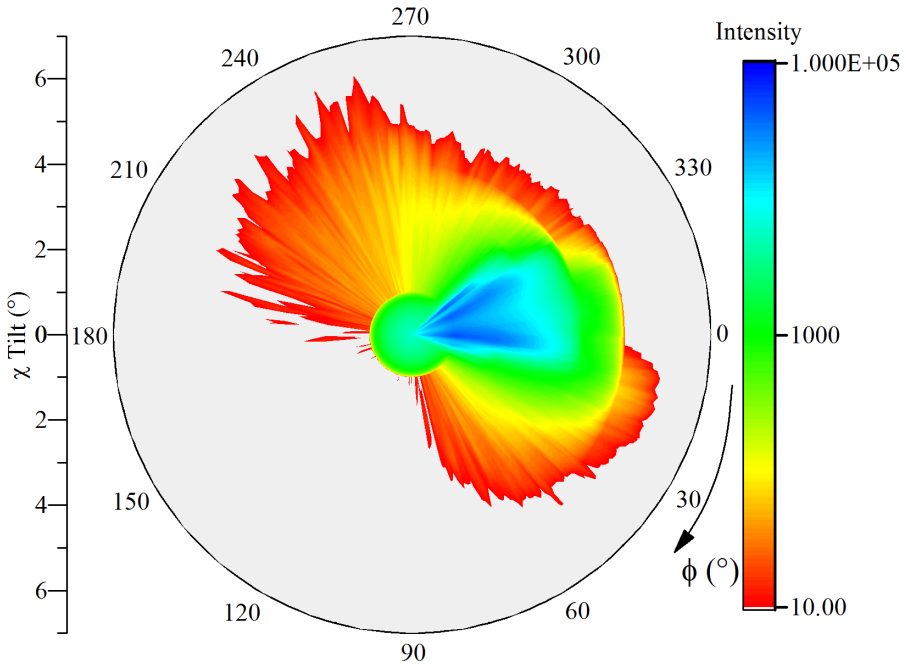


Figure 7.22: MgO 300 $\chi - \phi$ mesh aligned to MgO(111) peak.

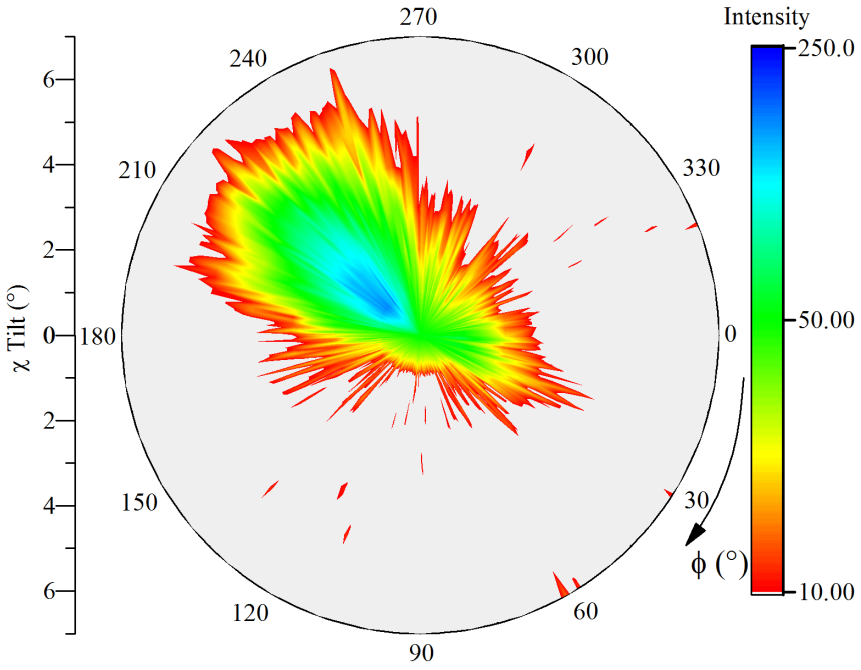


Figure 7.23: MgO 300 $\chi - \phi$ mesh about $Fe_3O_4(400)$ peak, aligned to the substrate (111) peak as in Figure 7.22. The film is mostly single domain and has a change in $\phi$ of between 100° and 130° with respects to the substrate.

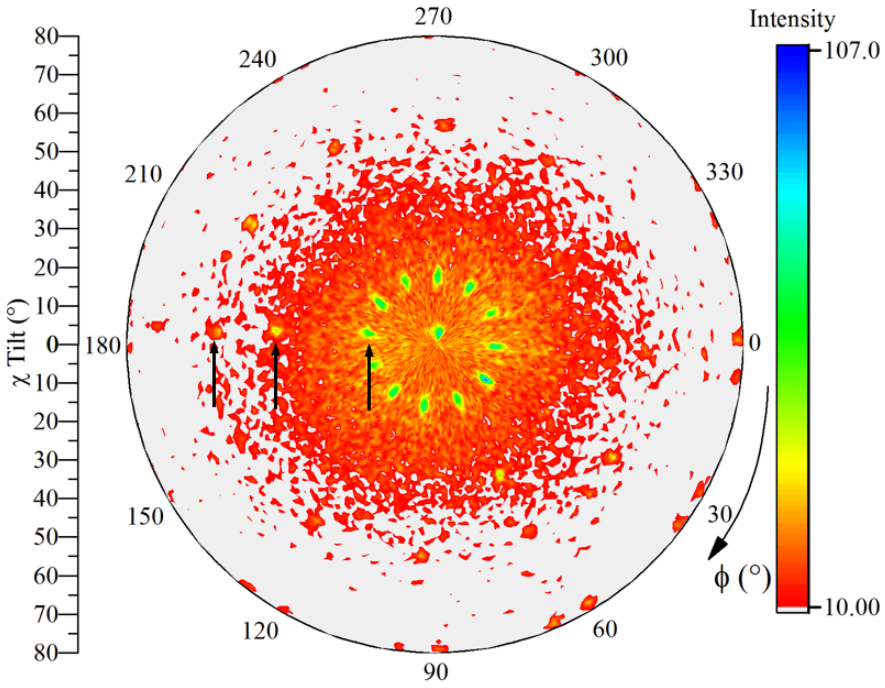


Figure 7.24: MgO 300 $\chi - \phi$ mesh around $Fe_3O_4$(333) peak revealing multiple reflections relating to both $Fe_3O_4$(111) and (400) out of plane orientations. $\Delta\chi = 80°$ and $\Delta\phi = 360°$. Black arrows guide the eye to the reflections which are repeated at set angles when rotated by $\phi$.

### MgO 300 Room Temperature Reflectivity

On the larger scales, reflectivity and magnetisation measurements have shown that both MgO 300 and MgO 950 are similar samples, where smaller scale measurements reveal they are considerably different. Using the model from MgO 950 and changing the film thickness reveals a very good fit to the data, which is then minimised (Figure 7.25). A model was also built up from a single layer in order to check for more simple solutions to the data, but none were found. There remains one interfacial layer and two surface layers. Again the surface is in agreement with other samples and also retains the bump in the NSLD where the layer thickness of the surface is 82 Å (49 Å and 33.4 Å respectively). The film is larger at 788 Å as predicted by reflectivity and suggested by the increase in magnetisation from the magnetometry. There is an additional interfacial layer of 61 Å before the substrate which is comparable to MgO 950. The film has an adjusted moment of 3.4(2) $\mu_B$/f.u. in agreement with MgO 950, as expected by the PNR critical edge splitting, and magnetometry when accounting for the larger film thickness. It is suggested that the change in crystal orientation and annealing temperature has no effect on the magnetism within the film at room temperature.

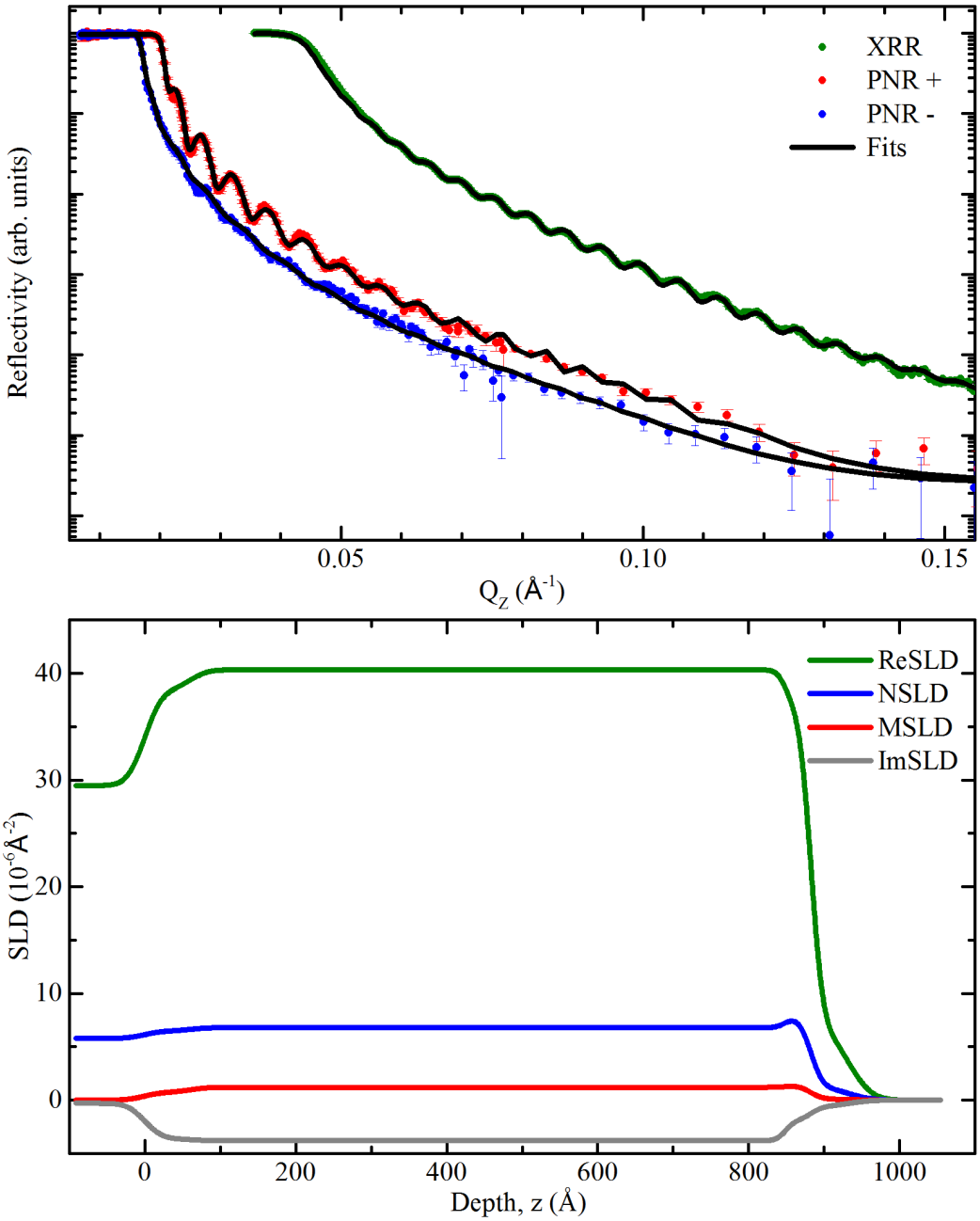


Figure 7.25: MgO 300 fitted reflectivity curves and the corresponding SLDs showing a large uniform film with surface and interfaces features that reduce the magnetism.

### 7.2.4 MgO Sample Comparison

The samples have been analysed individually and now can be compared in order to understand the effect growth temperature has on the quality of the film. Focus will

be on MgO 950 and 300 due to the belief there was an error in the growth of MgO 400.

Starting with the substrate, the quality of this crystal greatly impacts the quality of the film, especially at the interface where it epitaxially bonded. The TEM and texture map measurements from MgO 950 suggest either poor substrate growth quality or that the post-growth annealing allows the substrate to relax causing a tilts and mosaics through the crystal. Such a change in the tilt of the substrate could be the reason for the unusual epitaxial growth orientations of $Fe_3O_4(100)$ grown on MgO(111). Analysis of crystal d-spacings and orientations suggests that the epitaxial relationship could be MgO(110)$\|$$Fe_3O_4(100)$ due to a 6% mismatch. Further TEM analysis will be needed to confirm this. The larger the tilting/mosaics in the substrate, the more broad the film reflection becomes, showing how the film is strained to the substrate. Lower post-annealing temperatures retains (111) crystal ordering due to the substrate not being able to relex and to become mosaic. An increase in lattice constant is seen for MgO 950 and 300, as seen by the negative shift in $2\theta$ (Figure 7.26) which is at the same position as MgO(200) indicating a reduction in the lattice constant to double that of the MgO. If compared with MgO 400 a larger lattice constant is required for a more consistent film quality, as 400 has a large interface region unlike the other samples. Figure 7.27 shows the SLD of all samples. Both 950 and 300 samples have the same SL and magnetic moment within the film with a decrease though the interface. The gradient of this decrease is sharper in 950 suggesting it retains a slightly higher magnetisation towards the substrate. There is also a higher magnetism in the surface region believed to be Fe, possibly due to the higher annealing temperature allowing more O atoms to leave the film.

Having reliable magnetic profiles from the fitted PNR data now enables us to manipulate the SQUID magnetometry data showing at the beginning of the chapter (Figure 7.3). The MSLD (Figure 7.27) is integrated to find the area under the curve, which gives the depth of the magnetisation. As the sample sizes measured with SQUID are of similar size and illuminated sample area from the neutrons is the same for all samples, the integrated MSLD then becomes a sample dependent magnetic volume which can be used to confirm accuracy of magnetism within the sample. This is done by dividing the SQUID data by the integrated value. Figure 7.28 shows the new manipulated magnetic data where the apparent normalisation of the curves confirms accuracy of the MSLD PNR profiles. The discrepancy with the value of MgO 950 is in agreement within the 8 % error in the magnetometry. Otherwise the higher value could come from a slightly larger sample size than both

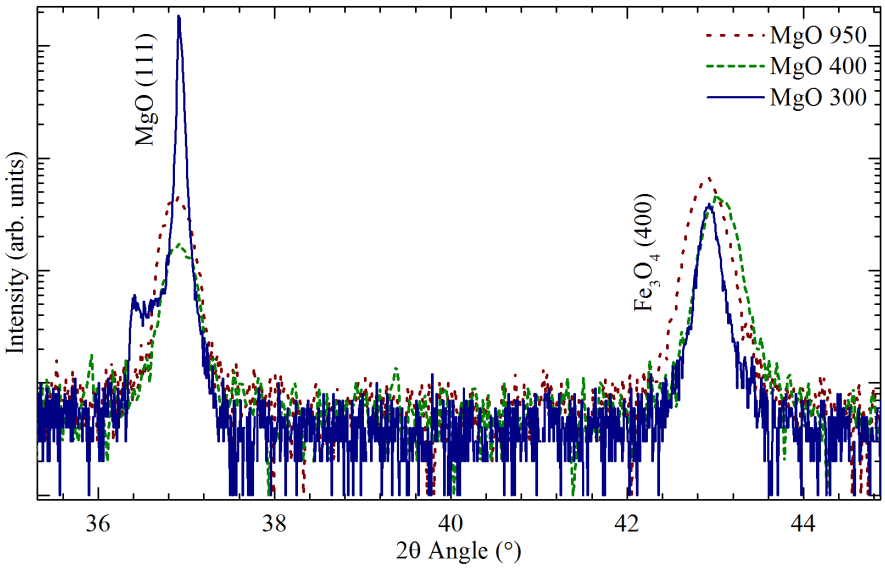


Figure 7.26: MgO $\theta - 2\theta$ scans of MgO(111) and $Fe_3O_4$(400) aligned to the $Fe_3O_4$(400) peak to show differences in peak position.

300 and 400, or a slight error in the fitting of the PNR data causing a decrease the MSLD. Both will need to be researched carefully before being confident of the outcome.

Again the hysteresis shape of both MgO 300 and 950 are similar, with the origin of the reduced magnetism in 400 appearing to be pinned by the large varying layer of composition towards the substrate. All samples appear to be saturated towards 2T, which is the field at which the PNR measurements were taken. To check the saturation of the sample, spin flip scattering would be needed, but in this case it seems unnecessary due to the tiny number of unaligned spins.

More experiments should be done, such as energy dependent XRR to find more accurate values for the density. MgO is known to be difficult to obtain as a uniform crystal in bulk, and therefore measurement of the substrate before growth of $Fe_3O_4$ would have been valuable. Rocking curves (in $\omega$) about the MgO(111) peak (not shown here but shown as pole figures) reveal multiple peaks for the substrate agreeing with this.

After obtaining the depth dependent magnetic profiles for the $Fe_3O_4$ at room temperature, it is interesting to see how the magnetic profiles change when the films are cooled through the Verwey transition. The next section explores this.

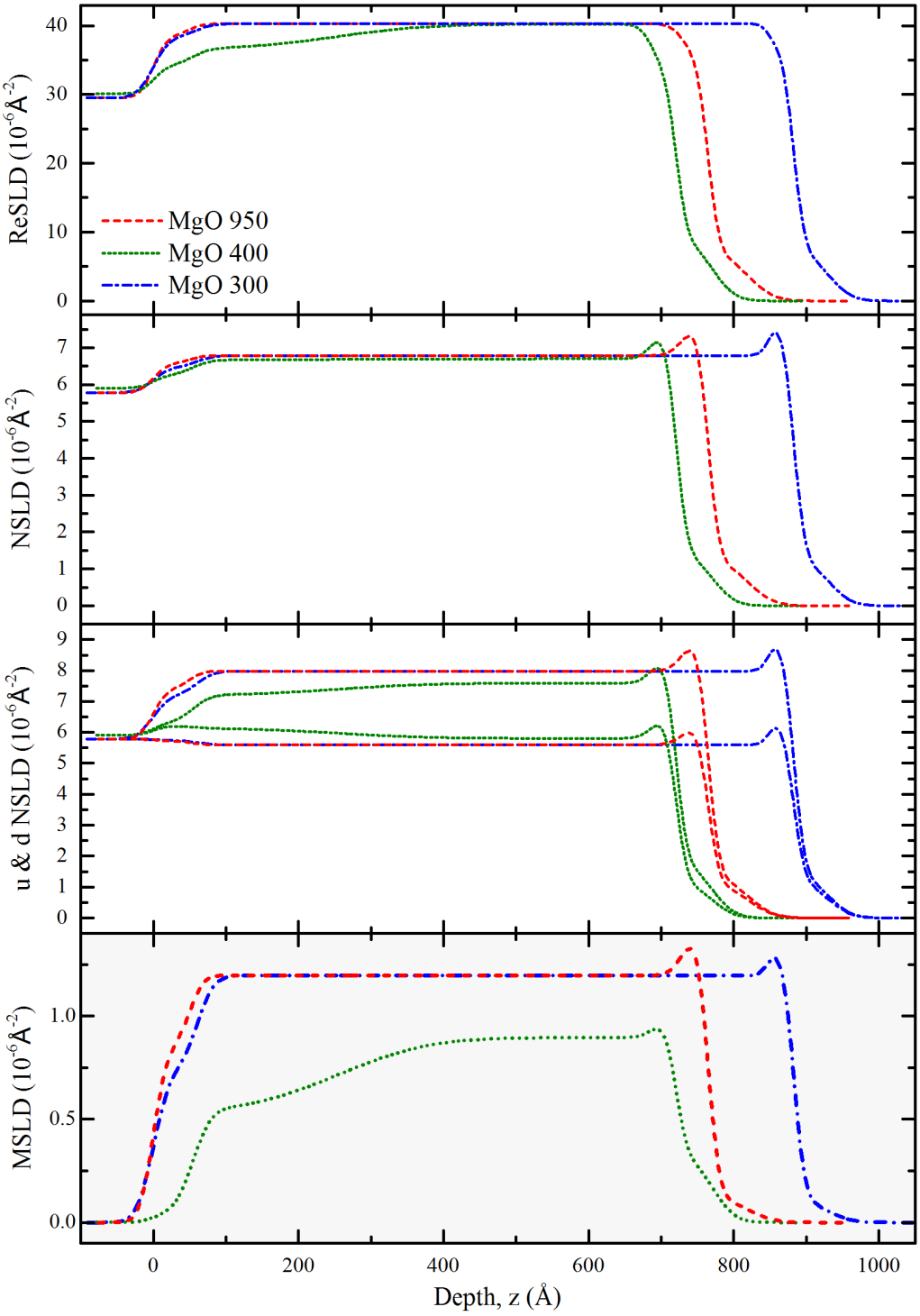


Figure 7.27: SLD corresponding to the fitted reflectivity curves of all MgO samples showing MgO 300 and 950 are similar in SLD but with different thickness and MgO 400 is very different. The XSLD and MSLD values for the main film component are the same for all samples showing consistent film growth.

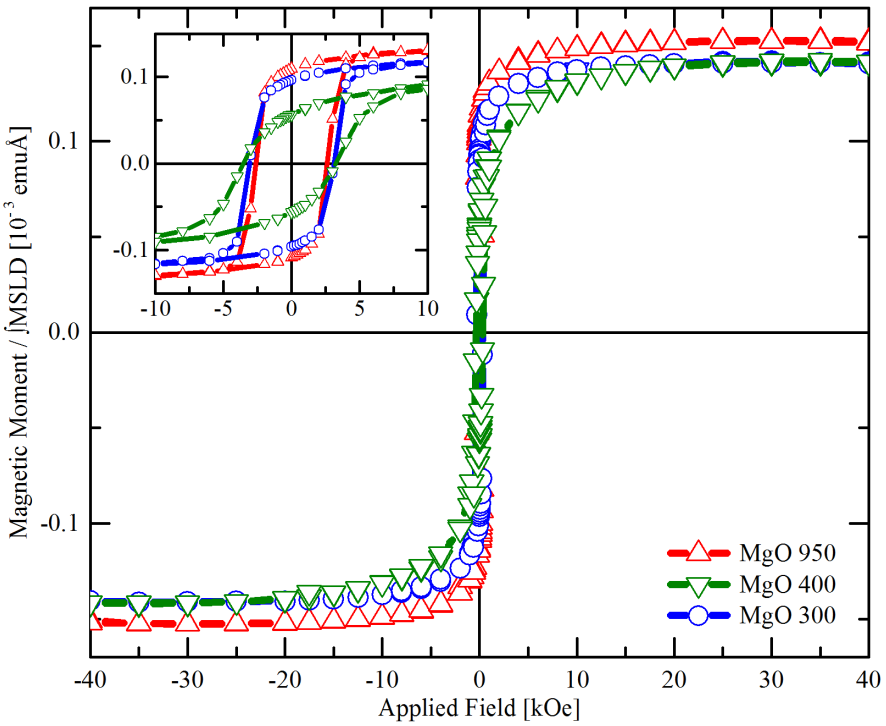


Figure 7.28: SQUID measurements of averaged magnetic moment for all MgO samples divided by the integral of the MSLD. The inset is zoomed into the central hysteresis.

## 7.3 Verwey Transition

$Fe_3O_4$ has a transition temperature at $T_V \sim 120\,\mathrm{K}$ which induces both a structural and electrical change in the material. Controversy surrounds these values, along with many other $Fe_3O_4$ parameters. A structure was initially proposed by Verwey [104] and later confirmed by neutron diffraction [105], but was proven incorrect due to a flawed experiment [106]. A comparison of crystal parameters can be seen in Table 7.3. A good approximation for the structure [106] is described by a monoclinic $a_c/\sqrt{2} \times a_c/\sqrt{2} \times 2a_c$ (where $a_c$ refers to the high-temperature lattice constant) with *Pmca* pseudosymmetry as first proposed by Iizumi et al. [107]. Below $T_V$ there have been reports of decreases in magnetic moment [108, 109] or no change [16, 92]. The decrease in magnetism has been linked to the change in saturation magnetisation not overcome by the experimental external field [109].

As the average density and composition of the $Fe_3O_4$ film remains the same above and below this transition, the Verwey transition is not observed in non spin-polarised reflectivity. It is however, observed in PNR if there are changes in magnetism. Room temperature PNR fitted models in the previous section are used to fit low temperature ($30\,\mathrm{K} - 300\,\mathrm{K}$) PNR data by allowing changes in roughness and $\mu_B$/f.u. value. For the analysis of the Verwey transition, the only data available is the temperature dependent PNR conducted during the same experimental sessions as the room temperature studies shown in the previous section.

Table 7.3: $Fe_3O_4$ lattice constants above and below $T_V$ [110].

| | 300K | 90K |
|---|---|---|
| $a$ (Å) | 8.394 | 5.944 |
| $b$ (Å) | 8.394 | 5.924 |
| $c$ (Å) | 8.394 | 16.775 |
| $\alpha$ ° | 90 | 90 |
| $\beta$ ° | 90 | 90.2363 |
| $\gamma$ ° | 90 | 90 |

The value of $T_V$ varies in $Fe_3O_4$ due to changes in film properties such as film thickness and crystal quality. For this reason measurements were not performed at $T_V$, instead the temperatures were chosen by observing the change in resistance of the film while decreasing through the region of $T_V$ (not shown in this thesis due to time constraints on obtaining the data). For some samples, additional changes in the reflectivity at 30 K influenced measurements to be taken at this lower temperature. It is important to note that the temperatures used have not been calibrated, and further low temperature measurements would require the observation of film

resistance to ensure the same temperature is measured.

### 7.3.1 Low Temperature Polarised Neutron Reflectivity

#### MgO 950

Figure 7.29 shows the PNR for three temperatures; 306 K, 70 K and 80 K. Measurements were taken in this order by observation of $T_V$. 70 K was chosen due to being safely below $T_V$, and 80 K was chosen as a temperature within the resistance transition towards RT. No change is seen in the reflectivity at the different temperatures. To enhance the possible differences the asymmetry ratio is plotted (Figure 7.30). The asymmetry is the difference between PNR+ and PNR−, therefore highlights the magnetic contribution to the data. Asymmetry $= R_+ - R_- \ / \ R_+ + R_-$. Small differences are all within error of the data and could be due to small changes in roughness due to crystal structure changes after the sample has been cooled.

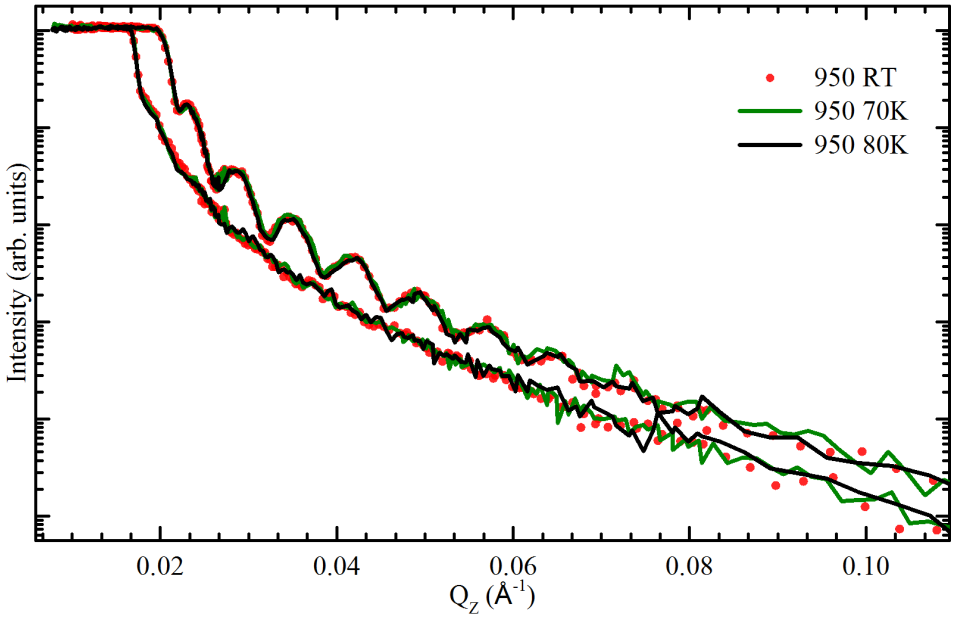


Figure 7.29: PNR data for MgO 950 at three different temperatures. No change in structural or magnetic behaviour observed.

#### MgO 400

Unlike MgO 950, changes are observed at lower temperatures in the MgO 400 reflectivity data. To check for further changes in the reflectivity, the choice was made to reduce the temperature to 30 K and take another set of measurements. Additional

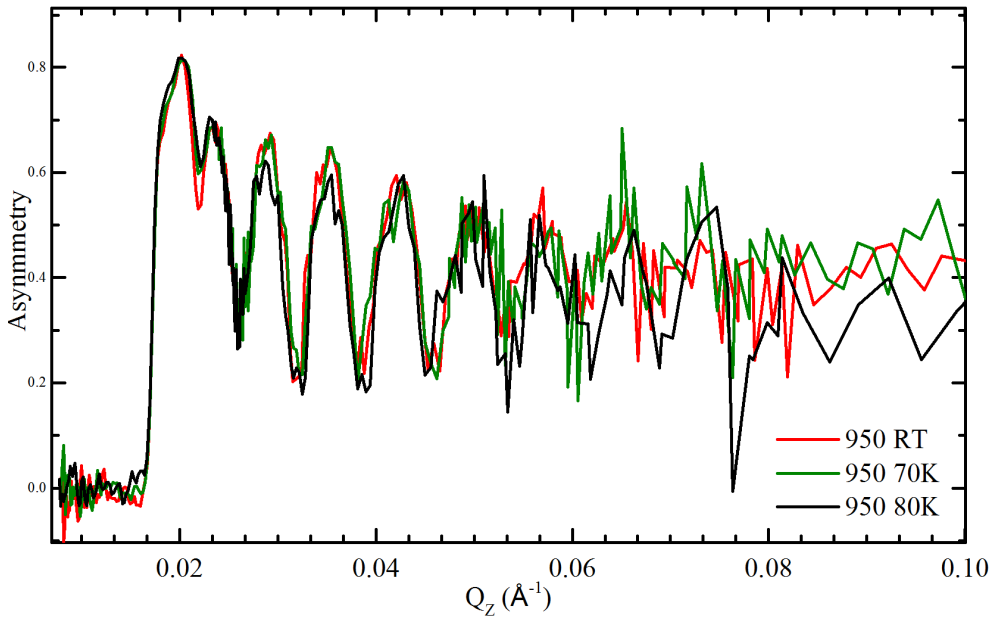


Figure 7.30: Asymmetry curve of MgO 950 to enhance the difference between PNR+ and PNR− highlighting the magnetic contribution within the film. Small differences observed are within error of the instrument.

changes to the reflectivity were observed. The reflectivity data is shown in Figure 7.31 where the the two lower temperatures have been plotted over the top of 306 K in order to analyse the differences. For 70 K there is an increase in magnetism from mid to high $Q$ shown by an increase in splitting, and for 30 K there is an increase in magnetism and an increase in the roughness seen as a decrease in intensity at $Q \sim 0.05\,\text{Å}^{-1}$.

Fits to all data sets are shown in Figure 7.33 where NSLD and XSLD corresponding to reflectivity at 306 K is shown in Figure 7.18. A comparison of the NSLD and MSLD for all temperatures is shown in Figure 7.34 where a large increase in magnetism can be seen in the film between 306 K and 70 K. The magnetic surface roughness has also decreased. At lower temperatures of 30 K, there is another increase in magnetism which is likely to relate to a further change in magnetic structure which is not expected and could be caused by the unusual film composition. For 306 K the magnetism is 2.6(1) $\mu_B$/f.u., 70 K is 3.0(1) $\mu_B$/f.u. and for 30 K is 3.1(1) $\mu_B$/f.u..

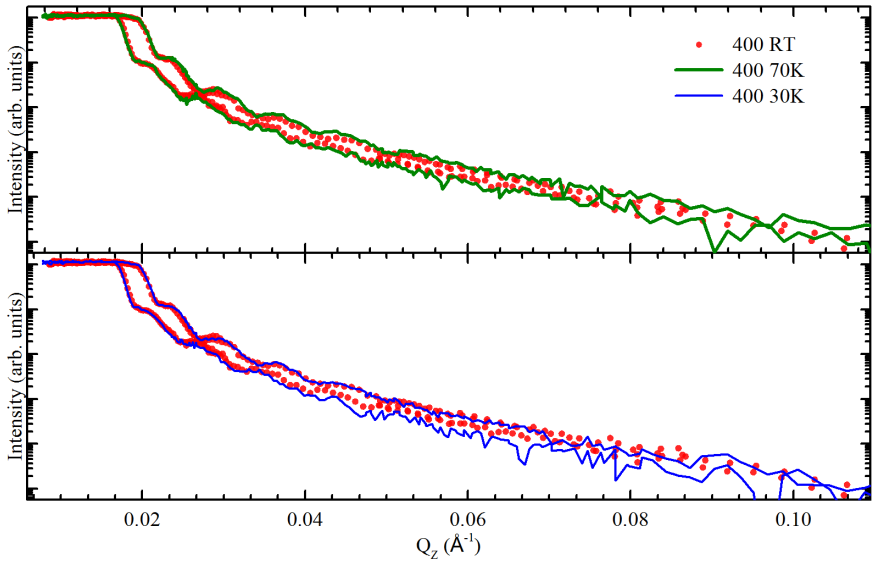


Figure 7.31: PNR data for MgO 400 at three different temperatures. Graphs are split in order to observe the differences in magnetism and roughness over the larger $Q$ range.

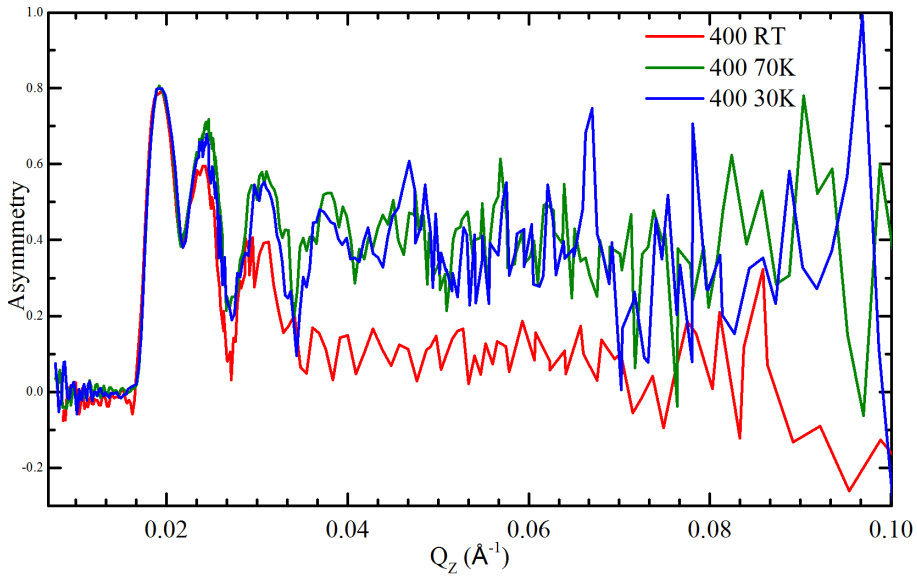


Figure 7.32: Asymmetry curve of MgO 400 to enhance the difference between PNR+ and PNR− representing the magnetic contribution within the film. There is a large change in the magnetic contribution at lower temperatures below the Verwey transition.

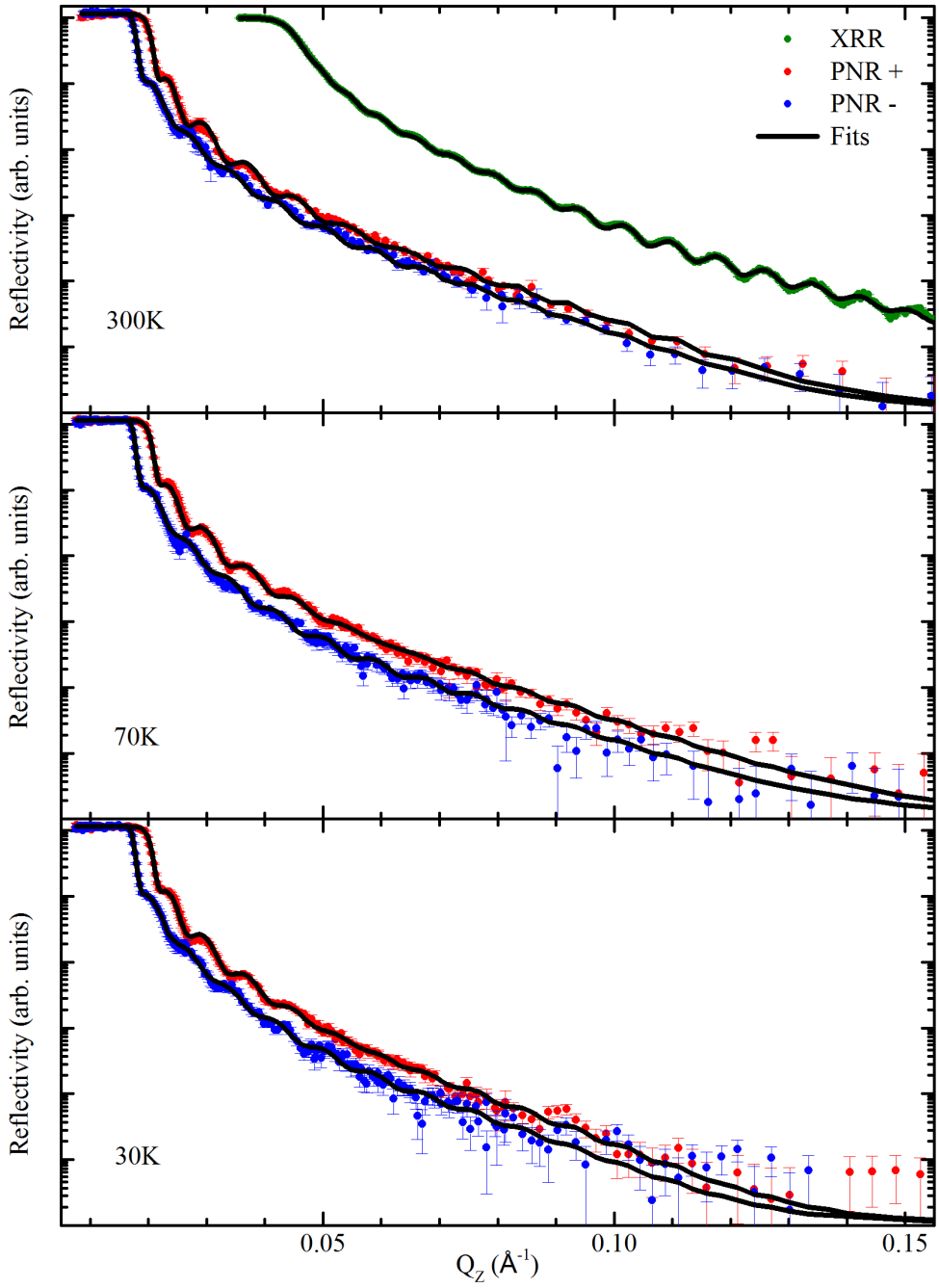


Figure 7.33: MgO 400 fits to PNR data for specified temperatures.

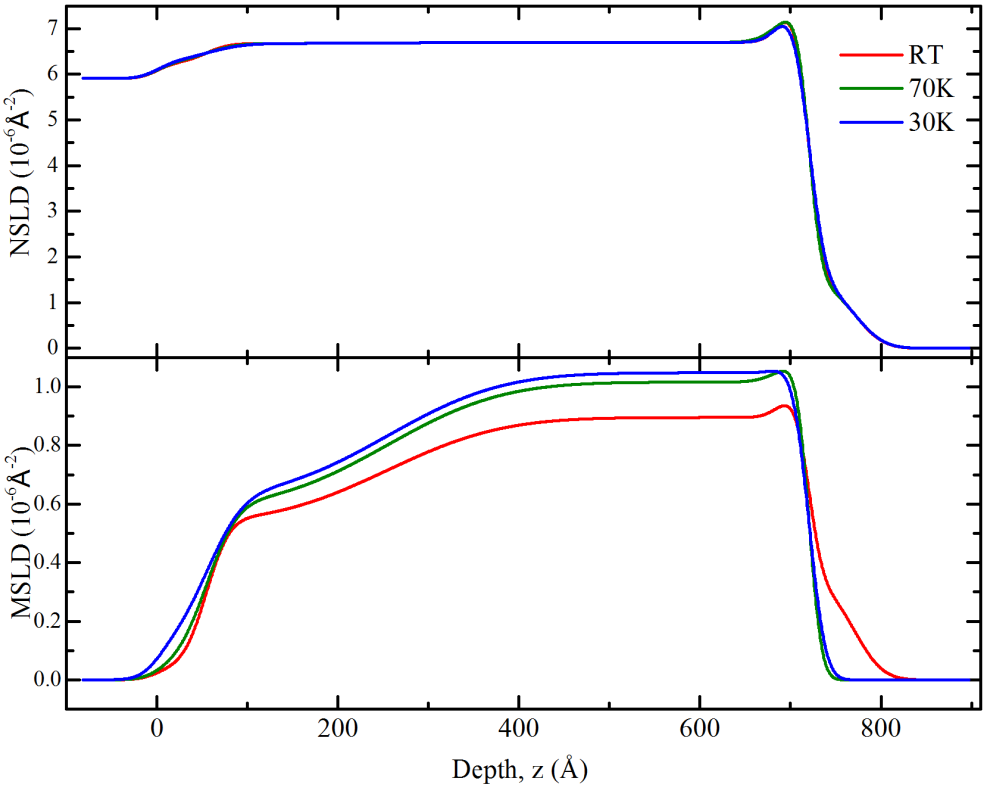


Figure 7.34: Fitted MgO 400 nuclear and magnetic profiles from Figure 7.31, in order to compare the effect that temperature change has on the $Fe_3O_4$ thin film.

### MgO 300

Due to the changes seen in MgO 400, the choice of temperatures were 306 K, 30 K and 70 K. It may be interesting to note that the sample was cooled to 30 K before returning to 70 K, unlike MgO 400 where 70 K was measured before the lower temperature. Similar changes in the reflectivity (Figure 7.35) are observed; an increase in splitting for both lower temperatures with a drop in intensity in 30 K signalling an increase in roughness. The magnetic difference is more clearly seen in the asymmetry curve, Figure 7.36. To fit the new reflectivity curves, only the magnetism and roughness are allowed to vary.

The fits to all temperature data sets are shown in Figure 7.37 where only 306 K data was simultaneously fitted with XRR. The NSLD and XSLD for the 306 K fits are earlier in the chapter (Figure 7.25) and the corresponding SLDs for the temperature measurements are shown in Figure 7.38. There is an increase in magnetism when lower than $T_V$ but unlike MgO 400, further decrease in temperature doesn't increase the magnetism. It does, however, change the magnetism at the surface by varying the magnetic value and changing the roughness parameters. From the fits to the data, more freedom in the magnetic profile is needed to fit this sample more accurately. For 306 K the magnetism is 3.4(2) $\mu_B$/f.u., 70 K is 3.7(2) $\mu_B$/f.u. and for 30 K is 3.7(2) $\mu_B$/f.u.. An increase in magnetism is different to the research previously mentioned where there was either no change in moment [16, 92] or a decrease in moment due to non-saturation of the sample [108, 109].

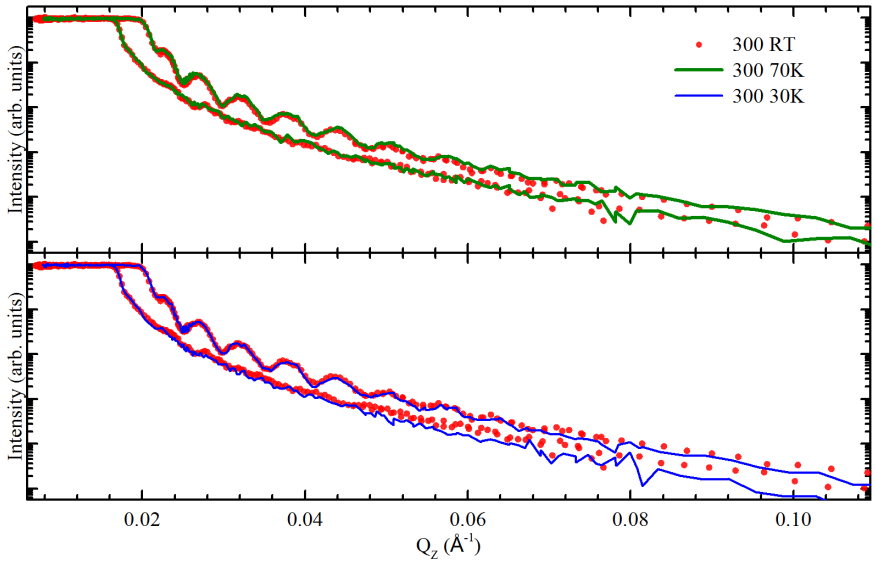


Figure 7.35: PNR data for MgO 300 at three different temperatures. Graphs are split and compared to 306 K in order to observe the differences in magnetism and roughness over the larger $Q$ range with respects to the reference data.

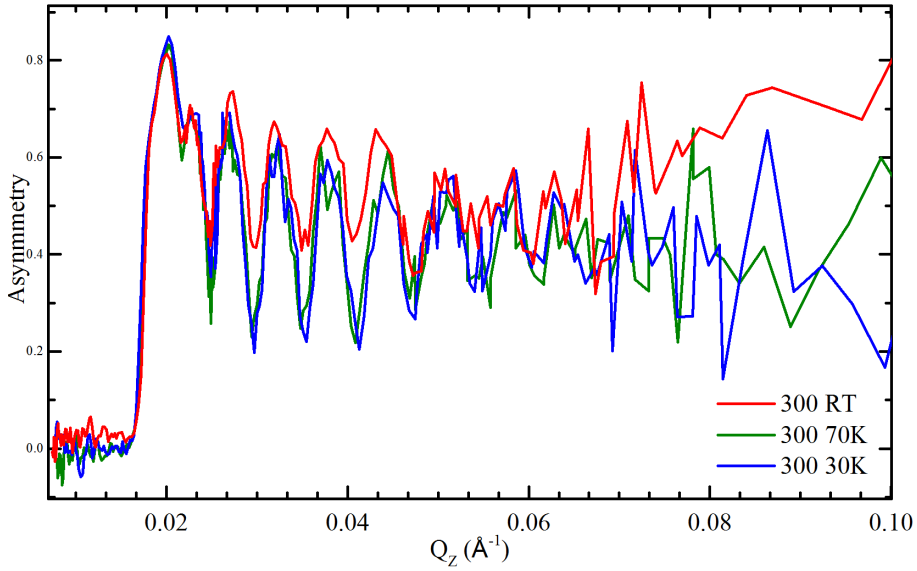


Figure 7.36: Asymmetry curve of MgO 300 to enhance the difference between PNR+ and PNR− highlighting the magnetic contribution within the film. The difference in magnetism below the Verwey transition is enhanced.

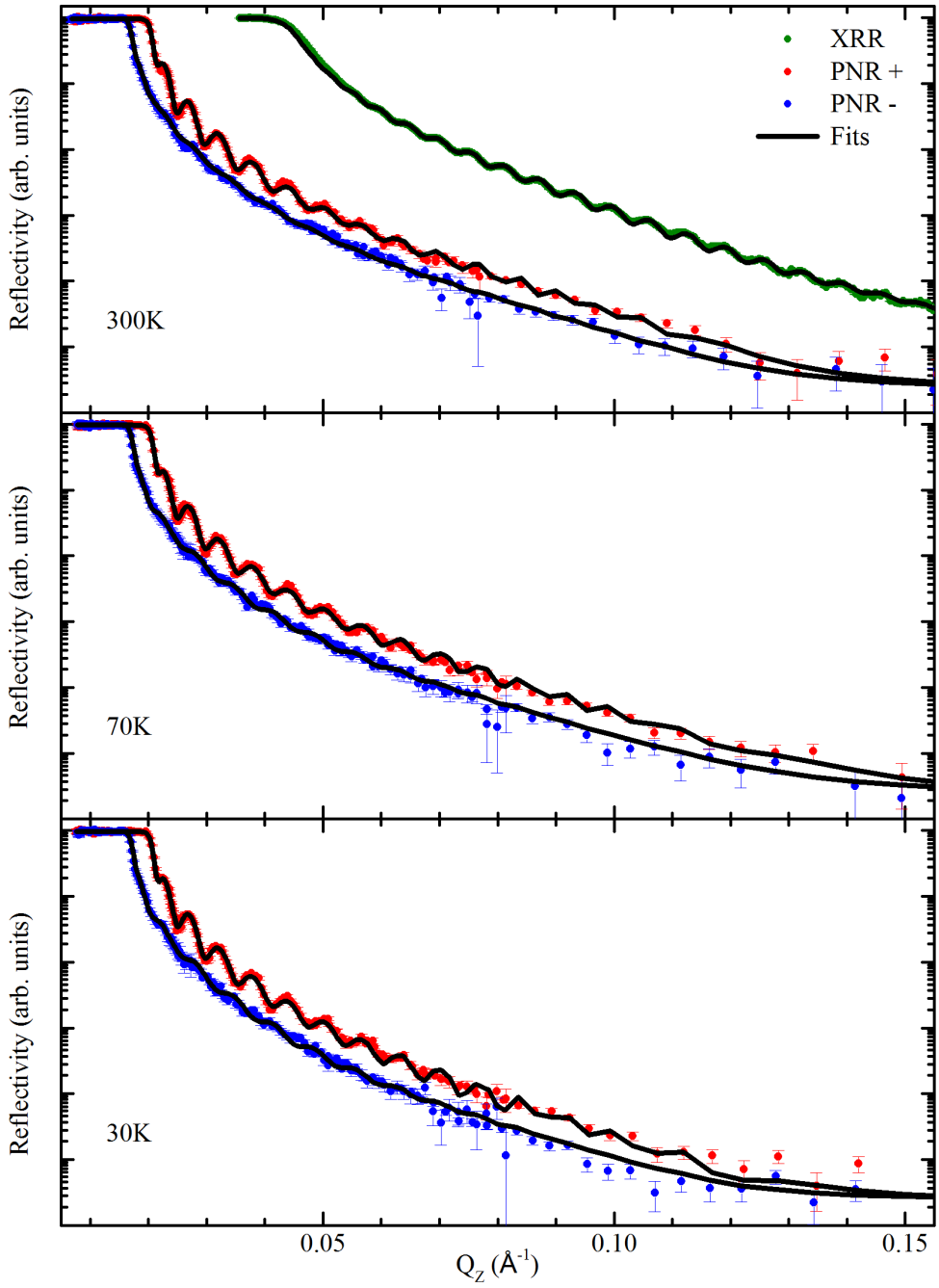


Figure 7.37: MgO 300 fits to PNR data for specified temperatures.

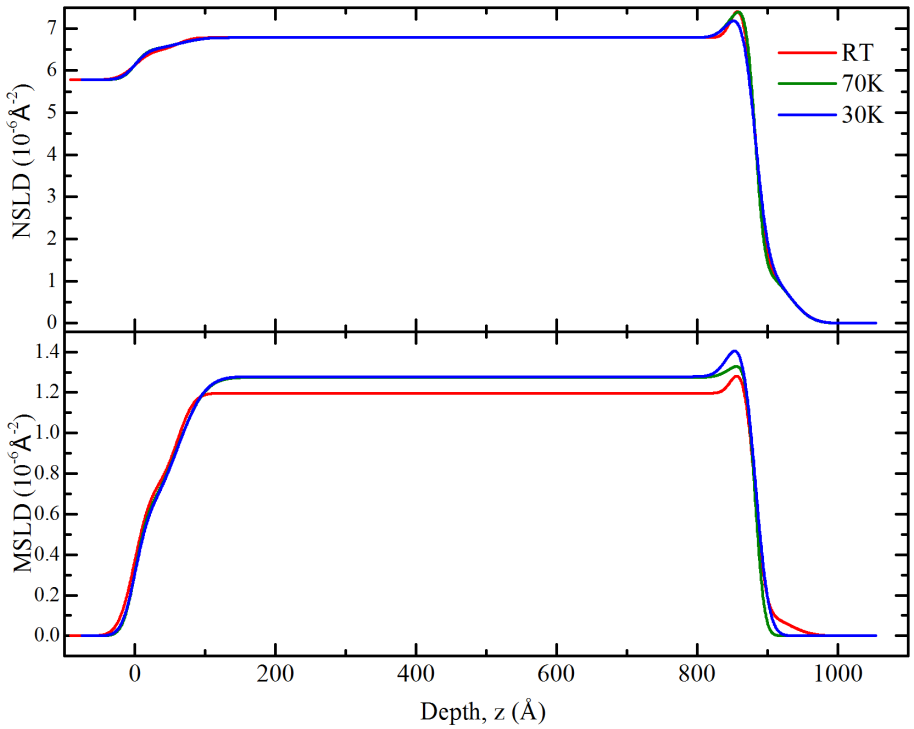


Figure 7.38: Fitted MgO 300 nuclear and magnetic profiles from Figure 7.35, in order to compare the effect that temperature change has on the $Fe_3O_4$ thin film.

### 7.3.2 Low Temperature Comparison

The high temperature annealing of MgO 950 appears to freeze the magnetic structure of the $Fe_3O_4$ thin film even when reducing the temperature of the material though $T_V$. This suggests that the magnetic properties can be reliable over a large temperature range. For sample MgO 300 post-annealed at a lower temperature, there are changes past $T_V$ and minimal changes at the lower temperature 30 K. A change in magnetism over the Verwey transition is a sign of a good quality film. MgO 400 is known to be a non-standard post-annealed sample, and changes are seen through all temperature variations. Table 7.4 compares all the magnetic moment values for the samples over the experimental temperature range. None reach the theoretical half-metallic value, suggesting better quality films are needed in order for them to be half-metallic. It is apparent through the fitting procedure that more variation is needed for the magnetic profiles when varying the temperature due to the parameter's maximum allowed values being reached. Allowing layer thicknesses to change without simultaneous fitting with other data sets wouldn't limit neutron data to the fitted SLD values previously modelled. Fitting simultaneously with 306 K XRR has not delivered results, suggesting a non standard change in magnetic profile is needed. Further work would need to use another modelling environment in GenX called "mag_refl" which would allow the MSLD to fit more freely without changing the NSLD. Allowing all data sets (varying temperatures) to fit simultaneously would also help refine the fit but increase computing time. Low temperature magnetometry must be performed to corroborate the increase in magnet moment observed when the sample temperature is lower than $T_V$.

Table 7.4: A comparison of the magnetic moment values extracted from the reflectivity fits for each MgO sample at the different experimental temperatures. Moment values are in $\mu_B$/f.u..

| Sample | 306 K | 70 K | 30 K |
|---|---|---|---|
| MgO 950 | 3.4(2) | 3.4(2) | 3.4(2) |
| MgO 300 | 3.4(2) | 3.7(2) | 3.7(2) |
| MgO 400 | 2.6(1) | 3.0(1) | 3.1(1) |

## 7.4 Conclusion

A growth and Verwey transition study has been performed on $Fe_3O_4$ thin films grown on MgO(111) orientated substrates. Samples of post-annealing temperatures 950 °C, 400 °C and 350 °C were analysed structurally and magnetically at 306 K in an attempt to understand the crystal quality and the effect on the magnetic depth profile within the film. Surprisingly, the epitaxial relationship between the substrate and film was MgO(111)‖$Fe_3O_4$(100), which must be due to growth conditions, and further TEM and XRD analysis is needed to understand the origins and how they are epitaxially related. It was found that the sample MgO 400 seemed unusual when compared to previous samples and the other two in the growth study, suggesting an error in the growth recipe. MgO 300 and 950 are samples with the same average composition and magnetism at 306 K, but different crystallographic orientations. The magnetic behaviour below $T_V$ is different where 950 had no magnetic transition and 300 increases in magnetism. MgO 400 increases in magnetism below $T_V$ and increases further at lower temperature 30 K. Further analysis needs to be performed on MgO 950 to ensure the accuracy of the XSLD and NSLD. Both MgO 300 and 400 require a different style of modelling for the lower temperature data where interfaces are sliced at small intervals in order to be able to change the roughness profiles without overlapping in the error functions used to model the roughness. This will give the freedom to vary the magnetic profile independently from the boundaries defining the NSLD, as the magnetism does not seem to be aligned to the structure of the material when the temperature is lowered, as observed by the model parameters being too confined.

# Chapter 8

# Conclusion

In this thesis depth dependent nuclear and magnetic profiles have been obtained for half-metallic thin film materials via the robust fitting of polarised neutron reflectivity data. Many other techniques, such as microscopy and X-ray diffraction, have been used both to aid fitting, and corroborate features in the extracted profiles. In each results chapter this thesis has demonstrated different modelling techniques required to confirm the accuracy of the profiles found and different fitting obstacles that have had to be overcome in order to model the data. The biggest challenge when fitting reflectivity data is decoupling parameters.

When modelling the PNR data for CFAS grown on Si (111) in Chapter 5, a 10% change in the film density and a large ill-defined 150 Å interfacial layer gave doubt to the accuracy of the fit. A new model was sought to test the validity of the original model. EELS microscopy data was used to build the compositional SL at the interface, and modify the main film composition. The new model had a similar quality of fit with a more defined interfacial region. A third model was fabricated closly relating to the second, but allowing the parameters more adjustment. The third model was deemed to be the best fit and verification was taken from complementary experimental techniques. During the fitting process it was found that large interfacial and surface regions give the SLD the ability to switch potential steps to either side of the main film. As the neutron and X-ray wavevector scatters at changes in potential barrier height, conservation of these at different locations in the SLD produces similar Kiessig fringes. From the three models a robust magnetic profile was found despite the differences in SLD. Large interface profiles created issues relating to the definition of the substrate z = '0' position where the best option was to normalise to the centre of the robust magnetic profile. Complementary data was used to confirm a final model and a magnetic moment of 4.9 $\mu_B$/f.u., which is lower

than the theorised 5.5 $\mu_B$/f.u.. There was also a drop in magnetism to zero before the SLD profile has stopped varying (before the bulk substrate value is constant), showing a magnetically dead region. EELS data and theoretical DFT calculations confirmed that the drop in magnetism is due to Si out diffusion from the substrate into the film. EELS at the surface also confirmed a Co depleted layer as seen in all NSLD, indicated by a peak. It was discovered that for complex alloys such as $Co_2FeAl_{0.5}Si_{0.5}$ and fitting both neutron and X-ray probes simultaneously, it is advisable to fit composition while keeping density at nominal value, in order to allow for different sensitivities to the elements for the individual probes.

Due to the CFAS/Si(111) sample no longer existing, further work would be based on a different modelling technique for the PNR data. As the density was varied in this set of fits where more flexibility is needed for the parameters, another model could be made where the composition varies. Due to successful extraction of the magnetic profile from the PNR data from three different models, it is unlikely that a different magnetic profile would be found.

The same CFAS material was seen in Chapter 6 but this time grown on Ge(111). The interface region was predicted to be minimised due to closer lattice matching and the inability for Si diffusion from the substrate. The model was fitted this time, varying composition and keeping density constant, learning of the complexity of materials from the previous chapter. The final model was found to have an interface thickness of only 18 Å. There is a drop in magnetic moment over this region but magnetism is retained up to the substrate with no dead region. The film also exhibits a magnetic moment of 5.5 $\mu_B$/f.u., in agreement with theoretical predictions for this material, indicating the possibility of an experimentally observed half-metallic material. The minimal interface region limited the switching possibilities of the potential steps and therefore removed the need for further investigation into modelling. Complementary techniques confirmed interfacial thickness.

The second part of Chapter 6 studied whether this film is reproducible; a necessity for mass production of devices. Robust modelling was needed in this case, due to the lack of complementary techniques available. The second Ge sample ("Ge2") was found to have both the same film thickness, interface thickness and very similar SLD and MSLD, confirming reproducibility. A large surface region was found on this secondary sample, but the origin was not confirmed, with the possibility of experimental mishap.

Further work for CFAS/Ge(111) would be to retake the Ge2 XRR data to verify the large surface profile. Magnetometry data is also useful for these samples to confirm the same saturation magnetisation and therefore give confidence to the

moment value extracted. TEM images could be another option of confirming the similar interfacial region of Ge2 and also observe surface anomalies.

Chapter 7 is also split into two parts. It focuses on thin film $Fe_3O_4$ grown on MgO(111) where different post-annealing temperatures (950 °C, 400 °C and 350 °C) have affected the properties of the film. Firstly an in-depth structural and magnetic review is completed at room temperature. TEM shows poor quality substrates with epitaxial $Fe_3O_4$ films on top that have defects and intermixing of crystal structures with interface regions between 2 nm and 5 nm. XRD reveals an unusual epitaxial relationship of MgO(111)$\|$$Fe_3O_4$ (100) for all samples with mixed film orientations of (111) and (100) in the sample annealed at 300 °C. Comparison of magnetometry data immediately distinguishes the sample annealed at 400 °C as a flawed growth due to its reduced average magnetism. Fringe thickness is similar for all samples in the XRR data indicating this is not due to reduced sample volume. A magnetisation reduction is confirmed by comparing PNR data, where the splitting of the critical edges is smaller than that of sample 300 and 950. Growth errors in MgO 400 are confirmed by fitting the reflectivity data and finding drastically different sample SLD profiles. MgO 300 and 950 are found to be near identical with a the same SLD and MSLD, but a different thickness and slight variations at the interface. No sample is found to have a magnetic moment of 4 $\mu_B$/f.u. as theorised for the half-metal, assuming accurate fitting of the data. Fe rich layers are found in all samples, possibly due to the post-annealing in a $CO/CO_2$ mix removing O atoms from the sample surface. Confirmation of successful moment extraction is found by finding the integral of the MSLD and dividing the magnetometry data by this value exhibiting a normalisation of all hysteresis loops.

Secondly the affect of the Verwey transition on the magnetic moment of the thin films is probed by temperature varied PNR measurements. Fitted SLDs from the RT measurements are used to limit the fit and the roughness and magnetic moment values are allowed to adjust. It was found that MgO 950 has no change in magnetism at lower temperatures. In contrast MgO 300 has an increase in magnetism below $T_V$ suggesting a better quality film due to the presence of a transition. MgO 400 has two increases in magnetism, one below $T_V$ and another at 30 K. It is apparent that high post-annealing temperatures limit the ability for a transition. Magnetic moment values below $T_V$ are still lower than the theorised half-metallic value.

Further work for the MgO samples could include temperature dependent magnetometry. This would confirm the change in magnetism as the temperature is decreased. Temperature dependent XRD would also give more insight into how

the change in structure across the Verwey transition is related to the increase in magnetic moment. Further analysis needs to be performed on the experimental data already obtained for these MgO films, especially the TEM images, to gain insight into the reasons for the unusual epitaxial relationship and how the different crystal orientations affect the magnetism. It is apparent while fitting the low temperature PNR data that the MSLD requires more freedom to fit the data. Converting the model into a different GenX profile, including slicing and independent movement of the MSLD will enable this and a better fit may be obtained.

Further experiments to limit the parameter values of the PNR data is always useful. Experiments such as energy dependent XRR would give an accurate value of the average sample density and therefore limit this parameter. From there, the SL can better be determined and any extracted sample characteristics, such as decreases in magnetism, can be linked to off stoichiometric composition. It has also been observed (not shown in this thesis) that XRR measurements taken at different intervals can help limit the data, as any observable changes will be due to the surface only, and not the bulk of the thin film. The PNR data can then be fitted alongside XRR taken at a similar time to the PNR experiment, and a later XRR measurement with the surface allowed to vary.

# Bibliography


[1] A. Paul. *Low-Angle Polarised Neutron and X-Ray Scattering from Magnetic Nanolayers and Nanostructures*. Springer, 2017. ISBN 9783319632247. doi: 10.1007/978-3-319-63224-7.

[2] C. Fong, J. Pask, and L. Yang. *Half-Metallic Materials and Their Properties*, volume 2, chapter *Half-Metallic Oxides*, pages 141–204. Imperial College Press, 2013. doi: 10.1142/9781908977137/0002.

[3] C. S. Kelley. *Spatially Resolved Infrared Spectroscopy for Spintronics*. Ph.D. Thesis, University of York, Feb 2014.

[4] E. Hirota, H. Sakakima, and K. Inomata. *Giant Magneto-Resistance Devices*. Springer-Verlag Berlin Heidelberg, 2002. doi: 10.1142/9781908977137/0002.

[5] Z. Nedelkoski. *The atomic and spin-electronic structure of interfaces and extended structural defects in the Co-based full Heusler alloys*. Ph.D. Thesis, University of York, Jan 2017.

[6] S. Ikeda, J. Hayakawa, Y. Ashizawa, Y. M. Lee, K. Miura, H. Hasegawa, M. Tsunoda, F. Matsukura, and H. Ohno. Tunnel magnetoresistance of 604% at 300K by suppression of Ta diffusion in CoFeBMgOCoFeB pseudo-spin-valves annealed at high temperature. *Applied Physics Letters*, 93(8):082508, 2008.

[7] H. Fecher and C. Felser. *Spintronics From Materials to Devices*. Springer, 2010. ISBN 978-90-481-3831-9. doi: 10.1007/978-90-481-3832-6.

[8] I. I. Mazin. How to define and calculate the degree of spin polarization in ferromagnets. *Phys. Rev. Lett.*, 83:1427–1430, Aug 1999.

[9] P. A. Dowben, N. Wu, and C. Binek. When measured spin polarization is not spin polarization. *Journal of Physics: Condensed Matter*, 23(17):171001, 2011.

[10] R. J. Soulen, J. M. Byers, M. S. Osofsky, B. Nadgorny, T. Ambrose, S. F. Cheng, P. R. Broussard, C. T. Tanaka, J. Nowak, J. S. Moodera, A. Barry, and J. M. D. Coey. Measuring the spin polarization of a metal with a superconducting point contact. 282(5386):85–88, 1998.

[11] R. J. Soulen, J. M. Byers, M. S. Osofsky, B. Nadgorny, T. Ambrose, S. F. Cheng, P. R. Broussard, C. T. Tanaka, J. Nowak, J. S. Moodera, A. Barry, and J. M. D. Coey. Measuring the spin polarization of a metal with a superconducting point contact. *Science*, 282(5386):85–88, 1998.

[12] A. F. Andreev. The thermal conductivity of the intermediate state in superconductors. *Soviet Physics JETP*, 19, Nov 1964.

[13] C. T. Tanaka, J. Nowak, and J. S. Moodera. Spin-polarized tunnelling in a half-metallic ferromagnet. *Journal of Applied Physics*, 86(11):6239–6242, 1999.

[14] K. P. Kämper, W. Schmitt, G. Güntherodt, R. J. Gambino, and R. Ruf. $Cro_2^-$ A New Half-Metallic Ferromagnet? *Phys. Rev. Lett.*, 59:2788–2791, Dec 1987.

[15] D. Kersh. *Electronic structure studies of exotic phenomena using magnetic Compton scattering.* Ph.D. Thesis, University of Warwick, January 2016.

[16] J. A. Duffy, J. W. Taylor, S. B. Dugdale, C. Shenton-Taylor, M. W. Butchers, S. R. Giblin, M. J. Cooper, Y. Sakurai, and M. Itou. Spin and orbital moments in $fe_3o_4$. *Phys. Rev. B*, 81:134424, Apr 2010.

[17] A. Hirohata and K. Takanashi. Future perspectives for spintronic devices. *Journal of Physics D: Applied Physics*, 47(19):193001, 2014.

[18] C. Burrows. *Growth and Characterisation on MnSb Thin Films and Interfaces.* Ph.D. Thesis, University of Warwick, August 2012.

[19] B. Huang, D. J. Monsma, and I. Appelbaum. Coherent spin transport through a 350 micron thick silicon wafer. *Phys. Rev. Lett.*, 99:177209, Oct 2007.

[20] C. Zucchetti, F. Bottegoni, C. Vergnaud, F. Ciccacci, G. Isella, L. Ghirardini, M. Celebrano, F. Rortais, A. Ferrari, A. Marty, M. Finazzi, and M. Jamet. Imaging spin diffusion in germanium at room temperature. *Phys. Rev. B*, 96: 014403, Jul 2017.

[21] C. J. Palstrøm. Heusler compounds and spintronics. *Progress in Crystal Growth and Characterization of Materials*, 62(2):371 – 397, 2016. Special Issue:

Recent Progress on Fundamentals and Applications of Crystal Growth; Proceedings of the 16th International Summer School on Crystal Growth (ISSCG-16).

[22] R. A. de Groot, F. M. Mueller, P. G. v. Engen, and K. H. J. Buschow. New class of materials: Half-metallic ferromagnets. *Phys. Rev. Lett.*, 50:2024–2027, Jun 1983.

[23] M. Björck and G. Andersson. Genx: an extensible X-ray reflectivity refinement program utilizing differential evolution. *Journal of Applied Crystallography*, 40:1174–1178, 2007.

[24] C. Fong, J. Pask, and L. Yang. *Half-Metallic Materials and Their Properties*, volume 2, chapter *Methods of Studying Half-metals*, pages 15–75. Imperial College Press, 2013.

[25] R. Cook. *The development of magnetic granulometry for application to heterogeneous catalysts.* Phd thesis, University of Warwick, May 2014.

[26] F. Hofer, F. P. Schmidt, W. Grogger, and G. Kothleitner. Fundamentals of electron energy-loss spectroscopy. *IOP Conference Series: Materials Science and Engineering*, 109(1):012007, 2016.

[27] B. Cullity. *Elements of X-ray Diffraction.* Addison Wesley, 1956.

[28] H. Fritzsche, J. Huot, and D. Fruchart. *Neutron Scattering and Other Nuclear Techniques for Hydrogen in Materials*, chapter Neutron Reflectometry. Springer International Publishing Switzerland, 2016. ISBN 978-3-319-22792-4.

[29] M. Birkholz. *Thin Film Analysis by X-ray Scattering.* Wiley, 2005. ISBN 9783527310524.

[30] J. Daillant and A. Gibaud. *X-ray and Neutron Reflectivity: Principles and Applications*, chapter Experiments on Solid Surfaces, pages 217–231. Lecture Notes in Physics. Springer, 1999. ISBN 9783540885887.

[31] P. Gutfreund, T. Saerbeck, M. A. Gonzalez, E. Pellegrini, M. Laver, C. Dewhurst, and R. Cubitt. Towards generalized data reduction on a chopper-based time-of-flight neutron reflectometer. *Journal of Applied Crystallography*, 51(3), Jun 2018.

[32] D17 - neutron reflectomeer with horizontal scattering geometry - description. URL https://www.ill.eu/users/instruments/instruments-list/d17/description/instrument-layout/.

[33] H. Zabel, K. Theis-Bröhl, and B. P. Toperverg. *Handbook of Magnetism and Advanced Magnetic Materials*, chapter Polarized Neutron Reflectivity and Scattering from Magnetic Nanostructures and Spintronic Materials. John Wiley and Sons, Ltd, 2007. ISBN 9780470022184.

[34] G. Shirane, S. M. Shapiro, and J. M. Tranquanda. *Neutron Scattering with a Triple-Axis Spectrometer*. Cambridge University Press, 2004. ISBN 0-511-03732-5.

[35] M. Björck. *A structural viewpoint of magnetism in Fe and Co based Superlattices*. Ph.D. Thesis, University of Uppsala, 2007.

[36] G. P. Felcher. Neutron reflectometry as a tool to study magnetism (invited). *Journal of Applied Physics*, 87(9):5431–5436, 2000.

[37] F. de Bergevin. *The Interaction of X-Rays (and Neutrons) with Matter*, pages 85–132. Lecture Notes in Physics. Springer, 2009. ISBN 978-3-540-885887-0.

[38] L. G. Parratt. Surface studies of solids by total reflection of x-rays. *Phys. Rev.*, 95:359–369, Jul 1954.

[39] Caruana, A.J. *Pulsed Laser Deposition of WOx and FeOx thin films*. Phd thesis, Loughborough University, August 2015.

[40] D. Burn. *Domain wall behaviour in ferromagnetic nanowires with interfacial and geometrical structuring*. PhD Thesis, Durham University, 2013.

[41] J. B. Hayter and H. A. Mook. Discrete thin-film multilayer design for X-ray and neutron supermirrors. *Journal of Applied Crystallography*, 22(1):35–41, Feb 1989.

[42] A. Gibaud and G. Vignaud. *X-ray and Neutron Reflectivity: Principles and Applications: Specular Reflectivity from Smooth and Rough Surfaces*, pages 85–132. Lecture Notes in Physics. Springer, 2009. ISBN 978-3-540-885887-0.

[43] T. Hase. *X-ray Scattering from magnetic metallic multilayers*. PhD Thesis, Durham University, 1998.

[44] C. Fermon, F. Ott, and A. Menelle. *X-ray and Neutron Reflectivity: Principles and Applications: Neutron Reflectivity*, pages 183–234. Lecture Notes in Physics. Springer, 2009. ISBN 978-3-540-885887-0.

[45] J. Penfold and R. K. Thomas. The application of the specular reflection of neutrons to the study of surfaces and interfaces. *Journal of Physics: Condensed Matter*, 2(6):1369, 1990.

[46] F. Ott. Neutron studies of magnetic oxide thin films. *Journal of Physics: Condensed Matter*, 20(26):264009, 2008.

[47] A. Dianoux and G. Lander. *Neutron Data Booklet*. Old City Publishing. ISBN 0-9704143-7-4.

[48] T. Gutberlet. Reflectometry with X-rays and Neutrons. URL https://www.psi.ch/sinq/amor/ManualsEN/Zuoz2006.pdf.

[49] T. Chatterji. *Magnetic Neutron Scattering*, pages 1 – 24. Elsevier Science, Amsterdam, 2006. ISBN 978-0-444-51050-1. doi: https://doi.org/10.1016/B978-044451050-1/50002-1.

[50] J. Schweizer. *Polarized Neutrons and Polarization Analysis*, pages 153 – 213. Elsevier Science, Amsterdam, 2006. ISBN 978-0-444-51050-1. doi: https://doi.org/10.1016/B978-044451050-1/50005-7.

[51] C. Majkrzak, K. O'Donovan, and N. Berk. *Polarized Neutron Reflectometry*, pages 397 – 471. Elsevier Science, Amsterdam, 2006. ISBN 978-0-444-51050-1. doi: https://doi.org/10.1016/B978-044451050-1/50010-0.

[52] R. James. *The optical principles of the diffraction of x-rays*. London: G. Bell and Sons Ltd, 1962.

[53] J. Als-Nielsen and D. McMorrow. *Elements of Modern X-ray Physics*. Wiley, second edition, 2011. ISBN 978-0-470-97394-3.

[54] H. Zabel. X-ray and neutron reflectivity analysis of thin films and superlattices. *Applied Physics A*, 58(3):159–168, Mar 1994.

[55] B. Henke, E. Gullikson, and J. Davis. The atomic scattering factor files. URL http://henke.lbl.gov/optical_constants/asf.html.

[56] H. Kiessig. Interferenz von rntgenstrahlen an dnnen schichten. *Annalen der Physik*, 402(7):769–788, 1931.

[57] A. Munter. Neutron scattering lengths and cross sections. URL https://www.ncnr.nist.gov/resources/n-lengths/.

[58] V. F. Sears. Neutron scattering lengths and cross sections. *Neutron News*, 3: 26–37, 1992.

[59] E. Chason and T. Mayer. Thin film and surface characterization by specular X-ray reflectivity. *Critical Reviews in Solid State and Materials Sciences*, 22 (1):1–67, 1997.

[60] L. Névot and P. Croce. Characterisaiton of surfaces by grazing reflection of X-rays. Application to the study of polishing of silicate glasses. *Rev. Phys. Appl.*, 15:761–779, 1980.

[61] S. K. Sinha, E. B. Sirota, S. Garoff, and H. B. Stanley. X-ray and neutron scattering from rough surfaces. *Phys. Rev. B*, 38:2297–2311, 1988.

[62] M. Björck. Fitting with differential evolution: an introduction and evaluation. *Journal of Applied Crystallography*, 44(6), 12 2011.

[63] M. Tolan. *X-ray Scattering from Soft-Matter Thin Films*. Springer-Verlag Berlin Heidelberg, 1999. ISBN 978-3-540-49525-3.

[64] Y. Zhu. *Modern Techniques for Characterizing Magnetic Materials*. Springer US, 2005. ISBN 978-0-387-23395-6.

[65] A. Gibaud, G. Vignaud, and S. K. Sinha. The correction of geometrical factors in the analysis of X-ray reflectivity. *Acta Crystallographica Section A*, 49(4): 642–648, Jul 1993.

[66] M. Björck. Genx. URL http://genx.sourceforge.net/index.html.

[67] H. Fecher and C. Felser. Substituting the main group element in colbalt-iron based Heusler alloys: $Co_2FeAl_{0.5}Si_{0.5}$. *Journal of Physics D: Applied Physics*, 40:1582–1586, 2007.

[68] T. M. Nakatani, A. Rajanikanth, Z. Gercsi, Y. K. Takahashi, K. Inomata, and K. Hono. Structure, magnetic property, and spin polarization of $Co_2FeAl_xSi_{1x}$ Heusler alloys. *Journal of Applied Physics*, 102(3):033916, 2007.

[69] R. Shan, H. Sukegawa, W. Wang, M. Kodzuka, T. Furubayashi, T. Ohkubo, S. Mitani, K. Inomata, and K. Hono. Demonstration of half-metallicity in

fermi-level-tuned Heusler alloy $Co_2FeAl_{1-x}Si_x$ at room temperature. *Physical Review Letters*, 102:246601, 2009.

[70] M. Vahidi, J. A. Gifford, S. K. Zhang, S. Krishnamurthy, Z. G. Yu, L. Yu, M. Huang, C. Youngbull, T. Y. Chen, and N. Newman. Fabrication of highly spin-polarized $Co_2FeAl_{0.5}Si_{0.5}$ thin-films. *APL Materials*, 2(4):046108, 2014.

[71] W. Wang, H. Sukegawa, R. Shan, and K. Inomata. Large tunnel magnetoresistance in $Co_2FeAl_{0.5}Si_{0.5}$/mgo $Co_2FeAl_{0.5}Si_{0.5}$magnetic tunnel junctions prepared on thermally oxidized si substrates with mgo buffer. *Applied Physics Letters*, 93(18):182504, 2008.

[72] N. Tezuka, N. Ikeda, A. Miyazaki, S. Sugimoto, M. Kikuchi, and K. Inomata. Tunnel magnetoresistance for junctions with epitaxial full-heusler $Co_2FeAl_{0.5}Si_{0.5}$ electrodes with b2 and l21 structures. *Applied Physics Letters*, 89(11):112514, 2006.

[73] I. Galanakis, P. H. Dederichs, and N. Papanikolaou. Slater-pauling behavior and origin of the half-metallicity of the full-Heusler alloys. *Phys. Rev. B*, 66: 174429, Nov 2002.

[74] P. Hasnip, C. Loach, J. Smith, M. Probert, D. Gilks, J. Sizeland, K. Yoshida, M. Oogane, A. Hirohata, and V. Lazarov. B2 atomic disorder in $Co_2FeAl_{0.5}Si_{0.5}$ /Si Heusler alloys. *Journal of the Magnetics Society of Japan*, 38:50–55, 2014.

[75] B. Peters, A. Alfonsov, C. G. F. Blum, S. J. Hageman, P. M. Woodward, S. Wurmehl, B. Bchner, and F. Y. Yang. Epitaxial films of heusler compound co2feal0.5si0.5 with high crystalline quality grown by off-axis sputtering. *Applied Physics Letters*, 103(16):162404, 2013.

[76] T. Saito, N. Tezuka, and S. Sugimoto. Structural and magnetic properties of $Co_2FeAl_{0.5}Si_{0.5}$ full-heusler alloy thin films on gaas substrates. *MATERIALS TRANSACTIONS*, 52(3):370–373, 2011.

[77] H. Fecher and A. Hirohata. *Heusler Alloys*. Springer, 2016. ISBN 978-3-319-21449-8. doi: 10.1007/978-3-319-21449-8.

[78] K. Tanikawa, S. Oki, S. Yamada, M. Kawano, M. Miyao, and K. Hamaya. High quality cfas heterostructures for spin injection in silicon spintronic devices. *Thin Solid Films*, 557:390–393, 2014.

[79] S. Yamada, K. Tanikawa, S. Oki, M. Kawano, M. Miyao, and K. Hamaya. Improvement of magnetic and structural stabilities in high-quality cfas heterointerfaces. *Applied Physics Letters*, 105:29–31, 2014.

[80] B. Kuerbanjiang, Z. Nedelkoski, D. Kepaptsoglou, A. Ghasemi, S. E. Glover, S. Yamada, T. Saerbeck, Q. M. Ramasse, J. Hasnip, T. P. A. Hase, G. R. Bell, K. Hamaya, and A. Hirohata. The role of chemical structure on the magnetic and electronic properties of $Co_2FeAl_{0.5}Si_{0.5}$. *Applied Physics Letters*, 108(172412), 2016.

[81] C. Koch. *Determination of Core Structure Periodicity and Point Defect Density Along Dislocations*. Ph.D. Thesis, Arizona State University, May 2002.

[82] P. Zaumseil. High-resolution characterization of the forbidden Si 200 and Si 222 reflections. *Journal of Applied Crystallography*, 48(2):528–532, Apr 2015.

[83] S. E. Glover, T. Saerbeck, B. Kuerbanjiang, A. Ghasemi, D. Kepaptsoglou, Q. M. Ramasse, S. Yamada, K. Hamaya, T. P. A. Hase, V. K. Lazarov, and G. R. Bell. Magnetic and structural depth profiles of Heusler alloy $Co_2FeAl_{0.5}Si_{0.5}$ epitaxial films on Si(111). *Journal of Physics: Condensed Matter*, 30(6):065801, 2018.

[84] OriginLab, Northampton, and MA. Origin, 2016.

[85] Z. Nedelkoski, B. Kuerbanjiang, S. E. Glover, A. M. Sanchez, D. Kepaptsoglou, A. Ghasemi, C. W. Burrows, S. Yamada, K. Hamaya, Q. M. Ramasse, P. J. Hasnip, T. P. A. Hase, G. R. Bell, A. Hirohata, and V. K. Lazarov. Realisation of magnetically and atomically abrupt half-metal/semiconductor interface: $Co_2FeAl_{0.5}Si_{0.5}$ / Ge(111). *Scientific Reports*, 6:37282, 2016.

[86] Z. Zhang and S. Satpathy. Electron states, magnetism, and the verwey transition in magnetite. *Phys. Rev. B*, 44:13319–13331, Dec 1991.

[87] S. van Dijken, X. Fain, S. M. Watts, K. Nakajima, and J. Coey. Magnetoresistance of Fe3O4/Au/Fe3O4 and Fe3O4/Au/Fe spin-valve structures. *Journal of Magnetism and Magnetic Materials*, 280(2):322 – 326, 2004.

[88] D. Gilks. *Atomistic study of magnetite thin film interfaces and defects for Spintronic applications*. Ph.d. thesis, University of York, June 2015.

[89] Spin-resolved photoelectron spectroscopy of fe3o4. *Surface Science*, 513(3): L451 – L457, 2002.

[90] M. Fonin, Y. S. Dedkov, R. Pentcheva, U. Rüdiger, and G. Güntherodt. Magnetite: a search for the half-metallic state. *Journal of Physics: Condensed Matter*, 19(31):315217.

[91] J. G. Tobin, S. A. Morton, S. W. Yu, G. D. Waddill, I. K. Schuller, and S. A. Chambers. Spin resolved photoelectron spectroscopy of fe 3 o 4 : the case against half-metallicity. *Journal of Physics: Condensed Matter*, 19(31): 315218, 2007.

[92] D. J. Huang, C. F. Chang, H.-T. Jeng, G. Y. Guo, H.-J. Lin, W. B. Wu, H. C. Ku, A. Fujimori, Y. Takahashi, and C. T. Chen. Spin and orbital magnetic moments of $fe_3o_4$. *Phys. Rev. Lett.*, 93:077204, Aug 2004.

[93] W. Q. Liu, Y. B. Xu, P. K. J. Wong, N. J. Maltby, S. P. Li, X. F. Wang, J. Du, B. You, J. Wu, P. Bencok, and R. Zhang. Spin and orbital moments of nanoscale fe3o4 epitaxial thin film on mgo/gaas(100). *Applied Physics Letters*, 104(14):142407, 2014.

[94] C. M. Fang, G. A. de Wijs, and R. A. de Groot. Spin-polarization in half-metals (invited). *Journal of Applied Physics*, 91(10):8340–8344, 2002.

[95] E. Verwey. Electronic conduction of magnetite ($Fe_3O_4$) and its transition point at low temperatures. *Nature*, 144(12):327–328, 1939.

[96] D. T. Margulies, F. T. Parker, M. L. Rudee, F. E. Spada, J. N. Chapman, P. R. Aitchison, and A. E. Berkowitz. Origin of the anomalous magnetic behavior in single crystal $Fe_3O_4$ films. *Phys. Rev. Lett.*, 79:5162–5165, Dec 1997.

[97] S. Celotto, W. Eerenstein, and T. Hibma. Characterization of anti-phase boundaries in epitaxial magnetite films. *The European Physical Journal B: Condensed Matter and Complex Systems*, 36(2):271–279, 2003.

[98] D. Gilks, L. Lari, K. Matsuzaki, H. Hosono, T. Susaki, and V. K. Lazarov. Structural study of $Fe_3O_4$ (111) thin films with bulk like magnetic and magnetotransport behaviour. *Journal of Applied Physics*, 115(17):17C107, 2014.

[99] K. Matsuzaki, V. K. Lazarov, L. Lari, H. Hosono, and T. Susaki. $Fe_3O_4$ (111) thin films with bulk-like properties: growth and atomic characterization. *Journal of Physics D: Applied Physics*, 46(2):022001, 2013.

[100] L. S. Darken and R. W. Gurry. The system ironoxygen. ii. equilibrium and thermodynamics of liquid oxide and other phases. *Journal of the American Chemical Society*, 68(5):798–816, 1946.

[101] K. Matsuzaki, V. K. Lazarov, L. Lari, H. Hosono, and T. Susaki. $Fe_3O_4$ (111) thin films with bulk-like properties: growth and atomic characterization. *Journal of Physics D: Applied Physics*, 46(2):022001, 2013.

[102] S. Yuasa, T. Nagahama, A. Fukushima, Y. Suzuki, and K. Ando. Giant room-temperature mangetoresistance in single-crystal Fe/MgO/Fe magnetic tunnel junctions. *Applied Physics Letters*, 105:29–31, 2014.

[103] V. K. Lazarov, M. Weinert, S. A. Chambers, and M. Gajdardziska-Josifovska. Atomic and electronic structure of the $Fe_3O_4$ (111) / MgO (111) model polar oxide interface. *Phys. Rev. B*, 72:195401, Nov 2005.

[104] E. Verwey and P. Haayman. Electronic conductivity and transition point of magnetite (fe3o4). *Physica*, 8(9):979 – 987, 1941.

[105] W. C. Hamilton. Neutron diffraction investigation of the 119°k transition in magnetite. *Phys. Rev.*, 110:1050–1057, Jun 1958.

[106] J. P. Wright, J. P. Attfield, and P. G. Radaelli. Charge ordered structure of magnetite $fe_3o_4$ below the verwey transition. *Phys. Rev. B*, 66:214422, Dec 2002.

[107] M. Iizumi and G. Shirane. Crystal symmetry of the low temperature phase of magnetite. *Solid State Communications*, 17(4):433 – 436, 1975.

[108] L. R. Bickford. Ferromagnetic resonance absorption magnetite. *Phys. Rev.*, 76:137–138, Jul 1949.

[109] M. Bohra, S. Prasad, N. Venketaramani, N. Kumar, S. Sahoo, and R. Krishnan. Magnetic properties of magnetite thin films close to the verwey transition. *Journal of Magnetism and Magnetic Materials*, 321(22):3738 – 3741, 2009.

[110] J. P. Wright, J. P. Attfield, and P. G. Radaelli. Charge ordered structure of magnetite $Fe_3O_4$ below the verwey transition. *Phys. Rev. B*, 66:214422, Dec 2002.